

# **Block copolymers – Nanoreactors for the synthesis of coordination polymers**

Dissertation

zur Erlangung des akademischen Grades eines Doktors  
der Naturwissenschaften (Dr. rer. nat.)  
in der Bayreuther Graduiertenschule für Mathematik und  
Naturwissenschaften (BayNAT) der Universität Bayreuth

vorgelegt von

Christoph Göbel  
geboren in Aschaffenburg  
Bayreuth, 2020



The presented doctoral thesis was prepared at the Department of Chemistry, Professorship for Inorganic Chemistry IV at the University of Bayreuth from 09/2016 until 08/2020 and was supervised by Prof. Dr. Birgit Weber.

This is a full reprint of the thesis submitted to obtain the academic degree of Doctor of Natural Sciences (Dr. rer. nat) and approved by the Bayreuth Graduate School of Mathematical and Natural Sciences (BayNAT) of the University of Bayreuth.

Date of submission: 03.09.2020

Date of defence: 29.01.2021

Acting director: Prof. Dr. Markus Lippitz

Doctoral committee:

Prof. Dr. Birgit Weber (reviewer)

Prof. Dr. Roland Marschall (reviewer)

Prof. Dr. Mukundan Thelakkat (chairman)

Prof. Dr. Rainer Schobert





*Every aspect of the world today  
– even politics and international relations –  
is affected by chemistry.*

Linus Pauling



## Table of Contents

Acknowledgement.....	I
List of Abbreviations.....	III
1. Summary .....	1
2. Zusammenfassung .....	5
3. Introduction.....	9
3.1. Spin crossover in 3d transition metal complexes .....	10
3.2. Nanostructuring of SCO coordination polymers.....	13
3.2.1. The microfluidic approach .....	15
3.2.2. The layer-by-layer technique.....	16
3.2.3. The inverse micelle technique.....	17
3.2.4. Inorganic and polymeric matrices .....	21
3.3. References .....	25
4. Synopsis.....	31
5. Contributions to joint publications.....	45
6. Synthesis of $[\text{Fe}(\text{L}_{\text{eq}})(\text{L}_{\text{ax}})]_n$ coordination polymer nanoparticles using blockcopolymer micelles.....	49
6.1. Introduction .....	50
6.2. Results and Discussion .....	52
6.2.1. Bulk complexes .....	52
6.2.2. Synthesis of the nanocomposite .....	54
6.2.3. Characterisation of the nanocomposite.....	55
6.3. Conclusion .....	59
6.4. Experimental .....	60
6.4.1. Synthesis.....	60
6.4.2. Characterisation methods .....	62
6.5. Acknowledgements.....	63
6.6. References .....	63
6.7. Supporting Information .....	67

7.	Confined Crystallization of Spin-Crossover Nanoparticles in Block-Copolymer Micelles .....	79
7.1.	Introduction .....	80
7.2.	Results and Discussion .....	81
7.3.	Conclusion .....	88
7.4.	Acknowledgements.....	89
7.5.	Conflict of interest .....	90
7.6.	References .....	90
7.7.	Supporting Information .....	93
7.7.1.	Table of Contents.....	93
7.7.2.	General Procedures.....	94
7.7.3.	Synthesis Procedures .....	97
7.7.4.	Characterization .....	98
7.7.5.	References.....	108
7.7.6.	Author Contributions .....	108
8.	Synthesis of Zn-based 1D and 2D coordination polymer nanoparticles in block copolymers	109
8.1.	Introduction .....	110
8.2.	Results and Discussion .....	111
8.2.1.	Synthetic procedures.....	111
8.2.2.	Characterisation of nanocomposites .....	113
8.2.3.	[Zn(OAc) <sub>2</sub> (bipy)] <sub>n</sub> nanocomposites.....	114
8.2.4.	[Zn(TFA) <sub>2</sub> (bppa) <sub>2</sub> ] <sub>n</sub> nanocomposites.....	116
8.3.	Conclusions .....	120
8.4.	Experimental section .....	121
8.4.1.	Materials .....	121
8.4.2.	Computation setting.....	122
8.4.3.	Synthesis.....	123
8.5.	Conflicts of interest.....	125
8.6.	Acknowledgements.....	125
8.7.	Notes and references.....	125

8.8.	Supporting Information .....	132
9.	Size and Shape Control of Spin-Crossover Nanoparticles via Confined Crystallization in Block Copolymer Micelles .....	149
9.1.	Introduction .....	150
9.2.	Results and Discussion .....	151
9.2.1.	Characterization of PS- <i>b</i> -P4VP BCPs: size and shape .....	151
9.2.2.	Characterization of SCO CP-BCP nanocomposites: size, shape, and magnetism ..	154
9.3.	Conclusion .....	166
9.4.	Acknowledgements.....	167
9.5.	References .....	167
9.6.	Supporting Information .....	171
9.6.1.	General Procedures.....	171
9.6.2.	Synthesis Procedures .....	174
9.6.3.	Characterization of the BCPs.....	178
9.6.4.	Characterization of the SCO CP-BCP nanocomposites.....	181
9.6.5.	References.....	207
10.	List of publications.....	209
11.	Contributions to national and international conferences.....	211
12.	(Eidesstattliche) Versicherungen und Erklärungen .....	213



### Acknowledgement

First, I thank my supervisor Prof. Dr. Birgit Weber for giving me the opportunity to do my PhD thesis in her workgroup and providing me with both an interesting and challenging topic. I very much appreciated her mentoring, her support, and the discussions over the years. Thank you for your trust in my chemical comprehension and skills and the freedom I had during my PhD.

Also, thanks to my lab colleagues Hannah Kurz, Sophie Schönfeld, and Dr. Gerald Hörner for providing a good working atmosphere in the lab and being supportive when I needed you. I cannot imagine better colleagues! I also thank the former PhD students of the workgroup that supported me during my under-graduate, graduate and PhD time and from whom I learned a lot for my own PhD thesis: Dr. Tatiana Parlamarciuc, Dr. Stephan Schlamp, Dr. Charles Lochenie, Dr. Ottokar Klimm, Dr. Johannes Weihermüller, and Dr. Katja Dankhoff.

I also thank the Chair of Inorganic Chemistry II for the good collaboration. Special thanks goes to Anna-Maria Dietel for servicing the elemental analysis, to Christine Fell for the IT support, the administrative work and her help during the SQUID fillings, and to Heidi Maisel for her administrative work and for being the contact person for nearly everything. Your experience is golden!

I am very grateful for the synthesis and characterisation of the various block copolymers that have been provided by the Macromolecular Chemistry II, the Keylab Synthesis and Molecular Characterization, and the Bavarian Polymer Institute, especially Prof. Dr. Andreas Greiner, Dr. Holger Schmalz, and Rika Schneider. Without their work on the block copolymers, this thesis would not have been possible.

I thank Dr. Markus Drechsler from the Keylab Electron and Optical Microscopy for his efforts in measuring my samples by cryo-TEM, Patrick Loch, Florian Puchtler, and Dr. Wolfgang Milius from the Chair of Inorganic Chemistry I for measuring the (temperature-dependent) powder X-ray diffraction, Marco Schwarzmann (Inorganic Chemistry I) for the thermogravimetric measurements, Christine Denner (Inorganic Chemistry II) for the scanning electron microscopy, and Prof. Jochen Litterst and Dr. Dirk Baabe for the measurement of the temperature-dependent Mössbauer spectroscopy.

Further thanks go to the mechanics, the glassblowers, the workers at the chemistry counter, and everyone in the purchasing department.

I also thank all my under-graduate, graduate and HiWi students that did some of their laboratory practical work with me during my PhD, namely: Cornelius Fischer, Anna-Lena Fechter, Christian

## Acknowledgement

---

Böhm, Samanta Jänsch, Sandra Schneider, Thomas Bindig, Tamino Rößler, Magdalena Weber, Theresia Brennecke, David Raithel, and Lisa Schönfelder.

A big thanks goes out to my family who supported me throughout my entire chemistry studies and my PhD time. I am so grateful that you gave me the opportunity to go my own way, make my own decisions and in the same way being there for me, every time I needed you. You are the best!

Finally, I want to thank my wife Katy for her continuous support and care I received. You are always there for me when I felt down or not motivated and tried to get me back on track. Thanks for listening to my chemical problems although it was hard to understand. But you are also there when we were able to celebrate an accepted manuscript or promising results. You are my sunshine, and you will ever be! I love you!



---

**List of Abbreviations**

1D	one dimensional
2D	two dimensional
3D	three dimensional
4VP	4-vinylpyridine
$A_2/A_1$	asymmetry of doublets
AOT	sodium dioctyl sulfosuccinate
azpy	3,3'-azopyridine
BCP	(di)block copolymer
bipy	4,4'-bipyridine
bpea	1,2-di(4-pyridyl)ethane
bpee	( <i>E</i> )-1,2-di(4-pyridyl)ethene
bpey	1,2-di(4-pyridyl)ethyne
bppa	1,3-di(4-pyridyl)propane
calc/calcd	calculated
CN	coordination network
CP	coordination polymer
cryo	cryogenic
$D_{\text{core}}$	core diameter in TEM measurements
$D_{\text{cryo}}$	core diameter in cryo-TEM measurements
$D_h$	hydrodynamic diameter in DLS measurements
DLS	dynamic light scattering
DSC	differential scanning calorimetry
endo	endothermic
eq./equiv	equivalents
EtOH	ethanol

---

## List of Abbreviations

---

<i>G</i>	Gibb's free energy
<i>g<sub>e</sub></i>	gyromagnetic factor
GPC	gel permeation chromatography
h	hours
<i>H</i>	enthalpy
hptrz	4-heptyl-1,2,4-triazole
HS	high-spin
Htrz	4 <i>H</i> -1,2,4-triazole
IR	infrared
L	ligand
LS	low-spin
MALDI-ToF	matrix-assisted laser desorption/ionisation – time of flight
MeOH	methanol
min	minutes
<i>n</i>	number of electrons
NMR	nuclear magnetic resonance
NP	nanoparticle
OAc	acetate
<i>P</i>	spin pairing energy
P4VP	poly(4-vinylpyridine)
PEG	polyethylene glycol
PS	polystyrene
PS- <i>b</i> -P4VP	polystyrene- <i>block</i> -poly(4-vinylpyridine)
PVA	polyvinyl alcohol
PVP	polyvinylpyrrolidone
PXRD	powder X-ray diffraction

---

## List of Abbreviations

---

pz	pyrazine
rt/RT	room temperature
$S$	entropy
SCO	spin crossover
SEM	scanning electron microscopy
SEM-EDX	scanning electron microscopy – energy dispersive X-ray spectroscopy
SQUID	superconducting quantum interference device
ST	spin transition
$T$	temperature
$T_{1/2}$	spin transition temperature
$T_{1/2}\downarrow$	spin transition temperature (cooling mode)
$T_{1/2}\uparrow$	spin transition temperature (heating mode)
TBA	tetrabutylammonium
TEM	transmission electron microscopy
TEM-EDX	transmission electron microscopy – energy dispersive X-ray spectroscopy
$T_g$	glass transition temperature
TGA	thermogravimetric analysis
THF	tetrahydrofuran
trz	triazole
UV-Vis	ultraviolet-visible
wt%	weight percentage
$\chi_M$	molar susceptibility
$\delta$	isomer shift
$\Delta_0$	ligand field splitting (octahedron)
$\Delta E_Q$	quadrupole splitting
$\bar{D}$	polydispersity

---

## List of Abbreviations

---

$\Gamma$	full width at half maximum
$\gamma_{\text{HS}}$	high-spin fraction
$\mu_{\text{B}}$	Bohr magneton
$\mu_{\text{eff}}$	effective magnetic moment
$\mu_{\text{so}}$	spin-only moment
$\nu$	wavenumber
$\sigma$	distribution width





## 1. Summary

This thesis aims for the synthesis and characterisation of coordination polymer (CP)/block copolymer (BCP) nanocomposites. The used coordination polymers are either based on Schiff base-like ligands with an iron(II) centre connected by bis(monodentate) bridging ligands. Alternatively, zinc(II) complexes are also reacted with bis(monodentate) bridging ligands. The diblock copolymer consists of one block polystyrene and another block poly(4-vinylpyridine) resulting in polystyrene-*block*-poly(4-vinylpyridine) (PS-*b*-P4VP). The PS-*b*-P4VP polymer self-assembles in suitable solvents like tetrahydrofuran or toluene to micelles where PS is building up the shell of the micelles and P4VP is forming the core. These block copolymer micelles are used as a size template for the formation of nanoparticles of the respective coordination polymer. The size of the micelle cores can be enlarged by raising the percentage of P4VP of the block copolymer. Above a certain ratio also the shape of the micelles can be altered to rods and worm-like structures. The synthesis method for the formation of nanocomposites is as follows: The block copolymer is dissolved together with the respective complex in the suitable solvent and the reaction mixture is heated to reflux. After the addition of the bridging ligand and the subsequent heating the solvent can either be removed by cold distillation or the complex and the bridging ligand can be added simultaneously up to four times. Thus, several different nanocomposites were obtained. The sizes in the solid state and in solution, the crystallinity, the composition and, additionally for iron(II)-based CPs, the spin crossover (SCO) properties were analysed.

Nanocomposites of three different one-dimensional iron(II) CPs  $[\text{FeL}(\text{bpea})]_n@BCP$ ,  $[\text{FeL}(\text{bpee})]_n@BCP$ , and  $[\text{FeL}(\text{bpey})]_n@BCP$  with varying bridging ligands were synthesised. Their size, magnetic, and SCO properties were investigated. Transmission electron microscopy (TEM) images and dynamic light scattering (DLS) revealed that the sizes of the nanoparticles were equal in size independent from the formed CP (TEM:  $\sim 50$  nm, DLS:  $\sim 150$  nm). Microcrystals were observed for some samples in TEM images. The appearance of microcrystals was explained by the stability of the CPs regarding their ligand field splitting, their electronic configuration, and the rigidity of the bridging ligands. The magnetic measurements showed that samples with microcrystals exhibit a bulk-like behaviour, whereas the nanocomposites without microcrystals undergo a gradual spin transition. In the case of the nanocomposite  $[\text{FeL}(\text{bpey})]_n@BCP$  a gradual, two-step spin transition was found whereas the bulk  $[\text{FeL}(\text{bpey})]_n$  features an abrupt, half complete spin transition with a hysteresis width of 10 K. Powder X-ray diffraction explained the variation in the spin transitions of the nanocomposite which showed a different polymorph than the bulk material.

By utilising another BCP as template, the particle core size of the BCP and the nanocomposite with the CP  $[\text{FeL}(\text{bipy})]_n$  could be reduced to 15 nm and 16 nm, respectively. The magnetic properties of these smaller particles were investigated and the influence of a stepwise increase of the annealing temperature on the SCO properties was evaluated. The SCO properties of the annealed nanocomposite improved compared to the as-synthesised product. The hysteresis width was broadened from 7 K to 14 K, while shifting the spin transition from 163 K to 203 K and lowering the residual high-spin fraction at 50 K from 52 % to 32 %. The change of the magnetic properties was supported by temperature-dependent Mössbauer spectroscopy, which also detected a decrease of the residual high-spin fraction. Furthermore, temperature-dependent powder X-ray diffraction revealed that the pattern of the nanocomposite resembled the bulk pattern after annealing. The integrity of the particles after the annealing was proven by subsequent TEM, DLS, and scanning electron microscopy measurements. The processability of the nanocomposite was demonstrated by electrospinning of fibres and non-woven.

The templated synthesis using BCPs is not only limited to one-dimensional iron-based CPs. This was demonstrated by the synthesis of nanocomposites with the one-dimensional  $[\text{Zn}(\text{OAc})_2(\text{bipy})]_n$  CP and the two-dimensional  $[\text{Zn}(\text{TFA})_2(\text{bppa})_2]_n$  coordination network. Two different PS-*b*-P4VP BCPs were used for this approach. Nanocomposites particle core sizes of 47 nm for the  $[\text{Zn}(\text{OAc})_2(\text{bipy})]_n$  CP in only one BCP and sizes of 46 nm and 15 nm for the  $[\text{Zn}(\text{TFA})_2(\text{bppa})_2]_n$  coordination network in two BCPs were achieved. TEM images revealed chain-like structures for the particles of the nanocomposites of  $[\text{Zn}(\text{TFA})_2(\text{bppa})_2]_n$  in the smaller particles and a tendency to worm-like structures in the larger particles. This is supported by DLS measurements showing an increase of the hydrodynamic diameter and a broadening of the size distribution in solution. The successful formation of the CP and the coordination network was confirmed by powder X-ray diffraction, by infrared measurements supported by computational calculations, and by scanning electron microscopy images.

Since BCPs are also known for their possibility to form all kinds of structures five different BCPs and their resulting nanocomposites with  $[\text{FeL}(\text{bipy})]_n$  were tested for the size and shape control. The BCPs were varied in the ratio between polystyrene and poly(4-vinylpyridine). Raising the poly(4-vinylpyridine) fraction to 61% resulted in an increase of the spherical particle core size verified by TEM, DLS, and cryo-TEM measurements. Introducing the CP into the BCPs also resulted in spherical particles when using the BCPs with poly(4-vinylpyridine) fractions up to 42 % and in worm-like structures with a fraction of 61 %. The magnetic properties of the nanocomposites were investigated regarding the particle size and shape. It was found that the abruptness of the spin transition increased in the larger particles and in the worm-like structures and that the residual high-spin fraction can be reduced to 14 % in the worm-like micelles. The spatial



## 1. Summary

---

distribution of the iron inside the nanocomposite with worm-like structures was detected by transmission electron microscopy – energy dispersive X-ray scattering showing that iron was only incorporated into the polymeric structure.

---

---

## 2. Zusammenfassung

Ziel dieser Dissertation ist die Synthese und Charakterisierung von Koordinationspolymer-Blockcopolymer Nanokompositen. Die dafür eingesetzten Koordinationspolymere basieren auf Schiff-Base ähnlichen Liganden mit einem Eisen(II) Zentrum welches über bismonodentate Brückenliganden verknüpft wird. Alternativ werden Zink(II) Komplexe mit bismonodentaten Liganden umgesetzt. Das Blockcopolymer besteht aus einem Block Polystyrol und einem Block Poly(4-vinylpyridin) (PS-*b*-P4VP). Durch Selbstassemblierung bildet dieses PS-*b*-P4VP Polymer in einem geeigneten Lösungsmittel Mizellen, z.B. in Tetrahydrofuran oder Toluol. In diesen Mizellen bildet das Polystyrol die Hülle und der Poly(4-vinylpyridin) Block den Kern. Diese Blockcopolymermizellen werden als Templat verwendet, um eine Größenkontrolle bei der Bildung von Nanopartikeln eines Koordinationspolymers zu ermöglichen. Der Mizellkern kann dabei durch die Erhöhung des P4VP Anteils vergrößert werden. Oberhalb eines gewissen Anteils kann auch die Form der Mizellen zu Stäbchen oder wurmartigen Strukturen verändert werden. Die Synthese der Nanokomposite läuft wie folgt ab: Das Blockcopolymer wird zusammen mit dem jeweiligen Komplex im geeigneten Lösungsmittel gelöst und die Reaktionslösung unter Rückfluss erhitzt. Nach der Zugabe des Brückenliganden und nachfolgenden Siedens kann das Lösungsmittel entweder über eine Kälteedestillation entfernt oder der Komplex und der Brückenligand bis zu vier weitere Male simultan hinzugegeben werden. Dadurch können viele verschiedene Nanokomposite erhalten werden. Für diese Nanokomposite werden die Größen im getrockneten und gelösten Zustand, die Kristallinität und die Zusammensetzung analysiert. Zusätzlich werden für die eisenbasierten Koordinationspolymere die Spin Crossover (SCO) Eigenschaften der Proben gemessen.

Die Größe und die SCO Eigenschaften der Nanokomposite von drei verschiedenen eindimensionalen Eisen(II) Koordinationspolymeren  $[\text{FeL}(\text{bpea})]_n@BCP$ ,  $[\text{FeL}(\text{bpee})]_n@BCP$  und  $[\text{FeL}(\text{bpey})]_n@BCP$  mit verschiedenen Brückenliganden wurden untersucht. Transmissionselektronenmikroskopie (TEM) Bilder und dynamische Lichtstreuung (DLS) ergaben, dass die Größen der Nanopartikel unabhängig vom gebildeten Koordinationspolymer waren (TEM:  $\sim 50$  nm, DLS:  $\sim 150$  nm). Auf den TEM Bildern wurden Mikrokristalle beobachtet. Deren Auftreten konnte über die Stabilität der Koordinationspolymere hinsichtlich der Ligandenfeldaufspaltung, der Elektronenkonfiguration und der Steifigkeit der Brückenliganden erklärt werden. Für die Proben mit Mikrokristallen wurden in den Magnetmessungen ein Verhalten ähnlich dem des Festkörpers beobachtet. Die Nanokomposite ohne Mikrokristalle zeigten einen graduellen Spinübergang. Im Falle des Nanokomposits  $[\text{FeL}(\text{bpey})]_n@BCP$  wurde ein gradueller, zweistufiger Spinübergang erhalten, wohingegen der Festkörper  $[\text{FeL}(\text{bpey})]_n$  einen abrupten, unvollständigen Spinübergang mit einer Hysteresenbreite von 10 K aufweist.

---

Über die Messung der Pulverdiffraktogramme konnte der Unterschied erklärt werden, da im Nanokomposite ein anderes Polymorph gebildet wurde.

Durch die Verwendung eines anderen Blockcopolymers als Templat konnte die Partikelkerngröße reduziert und Blockcopolymermizellen mit einem Kerndurchmesser von 15 nm erhalten werden. Der Kerndurchmesser der Nanokomposite mit  $[\text{FeL}(\text{bipy})]_n$  lag bei 16 nm. Die magnetischen Eigenschaften dieser kleineren Partikel und der Einfluss des Temperns mit einer schrittweisen Temperaturerhöhung auf die SCO Eigenschaften wurden untersucht. Die SCO Eigenschaften des getemperten Nanokomposits verbesserten sich im Vergleich zum Produkt direkt aus der Synthese. Die Hysteresenbreite vergrößerte sich von 7 K auf 14 K, die Spinübergangstemperatur verschob sich von 163 K auf 203 K und der finale high-spin Anteil bei 50 K verringerte sich von 52 % auf 32 %. Die Änderung der SCO Eigenschaften konnte mittels temperaturabhängiger Mößbauerspektroskopie bestätigt werden und zeigte ebenfalls eine Abnahme des high-spin Anteils. Zudem konnte durch die Messung temperaturabhängiger Pulverdiffraktogramme gezeigt werden, dass sich das Diffraktogramm des Nanokomposits beim Tempern dem Diffraktogramm des Festkörpers angleicht. Die Stabilität der Partikel wurde anschließend durch TEM, DLS und Rasterelektronenmikroskopie gezeigt. Die Verarbeitbarkeit des Nanokomposits wurde zudem durch Elektrosinnen von Fasern und Faservliesen demonstriert.

Die Templatsynthese mit Blockcopolymeren ist nicht auf eindimensionale eisenbasierte Koordinationspolymere limitiert. Dies konnte durch die Synthese von Nanokompositen mit dem eindimensionalen Koordinationspolymer  $[\text{Zn}(\text{OAc})_2(\text{bipy})]_n$  und dem zweidimensionalen Koordinationsnetzwerk  $[\text{Zn}(\text{TFA})_2(\text{bppa})_2]_n$  gezeigt werden. Hierfür wurden zwei verschiedene PS-*b*-P4VP Blockcopolymere verwendet. Für die Synthese der Nanokomposite mit dem  $[\text{Zn}(\text{OAc})_2(\text{bipy})]_n$  Koordinationspolymer wurde nur eines der BCPs verwendet und Partikelkerngrößen von 47 nm erhalten. Für die Synthese von Nanokompositen mit  $[\text{Zn}(\text{TFA})_2(\text{bppa})_2]_n$  wurden beide BCPs verwendet und Partikelgrößen von 46 nm und 15 nm erhalten. Die TEM Bilder der Nanokomposite mit  $[\text{Zn}(\text{TFA})_2(\text{bppa})_2]_n$  zeigten eine kettenartige Struktur für die kleineren Partikel und eine Tendenz zu wurmartigen Strukturen für die größeren Partikeln. Diese Beobachtung wird durch die DLS Messungen unterstützt, welche eine Zunahme des hydrodynamischen Durchmessers und eine breitere Größenverteilung in Lösung zeigt. Die erfolgreiche Bildung des Koordinationspolymers und -netzwerks wird durch Pulverdiffraktometrie, infrarotspektroskopische Messungen, unterstützt durch theoretische Rechnungen, und Rasterelektronenmikroskopie bestätigt.

Nachdem Blockcopolymere dafür bekannt sind viele verschiedene Formen anzunehmen, wurden fünf verschiedene Blockcopolymere hergestellt und die Größen- und Formkontrolle der resultierenden Nanokomposite mit  $[\text{FeL}(\text{bipy})]_n$  untersucht. Die Blockcopolymere unterscheiden

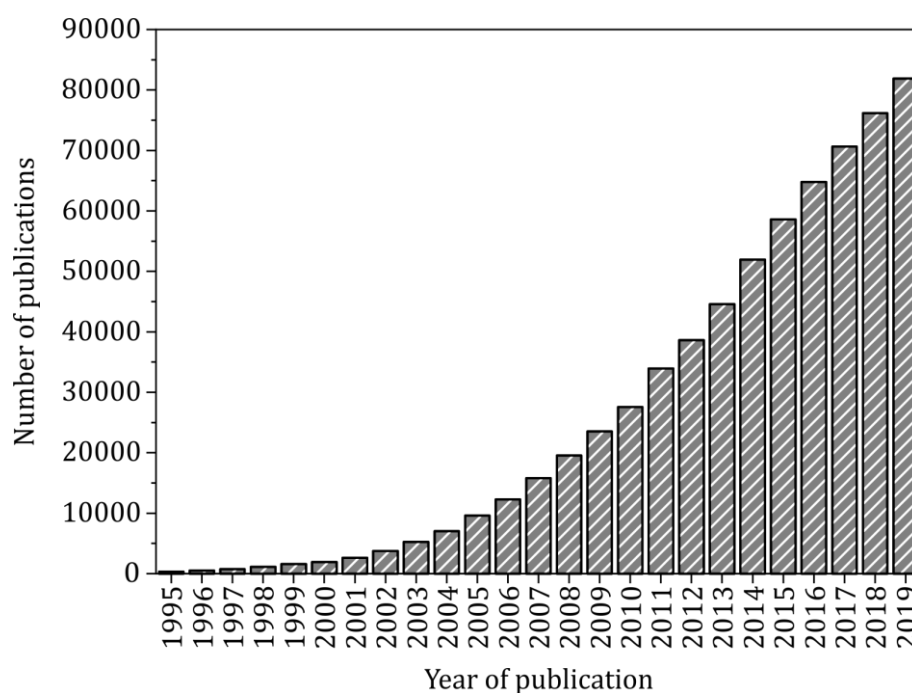
sich im Verhältnis Polystyrol zu Poly(4-vinylpyridin). Durch eine Erhöhung des Poly(4-vinylpyridin)-Anteils auf 61 % konnte die Größe der sphärischen Partikel kontinuierlich erhöht werden, was durch TEM, DLS und cryo-TEM Messungen verifiziert wurde. Beim Einbringen des Koordinationspolymers in die BCPs zeigten sich ebenfalls sphärische Partikel bis zu einem Anteil von 42 % P4VP im BCP und wurmartige Strukturen für die Nanokomposite mit dem BCP mit 61 % P4VP Anteil. Die magnetischen Eigenschaften wurden hinsichtlich der Größe bzw. Form untersucht. Dabei zeigte sich, dass der Spinübergang in den größeren Partikeln und auch in den wurmartigen Strukturen abrupter ist und dass der high-spin Anteil in den Wurmstrukturen auf 14 % gesenkt werden konnte. Die räumliche Verteilung des Eisens innerhalb der wurmartigen Nanokomposite wurde über eine TEM Messung gekoppelt mit einer energiedispersiven Röntgenstreuung nachgewiesen. Diese detektierte das Eisen des Koordinationspolymers nur innerhalb der Polymerstruktur.

---

---

### 3. Introduction

The miniaturisation of materials and compounds and their potential in different applications is, among others, one of the most investigated field of research. This fact can be visualised by the number of scientific articles and publications involving nanoparticles in the past 15 years (1995-2019). An increasing trend can be seen even until today reaching more than 80 000 publications in 2019, underlining the actuality of this topic.



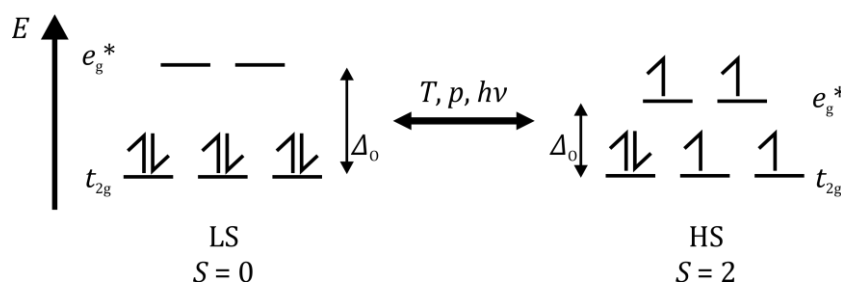
**Figure 1:** Increasing evolution of the number of publications per year in the time span from 1995 to 2019 (Data extracted from ISI Web of Knowledge, search term: nanoparticles).

Several scientific articles, books, and book chapters on the application of nanoparticles in catalysis<sup>[1-3]</sup>, energy conversion<sup>[1,4-6]</sup> and energy storage<sup>[2,5,6]</sup>, sensors<sup>[1,6-8]</sup>, display or light emitting devices<sup>[1,6,9]</sup>, contrast agents<sup>[10-12]</sup>, drug delivery<sup>[1,13]</sup>, and data storage<sup>[1,6,14]</sup> have been published during this time period.

Spin crossover (SCO) compounds correspond to the class of functional materials that have a potential field of application in sensors<sup>[15,16]</sup>, display devices<sup>[17,18]</sup>, contrast agents<sup>[19-21]</sup> and data storage<sup>[17,18]</sup> and this thesis aims for the combination of both fields.

### 3.1. Spin crossover in 3d transition metal complexes

The spin crossover phenomenon is a remarkably interesting effect in transition metal complexes. A SCO is mostly observed in octahedral complexes with an electronic configuration of  $d^{4-7}$ . Typically, the metal centre in a complex is either low-spin (LS) or high-spin (HS) depending on the spin pairing energy  $P$  and the ligand field splitting  $\Delta_0$  (in case of an octahedral coordination sphere of the metal centre). If  $P$  is smaller than  $\Delta_0$ , the electrons of the metal centre prefer to pair, resulting in a LS compound. Thus, a HS compound with unpaired electrons is on hand with  $P$  being larger than  $\Delta_0$ . However, it is possible that the spin pairing energy  $P$  and the ligand field splitting  $\Delta_0$  are of the same order of magnitude ( $P \approx \Delta_0$ ). As a result, reversible switching between the LS and the HS state is possible by external stimuli such as temperature<sup>[22,23]</sup>, pressure<sup>[24,25]</sup>, light irradiation<sup>[22,26]</sup>, or the adsorption of guest molecules<sup>[27]</sup>.



**Scheme 1:** Presentation of the SCO of an iron(II) complex with a  $d^6$  electronic configuration showing the diamagnetic LS state with a total spin of  $S = 0$  (left) and the paramagnetic HS state with a total spin of  $S = 2$  (right).

The total spin of an iron(II) complex changes from  $S = 2$  to  $S = 0$  when changing the spin state from HS to LS. As a result, the magnetism of the compound alters from paramagnetic in the HS state to diamagnetic in the LS state. Besides the variation in magnetism, other physical properties are also influenced. The metal-ligand bond lengths are elongated in the HS state compared to the LS state since the antibonding  $e_g^*$  orbitals are occupied in the HS state. This also leads to a volume change of the compound upon spin transition (ST). Furthermore, the colour of SCO compounds is altered drastically in the different spin states due to the dissimilar ligand field splitting.<sup>[28,29]</sup>

Several parameters matter when describing the SCO: (1) the residual HS fraction  $\gamma_{\text{HS}}$ , (2) the effective magnetic moment  $\mu_{\text{eff}}$  and (3) the transition temperature  $T_{1/2}$ . For iron(II) complexes, the HS fraction  $\gamma_{\text{HS}}$  can easily be calculated from a selected, experimentally obtained susceptibility value  $\chi_{\text{M}}T_{\text{select}}$  and the initial experimental value of the compound  $\chi_{\text{M}}T_{\text{init}}$ .

$$\gamma_{\text{HS}} = \frac{\chi_{\text{M}}T_{\text{select}}}{\chi_{\text{M}}T_{\text{init}}}$$



### 3. Introduction

---

The effective magnetic moment  $\mu_{\text{eff}}$  can be estimated by the spin-only equation for first-row transition metals. In the first equation, the gyromagnetic factor  $g_e$  of the electron and the total spin of the compound is used as follows:[30]

$$\mu_{\text{so}} = g_e \cdot \sqrt{S(S + 1)}$$

Alternatively, when  $g_e$  is fixed to the value 2, the before mentioned equation can be substituted by the successional equation. Here, the number of unpaired electrons  $n$  of the compound is used:[31]

$$\mu_{\text{so}} = \sqrt{n \cdot (n + 2)}$$

Experimentally,  $\mu_{\text{eff}}$  can be obtained from magnetic measurements via the molar magnetic susceptibility  $\chi_M T$  and the following equation:[32]

$$\mu_{\text{eff}} = 2.83 \cdot \sqrt{\chi_M T}$$

In the latter equation, the constant 2.83 comes from the term  $\sqrt{\frac{3k}{N\mu_B^2}}$ , where  $k$  is the Boltzmann constant,  $N$  is the Avogadro constant, and  $\mu_B$  is the Bohr magneton. Since the SCO is thermodynamically driven, the Gibbs equation can be used to describe a SCO, where  $G$  is the Gibbs free energy,  $H$  is the enthalpy,  $T$  is the temperature,  $S$  is the entropy and  $\Delta$  is the difference between the HS and LS state, respectively.

$$\Delta G = \Delta H - T\Delta S$$

The entropy in the HS state is higher than in the LS state due to the electronic configuration ( $^5T$  vs.  $^1A$ ) and due to the structural changes in the compound (elongation of the bond length, changes in bond angles) resulting in additional contributions of vibrational energies. If the spin transition is defined as a transition from HS to LS,  $\Delta S$  is negative. Since only the non-bonding  $t_{2g}$  orbitals are occupied in the LS state,  $\Delta H$  is also negative. As a result, at low temperatures the influence of the term  $T\Delta S$  on  $\Delta G$  is small leading to a negative  $\Delta G$  and a favoured LS state because  $\Delta S$  is also negative. In contrary, at elevated temperatures  $T\Delta S$  is the dominating term and since  $\Delta S$  is negative,  $\Delta G$  will be positive. Based on the preceding explanations, it is possible that  $\Delta G = 0$ . At this point, the ratio between LS and HS is equal and  $T_{1/2}$  can be calculated by the following equation:

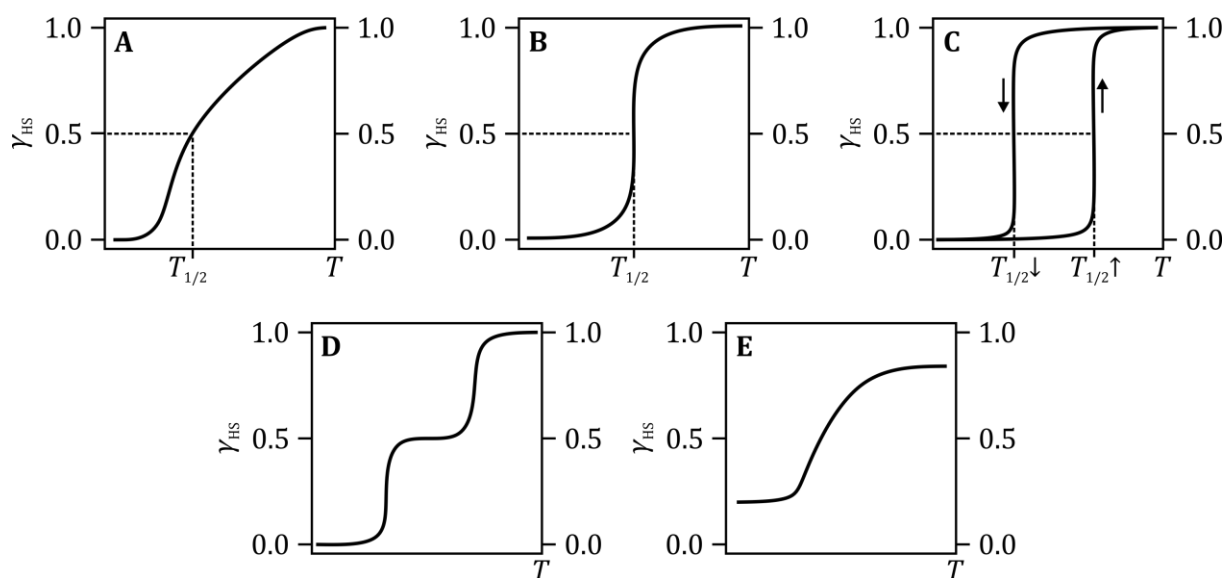
$$T_{1/2} = \frac{\Delta H}{\Delta S}$$

A temperature-dependent SCO can be followed by several different methods. NMR measurements are especially useful when the compounds magnetism changes from paramagnetic to diamagnetic. In the case of a paramagnetic compound, signals in the vicinity of the paramagnetic centre get

---

shifted, sometimes up to several hundred ppm.<sup>[33]</sup> Moreover, the SCO can be detected by spectroscopic methods like UV-Vis, IR and Raman spectroscopy, or Mössbauer spectroscopy<sup>[34]</sup>. Another commonly used method is the single crystal X-ray diffraction. Here, both the crystal structure of the HS and the LS state may be accessible in a small fraction of cases, depending on the coolant and the transition temperature of the compound. Also, powder X-ray diffraction (PXRD) is possible. Most frequently, magnetic measurements with a SQUID magnetometer are performed because the magnetism of the samples is measured directly and the change in magnetism can be followed over a wide temperature range.<sup>[35]</sup>

Several different types of SCOs are possible to describe the progression of the magnetic moment of a compound (Figure 2) and all of them were already observed in the literature. Gradual complete SCOs (A) are often observed in compound with low cooperativity.<sup>[36]</sup> Abrupt complete STs (B)<sup>[37]</sup> or abrupt complete STs with hysteresis (C)<sup>[38]</sup> occur in compounds with high cooperativity like coordination polymers. Stepwise STs (D)<sup>[39]</sup> are common in samples that incorporate different SCO active species and gradual incomplete SCOs (E)<sup>[39]</sup> are most common in solids but also in solution<sup>[40]</sup>. Moreover, combinations of all these SCOs are possible.<sup>[39–43]</sup>

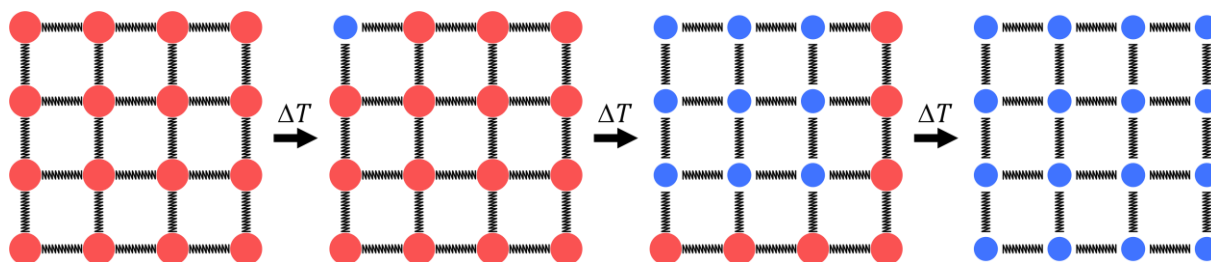


**Figure 2:** Different types of ST: gradual and complete (A), abrupt and complete (B), abrupt and complete with hysteresis (C), stepwise and complete (D), and gradual and incomplete (E).

### 3.2. Nanostructuring of SCO coordination polymers

The investigation on SCO coordination polymers (CPs) started around 1998 and accelerated since.<sup>[43]</sup> They are built up by a metal complex and a bridging ligand. One-dimensional, two-dimensional, and even three-dimensional CPs and coordination networks (CNs) can be realised depending on the used metal complex and the bridging ligand.<sup>[44]</sup>

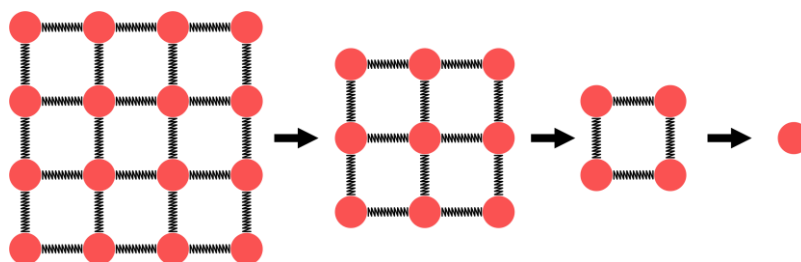
CPs often exhibit very abrupt STs upon temperature change due to their high cooperativity. CPs frequently experience cooperative behaviour through intramolecular interactions, which are almost entirely based on covalent bonds. Moreover, cooperativity can further be improved by additional intermolecular interactions like  $\pi$ - $\pi$  stacking, van der Waals interactions, and/or hydrogen bond networks. The cooperativity of compounds can be explained by the commonly used mechanoelastic model in which springs represent the bridging ligands and spheres represent the metal complexes (Figure 3).<sup>[45]</sup>



**Figure 3:** Progression of a thermally induced ST in a macroscopic material with the red spheres representing metal centre in the HS state, blue spheres representing metal centres in the LS state and the springs representing the bridging ligands. The compound is in the HS state and upon temperature change the SCO starts in the top left corner of the material and proceeds from this point on until the compound is completely LS (from left to right).

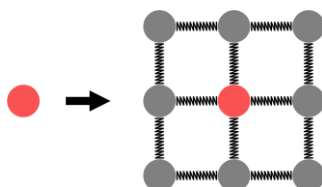
Several examples for macroscopic SCO CPs with  $\pi$ - $\pi$  stacking<sup>[46–48]</sup> and hydrogen bonds<sup>[49–51]</sup> have been reported showing abrupt STs with hysteresis. However, applications often demand the integration of the materials into devices. In many fields, macroscopic materials are not suitable because the space in the device is limited (e.g. sensors or displays) or the target use demands smaller materials (e.g. data storage, contrast agents). Therefore, miniaturising the macroscopic materials is key to meet the needs of the contemplated application. However, observations were made that the transition temperatures and the progression of the ST change or the hysteresis width diminish upon miniaturisation.<sup>[52–54]</sup> In some cases, the SCO properties are completely lost.<sup>[53]</sup> This can also be explained by the already mentioned mechanoelastic model. The number of covalently linked metal centres decreases upon miniaturisation and the cooperativity

decreases due to the smaller crystallites. As a result, in the ultimate size limit a single complex molecule exists (Figure 4).



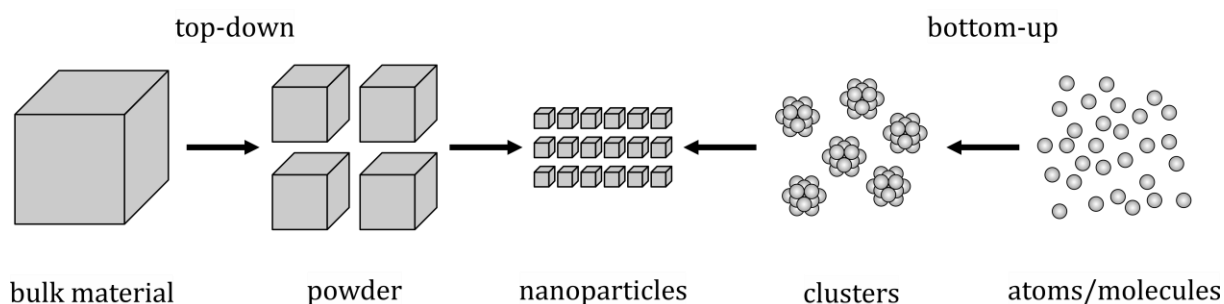
**Figure 4:** Miniaturisation of a macroscopic crystal of a CP over a microcrystalline system and a NP system to the ultimate size limit of a single molecule (from left to right).

Even though the ultimate size limit is mostly a theoretical concept for SCO CPs, another factor must be taken into account: the surface molecules (Figure 5). These molecules lack the necessary coordination sphere to undergo SCO since these complex molecules are often coordinated by solvent molecules or other ligands. As a result, the residual HS fraction in nanoparticles (NPs) is higher than in the bulk materials. Also, it has been observed that it is possible that the transition temperature is shifted both to higher<sup>[55,56]</sup> and lower<sup>[57,58]</sup> temperatures in nanoparticles.



**Figure 5:** Concept of the size limit of a SCO CP with metal centres on the surface (grey) that do not undergo SCO.

Two different approaches for the synthesis of nanoparticles can be utilised: the top-down approach and the bottom-up approach (Figure 6). Mechanical grinding, lithography, chemical etching, and thermal decomposition are commonly considered as top-down approaches. Since this thesis solely uses the bottom-up approach, top-down methods will not be discussed in detail.

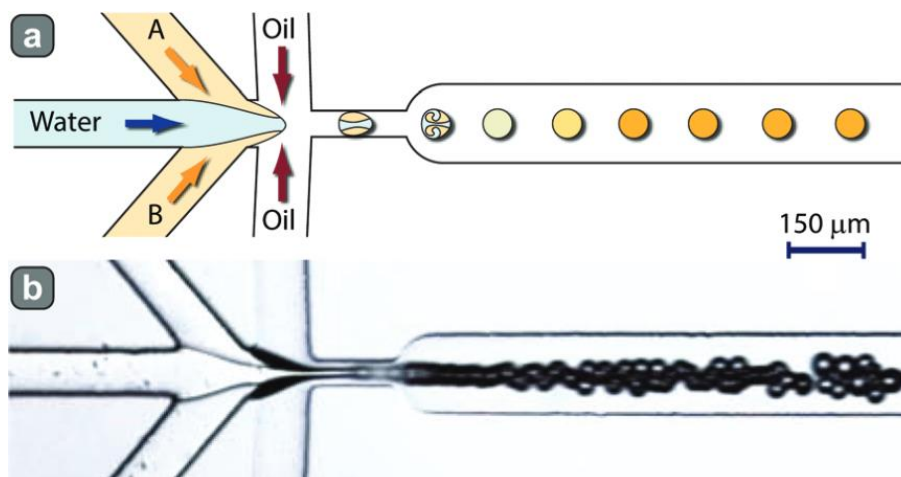


**Figure 6:** Schematic representation of the top-down and the bottom-up approach. The top-down approach is starting from a macroscopic bulk material (e.g. a crystal, left), which is scaled down to the desired NP size (e.g. by mechanical grinding, middle). The bottom-up approach starts from atoms and molecules (right) and assembles these starting materials to final NP size (middle).

In general, several different synthetic methods attributed to the bottom-up approach have been established for the synthesis of NPs like the chemical vapor deposition<sup>[59]</sup>, the solvo- and hydrothermal synthesis<sup>[60]</sup>, the sol-gel process<sup>[61]</sup>, the reduction of metal salts<sup>[1]</sup>, the microfluidic synthesis<sup>[62]</sup>, the layer-by-layer technique<sup>[63]</sup>, the inverse micelle technique<sup>[64]</sup> and the synthesis in polymers<sup>[65]</sup>. However, not all these methods are applicable for the synthesis of SCO CP NPs.

### 3.2.1. The microfluidic approach

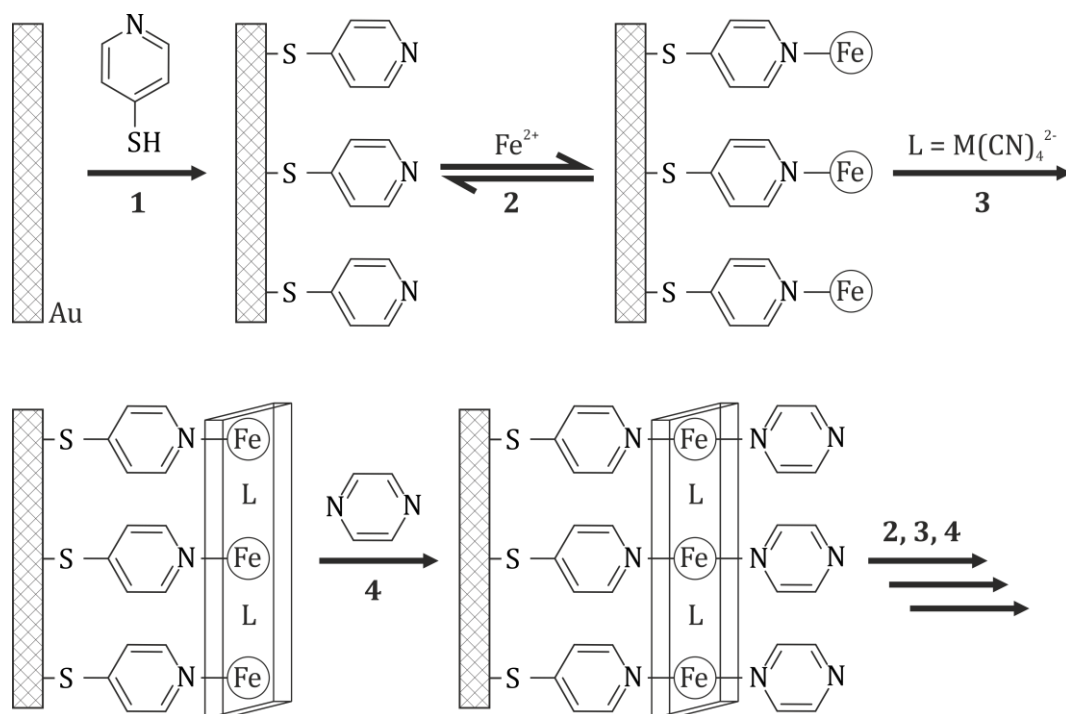
A rather new method for the synthesis of SCO CP NPs is the microfluidic method. It has been used in the formation of NPs of the known 3D SCO CP  $[\text{Fe}(\text{pz})\text{Pt}(\text{CN})_4]_n$  (pz = pyrazine)<sup>[66]</sup> and other materials<sup>[62]</sup>. Here, two solutions A and B were prepared. Solution A contained  $\text{K}_2[\text{Pt}(\text{CN})_4]$  and pyrazine in water and solution B contained  $\text{Fe}(\text{BF}_4)_2$  and pyrazine in water. The two reaction solutions were injected into the device together with an additional water stream. Droplets were formed by the injection of mineral oil (see Figure 7). The droplet containing liquid was collected at the exit, the excess of oil was removed, and the product was washed several times to yield NPs with an average size of 47 nm. As pointed out before, the material does not show a complete SCO and a HS fraction of 18 % remained in the synthesised NPs. Also, the transition temperature is shifted to lower temperatures and the hysteresis width decreases compared to the bulk material.<sup>[67]</sup>



**Figure 7:** Schematic representation of the synthetic setup and the designed device (top) and a digital photograph of the device in operation (bottom).<sup>[67]</sup>

### 3.2.2. The layer-by-layer technique

Other groups focused their interest on methods for the synthesis of nanostructures and the patterning of these structures. The layer-by-layer technique was already published for the synthesis of Hofmann clathrates.<sup>[63]</sup> This synthetic protocol was then transferred to Prussian Blue and Prussian Blue analogues to achieve nanostructures with a defined number of layers.<sup>[68–72]</sup> In the first published work for the synthesis of a layered SCO material, a silicon wafer with a gold layer was coated with an anchoring group of 4-mercaptopyridine. Subsequently, the wafers were soaked alternately in ethanol solutions of  $\text{Fe}(\text{BF}_4)_2$ ,  $(\text{TBA})_2[\text{Ni}(\text{CN})_4]$  (TBA = tetrabutylammonium), and pyrazine to build up the 3D structure  $[\text{Fe}(\text{pz})\text{Ni}(\text{CN})_4]$ . Instead of  $(\text{TBA})_2[\text{Ni}(\text{CN})_4]$ ,  $(\text{TBA})_2[\text{Pt}(\text{CN})_4]$  and  $(\text{TBA})_2[\text{Pd}(\text{CN})_4]$  were also used. Structures consisting of 20 layers were realised.<sup>[73]</sup> The synthesis is schematically displayed in Figure 8. The SCO properties of the synthesised films by the layer-by-layer technique and the bulk material were compared by temperature-dependent Raman spectroscopy. It was found that the generated films exhibit a more gradual spin transition than the bulk material, however, a similar transition temperature is observed. Several follow-up works with different CPs were published since<sup>[74–79]</sup> and even the patterning of the CPs on the surface of a before treated wafer was possible<sup>[75,77,78]</sup>.

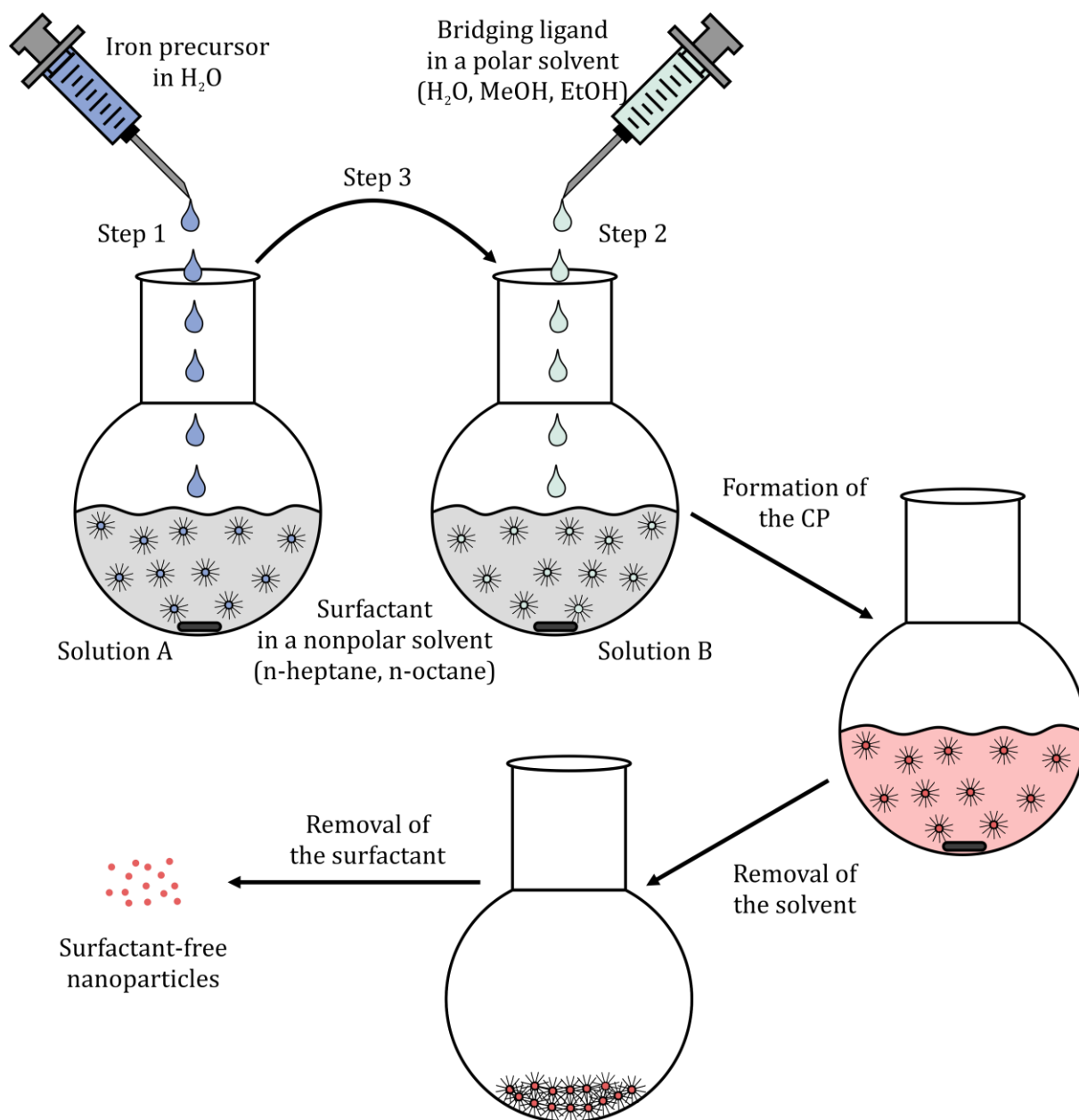


**Figure 8:** Reaction steps of the layer-by-layer synthesis of a 3D SCO CP  $[\text{Fe}(\text{pz})\text{M}(\text{CN})_4]$  ( $\text{M} = \text{Ni}, \text{Pt}, \text{Pd}$ ) on a silicon wafer coated with gold.<sup>[73]</sup>

### 3.2.3. The inverse micelle technique

Most frequently the inverse micelle technique is utilised for the formation of SCO CP NPs. This method was found to be suitable for the synthesis of 1D, 2D, and even 3D SCO CP NPs. Several different CP NPs were already published. However, the majority are based on the iron(II) tris(triazole) family, tris(triazole) derivatives or the iron(II) pyrazine family.

In general, the synthetic protocol for the synthesis of NPs with inverse micelles involves two separate solutions A and B. For solution A, the iron(II) precursor is dissolved in water and added to a mixture of the respective surfactant in a nonpolar solvent like n-heptane or n-octane under vigorous stirring. Another solution is prepared by the dissolution of the organic ligand in a polar solvent like water, methanol or ethanol, or a mixture of these. This solution is also added to a solution of the respective surfactant in n-heptane or n-octane under stirring to yield solution B. Both solutions A and B are then combined under heavy stirring. The formation of the intended SCO CP is indicated by a colour change of the solution. The reaction product is precipitated by an antisolvent and the surfactant-free CP NPs are obtained after several steps of washing, dispersing, and centrifuging.<sup>[80]</sup> A representation of the different reaction steps is given in Figure 9.



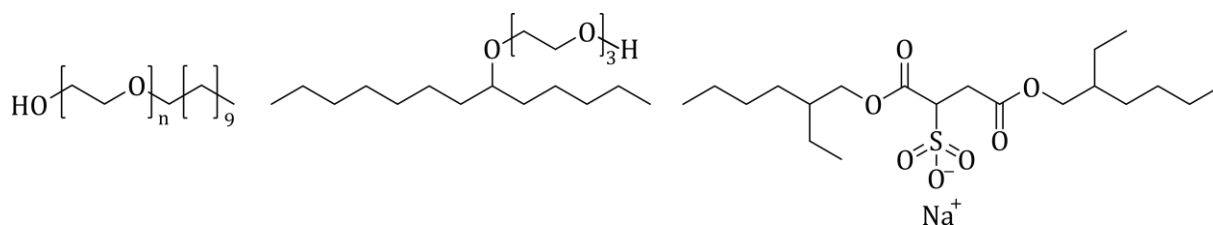
**Figure 9:** Schematic representation of the synthetic approach for the formation of surfactant-free SCO CP NPs employing the inverse micelle technique.

The size of the inverse micelles can easily be controlled in a wide range by the surfactant to solvent ratio, thus allowing a precise adjustment of the nanoparticle size and the study of the size-dependent SCO properties. Additionally, it is possible that the template has an influence on the transition temperatures, the hysteresis width or the residual HS fraction which can be analysed as well.

In this manner, NPs of the 1D SCO CP  $[\text{Fe}(\text{NH}_2\text{trz})_3](\text{Br})_2 \cdot 3\text{H}_2\text{O} \cdot 0.03(\text{surfactant})$  (surfactant = Lauropal, a secondary alcohol ethoxylate (Figure 10);  $\text{NH}_2\text{trz}$  = 4-amino-1,2,4-



triazole) were synthesised. The obtained NPs have a size of  $69 \pm 19$  nm and show rather abrupt SCO behaviour with a ST above RT similar to the bulk material. However, the hysteresis width was found to be narrowed down to 8 K compared to the one of the bulk material which is about twice as large with 15 K.<sup>[80]</sup> Subsequently, a control of the particle size to larger and smaller particles was possible by the adjustment of the surfactant to water ratio. It was found that the ST becomes more gradual and the hysteresis nearly vanished upon reduction of the particle size below 50 nm.<sup>[81]</sup> By changing the counterion to *p*-toluene sulfonate and the surfactant to Tergitol 15-S-3 (Figure 10), another secondary alcohol ethoxylate, NPs of the 1D SCO CP  $[\text{Fe}(\text{NH}_2\text{trz})_3](\text{OTs})_2$  were prepared in the surfactant micelles. Besides NPs with a size of 100 – 200 nm, it was also possible to achieve particle sizes as small as  $3.6 \pm 0.8$  nm. Interestingly, these small particles show quite abrupt SCO behaviour with a transition temperature  $T_{1/2} = 295$  K. Additionally, thermal treatment of the reaction products or solutions led to morphological changes of the NPs into rods or fibres.<sup>[82,83]</sup> Further NPs were prepared with the inverse micelle technique of the 1D SCO CP  $[\text{Fe}(\text{Htrz})_2(\text{trz})](\text{BF}_4)$  (Htrz = 4*H*-1,2,4-triazole). AOT (sodium dioctyl sulfosuccinate, Figure 10) was used as the surfactant in the reaction to yield particle sizes below 20 nm. The particles exhibit a SCO with a 43 K wide hysteresis above RT in the first measurement cycle. The hysteresis width stabilised in the following measurement cycles to 41 K.<sup>[84]</sup>

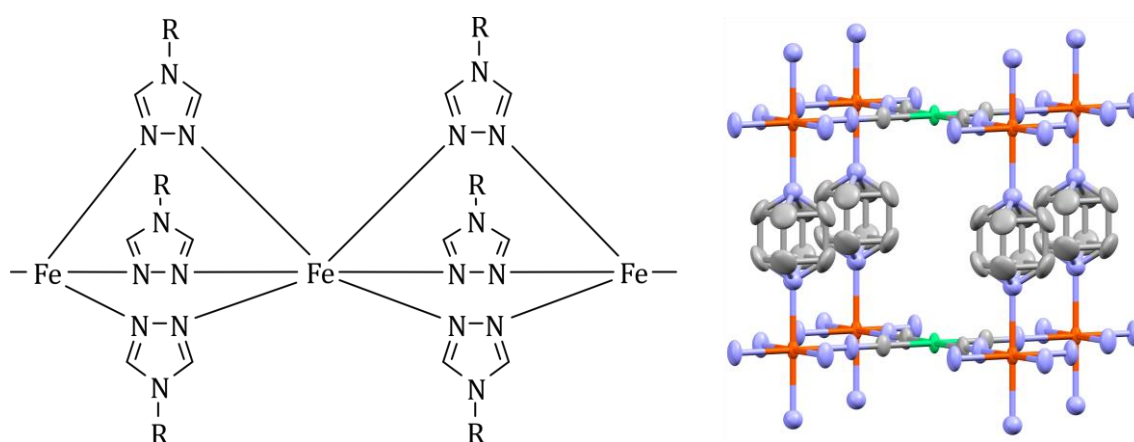


**Figure 10:** Chemical structures of the commonly used surfactants for the formation of inverse micelles: secondary alcohol ethoxylates Laupopal (left), Tergitol 15-S-3 (middle) and sodium dioctyl sulfosuccinate (AOT, right).

In accordance with the work of Forestier *et al.*<sup>[81]</sup> the particle sizes of the 1D CP  $[\text{Fe}(\text{Htrz})_2(\text{trz})](\text{BF}_4) \cdot \text{H}_2\text{O}$  can be tuned by the ratio AOT : water. Thus, the synthetic approach yielded NPs with sizes ranging from 4 nm to 16 nm. The ST of 16 nm particles is almost equal to the bulk material. Remarkably, an abrupt ST above RT was also found in the 4 nm particles and the progression of the ST is similar to the larger particles. The residual HS fraction is only marginally higher than the bulk material and the hysteresis width is lowered to 24 K.<sup>[58]</sup>

Other groups have also prepared 3D CP  $[\text{Fe}(\text{pz})\text{Pt}(\text{CN})_4]$  NPs in AOT micelles. These obtained 14 nm NPs showed a 6 K wide hysteresis with a transition temperature about 30 K below the bulk material<sup>[57]</sup>, while particles of the CP  $[\text{Fe}(\text{pz})\text{Pt}(\text{CN})_4] \cdot 2.5 \text{ H}_2\text{O}$  with a sizes of  $61 \pm 10$  nm revealed

a 10 K wide hysteresis with  $T_{1/2}$  values 20 K below the bulk material.<sup>[85]</sup> The 2D CP  $[\text{Fe}(\text{3-Fpy})_2\text{M}(\text{CN})_4]$  ( $\text{M} = \text{Ni}, \text{Pd}, \text{Pt}$ , 3-Fpy = 3-fluoropyridine) was synthesised in AOT with similar sizes for all three metal ions ( $\text{Ni}$ :  $444 \pm 175$  nm,  $\text{Pd}$ :  $483 \pm 128$  nm,  $\text{Pt}$ :  $481 \pm 146$  nm) and their SCO properties were located in a narrow temperature range ( $T_{1/2\downarrow}$   $\text{Ni}$  ( $\text{Pd}, \text{Pt}$ ): 192 K (205 K, 200 K),  $T_{1/2\uparrow}$   $\text{Ni}$  ( $\text{Pd}, \text{Pt}$ ): 205 K (225 K, 219 K)). In Figure 11 the chemical structure of the  $[\text{Fe}^{\text{II}}(\text{trz})_3]$  family and an excerpt of the crystal structure of the  $[\text{Fe}(\text{pz})\text{M}(\text{CN})_4]$  family is given and in Table 1 an overview over the SCO properties of the differently sizes NPs is given. Although several different SCO compounds were used, the trend can be seen that the hysteresis width is narrowed in smaller particles.



**Figure 11:** Chemical structure of the  $[\text{Fe}^{\text{II}}(\text{trz})_3]$  family ( $\text{R}$  = different substituents, e.g. hydrogen,  $\text{NH}_2$ , heptyl, left) and an excerpt of the crystal structure of the  $[\text{Fe}(\text{pz})\text{M}(\text{CN})_4]$ <sup>[86]</sup> family (right).

### 3. Introduction

**Table 1:** Overview over several CP NPs synthesised in inverse micelles with three different surfactants (Lauropal, Tergitol 15-S-3, and AOT), the resulting particle sizes, and the SCO properties ( $T_{1/2\downarrow}$ ,  $T_{1/2\uparrow}$ , and hysteresis width).

CP	Surfactant	Particle size [nm] <sup>a)</sup>	$T_{1/2\downarrow}$ [K]	$T_{1/2\uparrow}$ [K]	Hysteresis width [K]
[Fe(NH <sub>2</sub> trz) <sub>3</sub> ](Br) <sub>2</sub> ·3H <sub>2</sub> O·0.03(surfactant) <sup>[80]</sup>	Lauropal	69 ± 19	303	311	8
[Fe(NH <sub>2</sub> trz) <sub>3</sub> ](Br) <sub>2</sub> ·3H <sub>2</sub> O <sup>[81]</sup>	Lauropal	200	305	317	13
[Fe(NH <sub>2</sub> trz) <sub>3</sub> ](Br) <sub>2</sub> ·3H <sub>2</sub> O <sup>[81]</sup>	Lauropal	50	310	312	2
[Fe(NH <sub>2</sub> trz) <sub>3</sub> ](Br) <sub>2</sub> ·3H <sub>2</sub> O <sup>[81]</sup>	Lauropal	30	313	31	2
[Fe(NH <sub>2</sub> trz) <sub>3</sub> ](OTs) <sub>2</sub> <sup>[82]</sup>	Tergitol	3.6 ± 0.8	295	295	0
[Fe(Htrz) <sub>2</sub> (trz)](BF <sub>4</sub> ) <sup>[84]</sup>	AOT	<20	343	384	41
[Fe(Htrz) <sub>2</sub> (trz)](BF <sub>4</sub> )·H <sub>2</sub> O <sup>[58]</sup>	AOT	16 ± 4 <sup>b)</sup>	341	379	38
[Fe(Htrz) <sub>2</sub> (trz)](BF <sub>4</sub> )·H <sub>2</sub> O <sup>[58]</sup>	AOT	10 ± 3 <sup>b)</sup>	343	374	31
[Fe(Htrz) <sub>2</sub> (trz)](BF <sub>4</sub> )·H <sub>2</sub> O <sup>[58]</sup>	AOT	4 ± 2 <sup>b)</sup>	343	367	24
[Fe(pz)Pt(CN) <sub>4</sub> ] <sup>[57]</sup>	AOT	14.7 ± 2.3	262	268	6
[Fe(pz)Pt(CN) <sub>4</sub> ]·2.5 H <sub>2</sub> O <sup>[85]</sup>	AOT	61 ± 10	265	275	10
[Fe(3-Fpy) <sub>2</sub> Ni(CN) <sub>4</sub> ] <sup>[87]</sup>	AOT	444 ± 175	192	205	13
[Fe(3-Fpy) <sub>2</sub> Pd(CN) <sub>4</sub> ] <sup>[87]</sup>	AOT	483 ± 128	205	225	20
[Fe(3-Fpy) <sub>2</sub> Pt(CN) <sub>4</sub> ] <sup>[87]</sup>	AOT	481 ± 146	200	219	19

<sup>a)</sup> Analysed by TEM measurements as not stated otherwise; <sup>b)</sup> derived from DLS measurements.

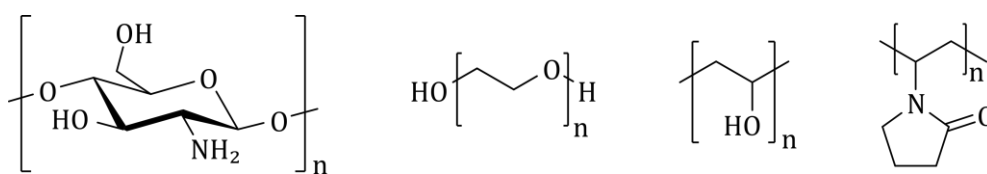
#### 3.2.4. Inorganic and polymeric matrices

In other publications, the influence of a matrices on the SCO properties of CP NPs were analysed. Matrices can not only be used as reactors for the formation of NPs, but they may have an influence on the SCO properties due to the generation of an external pressure. This can result in a shift of the transition temperature.

Therefore, NPs of the CP [Fe(Htrz)<sub>2</sub>(trz)](BF<sub>4</sub>) with sizes between 87 ± 8 nm and 28 ± 6 nm were coated with a thin silica shell (3 nm). As a result, the hysteresis width is lowered from 37 K to 22 K. Here, a distinctive rise of the residual HS fraction to 41 % is observed for the smallest particles.<sup>[88]</sup> The matrix effect on the ST was also analysed for already prepared NPs of the 3D CP [Fe(pz)Pt(CN)<sub>4</sub>]. Three different matrices were chosen for the particles with a size of about 10 nm: a macrocyclic ligand based on a calixarene (calix8 = C<sub>192</sub>H<sub>264</sub>N<sub>8</sub>O<sub>16</sub>S<sub>8</sub>), a thin silica shell of approximately 2 nm, and a thicker silica shell of around 4.5 nm. It was found that the hysteresis of the material is lost completely with both the calix8 ligand and the thicker silica shell. Also, the latter particles showed a distinct shift of the transition temperature to lower temperatures

compared to the bulk material ( $\sim 70$  K) and a larger residual HS fraction at 50 K ( $\sim 50$  %). The particles in the thin silica shell showed a ST with a 15 K wide hysteresis. However, the transition temperature is also shifted about 30 K to lower temperatures and the residual HS fraction at 50 K is still quite high with about 30 %. All particles show a more gradual progression of the ST than the bulk material.<sup>[89]</sup>

Some groups investigated the influence of polymers as matrices on the synthesis of SCO CP NPs. Besides synthesising The CP  $[\text{Fe}(\text{3-Fpy})_2\text{M}(\text{CN})_4]$  ( $\text{M} = \text{Ni}, \text{Pd}, \text{Pt}$ ) in AOT, the same authors also used PVP as micelles and particle sizes of  $209 \pm 54$  nm (Ni),  $292 \pm 43$  nm (Pd), and  $247 \pm 43$  nm are obtained. While the bulk materials undergo and (almost) complete STs with a hysteresis between 206 K and 234 K, the STs of the NPs in PVP are more gradual, no hysteresis is observed and the residual HS fraction rose to up to 38 % at 100 K as indicated by Mössbauer spectroscopy. Even smaller particles are prepared of the CP  $[\text{Fe}(\text{3-Fpy})_2\text{Ni}(\text{CN})_4]$  only showing the increase of the residual HS fraction.<sup>[87]</sup> NPs of the CP  $[\text{Fe}(\text{hptrz})_3](\text{OTs})_2$  were prepared in PEG (polyethylene glycol) with particles sizes of  $490 \pm 70$  nm,  $250 \pm 40$  nm and  $215 \pm 30$  nm, the SCO properties are similar to the bulk material.<sup>[90]</sup> The biopolymer chitosan was used in the formation of NPs of the 3D SCO CP  $[\text{Fe}(\text{pz})\text{Ni}(\text{CN})_4]$ . Particles as small as  $3.8 \pm 0.8$  nm were achieved. Interestingly, a 10 K wide thermal hysteresis near room temperature is observed with  $T_{1/2\downarrow} = 280$  K and  $T_{1/2\uparrow} = 290$  K. The hysteresis of the NPs became 20 K narrower (bulk: 277 K and 302 K), but the transition temperatures lie between the ones of the bulk material. Mössbauer spectroscopy determined the residual HS fraction to 34 % in the NPs at 80 K.<sup>[91]</sup> The chemical structures of the repetition units of the used polymers are given in Figure 12.



**Figure 12:** Chemical structures of the repetition units of the polymers used in the formation of 1D, 2D, and 3D SCO CP NPs. From left to right: chitosan, polyethylene glycol (PEG), polyvinyl alcohol (PVA), and polyvinylpyrrolidone (PVP).

The SCO properties of the NPs synthesised with different matrices are summarised in Table 2. Comparing NPs of the CP  $[\text{Fe}(\text{Htrz})_2(\text{trz})](\text{BF}_4)$  synthesised without (see Table 1) and with a 3 nm thin silica shell show that the matrix has an influence on the hysteresis width. It is nearly halved (22 K vs. 41 K), although the particles with the silica shell are still larger than the ones without. Other examples showed that the matrices altered the transition temperature mostly to lower temperatures and the hysteresis width was narrowed.

### 3. Introduction

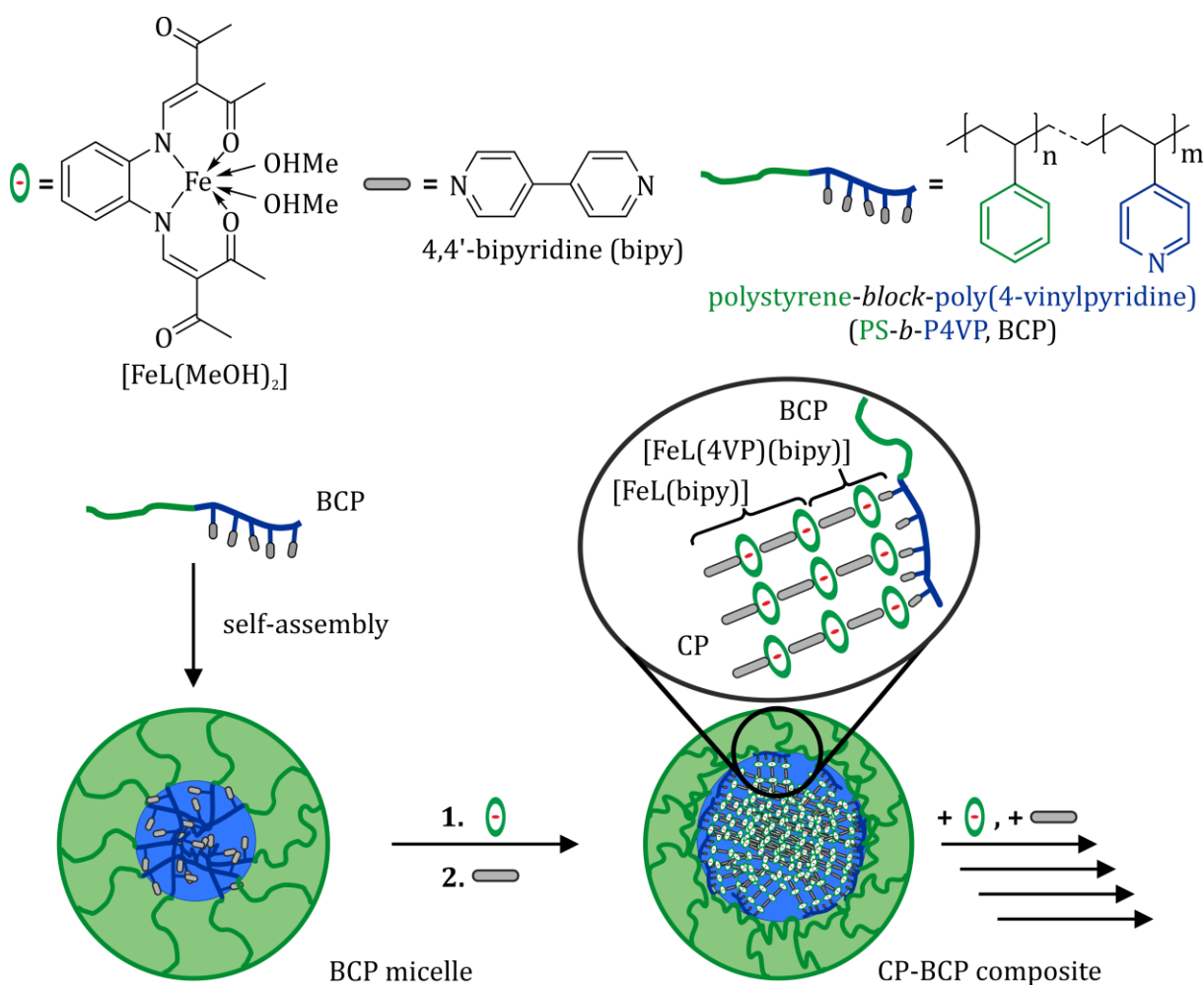
**Table 2:** Overview over CP NPs synthesised with matrices (SiO<sub>2</sub>, calix8, PVP, PEG, and chitosan), the resulting particle sizes, and the SCO properties ( $T_{1/2\downarrow}$ ,  $T_{1/2\uparrow}$ , and hysteresis width).

CP@Matrix	Thickness [nm]	Particle size [nm] <sup>a)</sup>	$T_{1/2\downarrow}$ [K]	$T_{1/2\uparrow}$ [K]	Hysteresis width [K]
[Fe(Htrz) <sub>2</sub> (trz)](BF <sub>4</sub> )@SiO <sub>2</sub> <sup>[88]</sup>	3	87 ± 8	339	376	37
[Fe(Htrz) <sub>2</sub> (trz)](BF <sub>4</sub> )@SiO <sub>2</sub> <sup>[88]</sup>	3	60 ± 8	344	373	29
[Fe(Htrz) <sub>2</sub> (trz)](BF <sub>4</sub> )@SiO <sub>2</sub> <sup>[88]</sup>	3	38 ± 7	342	366	24
[Fe(Htrz) <sub>2</sub> (trz)](BF <sub>4</sub> )@SiO <sub>2</sub> <sup>[88]</sup>	3	28 ± 6	342	364	22
[Fe(pz)Pt(CN) <sub>4</sub> ]@SiO <sub>2</sub> <sup>[89]</sup>	2	14.0 ± 2.4	~260	~275	15
[Fe(pz)Pt(CN) <sub>4</sub> ]@SiO <sub>2</sub> <sup>[89]</sup>	4.5	14.0 ± 2.4	~220	~220	0
[Fe(pz)Pt(CN) <sub>4</sub> ]@calix8 <sup>[89]</sup>	-	10.5 ± 1.8	~260	~260	0
[Fe(3-Fpy) <sub>2</sub> Ni(CN) <sub>4</sub> ]@PVP <sup>[87]</sup>	-	209 ± 54	180	180	0
[Fe(3-Fpy) <sub>2</sub> Pd(CN) <sub>4</sub> ]@PVP <sup>[87]</sup>	-	292 ± 43	190	190	0
[Fe(3-Fpy) <sub>2</sub> Pt(CN) <sub>4</sub> ]@PVP <sup>[87]</sup>	-	247 ± 43	185	185	0
[Fe(hptrz) <sub>3</sub> ](OTs) <sub>2</sub> @PEG <sup>[90]</sup>	-	490 ± 70	309	312	3
[Fe(hptrz) <sub>3</sub> ](OTs) <sub>2</sub> @PEG <sup>[90]</sup>	-	215 ± 30	307	315	8
[Fe(hptrz) <sub>3</sub> ](OTs) <sub>2</sub> @PEG <sup>[90]</sup>	-	250 ± 40	309	315	6
[Fe(pz)Ni(CN) <sub>4</sub> ]@chitosan <sup>[91]</sup>	-	3.8 ± 0.8	280	290	10

<sup>a)</sup> Analysed by TEM measurements.

Polymers for the formation of NPs were also used in our group. At first, microcrystals were synthesised of the 1D SCO CP [FeL(bipy)]<sub>n</sub> on the surface of a poly(4-vinylpyridine) matrix. The SCO properties were found to be dependent on the amount and the size of the formed CP. No ST is detectable in the sample with a low amount of CP. Raising the content of the CP leads to an appearance of the ST. The transition temperature and the abruptness of the ST were similar to the bulk material and the residual HS fraction reached 28 %.<sup>[92]</sup> A follow-up work aimed for the incorporation of the CP [FeL(bipy)]<sub>n</sub> (L = [3,3']-[1,2-phenylenebis(iminoethylidene)]bis-(2,4-pentanedionato)(2-), bipy = 4,4'-bipyridine) into polymeric micelles which may enable an easy control of the particle size. Therefore, the polymer was changed to a diblock copolymer (BCP) consisting of polystyrene-*block*-poly(4-vinylpyridine) (PS-*b*-P4VP). This block copolymer self-assembles into micelles in THF with the poly(4-vinylpyridine) block forming the core and the polystyrene block forming the shell of the micelle. Figure 13 shows the starting materials and the synthesis route. The diblock copolymer and the iron(II) complex were heated under reflux for 2 h in THF. The bridging ligand was added afterwards, followed by another heating period of 1 h. Subsequently, the complex and the ligand can be added simultaneously (Figure 13 bottom). The core size of the spherical micelles was determined to 48 nm. It was possible to incorporate the 1D

SCO CP  $[\text{FeL}(\text{bipy})]_n$  into the micellar core to obtain a nanocomposite. The size of the micelles was independent from the amount of CP introduced into the core underlining the templating effect of the BCP. It was found that the hysteresis width is narrowed to 8 K and the transition temperature of the nanocomposite is shifted about 60 K to lower temperatures compared to the bulk material.<sup>[93]</sup> In preliminary results, a morphological change of the polymeric micelles from spheres to rods, worm-like micelles, or vesicles was observed. It is also predicted that this approach can be adapted to the synthesis of NPs of 2D and 3D CNs.<sup>[94]</sup>



**Figure 13:** Schematic representation of the synthesis for the formation of SCO CP NPs inside the micellar core using a diblock copolymer as template.<sup>[93]</sup>

Based on the latter results, this thesis deals with the size and shape control of  $[\text{FeL}(\text{bipy})]_n$  CP-BCP nanocomposites. This can be achieved by altering the P4VP fraction the diblock copolymer PS-*b*-P4VP between 15 % and 61 %, while keeping a constant molecular weight. Since it is known that the transition temperature of the CP  $[\text{FeL}(\text{bipy})]_n$  is shifted about 60 K to lower temperatures

it is additionally investigated if elevated temperatures have an influence on the SCO properties of the [FeL(bipy)]<sub>n</sub> CP-BCP nanocomposites. In another step the prediction that the synthesis route can be extended to other 1D CP than [FeL(bipy)]<sub>n</sub> and even 2D CN is verified by the incorporation of several other 1D CPs and a 2D CN.

### 3.3. References

- [1] C. Altavilla, E. Ciliberto (Hrsg.) *Inorganic nanoparticles. Synthesis, applications, and perspectives*, CRC Press, Boca Raton, **2011**.
  - [2] Z.-Y. Zhou, N. Tian, J.-T. Li, I. Broadwell, S.-G. Sun, *Chem. Soc. Rev.* **2011**, *40*, 4167–4185.
  - [3] H. Ahmad, S. K. Kamarudin, L. J. Minggu, M. Kassim, *Renew. Sustain. Energy Rev.* **2015**, *43*, 599–610.
  - [4] K. Thorkelsson, P. Bai, T. Xu, *Nano Today* **2015**, *10*, 48–66.
  - [5] Q. Zhang, E. Uchaker, S. L. Candelaria, G. Cao, *Chem. Soc. Rev.* **2013**, *42*, 3127–3171.
  - [6] M. Meyyappan, M. K. Sunkara, *Inorganic Nanowires. Applications, Properties, and Characterization*, Taylor and Francis, Hoboken, **2013**.
  - [7] J. Linares, E. Codjovi, Y. Garcia, *Sensors* **2012**, *12*, 4479–4492.
  - [8] J. Li, N. Wu (Hrsg.) *Biosensors Based on Nanomaterials and Nanodevices*, CRC Press, Boca Raton, **2017**.
  - [9] T. Hegmann, H. Qi, V. M. Marx, *J. Inorg. Organomet. Polym. Mater.* **2007**, *17*, 483–508.
  - [10] D. P. Cormode, P. A. Jarzyna, W. J. M. Mulder, Z. A. Fayad, *Adv. Drug Deliv. Rev.* **2010**, *62*, 329–338.
  - [11] X. Zhao, H. Zhao, Z. Chen, M. Lan, *J. Nanosci. Nanotechnol.* **2014**, *14*, 210–220.
  - [12] B. Bonnemain, *J. Drug Target.* **1998**, *6*, 167–174.
  - [13] J. K. Patra, G. Das, L. F. Fraceto, E. V. R. Campos, M. D. P. Rodriguez-Torres, L. S. Acosta-Torres, L. A. Diaz-Torres, R. Grillo, M. K. Swamy, S. Sharma, S. Habtemariam, H.-S. Shin, *J. Nanobiotechnol.* **2018**, *16*, 71.
  - [14] Z. Nie, A. Petukhova, E. Kumacheva, *Nat. Nanotechnol.* **2010**, *5*, 15–25.
  - [15] R. Nowak, E. A. Prasetyanto, L. de Cola, B. Bojer, R. Siegel, J. Senker, E. Rössler, B. Weber, *Chem. Commun.* **2017**, *53*, 971–974.
  - [16] E. Coronado, M. Giménez-Marqués, G. Mínguez Espallargas, F. Rey, I. J. Vitórica-Yrezábal, *J. Am. Chem. Soc.* **2013**, *135*, 15986–15989.
  - [17] O. Kahn, C. J. Martinez, *Science* **1998**, *279*, 44–48.
  - [18] J.-F. Létard, P. Guionneau, L. Goux-Capes in *Topics in Current Chemistry* (Hrsg.: P. Gülich, H. A. Goodwin), Springer, Berlin, Heidelberg, **2004**, S. 221–249.
  - [19] V. Stavila, M. Allali, L. Canaple, Y. Stortz, C. Franc, P. Maurin, O. Beuf, O. Dufay, J. Samarut, M. Janier, J. Hasserodt, *New J. Chem.* **2008**, *32*, 428–435.
-

- [20] C. Rajadurai, M. Ruben, D. Kruk, EP2072062B1, **2012**.
- [21] R. N. Muller, L. Vander Elst, S. Laurent, *J. Am. Chem. Soc.* **2003**, *125*, 8405–8407.
- [22] P. Gütllich, A. Hauser, H. Spiering, *Angew. Chem. Int. Ed. Engl.* **1994**, *33*, 2024–2054.
- [23] P. Gütllich, H. A. Goodwin, *Spin Crossover in Transition Metal Compounds I*, Springer, Berlin, Heidelberg, **2004**.
- [24] P. Gütllich, V. Ksenofontov, A. B. Gaspar, *Coord. Chem. Rev.* **2005**, *249*, 1811–1829.
- [25] A. B. Gaspar, G. Molnár, A. Rotaru, H. J. Shepherd, *C. R. Chim.* **2018**, *21*, 1095–1120.
- [26] A. Hauser in *Topics in Current Chemistry* (Hrsg.: P. Gütllich, H. A. Goodwin), Springer, Berlin, Heidelberg, **2004**, S. 155–198.
- [27] Z.-P. Ni, J.-L. Liu, M. N. Hoque, W. Liu, J.-Y. Li, Y.-C. Chen, M.-L. Tong, *Coord. Chem. Rev.* **2017**, *335*, 28–43.
- [28] M. A. Halcrow, *Spin-Crossover Materials*, John Wiley & Sons Ltd, Oxford, UK, **2013**.
- [29] P. Gütllich, A. B. Gaspar, Y. Garcia, *Beilstein J. Org. Chem.* **2013**, *9*, 342–391.
- [30] R. L. Carlin in *Magnetochemistry* (Hrsg.: R. L. Carlin), Springer, Berlin, Heidelberg, **1986**, S. 1–18.
- [31] B. N. Figgis, J. Lewis in *Modern Coordination Chemistry* (Hrsg.: J. Lewis, R. G. Wilkins), Wiley, New York, **1960**, S. 406.
- [32] J. I. Hoppe, *J. Chem. Educ.* **1972**, *49*, 505.
- [33] B. Weber, F. A. Walker, *Inorg. Chem.* **2007**, *46*, 6794–6803.
- [34] P. Gütllich, *Z. Anorg. Allg. Chem.* **2012**, *638*, 15–43.
- [35] P. Gütllich, H. A. Goodwin in *Topics in Current Chemistry* (Hrsg.: P. Gütllich, H. A. Goodwin), Springer, Berlin, Heidelberg, **2004**, S. 1–47.
- [36] R. Kulmaczewski, O. Cespedes, M. A. Halcrow, *Inorg. Chem.* **2017**, *56*, 3144–3148.
- [37] P. Gütllich, A. B. Gaspar, V. Ksenofontov, Y. Garcia, *J. Phys.: Condens. Matter* **2004**, *16*, 1087–1108.
- [38] B. Weber, R. Tandon, D. Himsl, *Z. Anorg. Allg. Chem.* **2007**, *633*, 1159–1162.
- [39] W. Bauer, W. Scherer, S. Altmannshofer, B. Weber, *Eur. J. Inorg. Chem.* **2011**, 2803–2818.
- [40] S. A. Barrett, M. A. Halcrow, *RSC Adv.* **2014**, *4*, 11240–11243.
- [41] A.-M. Li, T. Hochdörffer, J. Wolny, V. Schünemann, E. Rentschler, *Magnetochemistry* **2018**, *4*, 34.
- [42] N. F. Sciortino, K. R. Scherl-Gruenwald, G. Chastanet, G. J. Halder, K. W. Chapman, J.-F. Létard, C. J. Kepert, *Angew. Chem. Int. Ed.* **2012**, *51*, 10154–10158.
- [43] R.-G. Xiong, S. R. Wilson, W. Lin, *Dalton Trans.* **1998**, 4089–4090.
- [44] Y. Garcia, V. Niel, M. C. Muñoz, J. A. Real in *Topics in Current Chemistry* (Hrsg.: P. Gütllich, H. A. Goodwin), Springer, Berlin, Heidelberg, **2004**, S. 229–257.



- [45] L. Stoleriu, P. Chakraborty, A. Hauser, A. Stancu, C. Enachescu, *Phys. Rev. B* **2011**, *84*, 134102.
  - [46] G. S. Matouzenko, G. Molnar, N. Bréfuel, M. Perrin, A. Bousseksou, S. A. Borshch, *Chem. Mater.* **2003**, *15*, 550–556.
  - [47] M. Nakaya, K. Shimayama, K. Takami, K. Hirata, A. S. Alao, M. Nakamura, L. F. Lindoy, S. Hayami, *Chem. Lett.* **2014**, *43*, 1058–1060.
  - [48] G. Juhász, S. Hayami, O. Sato, Y. Maeda, *Chem. Phys. Lett.* **2002**, *364*, 164–170.
  - [49] B. Weber, W. Bauer, J. Obel, *Angew. Chem. Int. Ed.* **2008**, *47*, 10098–10101.
  - [50] H. Hagiwara, S. Okada, *Chem. Commun.* **2016**, *52*, 815–818.
  - [51] M. A. Halcrow, *Chem. Lett.* **2014**, *43*, 1178–1188.
  - [52] P. Durand, S. Pillet, E.-E. Bendeif, C. Carteret, M. Bouazaoui, H. El Hamzaoui, B. Capoen, L. Salmon, S. Hébert, J. Ghanbaja, L. Aranda, D. Schaniel, *J. Mater. Chem. C* **2013**, *1*, 1933–1942.
  - [53] H. Peng, S. Tricard, G. Félix, G. Molnár, W. Nicolazzi, L. Salmon, A. Bousseksou, *Angew. Chem. Int. Ed.* **2014**, *53*, 10894–10898.
  - [54] S. Titos-Padilla, J. M. Herrera, X.-W. Chen, J. J. Delgado, E. Colacio, *Angew. Chem. Int. Ed.* **2011**, *50*, 3290–3293.
  - [55] H. Voisin, C. Aimé, A. Vallée, A. Bleuzen, M. Schmutz, G. Mosser, T. Coradin, C. Roux, *J. Mater. Chem. C* **2017**, *5*, 11542–11550.
  - [56] C. Faulmann, J. Chahine, I. Malfant, D. de Caro, B. Cormary, L. Valade, *Dalton Trans.* **2011**, *40*, 2480–2485.
  - [57] F. Volatron, L. Catala, E. Rivière, A. Gloter, O. Stéphan, T. Mallah, *Inorg. Chem.* **2008**, *47*, 6584–6586.
  - [58] M. Giménez-Marqués, M. L. García-Sanz de Larrea, E. Coronado, *J. Mater. Chem. C* **2015**, *3*, 7946–7953.
  - [59] H. O. Pierson, *Handbook of chemical vapor deposition. Principles, technology, and applications*, 2. Aufl., Noyes Publ, Norwich, NY, **1999**.
  - [60] J. Li, Q. Wu, J. Wu in *Handbook of Nanoparticles* (Hrsg.: M. Aliofkhazraei), Springer, Cham, **2016**, S. 295–328.
  - [61] M. J. Burger, B. J. Robinson, L. F. Pease in *Handbook of Nanoparticles* (Hrsg.: M. Aliofkhazraei), Springer, Cham, **2016**, S. 691–714.
  - [62] C.-X. Zhao, A. P. J. Middelberg in *Handbook of Nanoparticles* (Hrsg.: M. Aliofkhazraei), Springer, Cham, **2016**, S. 455–473.
  - [63] C. M. Bell, M. F. Arendt, L. Gomez, R. H. Schmehl, T. E. Mallouk, *J. Am. Chem. Soc.* **1994**, *116*, 8374–8375.
  - [64] K. Osseo-Asare, F. J. Arriagada, *Colloids and Surfaces* **1990**, *50*, 321–339.
-

- [65] L. D. Rampino, F. F. Nord, *J. Am. Chem. Soc.* **1941**, *63*, 2745–2749.
  - [66] V. Niel, J. M. Martinez-Agudo, M. C. Muñoz, A. B. Gaspar, J. A. Real, *Inorg. Chem.* **2001**, *40*, 3838–3839.
  - [67] J. H. González-Estefan, M. Gonidec, N. Daro, M. Marchivie, G. Chastanet, *Chem. Commun.* **2018**, *54*, 8040–8043.
  - [68] J. T. Culp, J.-H. Park, I. O. Benitez, Y.-D. Huh, M. W. Meisel, D. R. Talham, *Chem. Mater.* **2003**, *15*, 3431–3436.
  - [69] S. Lepoutre, D. Grosso, C. Sanchez, G. Fornasieri, E. Rivière, A. Bleuzen, *Adv. Mater.* **2010**, *22*, 3992–3996.
  - [70] R. C. Millward, C. E. Madden, I. Sutherland, R. J. Mortimer, S. Fletcher, F. Marken, *Chem. Commun.* **2001**, 1994–1995.
  - [71] V. Trannoy, M. Faustini, D. Grosso, F. Brisset, P. Beaunier, E. Rivière, M. Putero, A. Bleuzen, *Nanoscale* **2017**, *9*, 5234–5243.
  - [72] S. Tricard, C. Fabrice, T. Mallah, *Dalton Trans.* **2013**, *42*, 15835–15845.
  - [73] S. Cobo, G. Molnár, J. A. Real, A. Bousseksou, *Angew. Chem. Int. Ed.* **2006**, *45*, 5786–5789.
  - [74] G. Agustí, S. Cobo, A. B. Gaspar, G. Molnár, N. O. Moussa, P. Á. Szilágyi, V. Pálfi, C. Vieu, M. Carmen Muñoz, J. A. Real, A. Bousseksou, *Chem. Mater.* **2008**, *20*, 6721–6732.
  - [75] G. Molnár, S. Cobo, J. A. Real, F. Carcenac, E. Daran, C. Vieu, A. Bousseksou, *Adv. Mater.* **2007**, *19*, 2163–2167.
  - [76] C. Bartual-Murgui, A. Akou, C. Thibault, G. Molnár, C. Vieu, L. Salmon, A. Bousseksou, *J. Mater. Chem. C* **2015**, *3*, 1277–1285.
  - [77] C. Bartual-Murgui, A. Akou, L. Salmon, G. Molnár, C. Thibault, J. A. Real, A. Bousseksou, *Small* **2011**, *7*, 3385–3391.
  - [78] C. Bartual-Murgui, L. Salmon, A. Akou, C. Thibault, G. Molnár, T. Mahfoud, Z. Sekkat, J. A. Real, A. Bousseksou, *New J. Chem.* **2011**, *35*, 2089.
  - [79] S. Sakaida, T. Haraguchi, K. Otsubo, O. Sakata, A. Fujiwara, H. Kitagawa, *Inorg. Chem.* **2017**, *56*, 7606–7609.
  - [80] T. Forestier, S. Mornet, N. Daro, T. Nishihara, S. Mouri, K. Tanaka, O. Fouché, E. Freysz, J.-F. Létard, *Chem. Commun.* **2008**, 4327–4329.
  - [81] T. Forestier, A. Kaiba, S. Pechev, D. Denux, P. Guionneau, C. Etrillard, N. Daro, E. Freysz, J.-F. Létard, *Chem. Eur. J.* **2009**, *15*, 6122–6130.
  - [82] A. Tokarev, L. Salmon, Y. Guari, W. Nicolazzi, G. Molnár, A. Bousseksou, *Chem. Commun.* **2010**, *46*, 8011–8013.
  - [83] A. Tokarev, L. Salmon, Y. Guari, G. Molnár, A. Bousseksou, *New J. Chem.* **2011**, *35*, 2081–2088.
-

- [84] E. Coronado, J. R. Galán-Mascarós, M. Monrabal-Capilla, J. García-Martínez, P. Pardo-Ibañez, *Adv. Mater.* **2007**, *19*, 1359–1361.
- [85] I. Boldog, A. B. Gaspar, V. Martínez, P. Pardo-Ibañez, V. Ksenofontov, A. Bhattacharjee, P. Gütllich, J. A. Real, *Angew. Chem. Int. Ed.* **2008**, *47*, 6433–6437.
- [86] P. D. Southon, L. Liu, E. A. Fellows, D. J. Price, G. J. Halder, K. W. Chapman, B. Moubaraki, K. S. Murray, J.-F. Létard, C. J. Kepert, *J. Am. Chem. Soc.* **2009**, *131*, 10998–11009.
- [87] V. Martínez, I. Boldog, A. B. Gaspar, V. Ksenofontov, A. Bhattacharjee, P. Gütllich, J. A. Real, *Chem. Mater.* **2010**, *22*, 4271–4281.
- [88] R. Torres-Cavanillas, L. Lima-Moya, F. D. Tichelaar, H. W. Zandbergen, M. Giménez-Marqués, E. Coronado, *Dalton Trans.* **2019**, *48*, 15465–15469.
- [89] Y. Raza, F. Volatron, S. Moldovan, O. Ersen, V. Huc, C. Martini, F. Brisset, A. Gloter, O. Stéphan, A. Bousseksou, L. Catala, T. Mallah, *Chem. Commun.* **2011**, *47*, 11501–11503.
- [90] I. A. Gural'skiy, C. M. Quintero, G. Molnár, I. O. Fritsky, L. Salmon, A. Bousseksou, *Chem. Eur. J.* **2012**, *18*, 9946–9954.
- [91] J. Larionova, L. Salmon, Y. Guari, A. Tokarev, K. Molvinger, G. Molnár, A. Bousseksou, *Angew. Chem. Int. Ed.* **2008**, *47*, 8236–8240.
- [92] C. Göbel, T. Palamarciuc, C. Lochenie, B. Weber, *Chem. Asian J.* **2014**, *9*, 2232–2238.
- [93] O. Klimm, C. Göbel, S. Rosenfeldt, F. Puchtler, N. Miyajima, K. Marquardt, M. Drechsler, J. Breu, S. Förster, B. Weber, *Nanoscale* **2016**, *8*, 19058–19065.
- [94] B. Weber, *Chem. Eur. J.* **2017**, *23*, 18093–18100.

---

---

## 4. Synopsis

This thesis includes four scientific articles (Chapters 6 – 9). Three are accepted publications (Chapters 6 – 8) and one is to be submitted to a scientific journal (Chapter 9). The contribution of each author to the joint publications is given in Chapter 5.

This thesis follows up on the work of Ottokar Klimm who established a synthesis route employing the diblock copolymer (BCP) polystyrene-*block*-poly(4-vinylpyridine) (PS-*b*-P4VP) as a micellar template for the formation of NPs of a 1D SCO CP. This work aims for an advancement in the use of diblock copolymers as micellar template by expanding the synthesis route to a variety of coordination compounds like other SCO and non-SCO CPs and CNs. Furthermore, a control of the particle size and shape of the nanocomposites is investigated and the improvement of the SCO properties by the synthesis of larger particles or a thermal annealing is described.

Several different BCPs have been used throughout this thesis. The important characteristics (molecular weight  $M_n$ , weight fraction of the two blocks) and the indication in which chapter the polymer was used are given in Table 1. BCP-20 was provided by the workgroup of Prof. Förster. This BCP was used in the work of my predecessor Ottokar Klimm and was further utilized for the synthesis of the samples in chapter 6. During this time, it became clear that BCP-20 had to be reproduced for further synthetic use. This was done by the workgroup of Prof. Greiner resulting in the BCP  $S_{85}V_{15}^{154}$  (also SV-15). The characterisation of SV-15 revealed that the particle core sizes of SV-15 and BCP-20 differed greatly (15 nm vs. 45 nm). Due to this observation, BCP-20 was characterised again to find that the polymer contained an extensive amount of homopolymerised polystyrene. After extraction of the homopolymerised PS, the ratio of P4VP was found to be much greater than 15 wt% and the molecular weight was smaller than the stated 150 000 g mol<sup>-1</sup>. As a result, the polymer BCP-20 was discarded. The BCPs SV-21, SV-35, SV-42, and SV-61 were also provided by the workgroup of Prof. Greiner. Table 1 also states the use of these polymers in the different chapters.

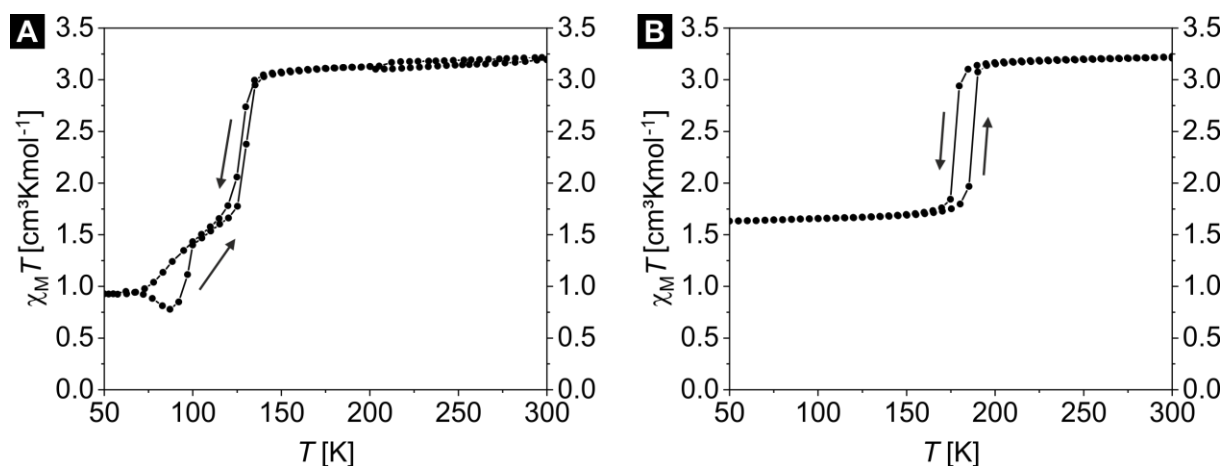
## 4. Synopsis

**Table 1:** Overview over the used block copolymers in this thesis.

BCP <sup>a)</sup>	Abbreviation	$M_n$ [g mol <sup>-1</sup> ]	Fraction PS [wt%]	Fraction P4VP [wt%]	Used in chapter
BCP-20 <sup>b)</sup>	-	150 000	85	15	6
S <sub>85</sub> V <sub>15</sub> <sup>154</sup>	SV-15	154 000	85	15	7, 8, 9
S <sub>79</sub> V <sub>21</sub> <sup>119</sup>	SV-21	119 000	79	21	9
S <sub>65</sub> V <sub>35</sub> <sup>131</sup>	SV-35	131 000	65	35	9
S <sub>58</sub> V <sub>42</sub> <sup>157</sup>	SV-42	157 000	58	42	8, 9
S <sub>39</sub> V <sub>61</sub> <sup>162</sup>	SV-61	162 000	39	61	9

<sup>a)</sup> subscripts denote the content of the respective block in wt%, superscript gives the number average molecular weight in kg mol<sup>-1</sup>, <sup>b)</sup> polymer characteristic provided by the workgroup of Prof. Förster.

Chapter 6 deals with the adaption of the synthetic procedure to the NP formation of three further 1D SCO CPs: [FeL(bpea)]<sub>n</sub>, [FeL(bpee)]<sub>n</sub>, and [FeL(bpey)]<sub>n</sub> (bpea = 1,2-di(4-pyridyl)ethane, bpee = (*E*)-1,2-di(4-pyridyl)ethene, bpey = 1,2-di(4-pyridyl)ethyne). Additionally, the influence of the flexibility of the bridging ligands on the formation of nanoparticles or microcrystals was investigated. At first, the respective CPs were prepared as bulk materials in tetrahydrofuran (THF) the characterisation was compared to the literature data in which the compounds were obtained from methanol (MeOH), since the SCO properties are often solvent dependent. All three CPs were obtained as crystalline powders from the reaction of the iron complex [FeL(MeOH)<sub>2</sub>] and the respective bridging ligand bpea, bpee, and bpey in THF. The magnetic properties of the CPs obtained from THF were nearly identical to their counterparts synthesised in MeOH. The CP [FeL(bpee)]<sub>n</sub> is a pure HS compound between 50 K and 300 K, whereas [FeL(bpey)]<sub>n</sub> undergoes an abrupt, but only half-complete SCO with a hysteresis width of 10 K at transition temperatures of  $T_{1/2\downarrow} = 177$  K and  $T_{1/2\uparrow} = 187$  K. The magnetic properties of the CP [FeL(bpea)]<sub>n</sub> synthesised in THF differ from its counterpart from MeOH. Obtained from MeOH, [FeL(bpea)]<sub>n</sub> shows a complete, two-step ST whereas from THF, the first transition step is identical to the CP from MeOH but the second transition step is gradual, incomplete, and shows a kinetic effect in the heating curve (Figure 1).

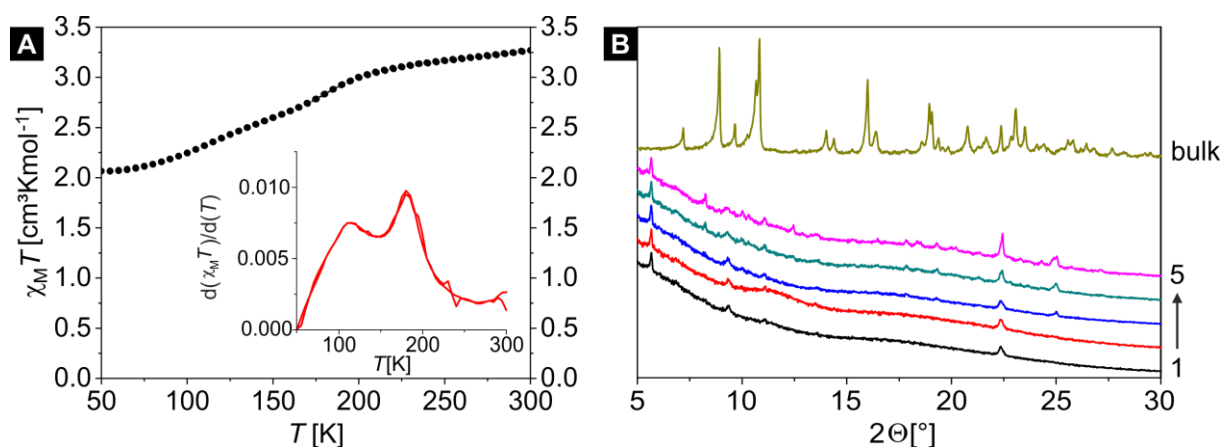


**Figure 1:** Magnetic susceptibility data  $\chi_M T$  vs.  $T$  for the two bulk SCO CPs  $[\text{FeL}(\text{bpea})]_n$  (A) and  $[\text{FeL}(\text{bpey})]_n$  (B) obtained from the reaction in THF in the temperature range from 50 K to 300 K.

The synthesis for the formation of the nanocomposites  $[\text{FeL}(\text{bpea})]_n@BCP$ ,  $[\text{FeL}(\text{bpee})]_n@BCP$ , and  $[\text{FeL}(\text{bpey})]_n@BCP$  was carried according out to the published protocol by Klimm *et al.* The iron(II) complex  $[\text{FeL}(\text{MeOH})_2]$  and the BCP were dissolved in THF under an argon atmosphere and heated to reflux for 2 h. After a cooling to RT, the respective bridging ligand was added, and the solution was heated to reflux again for 1 h. The amount of CP can be increased by up to four successive additions (called cycles) of the iron complex and the bridging ligand simultaneously and a subsequent 1 h reflux. After the reaction, the solvent was removed by cold distillation and the resulting product was dried *in vacuo*. It was proposed that the formation of NPs is dependent on the rigidity of the bridging ligand leading to the assumption that microcrystals should appear in the order  $[\text{FeL}(\text{bpea})]_n$ ,  $[\text{FeL}(\text{bpee})]_n$ , and finally  $[\text{FeL}(\text{bpey})]_n$ . The 15 different nanocomposites were all characterised by TEM measurements proving the independence of the particle size from the incorporated CP and the number of cycles, resulting in core sizes of around 45 nm. However, microcrystals outside the micelles were observed for the nanocomposites  $[\text{FeL}(\text{bpea})]_n@BCP$  after five cycles and for  $[\text{FeL}(\text{bpee})]_n@BCP$  already after four cycles, proving our prediction wrong. Microcrystals were absent in all five nanocomposites of  $[\text{FeL}(\text{bpey})]_n@BCP$ . Although, microcrystals were observed for the other 10 samples, DLS measurements for all 15 samples only resulted in particle sizes of around 150 nm and no larger particle sizes were detected. The synthesis of the nanocomposites was also tested in toluene, but larger crystalline material was already observed after two cycles for all three CPs. This led to the hypothesis that the formation of microcrystals of the CP at an early stage in toluene can be explained by a better solubility of the CPs, favouring the formation of the CPs outside of the BCP micelle. However, the crystal formation of the CPs in THF cannot solely be explained by the flexibility of the bridging ligand, since the rigidity rises from bpea over bpee to bpey, but microcrystals first appeared in the

$[\text{FeL}(\text{bpee})]_n@ \text{BCP}$  composites. The second explanation is given by the stability of the CPs regarding the M-L ligand exchange and the ligand field splitting. Octahedral HS complexes with a weak ligand field splitting show a fast ligand exchange due to the occupation of the antibonding orbitals which support the break the M-L bonds, thus increasing the likelihood of microcrystal formation. This explains the first occurrence of microcrystals after four cycles for the nanocomposites synthesised with the CP  $[\text{FeL}(\text{bpee})]_n$ , since it is a pure HS compound.

The magnetic properties of the nanocomposites with four and five cycles were also investigated. As expected, the nanocomposites with  $[\text{FeL}(\text{bpee})]_n$  remained in the HS state over the whole temperature range. The nanocomposite with  $[\text{FeL}(\text{bpea})]_n$  with four cycles undergoes a gradual ST, while the sample with five cycles revealed nearly bulk-like behaviour due to the existence of microcrystals ( $> 2 \mu\text{m}$ ). Interestingly, the magnetic measurements of nanocomposite samples with  $[\text{FeL}(\text{bpey})]_n$  gave a two-step gradual SCO as indicated by the first derivation of the  $\chi_M T$  vs.  $T$  plot showing two maxima. The first transition step occurs at a similar temperature as the bulk material, while the second step takes place at a lower temperature ( $\sim 110 \text{ K}$ ). This is an effect of a different polymorph obtained in the NPs as indicated by the differences in the PXRD pattern of the bulk and the nanocomposite samples (Figure 2).



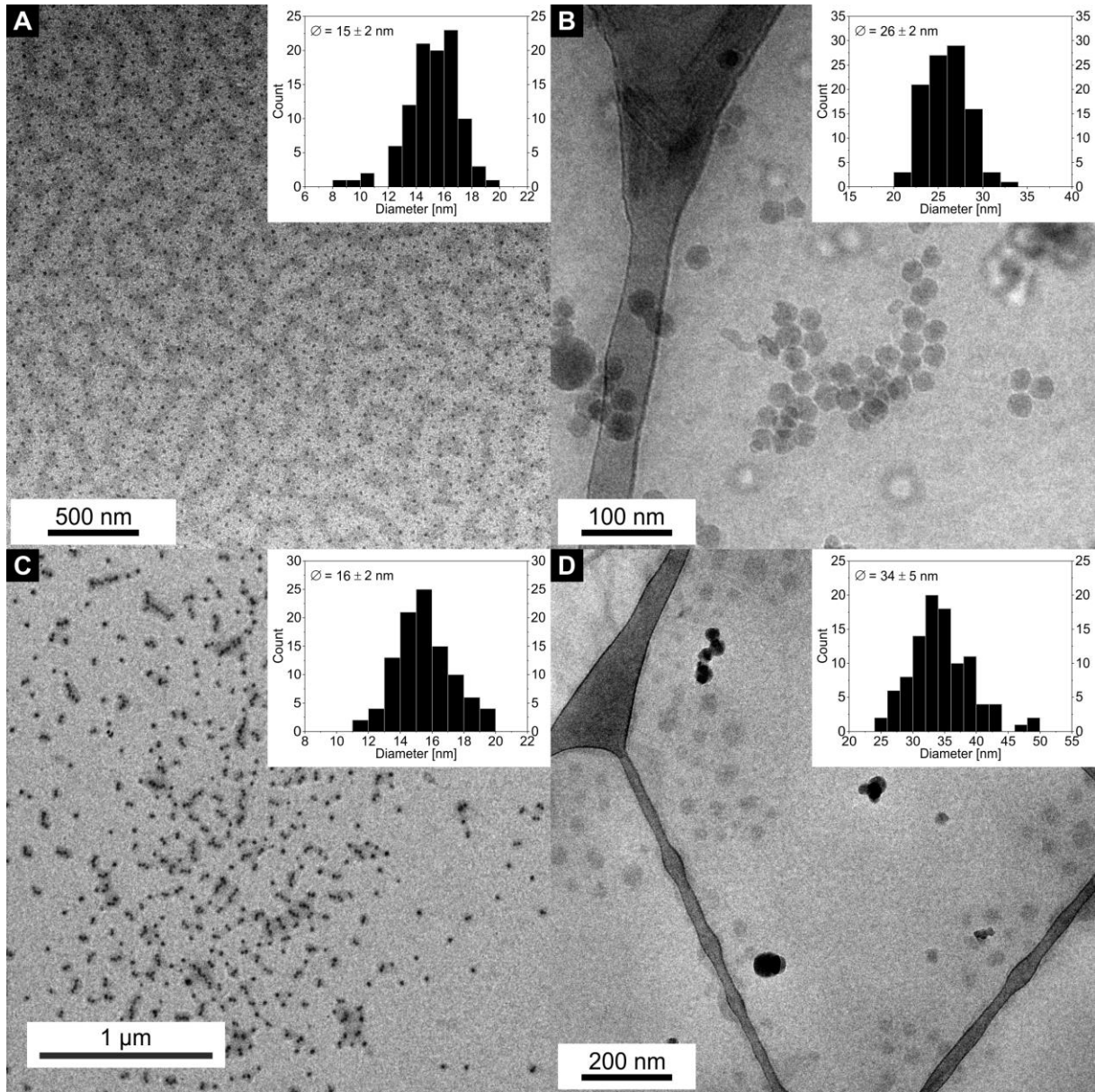
**Figure 2:** Magnetic susceptibility measurement of the nanocomposite with  $[\text{FeL}(\text{bpey})]_n$  with 5 cycles showing a gradual two-step ST and the inset with the first derivative of the ST curve (A). Differences in the PXRD pattern of the bulk  $[\text{FeL}(\text{bpey})]_n$  and the nanocomposites with  $[\text{FeL}(\text{bpey})]_n$  (1-5) indicating the formation of a different polymorph in the NPs (B).

In chapter 7 the incorporation of the 1D CP  $[\text{FeL}(\text{bipy})]_n$  (SCO CP) in smaller BCP micelles, the influence of a thermal annealing process on the SCO behaviour of the nanocomposites (SCO CP-BCP) and the processability of the nanocomposite by electrospinning is investigated. For this purpose, a new PS-*b*-P4VP diblock copolymer  $\text{S}_{85}\text{V}_{15}^{154}$  (BCP, SV-15) was synthesised with a



composition of PS/P4VP of 85/15 (wt/wt), a total molecular weight of  $154\,000\text{ g mol}^{-1}$ , and a polydispersity  $\bar{D} = 1.02$ . This polymer forms narrowly dispersed, spherical micelles with a core diameter  $D_{\text{core}} = 15 \pm 2\text{ nm}$  and  $D_{\text{cryo}} = 26 \pm 2\text{ nm}$  (Figure 3A, B) and a hydrodynamic diameter  $D_{\text{h}} = 75 \pm 28\text{ nm}$  determined by TEM, cryo-TEM, and DLS measurements. The particle sizes of the SCO CP-BCP were also evaluated and spherical micelles were found in TEM and cryo-TEM with sizes of  $D_{\text{core}} = 16 \pm 2\text{ nm}$  and  $D_{\text{cryo}} = 34 \pm 5\text{ nm}$  (Figure 3C, D). The hydrodynamic diameter  $D_{\text{h}}$  was determined to  $87 \pm 37\text{ nm}$ . Additional scanning electron microscopy (SEM) measurements on the SCO CP-BCP nanocomposite confirmed the absence of microcrystals on the surface of the sample.

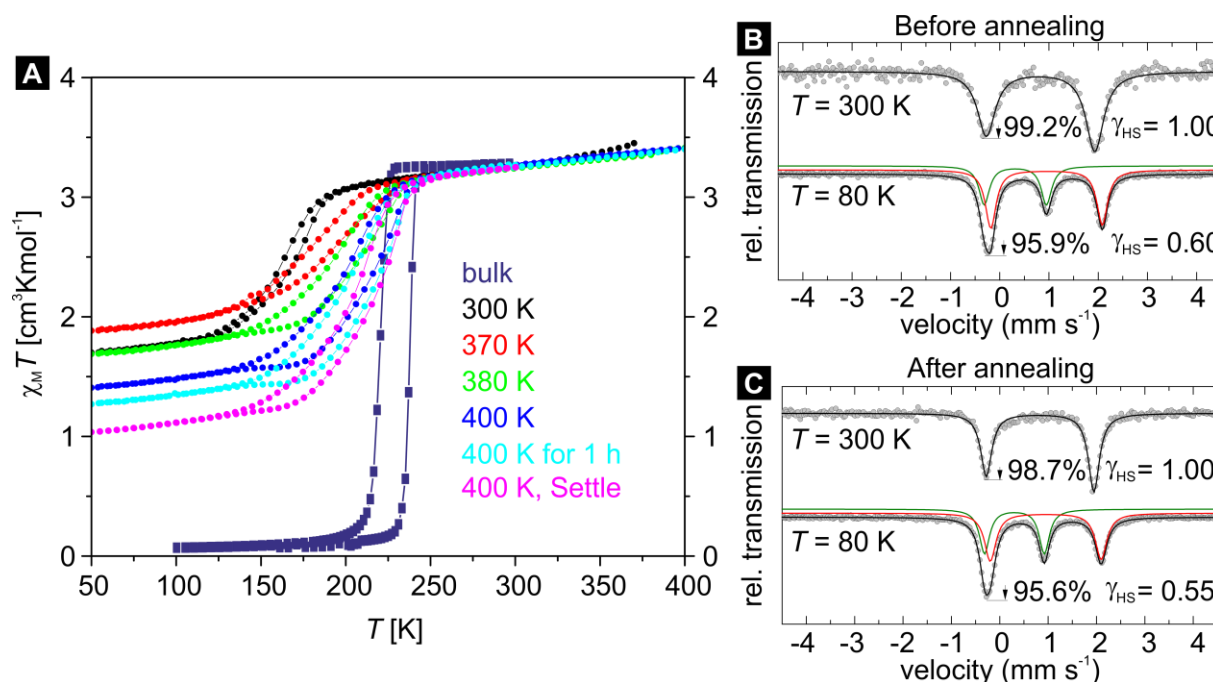
## 4. Synopsis



**Figure 3:** TEM and cryo-TEM images of the neat PS-*b*-P4VP diblock copolymer SV-15 (A, B) and the SCO CP-BCP nanocomposite (C, D) showing spherical nanoparticles in all measurements. The measured core sizes are given in the respective insets.

The magnetic properties of the nanocomposite were analysed by magnetic susceptibility measurements. The as-synthesised sample revealed a rather gradual SCO with transition temperatures  $T_{1/2\downarrow} = 163$  K and  $T_{1/2\uparrow} = 170$  K resulting in a hysteresis width of 7 K. The ST is shifted about 60 K to lower temperatures compared to the bulk material and is distinctly incomplete with a high residual HS fraction of  $\gamma_{\text{HS}} = 52$  %. Interestingly, it was found that the SCO behaviour (transition temperature, hysteresis width and  $\gamma_{\text{HS}}$ ) improved after the sample was heated stepwise to elevated temperatures (370 K, 380 K, and 400 K; Figure 4A) and measured

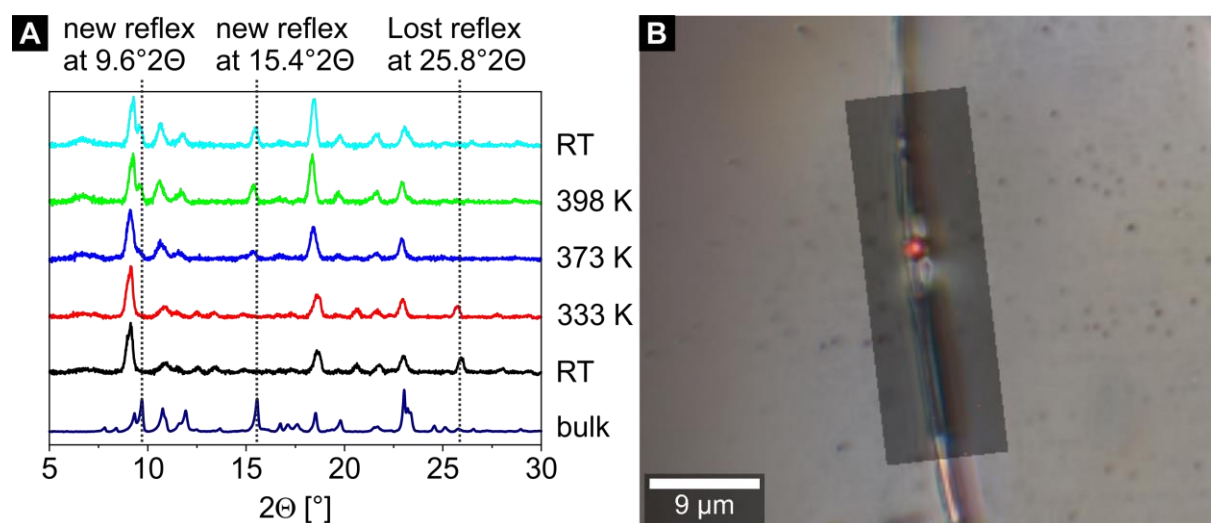
again. It was observed that the transition temperature is shifted back to higher temperatures ultimately reaching  $T_{1/2\downarrow} = 203$  K and  $T_{1/2\uparrow} = 217$  K and a hysteresis width of 14 K. The ST became gradually more complete – despite the value after heating to 370 K – and the residual HS fraction  $\gamma_{\text{HS}}$  is lowered to 32 %. The same behaviour is detectable by temperature-dependent Mössbauer spectroscopy where  $\gamma_{\text{HS}}$  is lowered after thermal annealing of the sample at 400 K (Figure 4B, C).



**Figure 4:** Magnetic susceptibility measurements of the SCO CP-BCP nanocomposite showing the influence of the thermal annealing on the transition temperatures  $T_{1/2\downarrow}$  and  $T_{1/2\uparrow}$ , the hysteresis width and the residual HS fraction  $\gamma_{\text{HS}}$  (A). Temperature-dependent Mössbauer spectroscopy also showed that  $\gamma_{\text{HS}}$  before annealing (B) was higher than after annealing at 400 K (C).

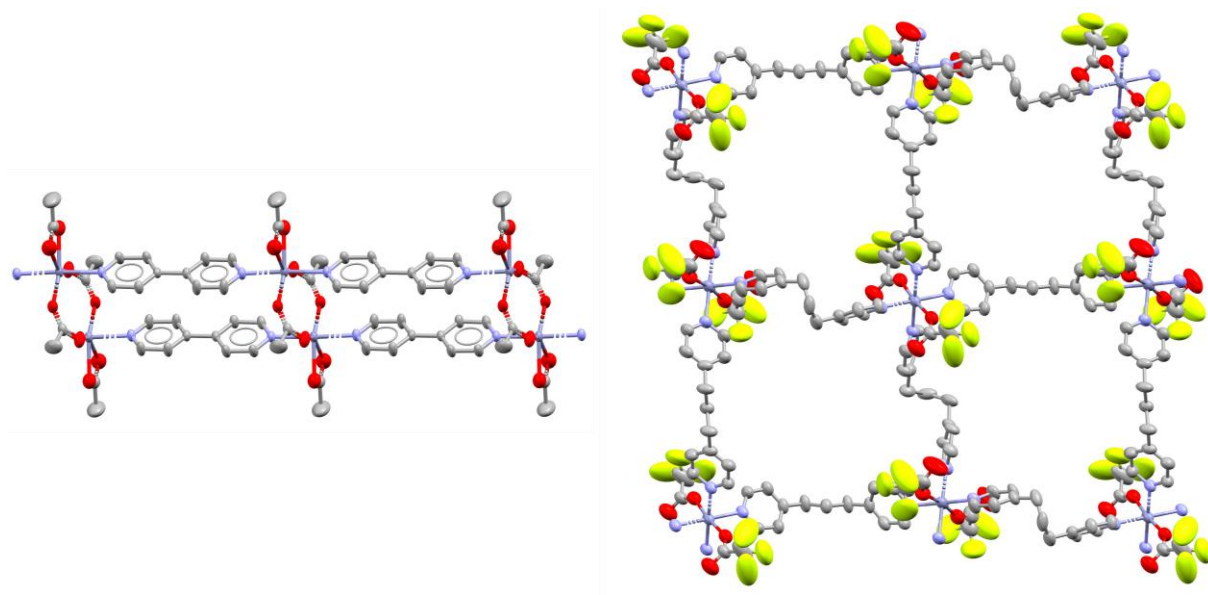
The reason for the improved SCO properties was evaluated by temperature-dependent PXRD measurements. The powder patterns of the SCO CP-BCP nanocomposite, which were measured at four different temperatures, were compared to the bulk material. It was found that the pattern of the SCO CP-BCP nanocomposite at RT and 333 K are identical but differ distinctively from the bulk material. Two prominent reflexes at  $9.6^\circ 2\theta$  and  $15.4^\circ 2\theta$  of the bulk material are absent in the SCO CP-BCP nanocomposite, whereas the nanocomposite shows a reflex at  $25.8^\circ 2\theta$  which is non-existent in the bulk material. Raising the temperature to 373 K or 398 K revealed reflexes at  $9.6^\circ 2\theta$  and  $15.4^\circ 2\theta$  for the nanocomposite and the reflexes at  $25.8^\circ 2\theta$  diminished. The powder pattern of the SCO CP-BCP nanocomposite is persistent even after the cooldown to RT (Figure 5A). It was proposed that raising the temperature to and above the glass transition  $T_g$  of the PS shell of about  $110^\circ\text{C}$  enabled a reorganisation of the CP inside the core of the polymeric micelle. This

enhanced the cooperativity between the separated strands of the CP, which led to a broadened hysteresis, a lower residual HS fraction and a shift of the transition temperature to higher temperatures. The nanocomposite was also characterised after the thermal annealing by TEM, DLS, and SEM. The particles remained intact, the NP sizes were found to be nearly identical and the surface of the sample was still crystal-free. Additionally, it was proven that the nanocomposite is processible by electrospinning. Fibres and non-woven were prepared from a PS/SCO CP-BCP mixture using this method. Raman imaging confirmed the presence of the CP inside the fibres. In Figure 5B, a single fibre is displayed, and the detected CP is coloured in red.



**Figure 5:** Temperature-dependent PXRD of the SCO CP-BCP nanocomposite at four different temperatures and the powder pattern of the bulk material as comparison (A). Digital image of a single electrospun fibre with an overlay of the Raman measurement showing the presence of the CP in red (B).

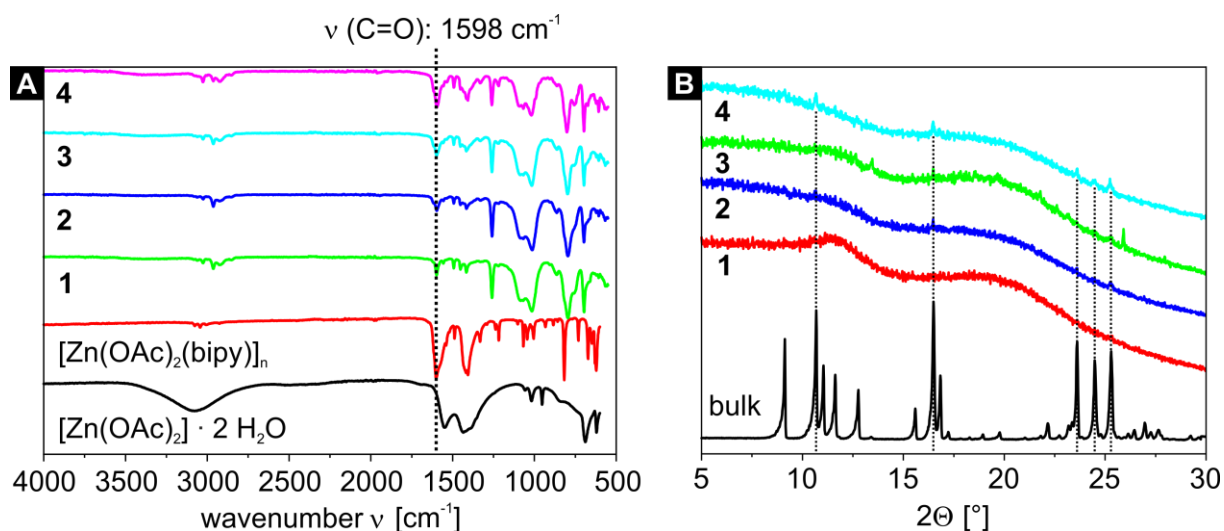
In chapter 8 the synthesis protocol is adapted to a 1D double-stranded CP  $[\text{Zn}(\text{OAc})_2(\text{bipy})]_n$  and a 2D layer-like CN  $[\text{Zn}(\text{TFA})_2(\text{bppa})_2]_n$  (bppa = 1,2-di(4-pyridyl)propane). The published crystals structures are given in Figure 6. This work aimed to prove the hypothesis that the templated synthesis inside a diblock copolymer micelle's core is neither limited to iron-based CPs nor to 1D CPs. Two different diblock copolymers were used for the formation of the nanocomposites.  $\text{S}_{85}\text{V}_{15}^{154}$  (SV-15) was already utilized in Chapter 7. Additionally,  $\text{S}_{58}\text{V}_{42}^{157}$  (SV-42) having a total molecular weight of  $157\,000\ \text{g mol}^{-1}$ , a composition of PS:P4VP of 58:42 (w/w), and a polydispersity  $\mathcal{D} = 1.09$  was used. The latter neat polymer also forms spherical nanoparticles like SV-15, but the particle core size  $D_{\text{core}}$  and the hydrodynamic diameter  $D_{\text{h}}$  increased to  $45 \pm 5\ \text{nm}$  and  $125 \pm 34\ \text{nm}$ , respectively.



**Figure 6:** Excerpts of the crystal structures of the double-stranded 1D CP  $[\text{Zn}(\text{OAc})_2(\text{bipy})]_n$  (left, CCDC 290063) and the layer-like 2D CN  $[\text{Zn}(\text{TFA})_2(\text{bppa})_2]_n$  (right, CCDC 947704).

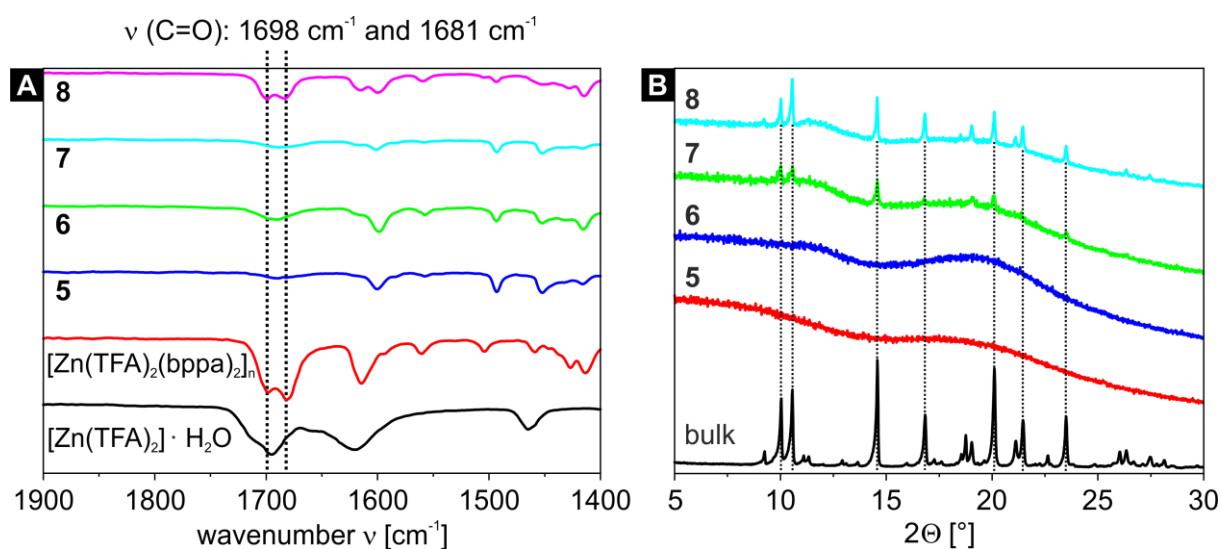
The synthetic protocol for the formation of NPs of the 1D CP  $[\text{Zn}(\text{OAc})_2(\text{bipy})]_n$  and the 2D CN  $[\text{Zn}(\text{TFA})_2(\text{bppa})_2]_n$  had to be adapted to the limited solubility of the starting materials and the products. Both zinc complexes  $[\text{Zn}(\text{OAc})_2] \cdot 2 \text{H}_2\text{O}$  and  $[\text{Zn}(\text{TFA})_2] \cdot \text{H}_2\text{O}$  are far less soluble in THF than the iron complex  $[\text{FeL}(\text{MeOH})_2]$ . Moreover, the CPs or CNs are less soluble, which may lead to a faster precipitation of microcrystals. Therefore, the amounts of the starting materials were decreased drastically to slow down the formation of the CP or CN. Additionally, the bridging ligand bppa was added dropwise during the reaction with  $[\text{Zn}(\text{TFA})_2] \cdot \text{H}_2\text{O}$  to further decelerate the reaction speed.

Only the BCP SV-42 was used for the synthesis of the 1D CP  $[\text{Zn}(\text{OAc})_2(\text{bipy})]_n$  nanocomposites and both BCPs SV-15 and SV-42 were used for the synthesis of the 2D CN  $[\text{Zn}(\text{TFA})_2(\text{bppa})_2]_n$  nanocomposites. The successful synthesis of both types of nanocomposites was proven by IR and PXRD measurements. For the  $[\text{Zn}(\text{OAc})_2(\text{bipy})]_n$  nanocomposites, IR measurements revealed an increase of the characteristic C=O stretching mode at  $1598 \text{ cm}^{-1}$  in the nanocomposites. This is in good agreement with the C=O stretching mode of the bulk CP at  $1600 \text{ cm}^{-1}$  (Figure 7A) and differs distinctively from the precursor complex with its C=O stretching mode at  $1549 \text{ cm}^{-1}$ . Although, the powder pattern of the nanocomposites showed that the samples are quite amorphous, PXRD pattern of the sample obtained after five reaction cycles contained five characteristic reflexes that correspond to the bulk material (Figure 7B).



**Figure 7:** IR spectra of the  $[\text{Zn}(\text{OAc})_2(\text{bipy})]_n$  nanocomposites (1–4) and the comparison of the bulk CP  $[\text{Zn}(\text{OAc})_2(\text{bipy})]_n$  and the precursor complex  $[\text{Zn}(\text{OAc})_2] \cdot 2 \text{H}_2\text{O}$  (A). The C=O stretching modes of the nanocomposites are marked with a dashed line. Comparison of the PXRD measurements of the nanocomposite samples (1–4) and the bulk material (B). The sample with five reaction cycles (sample 4 in image B) shows several characteristic reflexes that also exist in the bulk material.

Samples 5 to 7 of the  $[\text{Zn}(\text{TFA})_2(\text{bppa})_2]_n$  nanocomposites showed a single band for the C=O stretching mode at  $1690 \text{ cm}^{-1}$  in IR measurements. Only the sample 8 obtained after two reaction cycles in SV-42 showed two resolved bands for the C=O stretching mode identical to the bulk material. The two bands were detected at  $1699 \text{ cm}^{-1}$  and  $1684 \text{ cm}^{-1}$  which is in excellent agreement with the bulk material and different from the starting material  $[\text{Zn}(\text{TFA})_2] \cdot \text{H}_2\text{O}$  (Figure 8A). PXRD measurements proved the formation of the desired CN inside the BCP by the detection of several characteristic reflexes for the samples 7 and 8 (Figure 8B).



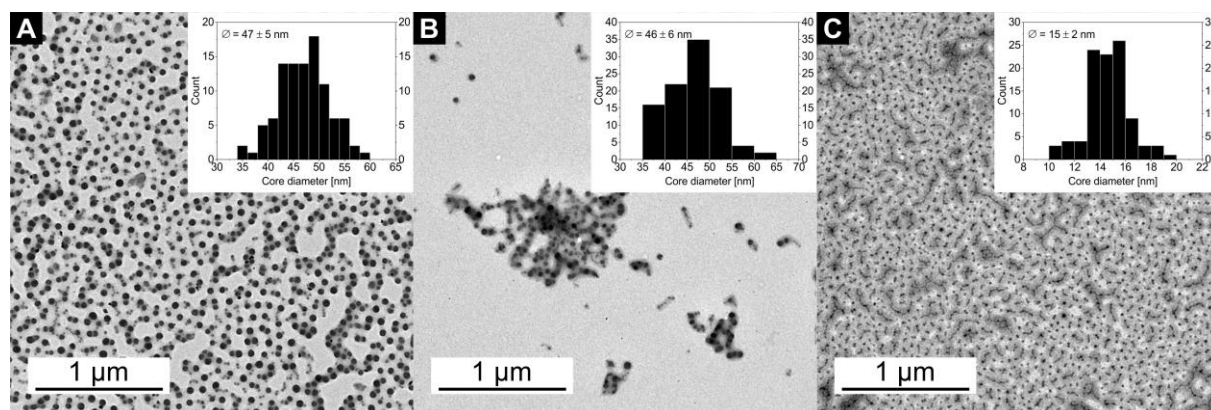


## 4. Synopsis

**Figure 8:** IR spectra of the  $[\text{Zn}(\text{TFA})_2(\text{bppa})_2]_n$  nanocomposites (5–8) and the comparison of the bulk CP  $[\text{Zn}(\text{TFA})_2(\text{bppa})_2]_n$  and the precursor complex  $[\text{Zn}(\text{TFA})_2] \cdot \text{H}_2\text{O}$  (A). The C=O stretching modes of the nanocomposites are marked with a dashed line. Comparison of the PXRD measurements of the nanocomposite samples (5–8) and the bulk material (B). The samples with two reaction cycles (samples 7 and 8 in image B) show several characteristic reflexes that also exist in the bulk material.

The experimental IR spectra were supported by DFT for both the CP and CN samples. Mono- or oligonuclear models of the CP and CN yielded theoretical IR spectra that matched the ones experimentally observed.

The size distribution of the nanocomposites was analysed by TEM and DLS. Spherical NPs of the CP  $[\text{Zn}(\text{OAc})_2(\text{bipy})]_n$  were achieved with a core size  $D_{\text{core}} = 47 \pm 5$  nm (Figure 9A) and a hydrodynamic diameter  $D_{\text{h}} = 157 \pm 46$  nm. NPs of the CN  $[\text{Zn}(\text{TFA})_2(\text{bppa})_2]_n$  in SV-42 also showed mostly spherical particles with a core size  $D_{\text{core}} = 46 \pm 6$  nm but it seemed that morphological changes started to form worm-like structures (Figure 9B). The same behaviour is observed for the NPs in SV-15, where mostly spherical particles were imaged but also worm-like structures existed. The particle core size  $D_{\text{core}}$  was determined to  $15 \pm 2$  nm (Figure 9C). The observation of worm-like structures is also underlined by DLS measurements which resulted in considerably broader size distributions of the measured hydrodynamic diameters ( $D_{\text{h}} = 340 \pm 153$  nm and  $177 \pm 57$  nm for the BCPs SV-42 and SV-15, respectively).



**Figure 9:** TEM images of NPs of the CP  $[\text{Zn}(\text{OAc})_2(\text{bipy})]_n$  in SV-42 showing separated spherical particles (A), and NPs of the CN  $[\text{Zn}(\text{TFA})_2(\text{bppa})_2]_n$  in SV-42 (B) and SV-15 (C) showing both spherical particles and worm-like structures. The particle core sizes are given in the insets.

## 4. Synopsis

The incorporation of the CPs into the BCP micelle cores was proven by scanning electron microscopy (SEM) imaging the surface of the nanocomposites. Microcrystals are absent on the polymers surface, indicating that the CP is build up inside the micelle core.

Chapter 9 concentrates on the control of the particle size and the particle shape by the variation of the composition of the BCP. Five different PS-*b*-P4VP BCPs were used for this purpose (Table 2). SV-15 and SV-42 were used in prior work. Additionally, SV-21, SV-35 and SV-61 were synthesised and the BCPs were fully characterised in terms of composition, molecular weight  $M_n$ , and polydispersity  $D$ . The formed micelles were characterised by TEM, cryo-TEM, and DLS.

**Table 2:** Overview over the used block copolymers in chapter 9.

BCP <sup>a)</sup>	Abbreviation	$M_n$ [g mol <sup>-1</sup> ]	Ratio PS [wt%]	Ratio P4VP [wt%]
S <sub>85</sub> V <sub>15</sub> <sup>154</sup>	SV-15	154 000	85	15
S <sub>79</sub> V <sub>21</sub> <sup>119</sup>	SV-21	119 000	79	21
S <sub>65</sub> V <sub>35</sub> <sup>131</sup>	SV-35	131 000	65	35
S <sub>58</sub> V <sub>42</sub> <sup>157</sup>	SV-42	157 000	58	42
S <sub>39</sub> V <sub>61</sub> <sup>162</sup>	SV-61	162 000	39	61

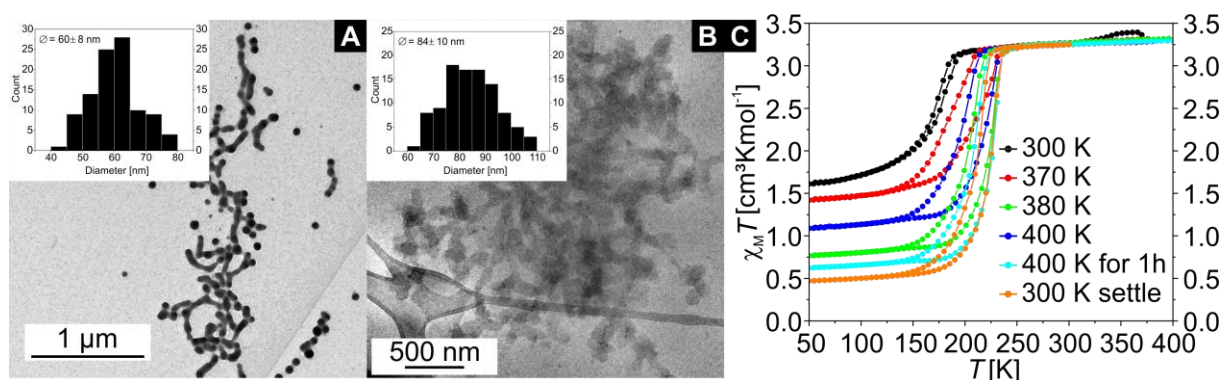
<sup>a)</sup> subscripts denote the content of the respective block in wt%, superscript gives the number average molecular weight in kg mol<sup>-1</sup>.

Only spherical particles were detected for all five BCPs by TEM and cryo-TEM. The core sizes of the neat BCPs correlate with the P4VP ratio and range from  $15 \pm 2$  nm (SV-15) to  $73 \pm 9$  nm (SV-61). The particle core diameters for the cryo-TEM samples are almost identical or slightly larger than the ones analysed by TEM, because the P4VP core is swollen in solution. Core diameters are  $26 \pm 2$  nm for SV-15 to  $71 \pm 4$  nm for SV-61.

The synthesis of NPs inside these five BCPs was tested with [FeL(bipy)]<sub>n</sub> and five different nanocomposites were prepared with increasing cycle count with each BCP. Spherical particles are observed for the nanocomposites in SV-15 to SV-42 with sizes between  $12 \pm 2$  nm and  $58 \pm 4$  nm and the core sizes derived from TEM measurements also correlate with the P4VP ratio of the BCP but are independent from the number of reaction cycles. Morphological changes began to appear in nanocomposites with SV-61 and worm-like structures were imaged after 3 reaction cycles and became dominant with 5 reaction cycles (Figure 10A). The core width was analysed to  $60 \pm 8$  nm. These worm-like structures were also detected in the cryo-TEM of the nanocomposite sample with five reaction cycles with SV-61 ( $D_{\text{cryo}} = 84 \pm 10$  nm, Figure 10B), whereas the cryo-TEM images of the nanocomposites with the other BCPs only revealed spherical particles ( $30 \pm 3$  nm to

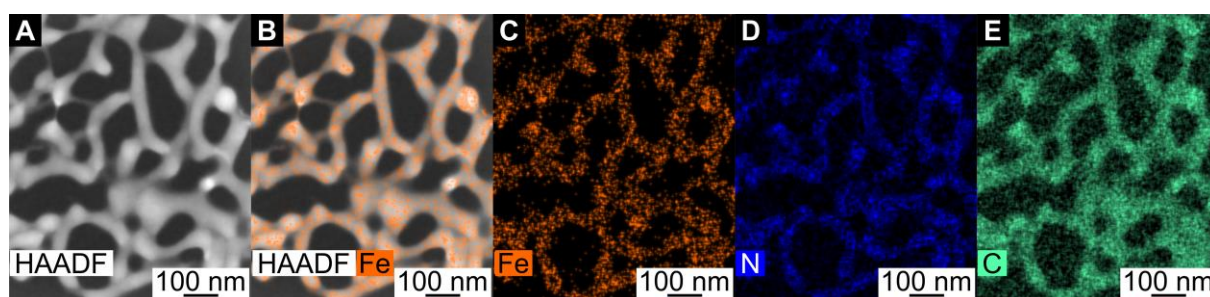


$65 \pm 5$  nm). The magnetic properties of the nanocomposites were analysed, showing the trend that the ST became more complete in the larger NPs ( $\gamma_{HS} = 14\%$  in SV-61 vs. 30% in SV-15) and that the ST became more abrupt (cf. Figure 4A and Figure 10C).



**Figure 10:** TEM (A) and cryo-TEM image (B) of the nanocomposite in SV-61 showing the worm-like structures and the magnetic properties of the nanocomposite (C).

The distribution of the iron inside the nanocomposite with SV-61 was analysed by transmission electron microscopy – energy dispersive X-ray (TEM-EDX) measurements (Figure 11). The high-angle annular dark field (HAADF) image (A) displayed the worm-like structure and the further images show the HAADF overlaid with the distribution of iron (B), and the solitary distributions of iron (C), nitrogen (D), and carbon (E). Figures 11B and 11C show that the detection of iron copied the structure of the worm-like micelles and the signal of iron is absent in the interspaces. This proves the incorporation of the CP into the worm-like polymeric micelles.



**Figure 11:** HAADF image the nanocomposite with SV-61 showing the worm-like structures (A). The HAADF image overlaid with the iron signal (B), and the individual images of the iron (C), nitrogen (D) and carbon (E) signals from TEM-EDX.

The preceding paragraphs impressively show that block copolymers are excellent for the control of the size and shape of coordination polymers nanoparticles. Several different spin crossover coordination polymer nanoparticles are accessible by the templating effect of the block copolymers. Nanocomposites of  $[\text{FeL}(\text{bipy})]_n$ ,  $[\text{FeL}(\text{bppa})]_n$ ,  $[\text{FeL}(\text{bpee})]_n$  and  $[\text{FeL}(\text{bpey})]_n$  have been synthesised in the BCPs SV-15 to SV-42 in spherical polymeric micelle cores with sizes between  $15 \pm 2$  nm and  $58 \pm 4$  nm. A morphological change of the polymeric structure from spherical to worm-like was observed in the polymer SV-61 and the incorporation of the CP was proven by TEM-EDX. The spin crossover properties were altered by a thermal annealing of the nanocomposites leading to spin transitions close to the bulk material. Moreover, the synthesis procedure was adapted to the coordination polymer  $[\text{Zn}(\text{OAc})_2(\text{bipy})]_n$  and the coordination network  $[\text{Zn}(\text{TFA})_2(\text{bppa})_2]_n$ . The latter one was incorporated in particles as small as  $15 \pm 2$  nm.

## 5. Contributions to joint publications

This thesis and the presented results were obtained in collaboration with others. The respective contributions of each co-author and the publication state (published, in revision, to be submitted) is listed in this chapter. Author(s) marked with an asterisk are the corresponding authors.

### Chapter 6

The work was published in the journal Beilstein Journal of Nanotechnology (*Beilstein J. Nanotechnol.* **2017**, *8*, 1318–1327) entitled:

*Synthesis of  $[Fe(L_{eq})(L_{ax})]_n$  coordination polymer nanoparticles using blockcopolymer micelles*

Christoph Göbel, Ottokar Klimm, Florian Puchtler, Sabine Rosenfeldt, Stephan Förster, Birgit Weber\*

I reproduced the synthesis of the nanoparticle samples and synthesised the bulk materials presented in this work, characterised my samples by TEM, DLS, magnetic susceptibility measurements, Mössbauer spectroscopy, elemental analysis, and IR spectroscopy and wrote the manuscript. Ottokar Klimm did the initial synthesis of the nanoparticle samples and its characterisation. Florian Puchtler measured the PXRDs of the samples and I and Ottokar Klimm treated and interpreted the data. Sabine Rosenfeldt was involved in scientific discussions and the correction of the manuscript. Stephan Förster and Birgit Weber supervised this work and were involved in scientific discussions and the correction of the manuscript.

## Chapter 7

This work was published in the journal *Angewandte Chemie International Edition* (*Angew. Chem. Int. Ed.* **2020**, *59*, 5765–5770; doi: 10.1002/anie.201914343) entitled:

### *Confined Crystallization of Spin-Crossover Nanoparticles in Block-Copolymer Micelles*

Christoph Göbel, Christian Hils, Markus Drechsler, Dirk Baabe, Andreas Greiner, Holger Schmalz,\*  
Birgit Weber\*

I synthesised the nanocomposite samples, characterised them by TEM, DLS, temperature-dependent PXRD, magnetic susceptibility measurements, room temperature Mössbauer spectroscopy, elemental analysis, IR spectroscopy, and paramagnetic NMR, and wrote the manuscript. Christian Hils performed the electrospinning and the characterisation of the fibres by optical microscopy. Markus Drechsler performed the cryo-TEM measurements and helped with the TEM measurements in general and the interpretation of the images. Dirk Baabe measured and interpreted the temperature-dependent Mössbauer spectroscopy. Andreas Greiner supervised the work. Holger Schmalz synthesised the block copolymer, characterised the block copolymer by GPC, DSC, NMR, and MALDI-ToF, characterised the nanocomposite and bulk samples by Raman spectroscopy, was involved in scientific discussions, helped with the correction of the manuscript and supervised the work. Birgit Weber supervised this work, was involved in scientific discussions and the correction of the manuscript.

## Chapter 8

This work was published in the journal *Nanoscale Advances* (*Nanoscale Adv.*, **2020**, *2*, 4557–4565; doi: 10.1039/D0NA00334D) entitled:

*Synthesis of Zn-based 1D and 2D coordination polymer nanoparticles in block copolymer micelles*

Christoph Göbel, Gerald Hörner, Andreas Greiner, Holger Schmalz\* and Birgit Weber\*

The samples were synthesised by me or under supervision by Samanta Jänsch, Thomas Bindig, and Magdalena Weber. I characterised them by TEM, DLS, PXRD, elemental analysis, and IR spectroscopy and wrote the manuscript. Gerald Hörner executed the computational calculations on the spectroscopic data. Andreas Greiner supervised the work. Holger Schmalz synthesised the block copolymers and characterised them by DSC, GPC, NMR, and MALDI-ToF and was involved in scientific discussions, the correction of the manuscript and the supervision of the work. Birgit Weber supervised the work, was involved in scientific discussions and the correction of the manuscript.

## Chapter 9

This work is to be submitted and is entitled:

*Size and Shape Control of Spin-Crossover Nanoparticles via Confined Crystallization in Block Copolymer Micelles*

Christoph Göbel, Katharina Marquardt, Markus Drechsler, Patrick Loch, Josef Breu, Holger Schmalz, Andreas Greiner,\* Birgit Weber\*

I synthesised the samples, characterised them by TEM, DLS, PXRD, magnetic susceptibility measurements, room temperature Mössbauer spectroscopy, elemental analysis, and IR spectroscopy. Katharina Marquardt performed the TEM-EDX measurements and helped with the interpretation of the data and images. Markus Drechsler performed the cryo-TEM measurements and helped with the interpretation of the images. Patrick Loch performed the temperature-dependent PXRD measurements and helped with the interpretation of the data. Josef Breu and Andreas Greiner supervised the work. Holger Schmalz synthesised the block copolymers and characterised them by DSC, GPC, NMR, and MALDI-ToF, was involved in scientific discussions, the correction of the manuscript and the supervision of the work. Birgit Weber supervised the work, was involved in scientific discussions and the correction of the manuscript.

## 6. Synthesis of $[\text{Fe}(\text{L}_{\text{eq}})(\text{L}_{\text{ax}})]_n$ coordination polymer nanoparticles using blockcopolymer micelles

Christoph Göbel<sup>1</sup>, Ottokar Klimm<sup>1</sup>, Florian Puchtler<sup>2</sup>, Sabine Rosenfeldt<sup>3</sup>, Stephan Förster<sup>3</sup> and Birgit Weber<sup>1</sup>

<sup>1</sup> Inorganic Chemistry II, University of Bayreuth, Universitätsstr. 30, 95440 Bayreuth, Germany

<sup>2</sup> Inorganic Chemistry I, University of Bayreuth, Universitätsstr. 30, 95440 Bayreuth, Germany

<sup>3</sup> Physical Chemistry I and Bavarian Polymer Institute, University of Bayreuth, Universitätsstr. 30, 95440 Bayreuth, Germany

Published in *Beilstein J. Nanotechnol.* **2017**, *8*, 1318–1327 (doi: 10.3762/bjnano.8.133) and reproduced under the terms of the CC-BY 4.0 licence.

**Abstract:** Spin-crossover compounds are a class of materials that can change their spin state from high spin (HS) to low spin (LS) by external stimuli such as light, pressure or temperature. Applications demand compounds with defined properties concerning the size and switchability that are maintained when the compound is integrated into composite materials. Here, we report the synthesis of  $[\text{Fe}(\text{L}_{\text{eq}})(\text{L}_{\text{ax}})]_n$  coordination polymer (CP) nanoparticles using self-assembled polystyrene-*block*-poly(4-vinylpyridine) (PS-*b*-P4VP) block copolymer (BCP) micelles as template. Variation of the solvent (THF and toluene) and the rigidity of the axial ligand  $\text{L}_{\text{ax}}$  ( $\text{L}_{\text{ax}}$  = 1,2-di(pyridin-4-yl)ethane (bpea), trans-1,2-di(pyridin-4-yl)ethene (bpee), and 1,2-di(pyridin-4-yl)ethyne (bpey);  $\text{L}_{\text{eq}}$  = 1,2-phenylenebis(iminomethylidyne)-bis(2,4-pentanedionato)(2-)) allowed the determination of the preconditions for the selective formation of nanoparticles. A low solubility of the CP in the used solvent and a high stability of the Fe–L bond with regard to ligand exchange are necessary for the formation of composite nanoparticles where the BCP micelle is filled with the CP, as in the case of the  $[\text{FeL}_{\text{eq}}(\text{bpey})]_n@BCP$ . Otherwise, in the case of more flexible ligands or ligands that lead to high spin complexes, the formation of microcrystals next to the CP–BCP nanoparticles is observed above a certain concentration of  $[\text{Fe}(\text{L}_{\text{eq}})(\text{L}_{\text{ax}})]_n$ . The core of the nanoparticles is about 45 nm in diameter due to the templating effect of the BCP micelle, independent of the used iron complex and  $[\text{Fe}(\text{L}_{\text{eq}})(\text{L}_{\text{ax}})]_n$  concentration. The spin-crossover properties of the composite material are similar to those of the bulk for  $[\text{FeL}_{\text{eq}}(\text{bpea})]_n@BCP$  while pronounced differences are observed in the case of  $[\text{FeL}_{\text{eq}}(\text{bpey})]_n@BCP$  nanoparticles.

### 6.1. Introduction

Nanomaterials and especially nanocomposites of coordination polymers (CPs) and (porous) coordination networks are of great interest in current research because of their various applications as sensors, data-storage devices, catalysts or contrast agents.<sup>[1-5]</sup> For these applications the formation of stable, uniform and monodisperse particles with defined properties is necessary. Synthetic procedures for nanoparticles with size control (gold<sup>[6,7]</sup>, metal oxides<sup>[8,9]</sup>) and/or shape control (gold and silver<sup>[10]</sup>) are already well known. The reduction of metal salts is very common for noble metals<sup>[11]</sup>, while (fast) precipitation or inverse-micelle technique are often used for metal oxides (mostly magnetite)<sup>[12]</sup>. For coordination polymers (CP) or networks a limited amount of methods are applicable because of the very demanding reaction conditions and/or incompatible reactants. Recently we demonstrated that the use of block copolymers (BCPs) is a highly promising and easy approach for the size control of CPs.<sup>[13]</sup> BCPs form micellar structures through self-assembly in specific solvents and can therefore be used as nanoreactors.<sup>[14-16]</sup> Using this approach, a very controlled miniaturisation of coordination polymers or networks can be envisioned, provided it is easily transferable to other systems. In this work we will analyse which preconditions need to be fulfilled for a successful synthesis of uniform CP-BCP nanoparticles.

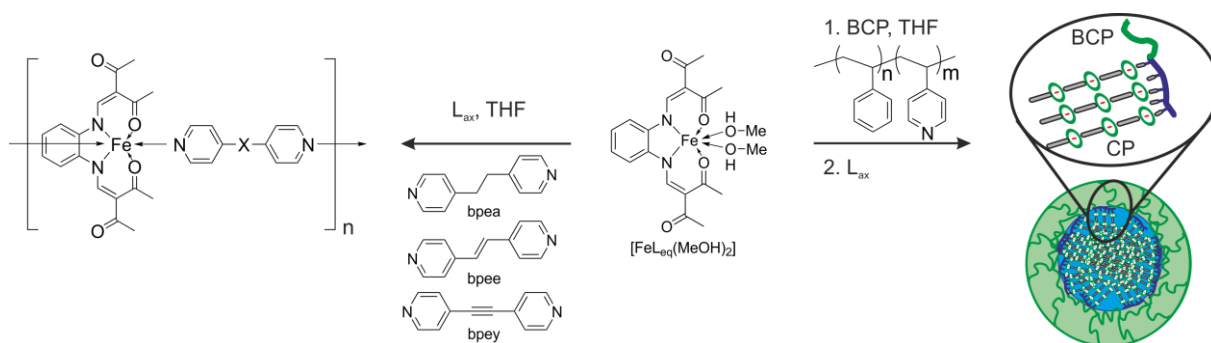
Coordination polymers with spin crossover (SCO) properties are well known in the literature<sup>[4,5,17,18]</sup>, but their miniaturisation into precisely defined nanomaterials with SCO properties comparable to those of the bulk material is still in its infancy.<sup>[19-23]</sup> SCO materials can be switched by external stimuli such as temperature, pressure or light between a high spin (HS) and a low spin (LS) state.<sup>[5,18]</sup> Switching between these two states alters physical properties such as magnetism, structure or colour, which make these materials interesting for sensors<sup>[2,24-26]</sup>, display devices<sup>[27-29]</sup> or as functional contrast agents<sup>[30-34]</sup>. The SCO properties deeply depend on the precise control of size and crystallinity of the nanocomposite. Most commonly the inverse-micelle technique is used for the preparation of nanoparticles.<sup>[35-39]</sup> However, the spin crossover properties of the bulk are often lost upon miniaturisation and only few examples preserving the hysteresis (bistability) in a nanostructured system are known.<sup>[21,40-43]</sup> This is most likely due to a loss of the crystallinity of the particles. Especially SCO complexes are highly sensitive to small changes in the crystal packing and thus excellently suited to investigate the impact of nanostructuration of the material. In our recent work<sup>[13]</sup> we used the block copolymer polystyrene-*b*-poly(4-vinylpyridine) (PS-*b*-P4VP) to prepare spherical nanoparticles of the 1D spin-crossover coordination polymer  $[\text{FeL}_{\text{eq}}(\text{bipy})]_n$ . We were able control the crystallinity of the  $[\text{FeL}_{\text{eq}}(\text{bipy})]_n$  core through successive addition of starting material and by variation of the



## 6. Synthesis of $[\text{Fe}(\text{L}_{\text{eq}})(\text{L}_{\text{ax}})]_n$ coordination polymer nanoparticles using blockcopolymer micelles

reaction time and temperature. Having a high crystallinity of the core, the SCO properties were closer to those of the bulk material (thermal hysteresis loop).

We herein report the synthesis of three further coordination polymer block copolymer nanocomposites (CP-BCP) using the same synthesis strategy. This allows us to investigate the influence of the coordination polymer on the formation and the SCO activity of the final nanocompound. The CPs differ in the axial ligands ( $\text{L}_{\text{ax}}$ ), namely 1,2-di(pyridin-4-yl)ethane (bpea), trans-1,2-di(pyridin-4-yl)ethene (bpee) and 1,2-di(pyridin-4-yl)ethyne (bpey) (Scheme 1). The ligands were chosen because of their different flexibility. From the synthesis of the bulk complexes it is known, that an increasing flexibility of the ligand leads to an increase in solubility of the obtained CP.<sup>[44,45]</sup> This way we can investigate the impact of the solubility of the CP on the selective formation of nanoparticles in the BCP micelle cores. In Scheme 1, the general approach and the abbreviations used for the different samples are given.

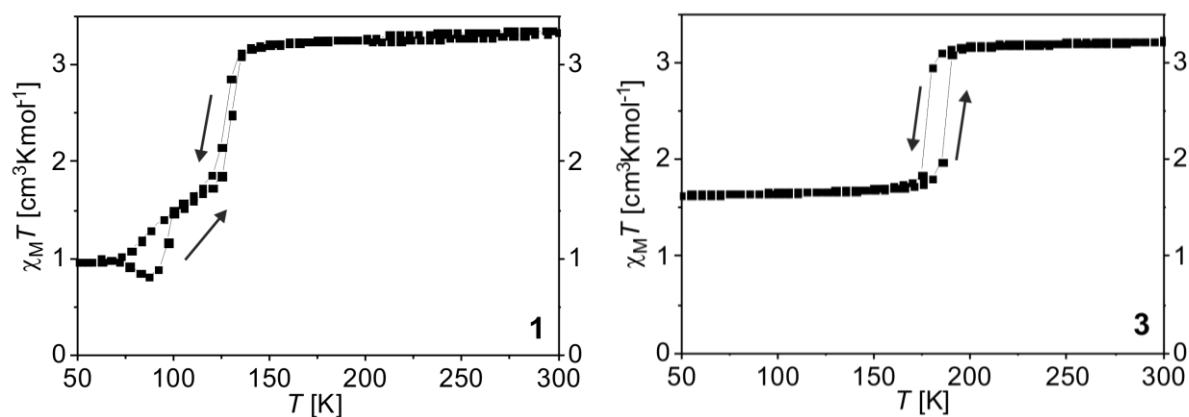


**Scheme 1:** Synthesis of the three different coordination polymers  $[\text{FeL}_{\text{eq}}(\text{bpea})]_n$  (**1**),  $[\text{FeL}_{\text{eq}}(\text{bpee})]_n$  (**2**) and  $[\text{FeL}_{\text{eq}}(\text{bpey})]_n$  (**3**) and the respective coordination polymer-block copolymer composites (CP-BCP)  $[\text{FeL}_{\text{eq}}(\text{bpea})]_n\text{@BCP}$  (**1a-e**),  $[\text{FeL}_{\text{eq}}(\text{bpee})]_n\text{@BCP}$  (**2a-e**) and  $[\text{FeL}_{\text{eq}}(\text{bpey})]_n\text{@BCP}$  (**3a-e**).

## 6.2. Results and Discussion

### 6.2.1. Bulk complexes

The magnetic properties of SCO coordination polymers often depend on solvent molecules included in the crystal packing.<sup>[46-49]</sup> To allow a comparison between bulk material and nanoparticles and to study the influence of nanostructuring on magnetism, the bulk complexes were synthesised in THF and their magnetic properties were investigated.  $[\text{FeL}_{\text{eq}}(\text{bpea})]_n$  and  $[\text{FeL}_{\text{eq}}(\text{bpee})]_n$  were already synthesised in methanol<sup>[44,50]</sup>, the coordination polymer  $[\text{FeL}_{\text{eq}}(\text{bpey})]_n$  is described here for the first time. The coordination polymers **1**, **2** and **3** were synthesised by dissolving the iron(II) complex  $[\text{FeL}_{\text{eq}}(\text{MeOH})_2]$  and the respective axial ligand in THF. The solution was refluxed for 1 h. After cooling down overnight, the fine crystalline precipitate was filtered off and dried in vacuo to yield brown or dark violet powders. The crystals were too small for single-crystal X-ray structure analysis. In Figure 1, the magnetic properties of  $[\text{FeL}_{\text{eq}}(\text{bpea})]_n$  (**1**) and  $[\text{FeL}_{\text{eq}}(\text{bpey})]_n$  (**3**) as plot of the  $\chi_M T$  product ( $\chi_M$  = magnetic susceptibility,  $T$  = temperature) as a function of the temperature is given. Sample **1** is paramagnetic at RT with a  $\chi_M T$  value of  $3.25 \text{ cm}^3 \cdot \text{K} \cdot \text{mol}^{-1}$ , typical for iron(II) in the HS state.<sup>[51]</sup>



**Figure 1:** Magnetic susceptibility data for the coordination polymers  $[\text{FeL}_{\text{eq}}(\text{bpea})]_n$  (**1**) and  $[\text{FeL}_{\text{eq}}(\text{bpey})]_n$  (**3**), which undergo spin crossover.

Upon cooling the  $\chi_M T$  value remains constant down to 140 K where an abrupt, incomplete spin crossover occurs. In the first step, the  $\chi_M T$  value descends to  $1.78 \text{ cm}^3 \cdot \text{K} \cdot \text{mol}^{-1}$  at 120 K corresponding to about 50% of the iron centres in the HS state. Further cooling reveals a second, gradual and incomplete step with a  $\chi_M T$  value of  $0.93 \text{ cm}^3 \cdot \text{K} \cdot \text{mol}^{-1}$  at 50 K; about one third of the iron centres remains in the HS state. Upon heating, a 3 K wide hysteresis is observed in the region

of the first step with  $T_{1/2}\uparrow = 127$  K and  $T_{1/2}\downarrow = 130$  K. In the temperature range between 75 and 100 K first a decrease and then an increase of the  $\chi_{\text{M}}T$  product upon heating is observed. This is due to a kinetic trapping effect, often observed in this temperature region when the thermal spin transition temperature ( $T_{1/2}$ ) and the transition temperature for the thermally trapped exited spin state ( $T_{\text{TIESST}}$ ) are in close proximity.<sup>[44,52-54]</sup> In such a case the completeness of the spin crossover, in this case the second step, strongly depends on the scan rate used for the magnetic measurements. For the measurements presented in Figure 1, the settle mode was used, which corresponds to an approximate scan rate of  $0.3 \text{ K}\cdot\text{min}^{-1}$ . This allows the system to equilibrate at each temperature step where a measurement point is taken and kinetic effects can be considered to be almost irrelevant. Despite the very slow measurements, upon cooling a part of the iron centres remain trapped in the HS state. Upon slow heating they equilibrate to the LS state as long as the temperature is below the thermal spin transition temperature, which leads to the observed decrease of the  $\chi_{\text{M}}T$  product upon heating. An even slower scan rate would lead to a more complete spin transition and the disappearance of the decrease of the  $\chi_{\text{M}}T$  product upon heating while a higher scan leads to the complete disappearance of the second step. The two-step behaviour is similar to the one observed for  $[\text{FeL}_{\text{eq}}\text{bpea}]\cdot 0.25\text{MeOH}]_n$ , where the temperatures differ slightly and the second step is complete.<sup>[44]</sup> The differences due to the impact of the different solvents are also reflected in the powder diffraction patterns (Supporting Information File 1, Figure S1) in which some of the reflexes are shifted compared to the sample prepared in methanol. Sample **2** ( $[\text{FeL}_{\text{eq}}(\text{bpee})]_n$ ) is paramagnetic at room temperature with a  $\chi_{\text{M}}T$  value of  $3.20 \text{ cm}^3\cdot\text{K}\cdot\text{mol}^{-1}$  (Supporting Information File 1, Figure S2). Upon cooling the sample remains in the HS state over the whole temperature range, as already reported for the complex synthesised from methanol.<sup>[50]</sup> Sample **3** ( $[\text{FeL}_{\text{eq}}(\text{bpey})]_n$ ) is paramagnetic at room temperature with a  $\chi_{\text{M}}T$  value of  $3.23 \text{ cm}^3\cdot\text{K}\cdot\text{mol}^{-1}$ , typical for iron(II) complexes in the HS state (bottom of Figure 1). Upon cooling the  $\chi_{\text{M}}T$  value remains almost constant down to 190 K ( $\chi_{\text{M}}T$  value:  $3.14 \text{ cm}^3\cdot\text{K}\cdot\text{mol}^{-1}$ ), where an abrupt and incomplete spin transition occurs with about 50% of the iron centres involved. The  $\chi_{\text{M}}T$  value drops to  $1.73 \text{ cm}^3\cdot\text{K}\cdot\text{mol}^{-1}$  at 165 K and no further changes are observed down to 50 K ( $\chi_{\text{M}}T$  value:  $1.63 \text{ cm}^3\cdot\text{K}\cdot\text{mol}^{-1}$ ). Upon heating up to 300 K an abrupt spin transition takes place revealing a hysteresis with a width of 10 K and  $T_{1/2}\downarrow = 177$  K and  $T_{1/2}\uparrow = 187$  K. For the sake of completeness, the complex was also synthesised from methanol yielding the same spin crossover properties, in good agreement with the absence of solvent molecules in the crystal packing. Mössbauer spectra were collected for all three samples to verify the HS state at room temperature. The spectra (Supporting Information File 1, Figure S3) reveal one quadrupole split doublet in each case with parameters for the quadrupole splitting  $\Delta E_{\text{Q}}$  and an isomer shift  $\delta$  (Supporting Information File 1, Table S1) in the range expected for iron(II) HS complexes of this ligand type.<sup>[55]</sup> The steps and the incomplete spin crossover observed in the magnetic measurements could be

due to inequivalent iron centres.<sup>[56,57]</sup> The Mössbauer spectra do not support this as no line broadening (FWHM  $\Gamma$  in Supporting Information File 1, Table S1) is observed and the doublet is very symmetric in each case. Thus, the steps observed in the transition curve are due to the packing of the CP in the crystal and will strongly depend on the crystallinity of the material.

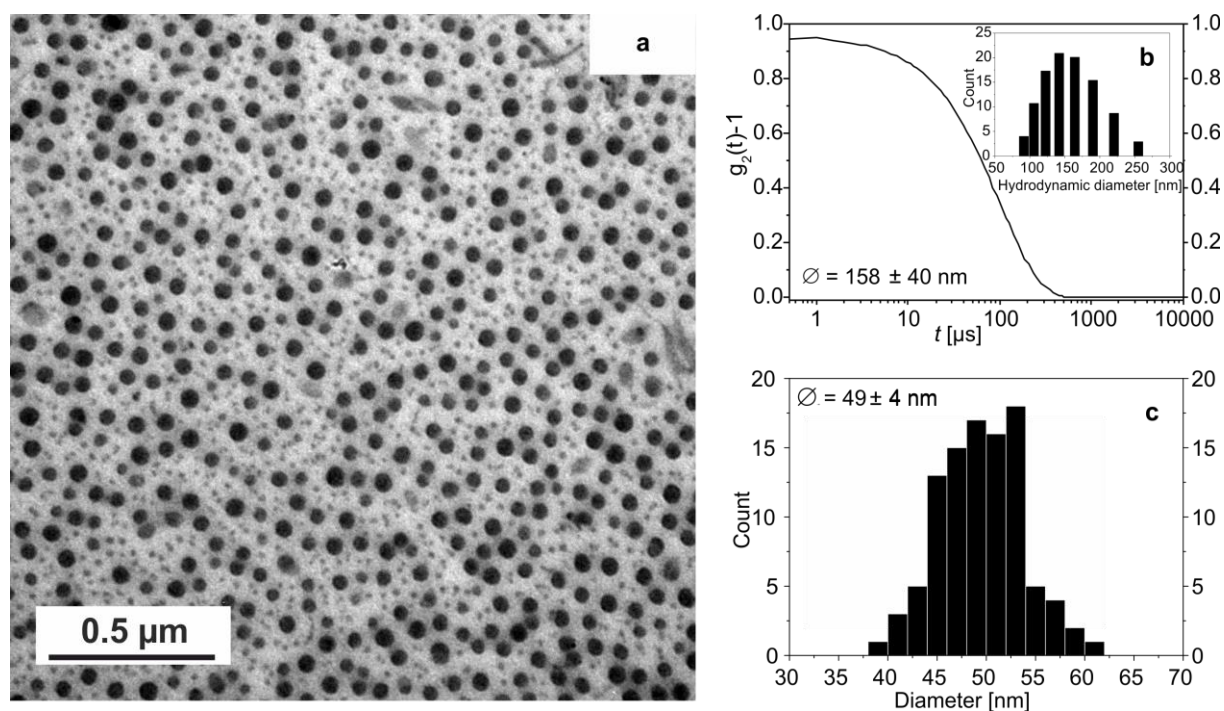
### 6.2.2. Synthesis of the nanocomposite

For the CP-BCP composites  $[\text{FeL}_{\text{eq}}(\text{bpea})]_n\text{@BCP}$  (**1a-e**),  $[\text{FeL}_{\text{eq}}(\text{bpee})]_n\text{@BCP}$  (**2a-e**) and  $[\text{FeL}_{\text{eq}}(\text{bpey})]_n\text{@BCP}$  (**3a-e**), the starting iron(II) complex  $[\text{FeL}_{\text{eq}}(\text{MeOH})_2]$  and the block copolymer were dissolved in THF and refluxed for 2 h. After cooling down to room temperature, the respective bridging ligand was added and the mixture was refluxed again for 1 h. Depending on the number of additions of starting material, either the solvent is removed by cold distillation (1 cycle, samples **1a**, **2a**, **3a**) or a further cycle of addition of  $[\text{FeL}_{\text{eq}}(\text{MeOH})_2]$  and axial ligand (simultaneously for all further cycles) followed by reflux for 1 h was performed prior to solvent removal (samples **1b-e**, **2b-e**, **3b-e** for 2 to 5 cycles). The resulting solids were dried in vacuo. IR spectroscopy was used to follow the formation of the coordination polymer in the BCP matrix. The corresponding spectra are given in Supporting Information File 1, Figure S4. The increasing relative intensity of the C=O stretching vibration of  $[\text{FeL}_{\text{eq}}]$  clearly indicates the formation of the coordination polymer in the matrix. Elemental analysis also confirms the increasing concentration of the coordination polymer in the BCP micelle with an increasing nitrogen content. Room temperature Mössbauer spectra were collected of  $[\text{FeL}_{\text{eq}}(\text{bpea})]_n\text{@BCP}$  after four and after five cycles (**1d** and **1e**) and of  $[\text{FeL}_{\text{eq}}(\text{bpey})]_n\text{@BCP}$  after four and five cycles (**3d** and **3e**) to get a deeper insight into the sample composition. Due to the long measurement time of the very diluted (low iron content) and soft (low Lamb-Mössbauer factor) composite materials, only the more crystalline samples with a high CP amount (**d** and **e**) showing spin crossover were characterised. The corresponding spectra are given in Figure 3 (**1d** and **3e**) and in Supporting Information File 1, Figure S5. The Mössbauer parameters are summarised in Supporting Information File 1, Table S2. For the composite materials, different iron species are possible due to the coordination of the starting complex  $[\text{Fe}(\text{L}_{\text{eq}})]$  to the vinylpyridine parts of the equatorial ligand, which can be distinguished using Mössbauer spectroscopy. Sample **1d** shows two different doublets which correspond to an iron(II) HS and iron(II) LS species (75% and 25%). The LS species derives from two P4VP units coordinated to the iron centre as already shown<sup>[13,58]</sup>, with the formula  $[\text{Fe}(\text{L}_{\text{eq}})(\text{VP})_2]$  (VP = vinyl pyridine) The HS species corresponds to the desired  $[\text{Fe}(\text{L}_{\text{eq}})(\text{bpea})]_n$  unit. For sample **1e** again two doublets are observed with a similar HS/LS ratio (Supporting Information File 1, Table S2). The sample **3d** also shows two different iron species of which one corresponds to an iron(II) in the HS state and the other one to an iron(II) in the LS state. However, the HS/LS ratio changes to 83%:17%. For sample **3e** only one doublet is observed that can be

assigned to an iron(II) HS species. It concludes that in the case of  $[\text{FeL}_{\text{eq}}(\text{bpey})]_n@BCP$  the HS fraction increases with higher cycles since more or longer coordination polymer is formed in the BCP micelle, in agreement with previous observations for  $[\text{FeL}_{\text{eq}}(\text{bipy})]_n@BCP$ .<sup>[13,58]</sup> In the case of  $[\text{FeL}_{\text{eq}}(\text{bpea})]_n@BCP$  a different behaviour is observed that is indicative for differences in the sample composition.

### 6.2.3. Characterisation of the nanocomposite

Particle sizes of the nanocomposites were determined by dynamic light scattering (DLS) in solution, transmission electron microscopy (TEM) and powder X-ray diffraction (PXRD) in the solid. The hydrodynamic diameter of the polymeric micelles loaded with the CP measured by DLS is constant within the error of the measurement throughout all measured samples with sizes around 150 nm (Supporting Information File 1, Figure S6). This is in agreement with the results reported previously for similar composite nanoparticles with 4,4'-bipyridine as bridging axial ligand.<sup>[13]</sup> In Figure 2, a TEM picture and the size distribution obtained from TEM and DLS of **3e** ( $[\text{FeL}_{\text{eq}}(\text{bpey})]_n@BCP$ , five cycles) is given as typical representative of all samples. A detailed characterisation of all samples with TEM is given in Supporting Information File 1, Table S3. The TEM picture of **3e** in Figure 2a clearly reveals the formation of spherical nanoparticles with a core-shell nature. The differences in contrast of the iron-containing CP and the BCP prove that the CP nanoparticles are solely formed in the core of the nanocomposite.



**Figure 2:** Characterisation of CP-BCP composite micelles. a) TEM picture of **3e** ( $[\text{FeL}_{\text{eq}}(\text{bpey})]_n@BCP$ , five cycles) illustrating the core-shell nature of the particles. b) Autocorrelation function from dynamic light scattering of **3e** in THF (43 wt%) with size histogram. c) Size histogram of the core from the TEM picture given in panel a).

The particle core diameter is significantly smaller than the hydrodynamic radius because of the polymeric nature of the BCP (solvent-swollen). Within the error of the measurement, the NP core size is in the same order of magnitude for all samples with an average size of 45 nm (Table 1), demonstrating the excellent size control by the micelles themselves. The NP core size is independent of the number of cycles and independent of the used coordination polymer clearly demonstrating the high potential of the templating effect of BCP micelles (cage effect). This is in very good agreement with our first observation on the similar system with 4,4'-biyridine as bridging ligand. It can be explained with the assumption, that the nanocomposite is very amorphous at the beginning with a low density in the core. With increasing coordination polymer concentration the crystallinity of the core and therefore its density increases, while the size does not change significantly.<sup>[13]</sup>

In order to investigate, whether the flexibility of the used bridging ligand has an impact on regioselectivity of the nanoparticle core formation, the samples were carefully analysed for the observation of microcrystals as function of the increasing CP concentration (number of cycles, e.g.,  $[\text{FeL}_{\text{eq}}(\text{bpea})]_n@BCP = \mathbf{1a-e}$  for one to five cycles of addition of starting material) in the composite material. The results are summarised in Table 1.

The first microcrystals (3–6  $\mu\text{m}$ ) were observed for bpee as bridging ligand after four cycles of addition of starting material (**2d**), while for the more flexible bpea the first microcrystals are observed only after five cycles (**1e**, 1.5–2.0  $\mu\text{m}$ ). In the case of the more rigid bpey, no microcrystals are observed. This cannot solely be explained with the rigid nature of the ligand, which increases in the order bpea < bpee < bpey. One possibility to explain the observed order is to consider the stability of the complexes with regard to M-L ligand exchange with excess axial ligands and/or solvent molecules. For octahedral complexes, a weak ligand field splitting leads to the occupation of antibonding orbitals (HS complexes) and by this supports ligand exchange. A fast ligand exchange will increase the probability of the formation of microcrystals outside the BCP micelle. In this case the templating effect of the BCP micelles does not work. In agreement with this consideration, the pure HS complex  $[\text{FeL}_{\text{eq}}(\text{bpee})]_n$  with the weakest ligand field splitting is the first one where microcrystals are observed, while for the spin crossover complexes  $[\text{FeL}_{\text{eq}}(\text{bpea})]_n$ ,  $[\text{FeL}_{\text{eq}}(\text{bpey})]_n$  and the previously investigated  $[\text{FeL}_{\text{eq}}(\text{bipy})]_n$  the expected order with regard to the rigid nature of the ligand is observed. With increasing solubility of the complex (increasing flexibility of the ligand) in the solvent used for the synthesis of the nanomaterial, the probability for the formation of microcrystals outside the BCP micelles increases. In agreement with this, it was not possible to synthesise nanoparticles of the coordination polymer  $[\text{FeL}_{\text{eq}}(\text{bppa})]_n$ <sup>[44]</sup>, when bppa = 1,3-di(pyridin-4-yl)propane, a very flexible ligand (high solubility), is used. Syntheses were also performed in toluene to investigate the influence of the solvent on the nanoparticle synthesis. It should be pointed out that previous investigations showed that the complexes have a higher solubility in toluene compared to tetrahydrofuran. In agreement with this, first microcrystals were observed already after two cycles for all ligands. In Supporting Information File 1, Figure S7, a TEM picture of  $[\text{FeL}_{\text{eq}}(\text{bpea})]_n\text{@BCP}$  after two cycles synthesised in toluene is given as typical representative. Thus, the higher solubility of the coordination polymers in toluene favours the formation of microcrystals outside of the block copolymer micelle and reduces the regioselectivity. The influence of the CP concentration on the crystallinity of the CP-BCP nanocomposite core was investigated using PXRD. In Supporting Information File 1, Figure S8, the PXRD patterns of the composite materials are compared with those of the bulk materials **1-3**. In all cases, the crystallinity of the particles increases with higher CP concentration, which is indicated by sharper reflexes. It should be pointed out, that in the case of the samples **3a-e** even after five cycles some of the prominent reflexes observed for the bulk material are missing. Either the crystallinity of the obtained NPs is still very low or a different packing compared to the bulk material is obtained.

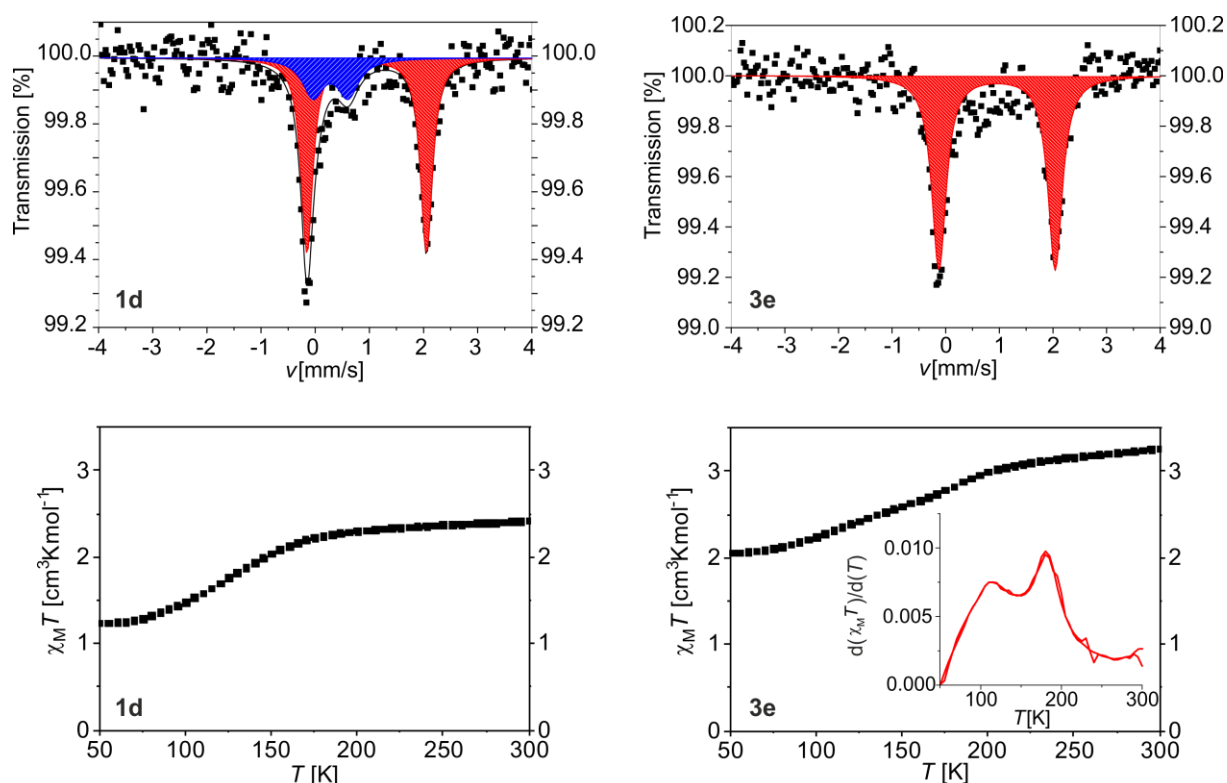
## 6. Synthesis of $[\text{Fe}(\text{L}_{\text{eq}})(\text{L}_{\text{ax}})]_n$ coordination polymer nanoparticles using blockcopolymer micelles

**Table 1:** Investigation of the core size [nm] and crystallinity of the CP-BCP composite obtained from TEM. “MC” denotes the observation of microcrystals.

$\text{L}_{\text{ax}}$	cycles				
	1 (a)	2 (b)	3 (c)	4 (d)	5 (e)
<b>bpea (1a-e)</b>	42±5	46±4	49±4	46±4	49±4 /MC
<b>bpee (2a-e)</b>	40±4	46±5	42±4	48±4 /MC	47±4 /MC
<b>bpey (3a-e)</b>	48±5	46±4	49±6	49±4	49±4
<b>bipy<sup>[13]</sup></b>	52±8	57±8	62±13	44±6	49±5

In Figure 3 (**1d** and **3e**) and Supporting Information File 1, Figure S9 (**1d,e**, **2d,e** and **3d,e**) the  $\chi_{\text{M}}T$ -versus- $T$  plots of the composite materials after four and five cycles are given. Previous investigations showed, that amorphous nanoparticles of  $[\text{FeL}_{\text{eq}}(\text{bipy})]_n$  (1–3 cycles) showed gradual and incomplete spin crossover very different to that of the bulk material.<sup>[13]</sup> Additionally, the samples **a–c** are magnetically very diluted and the change in the spin state of the few SCO-active iron centres is difficult to be reliably detected. An increasing crystallinity of the nanoparticles did change the spin crossover behaviour towards that of the bulk complexes. Consequently, magnetic measurements were done for the samples **d** and **e** after four and five cycles of addition of complex in the temperature range between 50 and 300 K in the cooling and heating mode. In the case of **1d**, a gradual spin transition is observed with about 30% of the iron centres involved and  $T_{1/2} = 122$  K, close to the first step of the bulk material. In contrast, sample **1e** (containing microcrystals) shows a less gradual but still incomplete spin crossover with a small hysteresis of 5 K. The  $\chi_{\text{M}}T$  value is  $3.25 \text{ cm}^3 \cdot \text{K} \cdot \text{mol}^{-1}$  at room temperature and decreases to  $1.03 \text{ cm}^3 \cdot \text{K} \cdot \text{mol}^{-1}$  at 50 K with  $T_{1/2\downarrow}$  of 109 K and  $T_{1/2\uparrow}$  of 114 K. Interestingly, the step in the transition curve that is present in the bulk material is not observed for sample **1e**. **3d** shows a very gradual spin crossover in the temperature range between 100 and 225 K with about 30% of the iron centres involved. This is very different to the abrupt spin transition with hysteresis of the bulk material. For sample **3e**, also a very gradual spin crossover is observed upon cooling. Two steps can be distinguished around 175 K and 110 K (see first derivative in Figure 2c). While the first step is in a similar range as the one observed for the bulk material, the second step has no relation to the spin-crossover properties of the bulk material. This is in good agreement with the results from the PXRD measurements, where pronounced differences between the diffraction pattern of the bulk CP and the nanocomposite are observed. Apparently, a different crystalline polymorph is obtained. The  $\chi_{\text{M}}T$  value is  $2.07 \text{ cm}^3 \cdot \text{K} \cdot \text{mol}^{-1}$  at 50 K indicating that 65% of the iron centres are still in the HS state.





**Figure 3:** Characterisation of the magnetic properties of **1d** and **3e** Top: Mössbauer spectra of **1d** (left) and **3e** (right). Bottom: Magnetic susceptibility data displayed as  $\chi_M T$  vs  $T$  of **1d** (left) and **3e** (right). In the case of **3e** in the inset the first derivative of the  $\chi_M T$  vs  $T$  plot is given to illustrate the steps in the transition curve more clearly.

### 6.3. Conclusion

This work focused on the transfer of the concept for the formation of nanoparticles of coordination polymers in a block copolymer matrix. The central goal was to demonstrate that this concept of block copolymers as microreactors is not restricted to one specific coordination polymer and can easily be applied to other systems. Therefore, three coordination polymers have been chosen to be incorporated inside the block copolymer as nanoparticles. In our previous work<sup>[13]</sup> we did show that longer reaction times, higher reaction temperatures and higher amounts of CP in the BCP micelles (number of cycles) improve the crystallinity of the CP nanoparticle core while the cores size is almost constant. The improved crystallinity did change the SCO properties from gradual to abrupt with hysteresis. Here we show that the coordination polymer does not have an influence on the size of the CP-BCP composite and that the final size arises mainly from the BCP. In agreement with our previous observations, the NP size does not change significantly with increasing CP concentration in the BCP micelle. However, the formation of stable nanoparticles critically depends on the coordination polymer and the solvent used for the synthesis. The investigations reveal an interplay between two different effects: (1) The rigidity

and stacking features of the bridging ligand influences the solubility of the CP and a low solubility is favourable for the selective formation of crystalline nanoparticles in the BCP micelle. (2) Weak-field ligands lead to HS complexes where anti-bonding orbitals are occupied. This supports ligand exchange and prevents the templating effect of the BCP micelle. We found that the CP-BCP composites with the most rigid ligand  $[\text{FeL}_{\text{eq}}(\text{bpey})]_n@BCP$ , **3a-e**) form the most stable crystalline nanoparticles that are spin-crossover active. For the HS complexes  $[\text{FeL}_{\text{eq}}(\text{bpee})]_n@BCP$ , (**2a-e**), first microcrystals are observed after four cycles and for  $[\text{FeL}_{\text{eq}}(\text{bpea})]_n@BCP$ , (**1a-e**) with the most flexible ligand microcrystals are observed after five cycles in THF. The differences observed for the SCO properties and the PXRD data of the bulk material **3** and the composite material **3e** are one further example for the influence of micelle formation on the crystallisation of a material.<sup>[59]</sup>

## 6.4. Experimental

All syntheses were performed under inert conditions using argon 5.0 (purity  $\geq 99.999\%$ ) and Schlenk technique. The synthesis of all samples was repeated at least twice. Polystyrene-*b*-poly(4-vinylpyridine) (PS-P4VP, purum, MW  $\approx 150.000$ ) was synthesised as described before.<sup>[15]</sup> 1,2-di(pyridin-4-yl)ethane (bpea) and trans-1,2-di(pyridin-4-yl)ethene (bpee) were obtained from Sigma-Aldrich and used as received. Tetrahydrofuran (THF) p.a. and toluene were obtained from Sigma-Aldrich and degassed with argon for at least 30 min.  $[\text{FeL}_{\text{eq}}(\text{MeOH})_2]$  was synthesized as described before.<sup>[60]</sup> The ligand bpey was synthesised according to the literature.<sup>[61]</sup>

### 6.4.1. Synthesis

The same synthesis procedures were used for all samples independent of the used  $\text{L}_{\text{ax}}$ . Therefore, the general procedures are given for  $[\text{FeL}_{\text{eq}}(\text{bpea})]_n$  (**1**) and the composite materials  $[\text{FeL}_{\text{eq}}(\text{bpea})]_n@BCP$  (**1a-e**), and the specific values for  $[\text{FeL}_{\text{eq}}(\text{bpee})]_n$  (**2**)/ $[\text{FeL}_{\text{eq}}(\text{bpey})]_n$  (**3**) and the composite materials  $[\text{FeL}_{\text{eq}}(\text{bpee})]_n@BCP$  (**2a-e**)/ $[\text{FeL}_{\text{eq}}(\text{bpey})]_n@BCP$  (**3a-e**) are given in brackets. The synthesis of the composite materials in toluene was done using the same procedures and amounts as described for THF. Due to the observation of microcrystals at a very early stage, the products were not characterized further.

**1 (2/3):** 200 mg (0.45 mmol)  $[\text{FeL}_{\text{eq}}(\text{MeOH})_2]$  and 206 mg (204 mg/202 mg) (1.125 mmol, 2.5 equiv) bpea (bpee/bpey) were dissolved in 20 mL THF in a 50 mL flask. The solution was refluxed for 1 h. After cool-down to room temperature, the solution was let for crystallisation overnight. The solid was filtered, washed with THF once and dried in vacuo to yield a brown (dark violet) powder. Elemental analysis, Anal. calcd for  $\text{C}_{30}\text{H}_{30}\text{N}_4\text{O}_4\text{Fe}$  (**1**): C, 63.61; H, 5.34; N, 9.89; found: C, 62.91; H, 5.19; N, 9.22; (Anal. calcd for  $\text{C}_{30}\text{H}_{28}\text{N}_4\text{O}_4\text{Fe}$  (**2**): C, 63.84; H, 5.00; N, 9.93; found:

C, 63.15; H, 6.05; N, 9.18/Anal. calcd for  $\text{C}_{30}\text{H}_{26}\text{N}_4\text{O}_4\text{Fe}$  (**3**): C, 64.07; H, 4.66; N, 9.96; found: C, 63.63; H, 4.77; N, 9.25).

**1a**, one cycle (**2a/3a**): 50 mg (0.33  $\mu\text{mol}$ ) PS-*b*-P4VP and 6.7 mg (15  $\mu\text{mol}$ )  $[\text{FeL}_{\text{eq}}(\text{MeOH})_2]$  were dissolved in 20 mL THF in a 50 mL flask. The solution was refluxed for 2 h. After, 6.9 mg (6.8 mg/6.8 mg) (37.5  $\mu\text{mol}$ , 2.5 equiv) bpea (bpee/ bpey) was added and refluxed again for 1 h. The solution was cooled down to room temperature and the solvent was removed via cold distillation to yield a brown, polymer-like solid. Elemental analysis, found: C, 64.96; H, 7.44; N, 2.82; (C, 71.23; H, 7.24; N, 3.10/C, 59.99; H, 7.46; N, 2.48).

**1b**, two cycles (**2b/3b**): The synthesis for one cycle was repeated. Prior to solvent removal, 6.7 mg (15  $\mu\text{mol}$ )  $[\text{FeL}_{\text{eq}}(\text{MeOH})_2]$  and 6.9 mg (6.8 mg/6.8 mg) (37.5  $\mu\text{mol}$ , 2.5 equiv) bpea (bpee/bpey) were added for a new cycle and refluxed for another hour. The solvent was removed via cold distillation to yield a dark brown, polymer-like solid. Elemental analysis, found: C, 61.98; H, 7.35; N, 3.38; (C, 59.75; H, 7.43; N, 3.37/C, 57.18; H, 7.42; N, 3.05).

**1c**, three cycles (**2c/3c**): The synthesis for two cycles was repeated and one more cycle was carried out. 6.7 mg (15  $\mu\text{mol}$ )  $[\text{FeL}_{\text{eq}}(\text{MeOH})_2]$  and 6.9 mg (6.8 mg/6.8 mg) (37.5  $\mu\text{mol}$ , 2.5 equiv) bpea (bpee/bpey) were added and refluxed for another hour before the solvent was removed via cold distillation to yield a dark brown, polymer-like solid. Elemental analysis, found: C, 69.43; H, 7.30; N, 5.00 (C, 63.08; H, 7.21; N, 3.71/C, 70.94; H, 6.67; N, 4.88).

**1d**, four cycles (**2d/3d**): The synthesis for three cycles was repeated and one more cycle was run. 6.7 mg (15  $\mu\text{mol}$ )  $[\text{FeL}_{\text{eq}}(\text{MeOH})_2]$  and 6.9 mg (6.8 mg/6.8 mg) (37.5  $\mu\text{mol}$ , 2.5 equiv) bpea (bpee/bpey) were added and refluxed for another hour before the solvent was removed via cold distillation to yield a dark brown, polymer-like solid. Elemental analysis, found: C, 68.18; H, 6.55; N, 5.64 (C, 71.09; H, 6.79; N, 5.90/C, 68.04; H, 6.18; N, 5.48).

**1e**, five cycles (**2e/3e**): The synthesis for four cycles was repeated and one more cycle was run. 6.7 mg (15  $\mu\text{mol}$ )  $[\text{FeL}_{\text{eq}}(\text{MeOH})_2]$  and 6.9 mg (6.8 mg/6.8 mg) (37.5  $\mu\text{mol}$ , 2.5 equiv) bpea (bpee/bpey) were added and refluxed for another hour before the solvent was removed via cold distillation to yield a dark brown, polymer-like solid. Elemental analysis, found: C, 68.09; H, 6.97; N, 5.86; (C, 68.12; H, 6.63; N, 6.09/C, 65.92; H, 6.04; N, 5.70).

The colour of the samples became darker with increasing cycles due to the higher amount of iron inside the samples. The increasing nitrogen content in the elemental analysis from **a–e** also confirms the increasing amount of coordination polymer in the samples.

#### 6.4.2. Characterisation methods

**Transmission electron microscopy:** Transmission electron microscopy was carried out at a Zeiss CEM902 electron microscope (Zeiss, Oberkochen, Germany). Samples were dispersed in toluene applying vortex. The solution was dropped on a copper grid (mesh 200, Science Services, Munich). Electron acceleration voltage was set to 80 kV. Micrographs were taken with a MegaView III/iTEM image acquiring and processing system from Olympus Soft Imaging Systems (OSIS, Münster, Germany) and an Orius 830 SC200W/DigitalMicrograph system from Gatan (Munich, Germany). Particles size measurements were done with “ImageJ” image processing software by Wayne Rasband (National Institutes of Health, USA).

**Elemental analysis:** Carbon, nitrogen and hydrogen content was measured using a Vario EL III with acetanilide as standard. The samples were placed in tin boats and measured at least twice. The average of the measurements was used.

**Infrared spectroscopy measurements:** Transmission infrared spectra were collected using a Perkin Elmer Spectrum 100 FTIR (ATR). The samples were measured directly as solids.

**Magnetic measurements:** Magnetic susceptibility measurements were performed with a Quantum Design MPMS-XL-5 SQUID magnetometer. Field strength of 3 T was applied and a temperature range of 50–300 K was used to determine the temperature dependency of the magnetism and the spin-crossover behaviour. Settle mode was used in all measurements with a cooling and heating rate of 5 K min<sup>-1</sup>. The samples were prepared in gelatine capsules placed in a plastic straw. The measured values were corrected for the diamagnetism of the sample holder, the polymer matrix (measured values) and the ligand (tabulated Pascal constants).

**Dynamic light scattering:** The samples were measured using a Malvern Instruments Zetasizer Nano ZS90 in glass cuvettes from Carl Roth GmbH + Co. KG at 25 °C. One measurement consisted of three consecutive runs.

**Mössbauer spectroscopy:** <sup>57</sup>Fe Mössbauer spectra were recorded in transmission geometry under constant acceleration using a conventional Mössbauer spectrometer with a 50 mCi <sup>57</sup>Co(Rh) source. The samples were sealed in the sample holder in an argon atmosphere. The spectra were fitted using Recoil 1.05 Mössbauer Analysis Software.<sup>[62]</sup> The isomer shift values are given with respect to  $\alpha$ -Fe as reference at room temperature. At present, only measurements at room temperature are possible with the instrumental setup.

**Powder X-ray diffraction:** Powder X-ray diffraction data for all samples were collected at a STOE StadiP X-Ray diffractometer in transmission geometry in a 2 $\theta$  range of 5–30°. Samples **1**, **2** and **3** were placed in capillaries and composite samples **1a–3e** were placed on flat surfaces. Cu K $\alpha_1$

radiation was used for the measurement and the radiation was detected with a Mythen 1K detector.

## 6.5. Acknowledgements

Financial support of the University of Bayreuth and the SFB 840 (TP A10 and B10) is gratefully acknowledged. O.K. was supported by the BayNAT program of the UBT. We thank Juliane Kary for her contribution to the synthesis of the CP and CP-BCP composites.

## 6.6. References

- [1] M. Sindoro, N. Yanai, A.-Y. Jee, S. Granick, *Acc. Chem. Res.* **2014**, *47*, 459–469.
- [2] E. Coronado, M. Giménez-Marqués, G. Mínguez Espallargas, F. Rey, I. J. Vitórica-Yrezábal, *J. Am. Chem. Soc.* **2013**, *135*, 15986–15989.
- [3] O. S. Zhao-Yang Li, Z.-S. Yao, S. Kang, S. Kanegawa in *Spin-Crossover Materials* (Ed.: M. A. Halcrow), John Wiley & Sons Ltd, Chichester, United Kingdom, **2013**, pp 303–319.
- [4] A. B. Gaspar, B. Weber in *Molecular Magnetic Materials* (Eds.: B. Sieklucka, D. Pinkowicz), Wiley-VCH Verlag GmbH & Co. KGaA: Weinheim, Germany, **2017**, pp 231–252.
- [5] M. A. Halcrow, Ed. *Spin-Crossover Materials: Properties and Applications*, John Wiley & Sons Ltd, Chichester, United Kingdom, **2013**.
- [6] J. Turkevich, P. C. Stevenson, J. Hillier, *Discuss. Faraday Soc.* **1951**, *11*, 55.
- [7] G. Frens, *Nature* **1973**, *241*, 20–22.
- [8] S. Sun, H. Zeng, *J. Am. Chem. Soc.* **2002**, *124*, 8204–8205.
- [9] A.-H. Lu, E. L. Salabas, F. Schüth, *Angew. Chem., Int. Ed.* **2007**, *46*, 1222–1244.
- [10] Y. Sun, Y. Xia, *Science* **2002**, *298*, 2176–2179.
- [11] M. Brust, J. Fink, D. Bethell, D. J. Schiffrin, C. Kiely, *J. Chem. Soc., Chem. Commun.* **1995**, 1655.
- [12] A K. Gupta, M. Gupta, *Biomaterials* **2005**, *26*, 3995–4021.
- [13] O. Klimm, C. Göbel, S. Rosenfeldt, F. Puchtler, N. Miyajima, K. Marquardt, M. Drechsler, J. Breu, S. Förster, B. Weber, *Nanoscale* **2016**, *8*, 19058–19065.
- [14] S. Förster, M. Zisenis, E. Wenz, M. Antonietti, *J. Chem. Phys.* **1996**, *104*, 9956.
- [15] S. Förster, M. Antonietti, *Adv. Mater.* **1998**, *10*, 195–217.

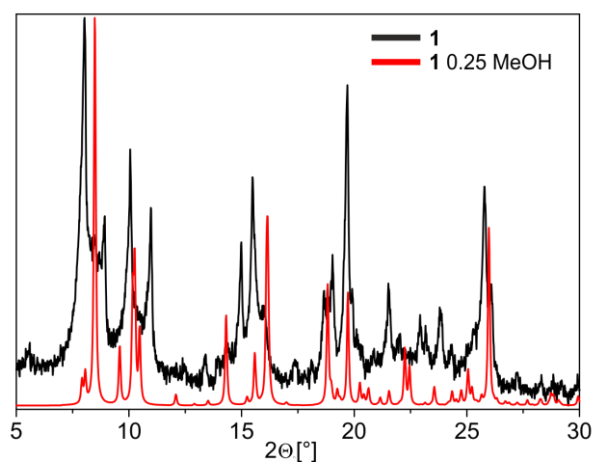
- [16] Z. Fan, X. Chen, M. Köhn Serrano, H. Schmalz, S. Rosenfeldt, S. Förster, S. Agarwal, A. Greiner, *Angew. Chem., Int. Ed.* **2015**, *54*, 14539–14544.
- [17] M. Carmen Muñoz, J. Antonio Real in *Spin-Crossover Materials* (Ed.: M. A. Halcrow), John Wiley & Sons Ltd., Chichester, United Kingdom, **2013**, pp 121–146.
- [18] P. Gülich, A. B. Gaspar, Y. Garcia, *Beilstein J. Org. Chem.* **2013**, *9*, 342–391.
- [19] P. N. Martinho, C. Rajnak, M. Ruben in *Spin-Crossover Materials: Properties and Applications* (Ed.: M. A. Halcrow), John Wiley & Sons Ltd, Chichester, United Kingdom, **2013**, pp 375–404.
- [20] J. M. Herrera, S. Titos-Padilla, S. J. A. Pope, I. Berlanga, F. Zamora, J. J. Delgado, K. V. Kamenev, X. Wang, A. Prescimone, E. K. Brechin, E. Colacio, *J. Mater. Chem. C* **2015**, *3*, 7819–7829.
- [21] M. Giménez-Marqués, M. L. García-Sanz de Larrea, E. Coronado, *J. Mater. Chem. C* **2015**, *3*, 7946–7953.
- [22] O. Roubeau, *Chem. Eur. J.* **2012**, *18*, 15230–15244.
- [23] Y.-H. Luo, Q.-L. Liu, L.-J. Yang, Y. Sun, J.-W. Wang, C.-Q. You, B.-W. Sun, *J. Mater. Chem. C* **2016**, *4*, 8061–8069.
- [24] E. Coronado, G. Mínguez Espallargas, *Chem. Soc. Rev.* **2013**, *42*, 1525.
- [25] M. Ohba, K. Yoneda, G. Agustí, M. C. Muñoz, A. B. Gaspar, J. A. Real, M. Yamasaki, H. Ando, Y. Nakao, S. Sakaki, S. Kitagawa, *Angew. Chem., Int. Ed.* **2009**, *48*, 4767–4771.
- [26] J. Linares, E. Coddjovi, Y. Garcia, *Sensors* **2012**, *12*, 4479–4492.
- [27] J.-F. Létard, P. Guionneau, L. Goux-Capes in *Spin Crossover in Transition Metal Compounds I-III* (Eds.: P. Gülich, H. Goodwin), *Topics in Current Chemistry*, Vol. 233–235, Springer, Berlin, Germany, **2004**, pp 221–249.
- [28] O. Kahn, C. Jay Martinez, *Science* **1998**, *279*, 44–48.
- [29] O. Kahn, C. Jay, J. Krober, R. Claude, F. Groliere, Spin-transition chemical compounds, and devices comprising read-, memory-, and erase-units, active medium which contains at least one of those compounds. Eur. Pat. EP0666561, Aug 9, 1995.
- [30] R. N. Muller, L. Vander Elst, S. Laurent, *J. Am. Chem. Soc.* **2003**, *125*, 8405–8407.
- [31] S. Venkataramani, U. Jana, M. Dommaschk, F. D. Sönnichsen, F. Tuczek, R. Herges, *Science* **2011**, *331*, 445–448.
-

- [32] M. Dommaschk, M. Peters, F. Gutzeit, C. Schütt, C. Näther, F. D. Sönnichsen, S. Tiwari, C. Riedel, S. Boretius, R. Herges, *J. Am. Chem. Soc.* **2015**, *137*, 7552–7555.
  - [33] J. Hasserodt, J. L. Kolanowski, F. Touti, *Angew. Chem., Int. Ed.* **2014**, *53*, 60–73.
  - [34] R. Nowak, E. A. Prasetyanto, L. de Cola, B. Bojer, R. Siegel, J. Senker, E. Rössler, B. Weber, *Chem. Commun.* **2017**, *53*, 971–974.
  - [35] F. Volatron, L. Catala, E. Rivière, A. Gloter, O. Stéphan, T. Mallah, *Inorg. Chem.* **2008**, *47*, 6584–6586.
  - [36] T. Forestier, S. Mornet, N. Daro, T. Nishihara, S.-i. Mouri, K. Tanaka, O. Fouché, E. Freysz, J.-F. Létard, *Chem. Commun.* **2008**, 4327–4329.
  - [37] I. Boldog, A. B. Gaspar, V. Martínez, P. Pardo-Ibañez, V. Ksenofontov, A. Bhattacharjee, P. Gülich, J. A. Real, *Angew. Chem., Int. Ed.* **2008**, *47*, 6433–6437.
  - [38] T. Forestier, A. Kaiba, S. Pechev, D. Denux, P. Guionneau, C. Etrillard, N. Daro, E. Freysz, J.-F. Létard, *Chem. Eur. J.* **2009**, *15*, 6122–6130.
  - [39] V. Martínez, I. Boldog, A. B. Gaspar, V. Ksenofontov, A. Bhattacharjee, P. Gülich, J. A. Real, *Chem. Mater.* **2010**, *22*, 4271–4281.
  - [40] J. Larionova, L. Salmon, Y. Guari, A. Tokarev, K. Molvinger, G. Molnár, A. Bousseksou, *Angew. Chem., Int. Ed.* **2008**, *47*, 8236–8240.
  - [41] S. Cobo, G. Molnár, J. A. Real, A. Bousseksou, *Angew. Chem., Int. Ed.* **2006**, *45*, 5786–5789.
  - [42] G. Molnár, S. Cobo, J. A. Real, F. Carcenac, E. Daran, C. Vieu, A. Bousseksou, *Adv. Mater.* **2007**, *19*, 2163–2167.
  - [43] C. Bartual-Murgui, E. Natividad, O. Roubeau, *J. Mater. Chem. C* **2015**, *3*, 7916–7924.
  - [44] W. Bauer, W. Scherer, S. Altmannshofer, B. Weber, *Eur. J. Inorg. Chem.* **2011**, 2803–2818.
  - [45] C. Baldé, W. Bauer, E. Kaps, S. Neville, C. Desplanches, G. Chastanet, B. Weber, J.-F. Létard, *Eur. J. Inorg. Chem.* **2013**, 2744–2750.
  - [46] I. Šalitroš, O. Fuhr, M. Ruben, *Materials* **2016**, *9*, 585.
  - [47] K. Dankhoff, C. Lochenie, F. Puchtler, B. Weber, *Eur. J. Inorg. Chem.* **2016**, 2136–2143.
  - [48] C. Lochenie, W. Bauer, A. P. Railliet, S. Schlamp, Y. Garcia, B. Weber, *Inorg. Chem.* **2014**, *53*, 11563–11572.
  - [49] R. Nowak, W. Bauer, T. Osslander, B. Weber, *Eur. J. Inorg. Chem.* **2013**, 975–983.
-

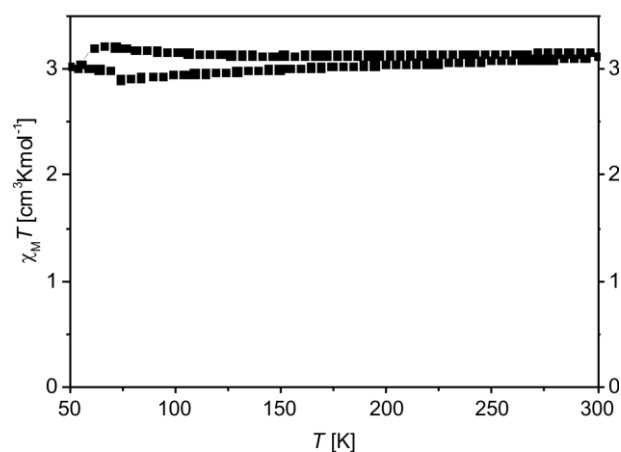
- [50] B. Weber, *Coord. Chem. Rev.* **2009**, *253*, 2432–2449.
- [51] B. Weber, *Koordinationschemie. Grundlagen und aktuelle Trends*, Springer Spektrum, Berlin, Germany, **2014**.
- [52] S. Brooker, *Chem. Soc. Rev.* **2015**, *44*, 2880–2892.
- [53] S. Schönfeld, C. Lochenie, P. Thoma, B. Weber, *CrystEngComm* **2015**, *17*, 5389–5395.
- [54] V. A. Money, C. Carbonera, J. Elhaik, M. A. Halcrow, J. A. K. Howard, J.-F. Létard, *Chem. Eur. J.* **2007**, *13*, 5503–5514.
- [55] W. Bauer, T. Pfaffeneder, K. Achterhold, B. Weber, *Eur. J. Inorg. Chem.* **2011**, 3183–3192.
- [56] B. Weber, E. Kaps, *Heteroat. Chem.* **2005**, *16*, 391–397.
- [57] B. Weber, C. Carbonera, C. Desplances, J.-F. Létard, *Eur. J. Inorg. Chem.* **2008**, 1589–1598.
- [58] C. Göbel, T. Palamarciuc, C. Lochenie, B. Weber, *Chem. Asian J.* **2014**, *9*, 2232–2238.
- [59] L. Xu, L. Jiang, M. Drechsler, Y. Sun, Z. Liu, J. Huang, B. Z. Tang, Z. Li, M. A. C. Stuart, Y. Yan, *J. Am. Chem. Soc.* **2014**, *136*, 1942–1947.
- [60] B. Weber, E.-G. Jäger, *Eur. J. Inorg. Chem.* **2009**, 465–477.
- [61] M. Tanner, A. Ludi, *Chimia* **1980**, *34*, 23–24.
- [62] Recoil, *Mössbauer spectral analysis software for windows*, Version 1.0, Department of Physics, University of Ottawa, Ottawa, Canada, **1998**.



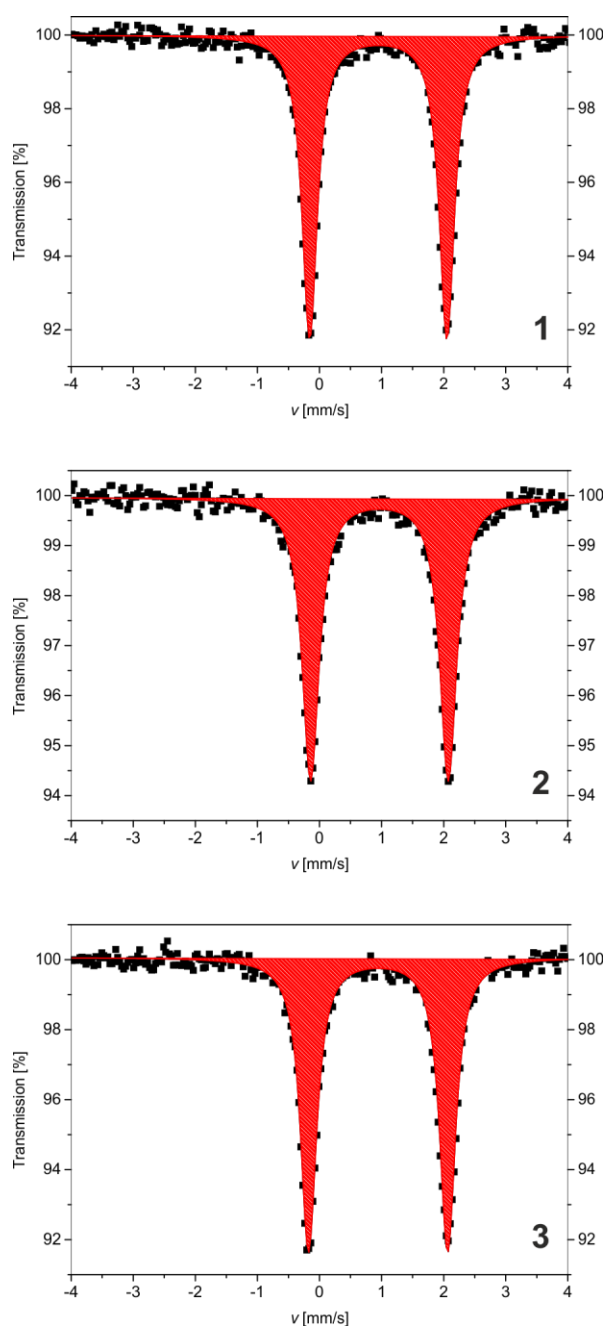
## 6.7. Supporting Information



**Figure S1:** Comparison of the powder X-ray diffraction pattern of  $[\text{Fe}(\text{L}_{\text{eq}})(\text{bpea})]_n$  (**1**) and  $\{[\text{Fe}(\text{L}_{\text{eq}})(\text{bpea})] \cdot 0.25 \text{ MeOH}\}_n$  (synthesised in methanol, calculated from single crystal data)<sup>[1]</sup>.



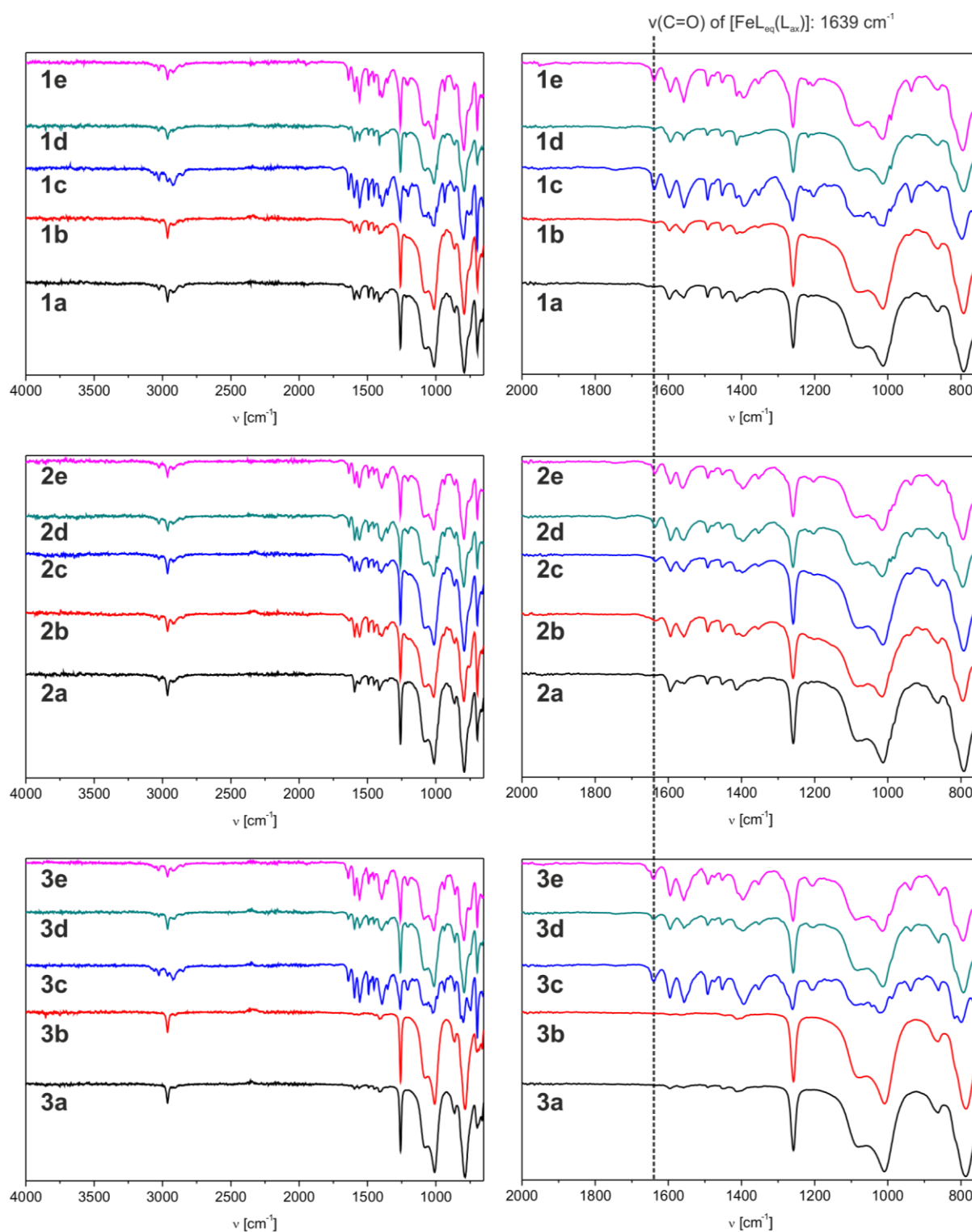
**Figure S2:** Plot of the  $\chi_M T$  product versus temperature for **2**.



**Figure S3:** Mössbauer spectra of **1** (top), **2** (centre) and **3** (bottom). In each case one single doublet is observed with Mössbauer parameters (Table S1) characteristic for an iron(II) HS complex.

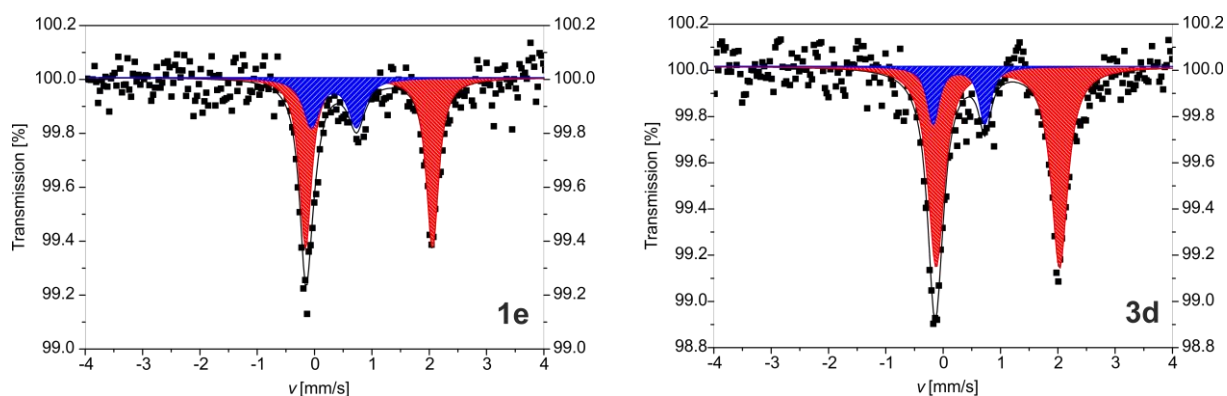
**Table S1:** Mössbauer parameters of the samples **1**, **2** and **3**.

sample	site	$\delta$ [mm/s]	$\Delta E_Q$ [mm/s]	$\Gamma$ [mm/s]	Area [%]
1	Fe(II) HS	0.947(3)	2.210(6)	0.147(5)	100
2	Fe(II) HS	0.966(4)	2.216(7)	0.164(6)	100
3	Fe(II) HS	0.944(3)	2.240(6)	0.156(5)	100



**Figure S4:** IR spectra of **1a-e** (top left), **2a-e** (centre left) and **3a-e** (bottom left) and the relevant area between 2000 and 750  $\text{cm}^{-1}$  to show the C=O vibration band the samples **1a-e** (top right), **2a-e** (centre right) and **3a-e** (bottom right).

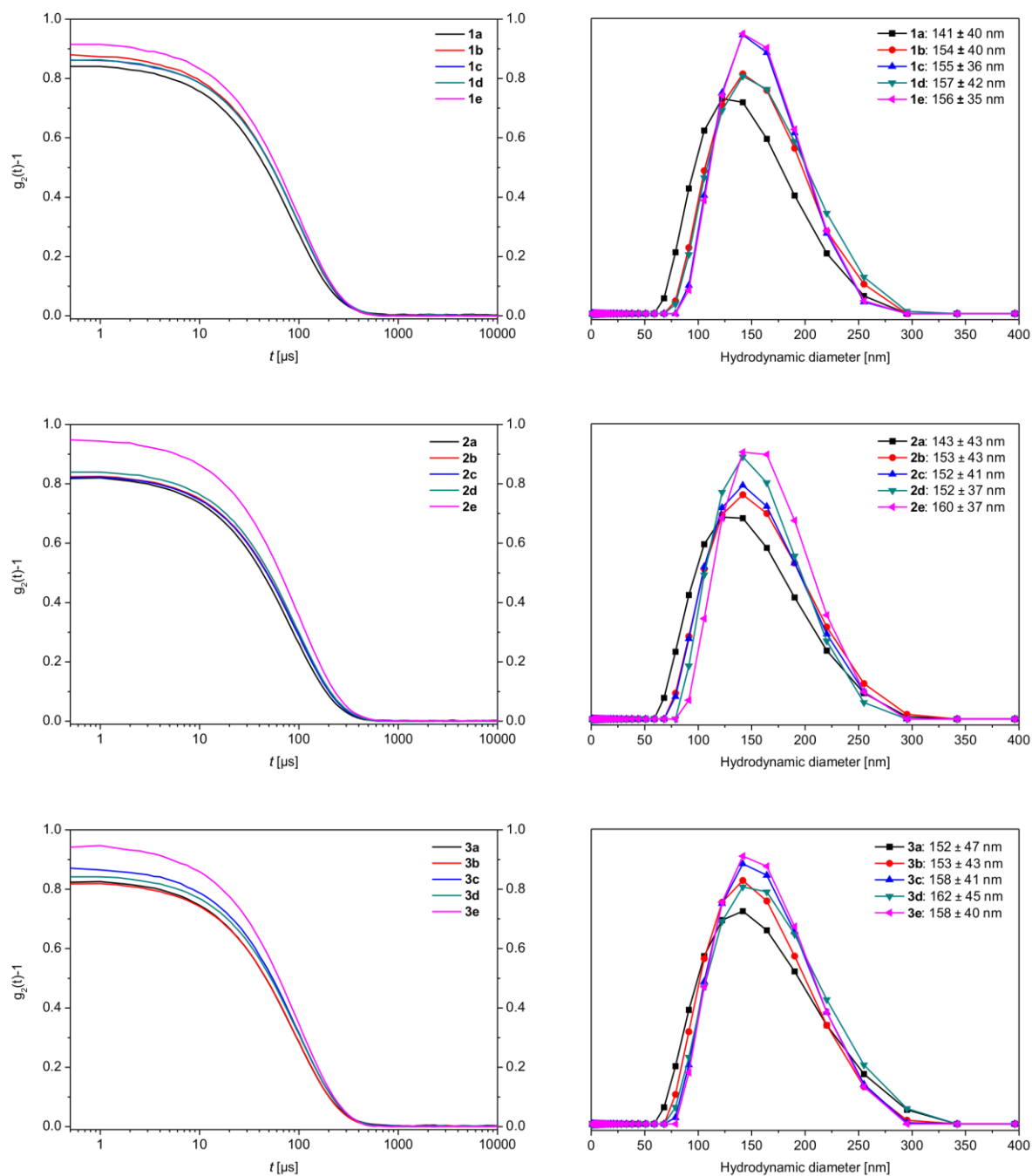
## 6. Synthesis of $[\text{Fe}(\text{L}_{\text{eq}})(\text{L}_{\text{ax}})]_n$ coordination polymer nanoparticles using blockcopolymer micelles



**Figure S5:** Mössbauer spectra of **1e** (left) and **3d** (right). The red doublet corresponds to an iron(II) HS species and the blue doublet corresponds to an iron(II) LS species. The Mössbauer parameters are given in Table S2.

**Table S2:** Mössbauer parameters of the samples **1d**, **1e**, **3d** and **3e**.

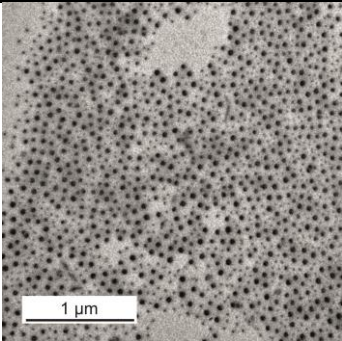
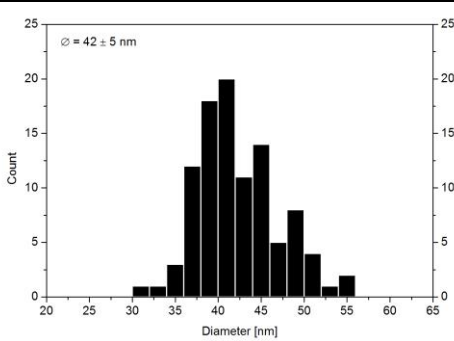
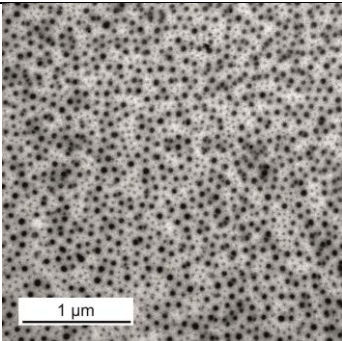
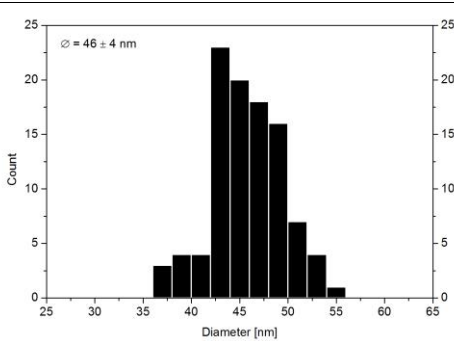
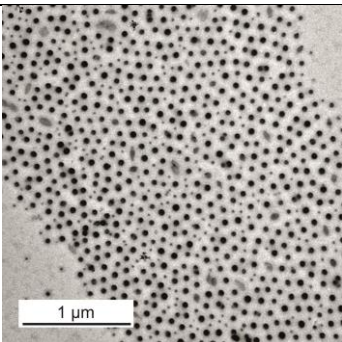
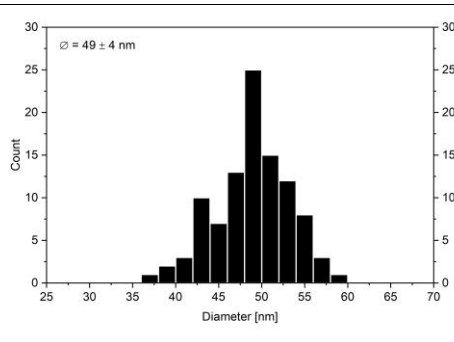
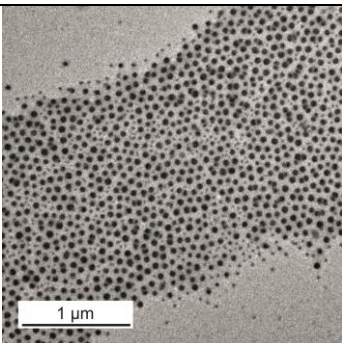
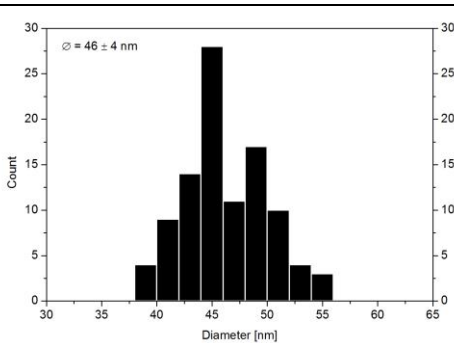
sample	site	$\delta$ [mm/s]	$\Delta E_Q$ [mm/s]	$\Gamma$ [mm/s]	Area [%]
1d	Fe(II) LS	0.28(11)	0.65(18)	0.24(14)	26(9)
	Fe(II) HS	0.951(14)	2.21(3)	0.132(19)	74(9)
1e	Fe(II) LS	0.34(6)	0.79(12)	0.17(8)	28(9)
	Fe(II) HS	0.951(14)	2.21(3)	0.12(2)	72(9)
3d	Fe(II) LS	0.28(6)	0.90(12)	0.12(6)	17(6)
	Fe(II) HS	0.95(2)	2.15(4)	0.17(2)	83(9)
3e	Fe(II) HS	0.958(12)	2.17(2)	0.161(18)	100



**Figure S6:** DLS measurement of the nanocomposites in THF, 43 wt%. Correlation functions of **1a–e** (top left), **2a–e** (centre left) and **3a–e** (bottom left) and the resulting hydrodynamic diameter of the polymeric micelles in THF of **1a–e** (top right), **2a–e** (centre right) and **3a–e** (bottom right).

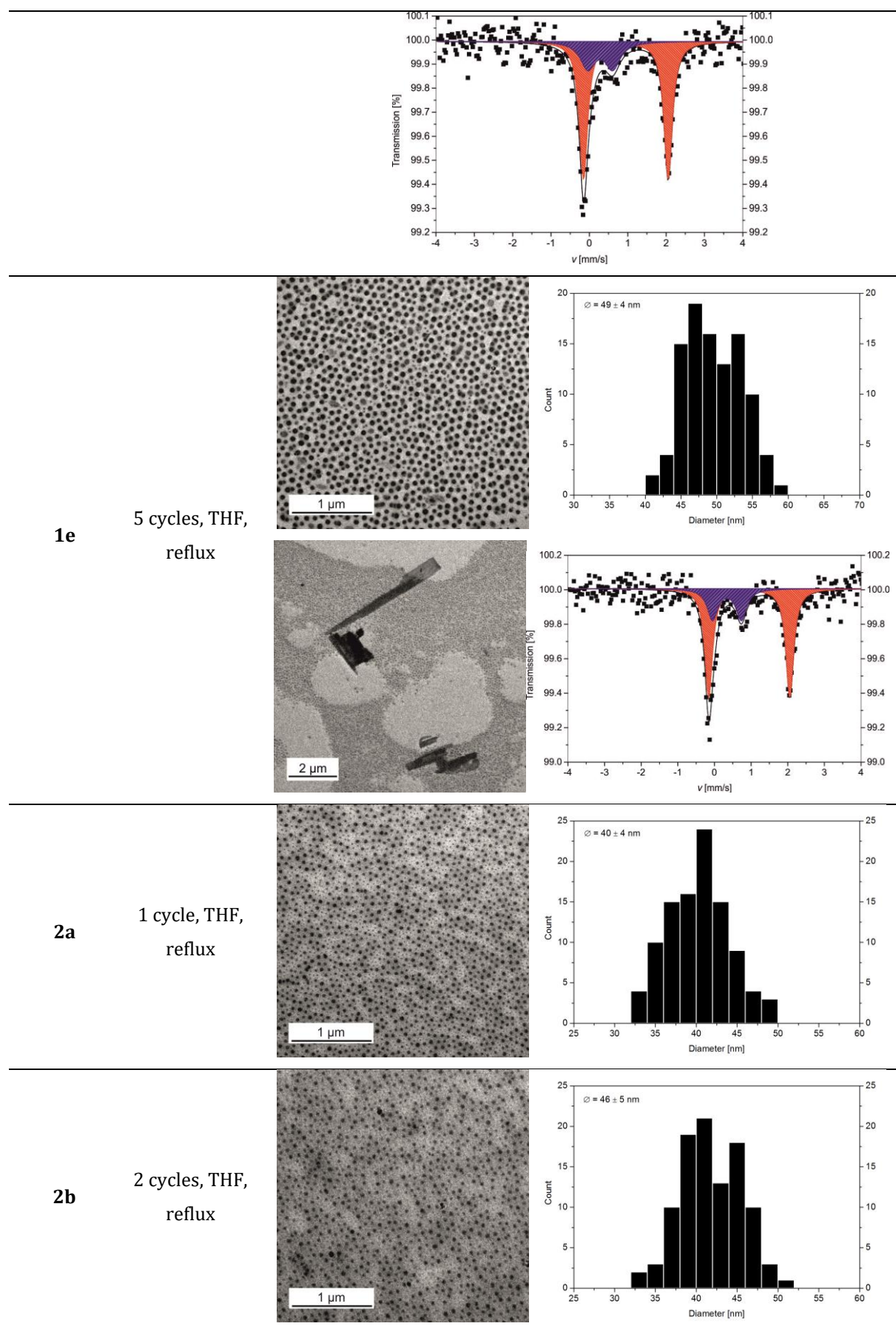
## 6. Synthesis of $[\text{Fe}(\text{L}_{\text{eq}})(\text{L}_{\text{ax}})]_n$ coordination polymer nanoparticles using blockcopolymer micelles

**Table S3:** Summarised characterisation for the different composite samples (**1a–3e**). An exemplary TEM picture and the size distribution are given for TEM measurements. The particle sizes are given in the pictures.

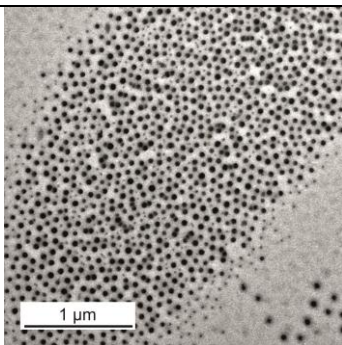
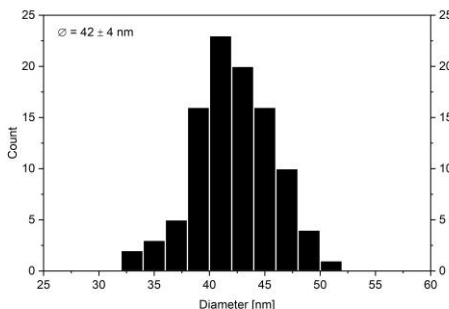
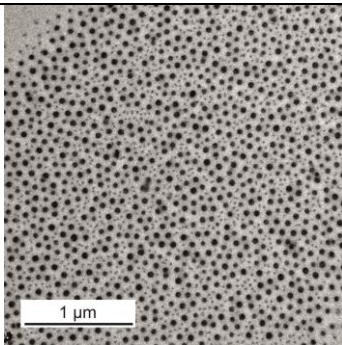
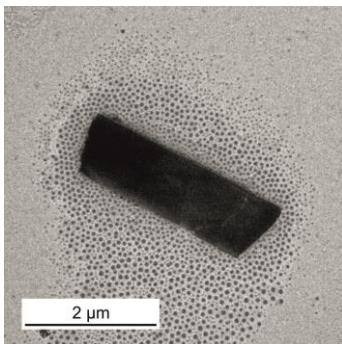
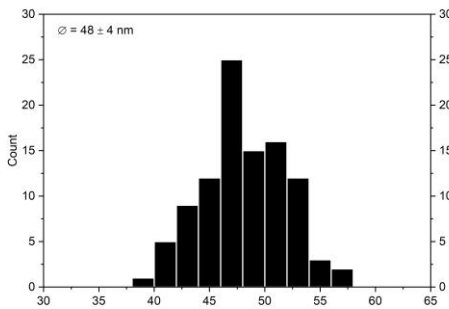
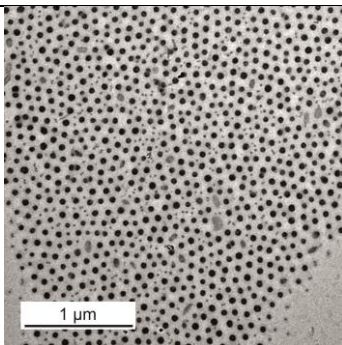
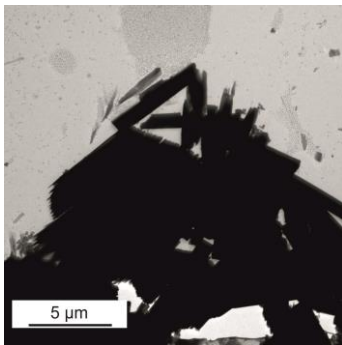
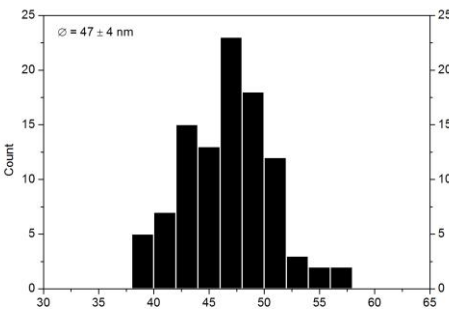
Sample	Reaction conditions	TEM nanoparticles, TEM size distribution, TEM microcrystals (if any) and Mössbauer spectra (if any)
<b>1a</b>	1 cycle, THF, reflux	 
<b>1b</b>	2 cycles, THF, reflux	 
<b>1c</b>	3 cycles, THF, reflux	 
<b>1d</b>	4 cycles, THF, reflux	 



## 6. Synthesis of $[\text{Fe}(\text{L}_{\text{eq}})(\text{L}_{\text{ax}})]_n$ coordination polymer nanoparticles using blockcopolymer micelles

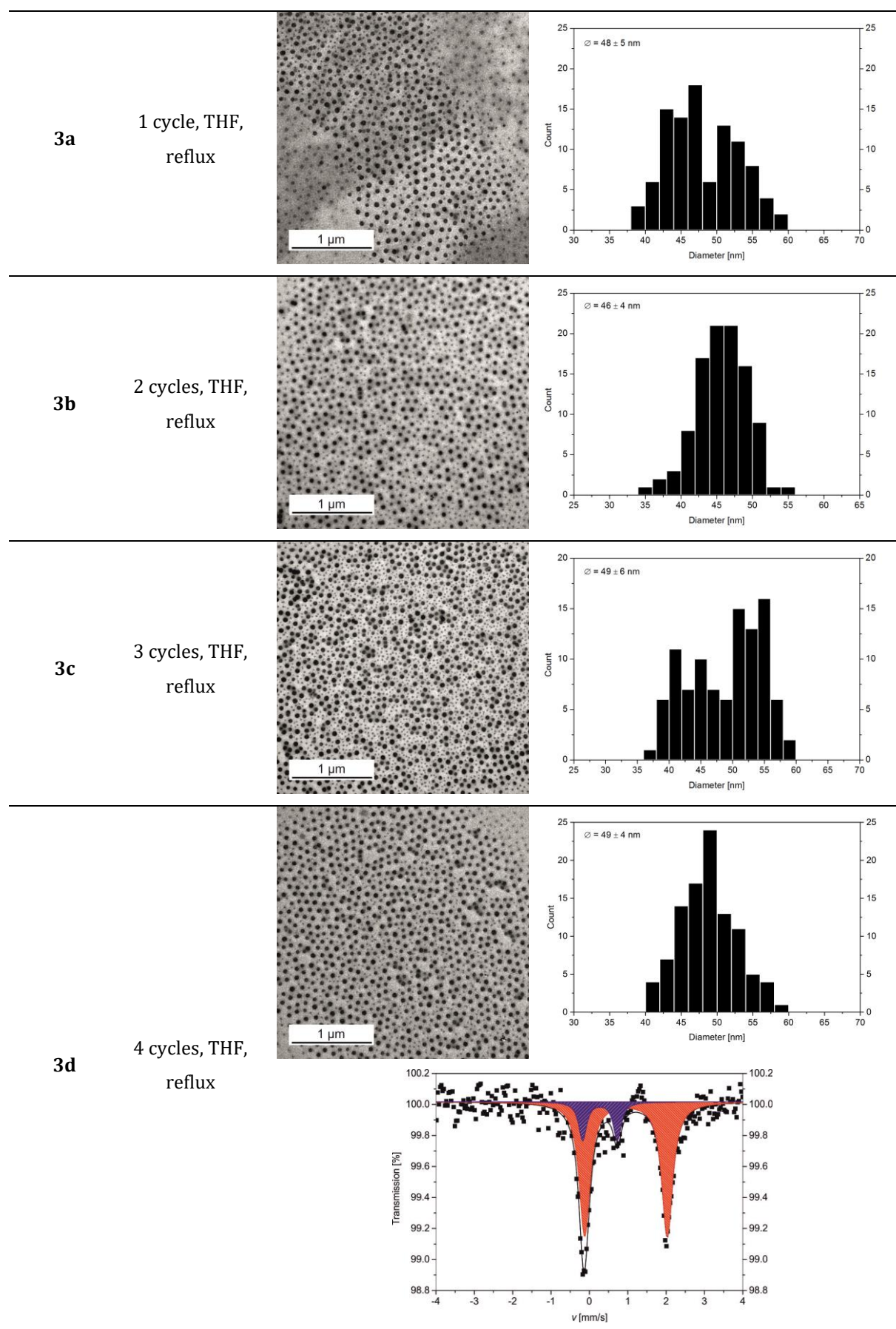


## 6. Synthesis of $[\text{Fe}(\text{L}_{\text{eq}})(\text{L}_{\text{ax}})]_n$ coordination polymer nanoparticles using blockcopolymer micelles

2c	3 cycles, THF, reflux		
2d	4 cycles, THF, reflux	 	
2e	5 cycles, THF, reflux	 	

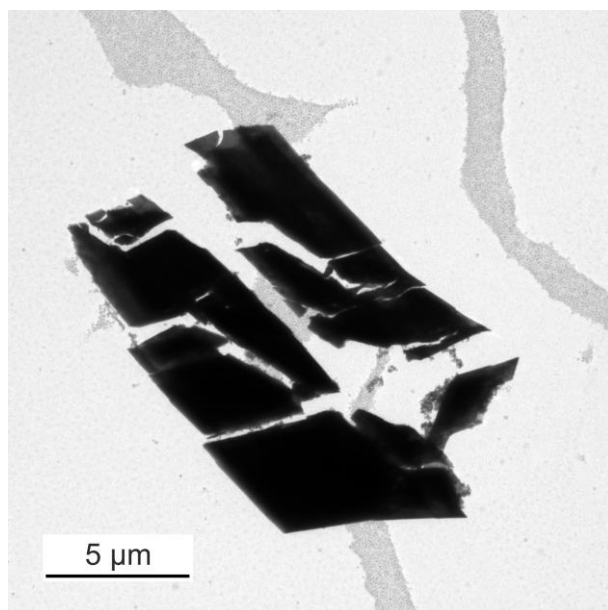
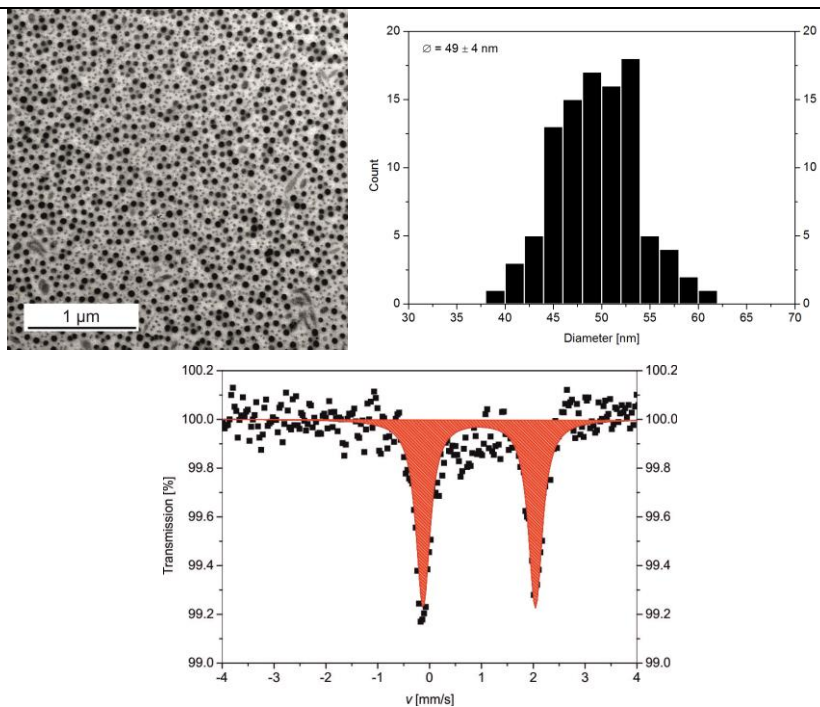


## 6. Synthesis of $[\text{Fe}(\text{L}_{\text{eq}})(\text{L}_{\text{ax}})]_n$ coordination polymer nanoparticles using blockcopolymer micelles

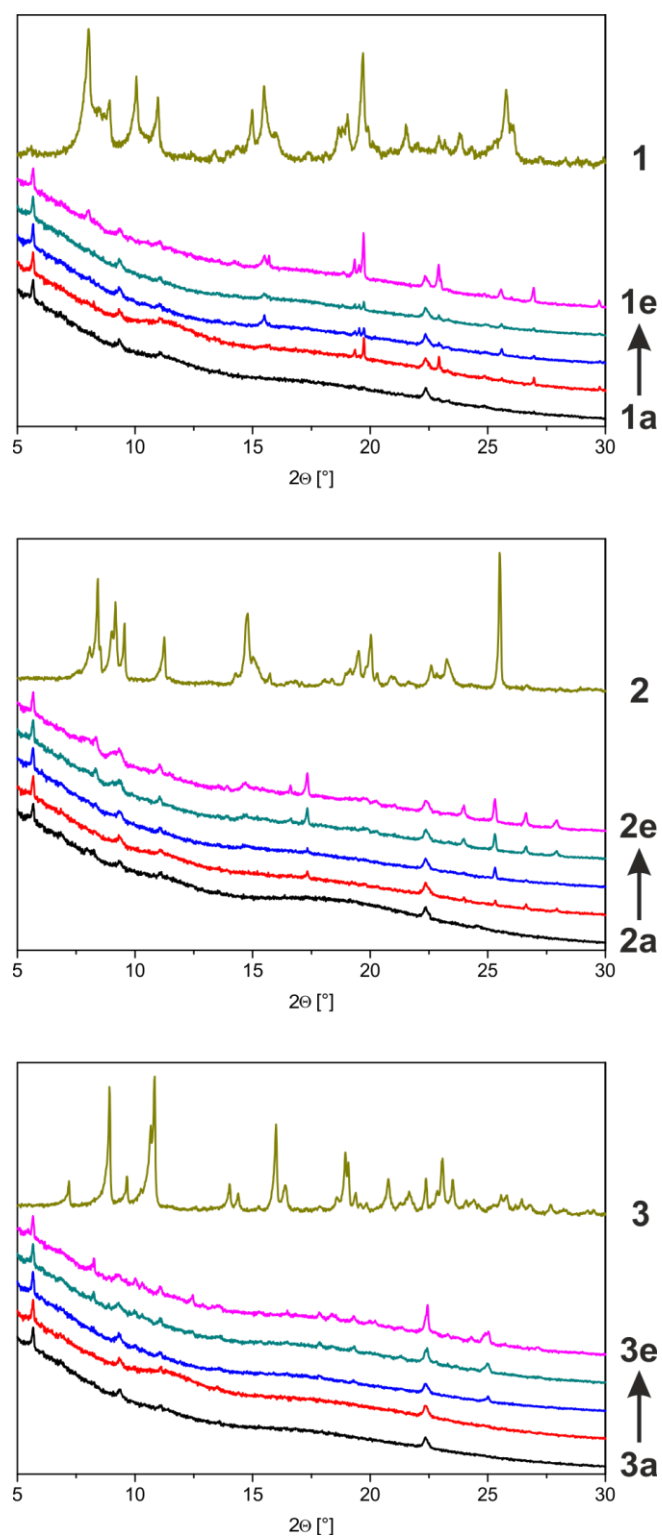


**3e**

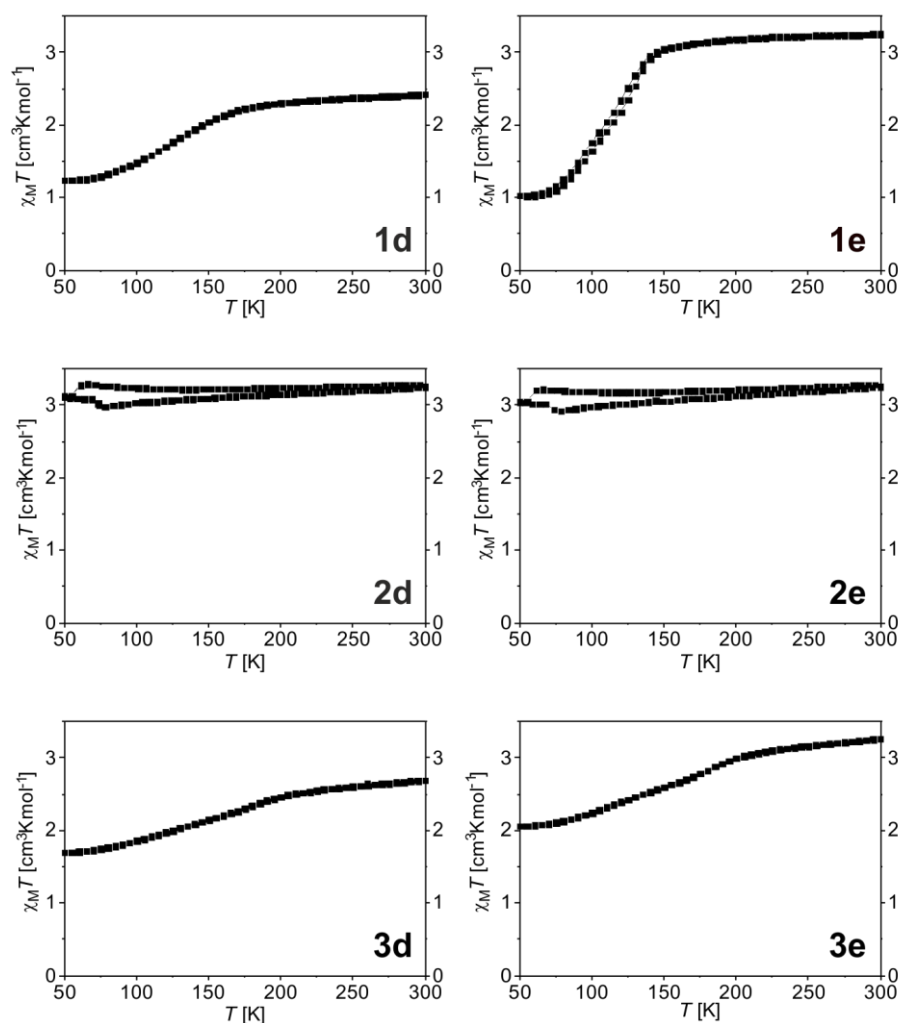
5 cycles, THF,  
reflux



**Figure S7:** Exemplary TEM picture of  $[\text{Fe}(\text{L}_{\text{eq}})(\text{bpea})]_n@BCP$  after two cycles synthesised in toluene to show microcrystals of the coordination polymer.



**Figure S8:** Powder X-ray diffraction pattern of **1** and **1a-e** (top), **2** and **2a-e** (centre) and **3** and **3a-e** (bottom).



**Figure S9:**  $\chi_M T$  vs  $T$  plots of the samples **1d** (top left), **1e** (top right), **3d** (bottom left) and **3e** (bottom right). The results for the samples **2d** (centre left) to **2e** (centre right) are identical to the bulk material  $[\text{FeL}_{\text{eq}}(\text{bpee})]_n$ ; the  $\chi_M T$  product is constant in the temperature region investigated and no indication for spin crossover is observed. This is not surprising, as relatively large microcrystals are observed.

## References

- [1] W. Bauer, W. Scherer, S. Altmannshofer, B. Weber, *Eur. J. Inorg. Chem.* **2011**, 2803–2818.

## 7. Confined Crystallization of Spin-Crossover Nanoparticles in Block-Copolymer Micelles

Christoph Göbel, Christian Hils, Markus Drechsler, Dirk Baabe, Andreas Greiner, Holger Schmalz,\* and Birgit Weber\*

C. Göbel, Prof. Dr. B. Weber, Department of Chemistry, Inorganic Chemistry IV, Universität Bayreuth, Universitätsstrasse 30, 95440 Bayreuth (Germany)

C. Hils, Department of Chemistry, Macromolecular Chemistry II, Universität Bayreuth, Universitätsstr. 30, 95440 Bayreuth (Germany)

Prof. Dr. A. Greiner, Dr. H. Schmalz, Department of Chemistry, Macromolecular Chemistry II and Keylab Synthesis and Molecular Characterization, Bavarian Polymer Institute, Universität Bayreuth, Universitätsstrasse 30, 95440 Bayreuth (Germany)

M. Drechsler, Keylab Electron and Optical Microscopy, Bavarian Polymer Institute, Universität Bayreuth, Universitätsstrasse 30, 95440 Bayreuth (Germany)

Dr. D. Baabe, Institut für Anorganische und Analytische Chemie, Technische Universität Braunschweig, Hagenring 30, 38106 Braunschweig (Germany)

Published in *Angew. Chem. Int. Ed.* **2020**, 59, 5765–5770 (doi: 10.1002/anie.201914343) and reproduced under the terms of the CC-BY-NC-ND 4.0 license.

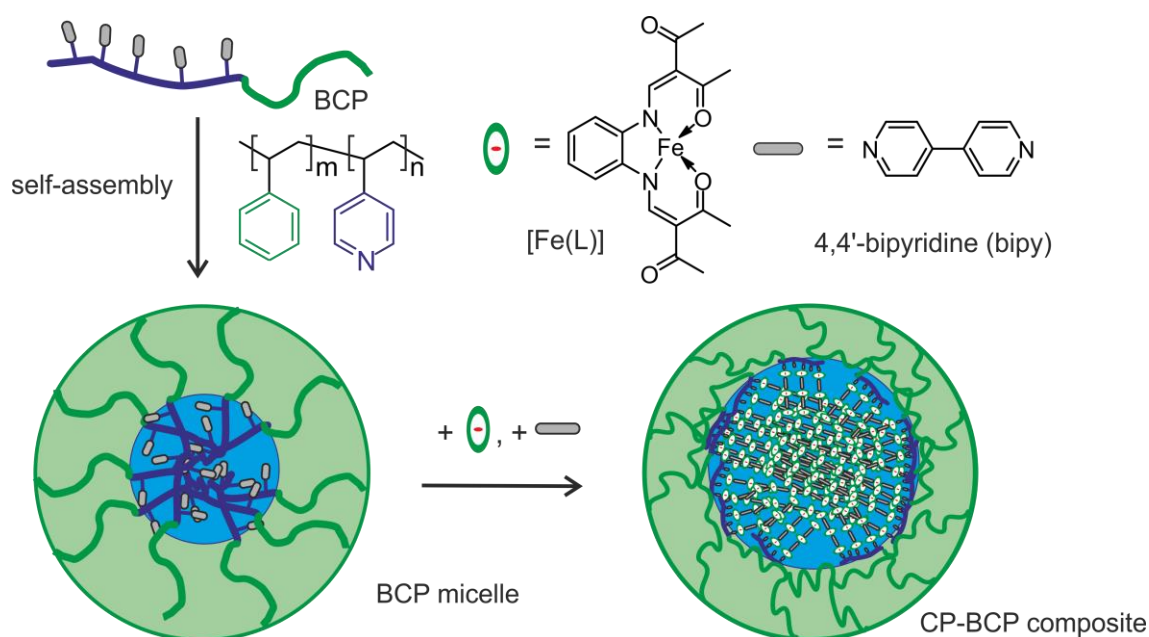
**Abstract:** Nanoparticles of the spin-crossover coordination polymer  $[\text{FeL}(\text{bipy})]_n$  were synthesized by confined crystallization within the core of polystyrene-*block*-poly(4-vinylpyridine) (PS-*b*-P4VP) diblock copolymer micelles. The 4VP units in the micellar core act as coordination sites for the Fe complex. In the bulk material, the spin-crossover nanoparticles in the core are well isolated from each other allowing thermal treatment without disintegration of their structure. During annealing above the glass transition temperature of the PS block, the transition temperature is shifted gradually to higher temperatures from the as-synthesized product ( $T_{1/2\downarrow} = 163 \text{ K}$  and  $T_{1/2\uparrow} = 170 \text{ K}$ ) to the annealed product ( $T_{1/2\downarrow} = 203 \text{ K}$  and  $T_{1/2\uparrow} = 217 \text{ K}$ ) along with an increase in hysteresis width from 6 K to 14 K. Thus, the spin-crossover properties can be shifted towards the properties of the related bulk material. The stability of the nanocomposite allows further processing, such as electrospinning from solution.

### 7.1. Introduction

The synthesis of nanoparticles (NPs) of functional materials is often considered an important step towards application.<sup>[1]</sup> A highly relevant aspect to consider is the stability of the obtained NPs, the conservation of their functional properties down to very small sizes (if possible the observation of additional size-dependent properties) and the suitability for integration into devices. The spin crossover (SCO) phenomenon has gained interest in many different fields over the last decades.<sup>[2-6]</sup> SCO complexes can be switched between two states, the high-spin (HS) and the low-spin (LS) state, by a wide range of external stimuli<sup>[7]</sup> such as temperature, pressure, light irradiation or the inclusion of guest molecules.<sup>[4,8]</sup> Furthermore, the physical properties of either the complex itself (e.g. color, magnetism, structure)<sup>[5,9]</sup> or associated properties in multifunctional systems (e.g. conductivity,<sup>[10]</sup> luminescence<sup>[11]</sup>) change upon switching and raise their interest for applications, especially as sensors.<sup>[12]</sup> In order to realize such applications, an easy processing of the complexes is indispensable for the integration in devices. This task (including down-sizing) is challenging as most of the SCO properties, especially the observation of wide thermal hysteresis loops, depend on the crystal packing.<sup>[6]</sup> So far, to our knowledge, only five examples are known in which thermal hysteresis loops can be maintained for particle sizes below 20 nm.<sup>[13-16]</sup> In general, SCO systems are excellently suited to investigate the influence of decreasing particle size,<sup>[15,17-19]</sup> crystallinity and matrix effects<sup>[16,20-22]</sup> on the nanomaterial as a wide range of different methods can be used to follow the SCO. Those investigations lead to the observation of different phenomena like the predicted re-appearance of hysteresis loops below a 8 nm particle size<sup>[18]</sup> or the stabilizing effect of a rigid SiO<sub>2</sub> shell on the hysteresis for 10 nm<sup>[16]</sup> particles as well as larger ones.<sup>[22]</sup> In a prior work, we reported a new approach for the synthesis of narrowly distributed 50 nm SCO nanoparticles within the P4VP cores of PS-*b*-P4VP block copolymer (BCP) micelles, where a shift of the SCO transition temperature to lower temperatures and a significantly smaller thermal hysteresis loop was observed.<sup>[23,24]</sup> Herein, we show that it is possible to trigger the crystallization of even smaller nanoparticles in the micellar confinement, if the material is heated above the glass transition temperature of the PS shell. This leads to a significant improvement of the SCO properties down to particle sizes as small as 16 nm.

## 7.2. Results and Discussion

The spin crossover coordination polymer–block copolymer (SCO CP-BCP) composite particles were synthesized as described previously by dissolving the PS-*b*-P4VP diblock copolymer ( $S_{85}V_{15}^{154}$ : subscripts denote content of the respective block in wt%, superscript gives the number average molecular weight in kg mol<sup>-1</sup>) and the complex [FeL(MeOH)<sub>2</sub>] in tetrahydrofuran (THF) followed by subsequent addition of the bridging ligand 4,4'-bipyridine (bipy) and iron complex under reflux conditions (Scheme 1, see Supporting Information for details).<sup>[20]</sup>

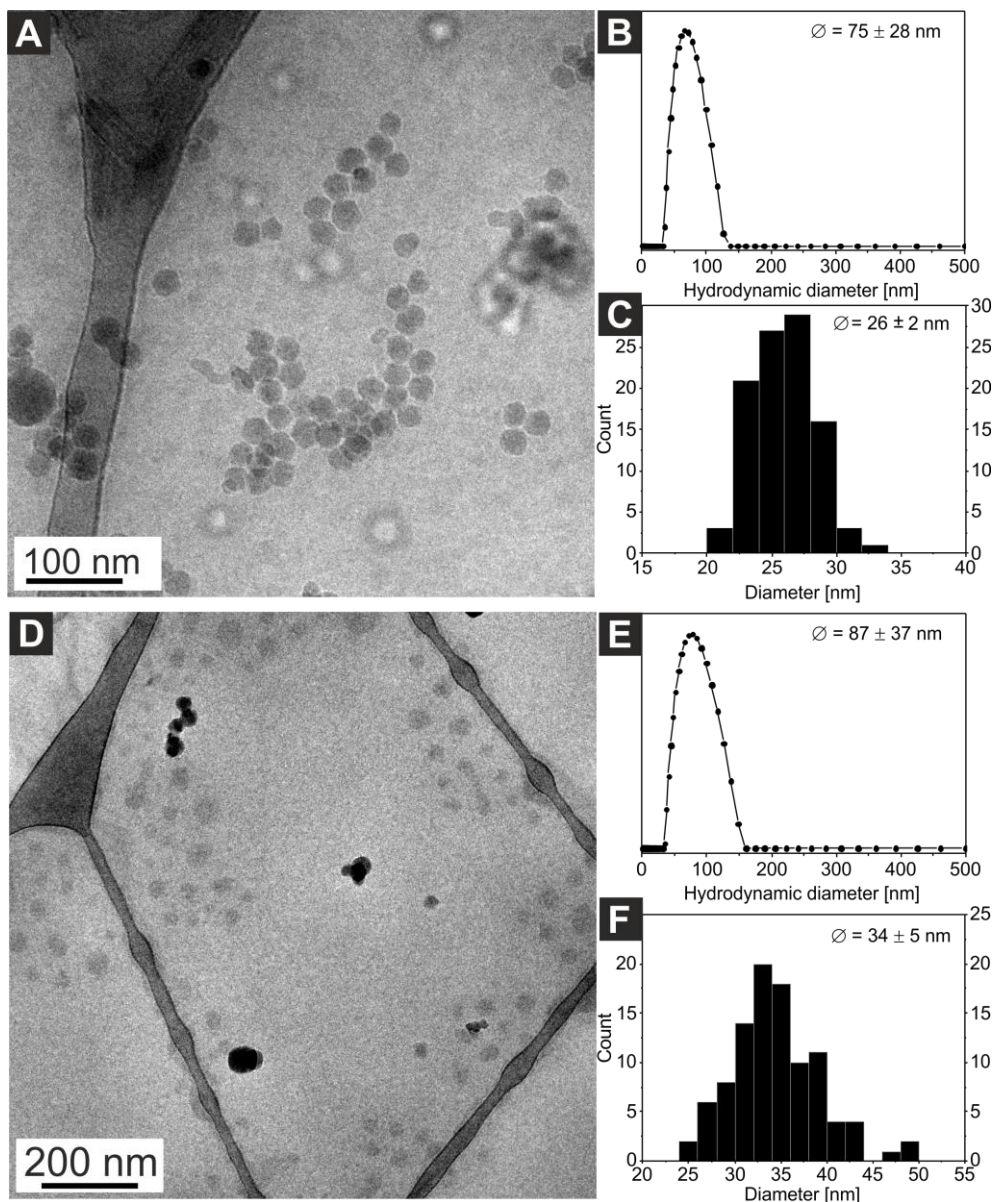


**Scheme 1:** General synthesis approach and abbreviations used.

In total five cycles of addition of complex and bridging ligand were carried out, leading to a ratio of about 33.5 mg of iron complex in 50 mg BCP. Raman measurements on the produced SCO CP-BCP composite particles revealed identical Raman spectra compared to that observed for the neat SCO CP crystals, confirming the successful formation of SCO CP in the micellar core of the  $S_{85}V_{15}^{154}$  micelles (Figure S1 in the Supporting Information); also confirmed by IR spectroscopy (Figure S2). The average hydrodynamic diameter of the SCO CP-BCP particles in solution was determined to  $D_h = 87 \pm 37$  nm (Figure 1E, for corresponding autocorrelation function see Figure S3) by dynamic light scattering (DLS), which is slightly larger compared to that of the empty BCP micelles ( $D_h = 75 \pm 28$  nm, Figure 1C and Figure S3). This might be attributed to the incorporation of the SCO CP inside the P4VP core of the micelle. The different sizes are also reflected in the cryo-TEM pictures for the empty BCP micelles (Figure 1A) and the SCO CP-BCP



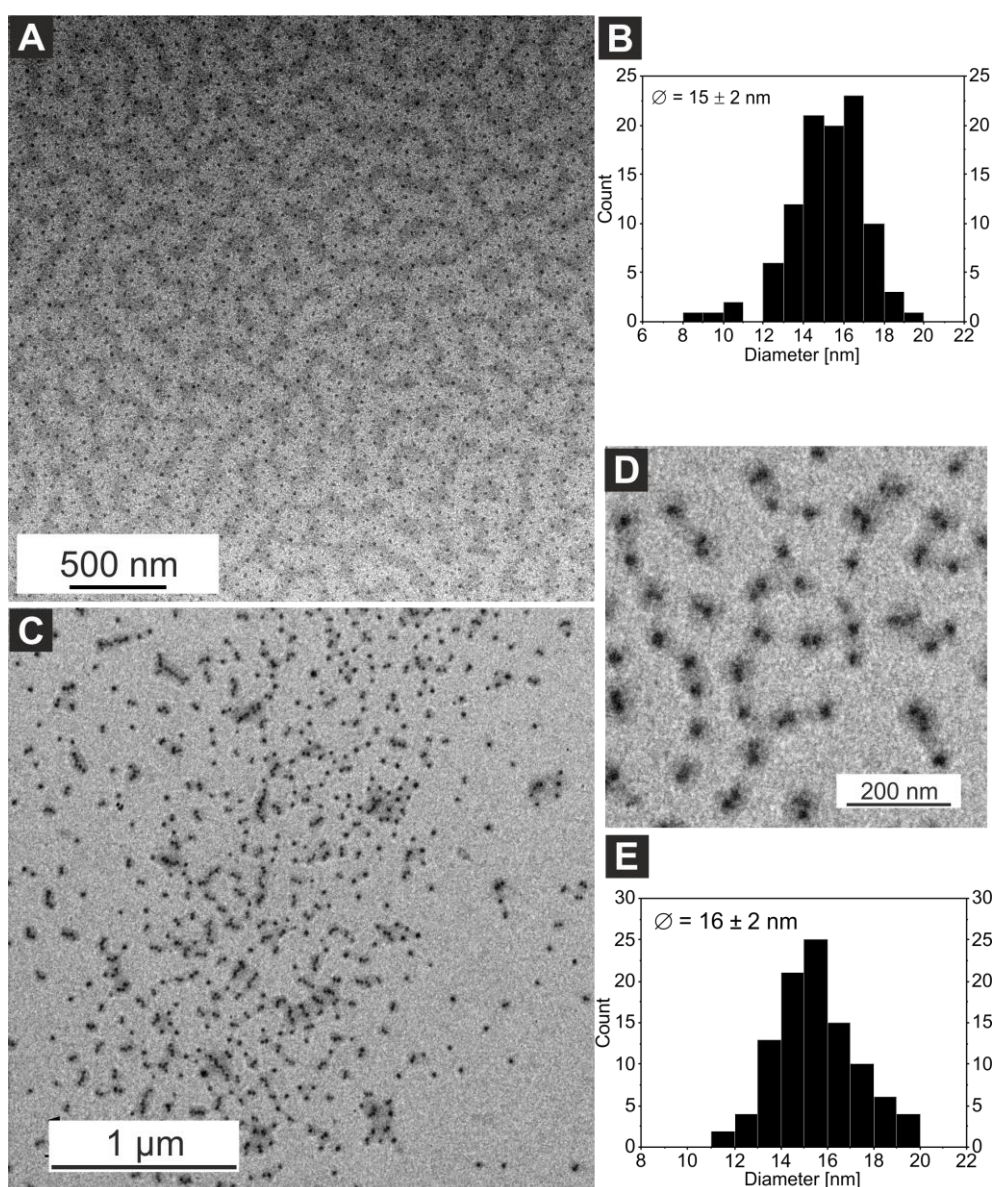
particles (Figure 1D). Cryo-TEM confirms the spherical shape of both the empty BCP micelle cores with a size of  $26 \pm 2$  nm (Figure 1C) as well as the composite nanoparticles with a size of  $34 \pm 5$  nm (Figure 1F).



**Figure 1:** Cryo-TEM image of the narrowly dispersed spherical BCP micelles (A) with the hydrodynamic diameter distribution determined by DLS (B) and the size distribution derived from the image (C). Cryo-TEM image of the narrowly dispersed spherical SCO CP-BCP particles (D) with the hydrodynamic diameter distribution determined by DLS (E) and the size distribution derived from the image (F). (Corresponding DLS autocorrelation functions of both samples can be found in Figure S3.)

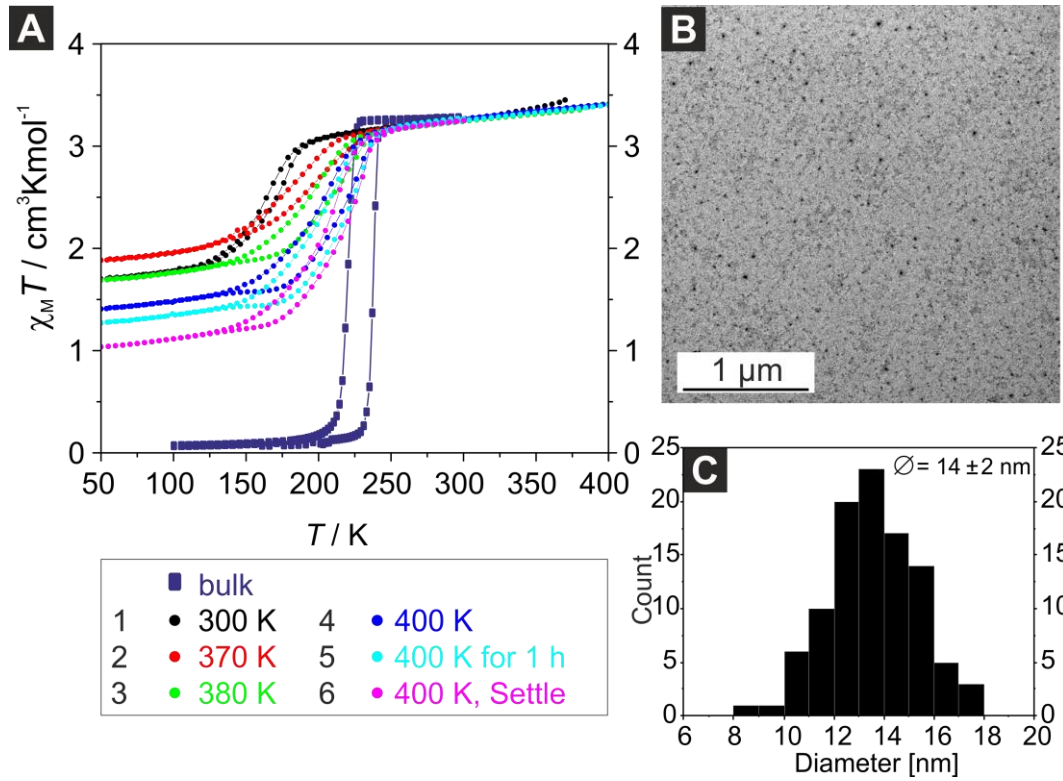


TEM measurements of the SCO CP-BCP composite particles in the dry state, clearly reveal the core-shell structure of the particles, with the dark appearing domains corresponding to the P4VP core containing the iron CP and the grey appearing domains to the PS block forming the shell (Figure 2C). For the size distribution of the particles only the core of the particles was measured and a core diameter of  $D_{\text{core}} = 16 \pm 2$  nm is obtained (Figure 2E), while the empty BCP micelle cores have a diameter of  $D_{\text{core}} = 15 \pm 2$  nm (Figure 2B). The coordination of the paramagnetic complex [FeL] to the P4VP units is also confirmed by the paramagnetic shift of the 4VP signals in the  $^1\text{H}$  NMR spectrum of the nanocomposite (Figure S11) compared to the pure BCP.



**Figure 2:** TEM image of the empty BCP micelles (A) with size distribution of the P4VP cores (B). TEM image of the narrowly dispersed SCO CP-BCP particles at low (C) and high (D) magnifications with size distribution of the SCO CP-BCP composite cores (E).

The magnetic properties of the SCO CP-BCP composite particles were analyzed using temperature-dependent magnetic measurements and Mössbauer spectroscopy. The room temperature Mössbauer spectrum of the composite allows to identify the different iron species that may occur during the synthesis and is given in Figure S4.<sup>[20]</sup> It shows one distinct doublet that can be attributed to a Fe<sup>II</sup> HS species. The doublet has an isomer shift  $\delta$  of 0.937(6) mm s<sup>-1</sup>, a quadrupole splitting  $\Delta E_Q$  of 2.177(13) mm s<sup>-1</sup> and a line width (HWHM) of 0.193(10) mm s<sup>-1</sup> that is characteristic for the CP [FeL(bipy)]<sub>n</sub>.<sup>[23]</sup> Figure 3 shows the  $\chi_M T$  vs.  $T$  plot for the sample measured in sweep and settle mode to investigate the effect of the BCP confinement and thermal annealing on the SCO properties of the CP. Different cooling and heating cycles were performed to trace the change of the spin transition regarding final  $\chi_M T$  values, transition temperature and hysteresis width. A pure Fe<sup>II</sup> HS compound of the used CP typically has a  $\chi_M T$  value of around 3.25 cm<sup>3</sup> K mol<sup>-1</sup> at 300 K. Since the Mössbauer spectrum shows that the compound is a pure HS Fe<sup>II</sup> species, the starting value of the as-synthesized product is adjusted to 3.25 cm<sup>3</sup> K mol<sup>-1</sup> at 300 K. All information on cooling and heating cycles performed on the SCO CP-BCP are summarized in Table 1. Upon cycle 1 (black curve, Figure 3A) down to 50 K the  $\chi_M T$  value stays approximately constant down to 200 K, where a rather gradual spin transition takes place with  $T_{1/2\downarrow} = 163$  K. The  $\chi_M T$  value drops to 1.70 cm<sup>3</sup> K mol<sup>-1</sup> at 50 K leaving around 52% of the Fe<sup>II</sup> centers in the HS state. Heating to 370 K reveals a 7 K wide hysteresis with  $T_{1/2\uparrow} = 170$  K. With cycles 2 to 5 the transition temperatures are shifted to higher temperatures, reaching  $T_{1/2\downarrow} = 200$  K and  $T_{1/2\uparrow} = 217$  K, while also lowering the  $\chi_M T$  values at 50 K down to 1.27 cm<sup>3</sup> K mol<sup>-1</sup> after cycle 5 (Table 1). Thus, the SCO is more complete after the annealing process revealing a molar fraction of high-spin molecules of  $\gamma_{HS} = 0.39$ . Although the CP is confined inside the micellar core, the hysteresis width of the SCO CP-BCP particles of 17 K is similar to the one of the bulk material (18 K). However, it is already known that a higher scan rate can lead to kinetic effects that broaden the hysteresis width.<sup>[6,26]</sup> These effects can be eliminated by using the settle mode because the effective scan rate is reduced, giving the system time to adapt to the changed temperature. Therefore, the final cooling and heating cycle 6 from 400 K to 50 K and back to 300 K is performed in settle mode to show that the change induced by the thermal treatment is persistent and the hysteresis is smaller in the composite particles (Figure 3A, pink). In fact, the transition is even more complete than the one measured in sweep mode with a  $\chi_M T$  value of 1.04 cm<sup>3</sup> K mol<sup>-1</sup> at 50 K ( $\gamma_{HS} = 0.32$ ). This is in good agreement with the expected HS fraction of  $\gamma_{HS} = 0.22$  for spherical 16 nm particles assuming that each iron center and the surrounding ligand occupies the space of 1 nm<sup>3</sup>. The hysteresis width is narrowed to 14 K with  $T_{1/2\downarrow} = 203$  K and  $T_{1/2\uparrow} = 217$  K (Table 1).



**Figure 3:** Magnetic susceptibility data for the SCO CP-BCP composite particles given as  $\chi_M T$  vs.  $T$  plot measured in sweep and settle mode (A). The colors represent different cooling and heating cycles as stated in the bottom left corner. For comparison, the results for the bulk material<sup>[25]</sup> are included as well. TEM image of the SCO CO-BCP particles after annealing showing no agglomeration or enlargement of the particles (B). Size distribution of the particles derived from the given TEM image (C).

**Table 1:** Data of the magnetic measurements for the different heating cycles. The measurement modes, transition temperatures, hysteresis widths and  $\chi_M T$  values are given.

#	Heating cycle [K]	Mode	$T_{1/2\downarrow}$ [K]	$T_{1/2\uparrow}$ [K]	Hysteresis width [K]	$\chi_M T$ at 50 K [ $\text{cm}^3 \text{K mol}^{-1}$ ]
1	300-50-370 <sup>[a]</sup>	sweep	163	170	7	1.70
2	370-50-380 <sup>[b]</sup>	sweep	179	192	13	1.88
3	380-50-400 <sup>[c]</sup>	sweep	192	207	15	1.69
4	400-50-400 <sup>[d]</sup>	sweep	198	215	17	1.40
5	400-50-300 <sup>[e]</sup>	sweep	200	217	17	1.27
6	300-50-300 <sup>[f]</sup>	settle	203	217	14	1.04

[a] Figure 3A, curve 1. [b] Figure 3A, curve 2. [c] Figure 3A, curve 3. [d] Figure 3A, curve 4. [e] Figure 3A, curve 5. [f] Figure 3A, curve 6.

Temperature-dependent Mössbauer spectra were used to confirm the results from the magnetic measurements, the results are summarized in Table 2 and Table S1 and in Figure S12. Please note that due to the long measurement times only settle measurements are possible and the thermal annealing was done at 393 K for 1 h leading to HS fractions more comparable to curve 3 or 4 in Figure 3 (see Table 2). Thermogravimetric analysis (TGA) of the sample before the annealing process shows no significant mass loss (relative loss around 0.1% until 100 °C, Figure S5). This indicates that a loss of residual solvent cannot be responsible for the improved SCO behavior.

**Table 2:** The molar fraction of high-spin molecules ( $\gamma_{\text{HS}}$ ) determined by Mössbauer spectroscopy (see Table S1) and magnetic susceptibility measurements (see Figure 3).

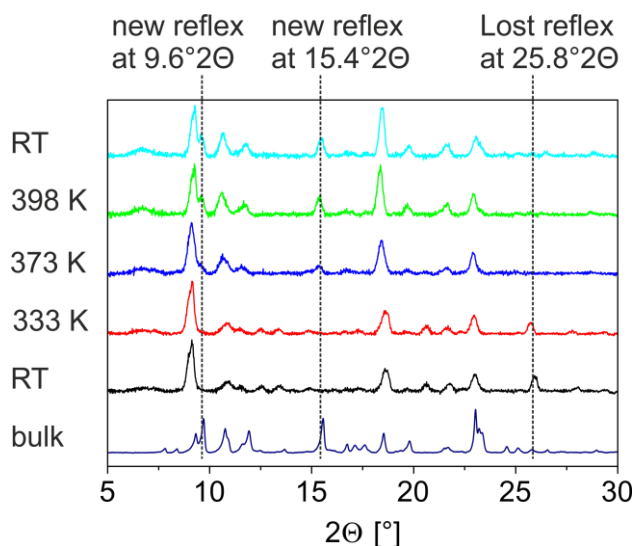
$T$ [K]	$\gamma_{\text{HS}}^{[\text{a}]}$	$\gamma_{\text{HS}}^{[\text{b}]}$	$\gamma_{\text{HS}}^{[\text{c}]}$	$\gamma_{\text{HS}}^{[\text{d}]}$	$\gamma_{\text{HS}}^{[\text{e}]}$
175 <sup>[f]</sup>	0.80	0.86	0.68	0.63	0.58
80	0.62	0.62	0.54	0.55	0.45
175 <sup>[g]</sup>	0.74	0.80	0.61	0.58	0.50

[a], [d] Values determined by Mössbauer spectroscopy before and after annealing, respectively. [b], [c], [e] Values determined by magnetic susceptibility measurements (Figure 3, curves “1”, “3”, and “4”, respectively). [f] Data recorded upon cooling. [g] Data recorded upon heating.

Moreover, the improved SCO behavior is also not a result of the formation of microcrystals or agglomerated particles due to the exposure to elevated temperatures as indicated by TEM and DLS measurements on the redispersed SCO CP-BCP particles taken after the magnetic measurement (Figure 3B and Figure S6). The TEM measurement of the sample after thermal annealing shows particles of similar size and shape compared to the ones before annealing with core sizes of  $14 \pm 2$  nm (Figure 3C). Consequently, DLS underlines that the composite particles are still intact after annealing with an average  $D_{\text{h}}$  of  $106 \pm 67$  nm (Figure S6). Further proof is given by SEM measurements that were performed before and after the annealing (Figure S7). No formation of microcrystals ( $>1$   $\mu\text{m}$ ) or larger nanoparticles was observed. SEM-EDX measurements show that the iron is homogeneously distributed throughout the sample.

Temperature-dependent powder X-ray diffraction (PXRD) was measured to follow any change in the crystallinity of the sample caused by the annealing process (Figure 4). The sample was heated stepwise from RT to 333 K, 373 K, and 398 K and then cooled down back to RT to follow a possible change on the diffraction pattern induced by the temperature increase and to show that the changes are persistent after the annealing process. It was found that new reflexes appear at  $9.6^\circ 2\theta$  and  $15.4^\circ 2\theta$  not before 373 K and remain when the sample was cooled down to RT. In contrast, a reflex at  $25.8^\circ 2\theta$  disappears at 373 K and above and remains absent back at RT. This

led to the conclusion that some sort of reorientation occurs inside the SCO CP-BCP composite particles at temperatures above the glass transition temperature of the PS ( $T_g(\text{PS}) = 383 \text{ K}$ , Figure S9). After heating, the diffraction pattern shows more similarity with the one of the bulk material.

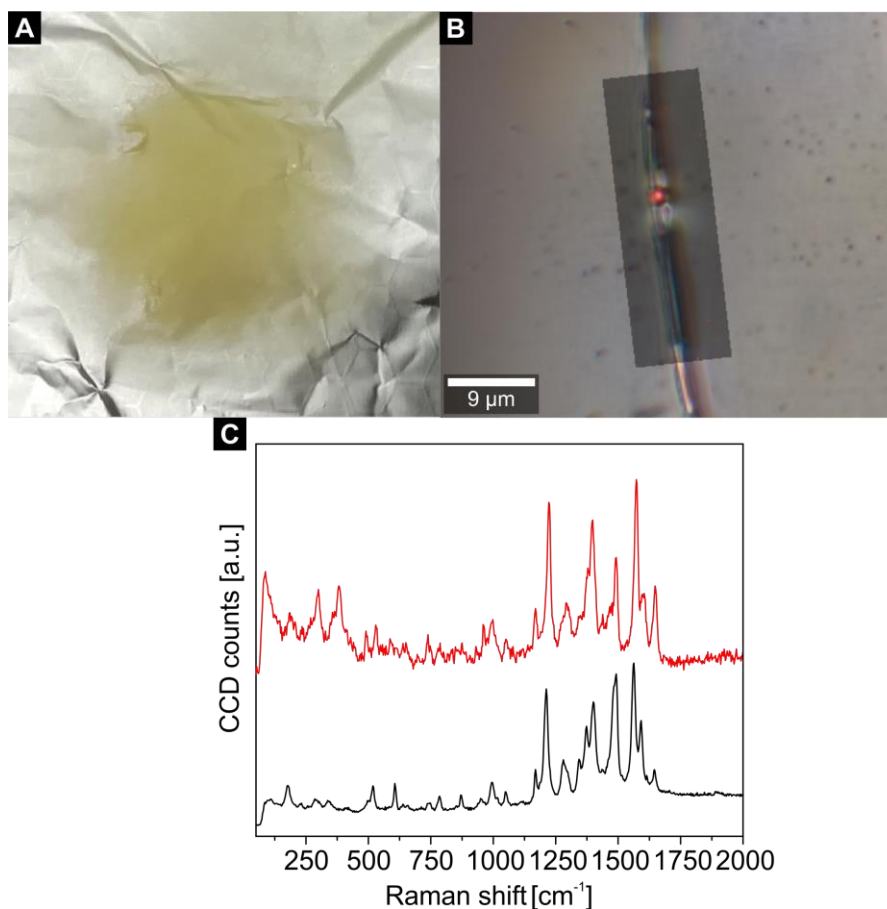


**Figure 4:** Temperature-dependent powder X-ray diffraction of the SCOCP-BCP composite particles.

The results indicate that by thermal treatment, especially when the composite particles are heated to and above  $T_g$  of the PS shell of 383 K, the crystallinity of the SCO CP inside the micellar core is improved because the PS chains become flexible, allowing the SCO CP to reorder inside the polymeric micelle.

The synthesized SCO CP-BCP particles can be used to prepare PS/SCO CP composite fibers by electrospinning, a widely used technique employed for the production of polymer fibers of various shapes and properties.<sup>[27]</sup> Figure 5A shows PS/SCO CP composite fibers, which were spun from a mixture of PS ( $M_n = 97\,000 \text{ g mol}^{-1}$ ,  $D = 1.02$ ) and SCO CP-BCP particles in THF on aluminum foil (details on electrospinning can be found in the SI). The obtained color is typical for iron complexes of this ligand type, however, probably due to the remaining HS fraction, no significant color change upon cooling was observed. The presence of the SCO complex particles in the fibers was confirmed by Raman imaging (Figure 5B,C). A very low laser power of 0.1 mW was employed, where only the SCO complex shows a Raman signal and, thus, a selective detection of the SCO complex in the composite fibers is possible. The overlay of the digital photograph with the Raman image clearly confirms the presence of the SCO complex (colored in red, Figure 5B) in the fibers. Moreover, the

Raman spectra of the SCO complex in the neat SCO CP-BCP particles and in the composite fibers are identical, showing that electrospinning does not alter the structure of the SCO complex.



**Figure 5:** Digital photograph of electrospun PS/SCO CP composite fibers on aluminum foil (A), digital photograph of a single fiber overlaid with the color-coded 2D Raman image (B) and corresponding Raman spectra (C) of the SCO CP in the BCP micelles (black) and in PS fibers (red). As the SCO CP crystals in the micellar core are strong Raman scatterers, Raman imaging with a very low laser intensity of 0.1 mW allows a selective detection of the SCO CP particles in the composite fibers. Under these conditions PS shows no Raman signal.

### 7.3. Conclusion

In conclusion, we have shown that the transition temperature of the SCO CP-BCP [FeL(bipy)]<sub>n</sub> can be shifted gradually by thermal annealing. Starting with the as-synthesized product and the transition temperatures  $T_{1/2\downarrow}$  and  $T_{1/2\uparrow}$  of 163 K and 170 K respectively, the transition temperature is shifted 40 K to higher temperatures to reach its final state after several annealing steps with  $T_{1/2\downarrow} = 203$  K and  $T_{1/2\uparrow} = 217$  K. Furthermore, the hysteresis width is also broadened by the annealing process from 6 K (sweep) for the as-synthesized product to 17 K (sweep) for the annealed product. The subsequent susceptibility measurement in settle mode showed that the



change in the transition temperature is persistent with a hysteresis width of 14 K and an improved completeness of the spin transition from  $\gamma_{\text{HS}} = 0.52$  to  $\gamma_{\text{HS}} = 0.32$ . Magnetic susceptibility, TGA and temperature-dependent PXRD data support the assumption that the transition temperature change is a consequence of the thermal annealing and recrystallization instead of a solvent loss of the sample or particle agglomeration. The demonstrated approach is potentially applicable to other polymeric SCO systems and offers an approach to fine-tune the transition temperatures by different polymer shells. It will be especially interesting to explore other linear polymers, such as the triazole-based systems that, with the methods used so far, often show stable hysteresis loops down to very small particle sizes.<sup>[13,19,20,22,28]</sup> The question arises if the different NP synthesis approaches (interaction with the polymer shell vs. surfactant) or differences in the SCO complexes (steric demand of the ligands, intermolecular interactions responsible of the observation of the hysteresis) are relevant factors. With regard to the relatively high remaining HS fraction observed, this can be clearly denoted to the ligand system, with the more bulky Schiff base-like ligands compared to the triazoles leading to a higher fraction of complexes on the surface not undergoing SCO. Thus, an increase in particle size should lead to a reduction of the remaining HS fraction. With the still relatively limited data available, the other questions can so far not be answered satisfactorily and are still under investigation. Furthermore, the SCO CP-BCP composite particles are suitable for polymer processing techniques, such as electrospinning, employing a mixture with PS as fiber-forming matrix.

### 7.4. Acknowledgements

Financial support of the University of Bayreuth and the SFB 840 (TP A10 and A2) is gratefully acknowledged. C.G. and C.H. were supported by the BayNAT program of the University of Bayreuth graduate school. We thank Dr. Jana Timm and Prof. Dr. Roland Marschall (Physikalische Chemie III, UBT) for their contribution to the temperature-dependent PXRD measurement and Dr. Wolfgang Milius (Anorganische Chemie I, UBT) for the measurement itself. We also thank Rika Schneider (Makromolekulare Chemie II, UBT) for DSC, GPC and NMR measurements of the BCP, Marco Schwarzmann (Anorganische Chemie I, UBT) for TGA and Dr. Christine Denner (Anorganische Chemie II, UBT) for SEM and SEM-EDX measurements. D.B. thanks Prof. Dr. F. J. Litterst (Institut für Physik der Kondensierten Materie) at TU Braunschweig for providing access to the  $^{57}\text{Fe}$  Mössbauer spectrometer.

## 7.5. Conflict of interest

The authors declare no conflict of interest.

## 7.6. References

- [1] a) E. Coronado, *Nat. Rev. Mater.* **2019**, *24*, 834; b) K. Senthil Kumar, M. Ruben, *Coord. Chem. Rev.* **2017**, *346*, 176; c) K. Otsubo, T. Haraguchi, H. Kitagawa, *Coord. Chem. Rev.* **2017**, *346*, 123; d) P. N. Martinho, C. Rajnak, M. Ruben in *Spin-Crossover Materials* (Ed.: M. A. Halcrow), Wiley, Chichester, **2013**, pp. 375–404; e) M. Sindoro, N. Yanai, A.-Y. Jee, S. Granick, *Acc. Chem. Res.* **2014**, *47*, 459; f) E. A. Flügel, A. Ranft, F. Haase, B. V. Lotsch, *J. Mater. Chem.* **2012**, *22*, 10119.
- [2] a) M.-L. Boillot, B. Weber, *C. R. Chim.* **2018**, *21*, 1196; b) P. G. Lacroix, I. Malfant, C. Lepetit, *Coord. Chem. Rev.* **2016**, *308*, 381; c) A. B. Gaspar, M. Seredyuk, *Coord. Chem. Rev.* **2014**, *268*, 41; d) *Spin-Crossover Materials* (Ed.: M. A. Halcrow), Wiley, Chichester, **2013**; e) D. J. Harding in *Advanced Nanomaterials* (Eds.: E. Rentschler, N. Domracheva, M. Caporali), Elsevier, Amsterdam, **2018**, pp. 401–426.
- [3] A. B. Gaspar, B. Weber in *Molecular Magnetic Materials* (Eds.: B. Sieklucka, D. Pinkowicz), Wiley-VCH, Weinheim, **2017**, pp. 231–252.
- [4] Z.-P. Ni, J.-L. Liu, M. N. Hoque, W. Liu, J.-Y. Li, Y.-C. Chen, M.-L. Tong, *Coord. Chem. Rev.* **2017**, *335*, 28.
- [5] D. J. Harding, P. Harding, W. Phonsri, *Coord. Chem. Rev.* **2016**, *313*, 38.
- [6] S. Brooker, *Chem. Soc. Rev.* **2015**, *44*, 2880.
- [7] a) P. Gülich, A. Hauser, H. Spiering, *Angew. Chem. Int. Ed. Engl.* **1994**, *33*, 2024; *Angew. Chem.* **1994**, *106*, 2109; b) *Topics in Current Chemistry, Vol. 233–235* (Eds.: P. Gülich, H. A. Goodwin), Springer Berlin/Heidelberg, Berlin, **2004**.
- [8] a) E. Coronado, M. Giménez-Marqués, G. Mínguez Espallargas, F. Rey, I. J. Vitórica-Yrezábal, *J. Am. Chem. Soc.* **2013**, *135*, 15986; b) M. Ohba, K. Yoneda, G. Agustí, M. C. Muñoz, A. B. Gaspar, J. A. Real, M. Yamasaki, H. Ando, Y. Nakao, S. Sakaki, et al., *Angew. Chem. Int. Ed.* **2009**, *48*, 4767; *Angew. Chem.* **2009**, *121*, 4861; c) P. D. Southon, L. Liu, E. A. Fellows, D. J. Price, G. J. Halder, K. W. Chapman, B. Moubaraki, K. S. Murray, J.-F. Létard, C. J. Kepert, *J. Am. Chem. Soc.* **2009**, *131*, 10998.



- 
- [9] a) F. J. Valverde-Muñoz, M. C. Muñoz, S. Ferrer, C. Bartual-Murgui, J. A. Real, *Inorg. Chem.* **2018**, *57*, 12195; b) M. Attwood, H. Akutsu, L. Martin, D. Cruickshank, S. S. Turner, *Dalton Trans.* **2019**, *48*, 90; c) E. Collet, P. Guionneau, *C. R. Chim.* **2018**, *21*, 1133.
- [10] a) H.-Y. Wang, J.-Y. Ge, C. Hua, C.-Q. Jiao, Y. Wu, C. F. Leong, D. M. D'Alessandro, T. Liu, J.-L. Zuo, *Angew. Chem. Int. Ed.* **2017**, *56*, 5465; *Angew. Chem.* **2017**, *129*, 5557; b) Y.-C. Chen, Y. Meng, Z.-P. Ni, M.-L. Tong, *J. Mater. Chem. C* **2015**, *3*, 945; c) Y.-S. Koo, J. R. Galán-Mascarós, *Adv. Mater.* **2014**, *26*, 6785; d) T. G. Gopakumar, F. Matino, H. Naggert, A. Bannwarth, F. Tuczek, R. Berndt, *Angew. Chem. Int. Ed.* **2012**, *51*, 6262; *Angew. Chem.* **2012**, *124*, 6367.
- [11] a) C. Lochenie, K. Schötz, F. Panzer, H. Kurz, B. Maier, F. Puchtler, S. Agarwal, A. Köhler, B. Weber, *J. Am. Chem. Soc.* **2018**, *140*, 700; b) B. Schäfer, T. Bauer, I. Faus, J. A. Wolny, F. Dahms, O. Fuhr, S. Lebedkin, H.-C. Wille, K. Schlage, K. Chevalier, et al., *Dalton Trans.* **2017**, *46*, 2289; c) I. Suleimanov, O. Kraieva, J. Sánchez Costa, I. O. Fritsky, G. Molnár, L. Salmon, A. Bousseksou, *J. Mater. Chem. C* **2015**, *3*, 5026; d) C.-F. Wang, R.-F. Li, X.-Y. Chen, R.-J. Wei, L.-S. Zheng, J. Tao, *Angew. Chem. Int. Ed.* **2015**, *54*, 1574; *Angew. Chem.* **2015**, *127*, 1594; e) I. Suleimanov, O. Kraieva, G. Molnár, L. Salmon, A. Bousseksou, *Chem. Commun.* **2015**, *51*, 15098.
- [12] a) R. G. Miller, S. Brooker, *Chem. Sci.* **2016**, *7*, 2501; b) O. Kraieva, C. M. Quintero, I. Suleimanov, E. M. Hernandez, D. Lagrange, L. Salmon, W. Nicolazzi, G. Molnár, C. Bergaud, A. Bousseksou, *Small* **2016**, *12*, 6325; c) J. Huang, R. Xie, W. Wang, Q. Li, J. Yang, *Nanoscale* **2016**, *8*, 609; d) J. Dugay, M. Aarts, M. Giménez-Marqués, T. Kozlova, H. W. Zandbergen, E. Coronado, H. S. J. van der Zant, *Nano Lett.* **2017**, *17*, 186; e) M. Bernien, H. Naggert, L. M. Arruda, L. Kipgen, F. Nickel, J. Miguel, C. F. Hermanns, A. Krüger, D. Krüger, E. Schierle, et al., *ACS Nano* **2015**, *9*, 8960; f) G. Molnár, L. Salmon, W. Nicolazzi, F. Terki, A. Bousseksou, *J. Mater. Chem. C* **2014**, *2*, 1360; g) L. Salmon, L. Catala, *C. R. Chim.* **2018**, *21*, 1230.
- [13] E. Coronado, J. R. Galán-Mascarós, M. Monrabal-Capilla, J. García-Martínez, P. Pardo-Ibáñez, *Adv. Mater.* **2007**, *19*, 1359.
- [14] a) H. Peng, S. Tricard, G. Félix, G. Molnár, W. Nicolazzi, L. Salmon, A. Bousseksou, *Angew. Chem. Int. Ed.* **2014**, *53*, 10894; *Angew. Chem.* **2014**, *126*, 11074; b) F. Volatron, L. Catala, E. Rivière, A. Gloter, O. Stéphan, T. Mallah, *Inorg. Chem.* **2008**, *47*, 6584.
- [15] J. R. Galán-Mascarós, E. Coronado, A. Forment-Aliaga, M. Monrabal-Capilla, E. Pinilla-Cienfuegos, M. Ceolin, *Inorg. Chem.* **2010**, *49*, 5706.
- [16] Y. Raza, F. Volatron, S. Moldovan, O. Ersen, V. Huc, C. Martini, F. Brisset, A. Gloter, O. Stephan, A. Bousseksou, et al., *Chem. Commun.* **2011**, *47*, 11501.
-

- [17] M. Giménez-Marqués, M. L. García-Sanz de Larrea, E. Coronado, *J. Mater. Chem. C* **2015**, *3*, 7946.
- [18] G. Félix, W. Nicolazzi, L. Salmon, G. Molnár, M. Perrier, G. Maurin, J. Larionova, J. Long, Y. Guari, A. Bousseksou, *Phys. Rev. Lett.* **2013**, *110*, 235701.
- [19] R. Torres-Cavanillas, L. Lima-Moya, F. D. Tichelaar, H. W. Zandbergen, D. M. Giménez Marqués, E. Coronado, *ChemRxiv* **2019**, <https://doi.org/10.26434/chemrxiv.7613984.v1>.
- [20] C. Bartual-Murgui, E. Natividad, O. Roubeau, *J. Mater. Chem. C* **2015**, *3*, 7916.
- [21] D. Tanaka, N. Aketa, H. Tanaka, S. Horike, M. Fukumori, T. Tamaki, T. Inose, T. Akai, H. Toyama, O. Sakata, et al., *Dalton Trans.* **2019**, *48*, 7074.
- [22] J. M. Herrera, S. Titos-Padilla, S. J. A. Pope, I. Berlanga, F. Zamora, J. J. Delgado, K. V. Kamenev, X. Wang, A. Prescimone, E. K. Brechin, E. Colacio, *J. Mater. Chem. C* **2015**, *3*, 7819.
- [23] O. Klimm, C. Göbel, S. Rosenfeldt, F. Puchtler, N. Miyajima, K. Marquardt, M. Drechsler, J. Breu, S. Förster, B. Weber, *Nanoscale* **2016**, *8*, 19058.
- [24] a) B. Weber, *Chem. Eur. J.* **2017**, *23*, 18093; b) C. Göbel, O. Klimm, F. Puchtler, S. Rosenfeldt, S. Förster, B. Weber, *Beilstein J. Nanotechnol.* **2017**, *8*, 1318.
- [25] a) B. Weber, R. Tandon, D. Himsl, *Z. Anorg. Allg. Chem.* **2007**, *633*, 1159; b) B. Weber, E. S. Kaps, C. Desplanches, J.-F. Létard, *Eur. J. Inorg. Chem.* **2008**, 2963.
- [26] a) J. Weihermüller, S. Schlamp, B. Dittrich, B. Weber, *Inorg. Chem.* **2019**, *58*, 1278; b) S. Schönfeld, C. Lochenie, P. Thoma, B. Weber, *CrystEngComm* **2015**, *17*, 5389.
- [27] a) S. Agarwal, A. Greiner, J. H. Wendorff, *Prog. Polym. Sci.* **2013**, *38*, 963; b) A. Greiner, J. H. Wendorff, *Angew. Chem. Int. Ed.* **2007**, *46*, 5670; *Angew. Chem.* **2007**, *119*, 5770.
- [28] a) T. Forestier, S. Mornet, N. Daro, T. Nishihara, S.-i. Mouri, K. Tanaka, O. Fouche, E. Freysz, J.-F. Létard, *Chem. Commun.* **2008**, 4327; b) T. Forestier, A. Kaiba, S. Pechev, D. Denux, P. Guionneau, C. Etrillard, N. Daro, E. Freysz, J.-F. Létard, *Chem. Eur. J.* **2009**, *15*, 6122; c) A. Tokarev, L. Salmon, Y. Guari, W. Nicolazzi, G. Molnár, A. Bousseksou, *Chem. Commun.* **2010**, 46, 8011.

## **7.7. Supporting Information**

### **7.7.1. Table of Contents**

General Procedures

Synthesis Procedures

Synthesis of the BCP S<sub>85</sub>V<sub>15</sub><sup>154</sup>

Synthesis of the SCO CP-BCP composite

Electrospinning

Characterization

Raman

IR

DLS autocorrelation functions of the empty BCP micelles and the SCO CP-BCP composite particles

Mössbauer spectroscopy of the SCO CP-BCP composite particles

TGA of the SCO CP-BCP composite particles

DLS of the SCO CP-BCP composite particles after annealing

SEM and SEM-EDX of the SCO CP-BCP composite particles before and after annealing

DSC of the BCP

GPC of the BCP

NMR of the BCP

### 7.7.2. General Procedures

**Materials:** All SCO CP-BCP syntheses were performed under inert conditions using argon 5.0 (purity  $\geq 99,999\%$ ) using Schlenk tube technique. The synthesis of the sample was repeated at least twice. Tetrahydrofuran (THF, Fischer Scientific,  $\geq 99.8\%$ ) for anionic polymerization was purified by successive distillation over calcium hydride ( $\text{CaH}_2$ , Merck) and potassium (K, Sigma-Aldrich) under  $\text{N}_2$  atmosphere. Styrene (S, Sigma-Aldrich,  $> 99\%$ ) was purified over dibutyl magnesium ( $\text{Bu}_2\text{Mg}$ , Sigma-Aldrich, 1M in heptane) and 4-vinylpyridine (4VP, Acros Organics, 95%) over triethyl aluminum ( $\text{Et}_3\text{Al}$ , Sigma-Aldrich, 1M in heptane), respectively, followed by condensing into storage ampoules. 1,1-Diphenylethylene (DPE, Acros Organics, 98%) was purified by addition of sec-butyl lithium (sec-BuLi, Acros Organics, 1.3M in cyclohexane/hexane 92/8) and subsequent distillation. 4,4'-bipyridine was obtained from Alfa Aesar and used as received. THF p.a. for the SCO synthesis was obtained from Bernd Kraft and degassed with argon for at least 30 min.  $[\text{FeL}(\text{MeOH})_2]$  was synthesized as described before.<sup>[1]</sup> THF for electrospinning (THF,  $\geq 99.8\%$ , Fisher Chemical, degassed with argon and consecutive freeze-pump-thaw cycles), polystyrene for electrospinning (PS,  $M_n = 97\,000\text{ g mol}^{-1}$ ,  $D = 1.02$ , synthesized by anionic polymerization and reprecipitated from MeOH).

**Transmission electron microscopy** (TEM) was taken at a Zeiss CEM902 electron microscope (Zeiss, Oberkochen, Germany) and a JEOL 2200FS electron microscope. Samples were dissolved in THF. The solution was dropped on a carbon coated copper grid (mesh 200, Science Services, Munich). Electron acceleration voltage was set to 80 kV (CEM902) and 200 kV (JEOL 2200FS). Micrographs were taken with a MegaView III / iTEM image acquiring and processing system from Olympus Soft Imaging Systems (OSIS, Münster, Germany) and an Orius 830 SC200W / DigitalMicrograph system from Gatan (Munich, Germany). Particles size measurements were done with "ImageJ" image processing software developed by Wayne Rasband (National Institutes of Health, USA).

**Dynamic light scattering** (DLS) measurements were done at an AntonPaar Litesizer 500 in quartz glass cuvettes from Helma at 25 °C. One measurement consists of six consecutive runs.

Temperature-dependent **powder X-ray diffraction** ( $T$ -PXRD) pattern were recorded using a Bragg-Brentano type diffractometer (X'PERT-Pro, PANalytical with  $\text{CuK}\alpha$ -radiation ( $\lambda = 1.541\text{ \AA}$ ), equipped with a secondary monochromator to suppress fluorescence. The sample was placed on a flat surface in a flowing nitrogen atmosphere in an XRD chamber during the measurement.

**Magnetic susceptibility** measurements were performed at a Quantum Design MPMS-XL-5 SQUID magnetometer. Field strength of 3 T was applied and a temperature range of 50 – 400 K was used to determine the temperature dependency of the magnetism and the spin crossover behavior.

---

Sweep mode was used for the five cycles with a cooling and heating rate of 5 K min<sup>-1</sup>. The final measurement was performed in settle mode with a cooling and heating rate of 5 K min<sup>-1</sup> between 50 K and 300 K. The samples were prepared in gelatin capsules placed in a plastic straw. The measured values were corrected for the diamagnetism of the sample holder, the polymer matrix (measured values) and the ligand (tabulated Pascal constants).

The room temperature <sup>57</sup>Fe **Mössbauer** spectrum was recorded in transmission geometry with constant acceleration using a conventional Mössbauer spectrometer with a 50 mCi <sup>57</sup>Co(Rh) source. The samples were sealed in the sample holder in an argon atmosphere. The spectra were fitted using Recoil 1.05 Mössbauer Analysis Software.<sup>[2]</sup> The isomer shift values are given with respect to a  $\alpha$ -Fe reference at room temperature.

Additional zero-field <sup>57</sup>Fe Mössbauer measurements on polycrystalline powders of SCO CP-BCP were also conducted at variable temperatures between  $T = 80$  and 300 K. A conventional transmission spectrometer with sinusoidal velocity sweep and a CryoVac continuous-flow cryostat were used for these measurements. After positioning the sample container, the sample chamber was evacuated, flushed five times with nitrogen gas, and kept at ca. 50 – 100 mbar during the measurement. The temperature was measured with a calibrated silicon diode located close to the sample container, providing a temperature stability of better than 0.1 K. The nominal activity of the <sup>57</sup>Fe Mössbauer source used was 50 mCi of <sup>57</sup>Co in a rhodium matrix, stored at ambient temperatures during the measurement. Velocity calibration was done with an  $\alpha$ -iron foil at ambient temperature and the minimum experimental line width (FWHM) was < 0.24 mm s<sup>-1</sup>. Isomer shifts ( $\delta$ ) were specified relative to metallic iron at room temperature but were not corrected in terms of the second-order Doppler shift. The spectra were analyzed by least-square fits using doublets of Lorentzian lines utilizing the software package NORMOS.<sup>[3]</sup>

Carbon, nitrogen and hydrogen contents were collected at a Vario EL III with acetanilide as standard. The samples were placed in tin boats and measured at least twice. The average of the measurements was used.

Transmission **infrared** (IR) spectra were collected from a Perkin Elmer Spectrum 100 FT-IR (ATR). The samples were measured directly as solids.

**Raman** spectra were recorded with a confocal WITec Alpha 300 RA+ Raman microscope equipped with a UHTS 300 spectrometer and a back-illuminated Andor Newton 970 EMCCD camera. A frequency-doubled Nd-YAG laser with a wavelength of  $\lambda = 532$  nm was used as the excitation source. All measurements were conducted using a 50  $\times$  long working distance (NA = 0.7, lateral resolution ca. 500 nm) Zeiss objective. The laser power used was 0.1 mW for the neat SCO CP crystals as well as the SCO CP-BCP particles and 10 mW for the neat S<sub>85</sub>V<sub>15</sub><sup>154</sup> diblock copolymer,

respectively. The instrument was operated by the integrated Witec Control Five software (version 5.1). All spectra were subjected to a cosmic ray removal routine and baseline correction using Witec Project Five software (version 5.1).

**Thermogravimetric analysis** (TGA) was performed on a Netzsch TG 209F1 Libra under nitrogen. The samples were heated from 25-600 °C at a heating rate of 10 K min<sup>-1</sup>.

For **gel permeation chromatography** (GPC) in N,N-dimethylformamide (DMF) with lithium bromide (5 g L<sup>-1</sup>), GRAM columns (300 x 8 mm, 10 µm particle size, PSS Mainz) with 100 and 3000 Å pore sizes were used. The sample was measured on a SEC 1260 Infinity system (Agilent Technologies) at a flow rate of 0.5 mL min<sup>-1</sup> at 23 °C, using a refractive index detector (Agilent Technologies). The calibration was done with narrowly distributed polystyrene standards (PSS calibration kit) and toluene (HPLC grade) was used as internal standard.

**MALDI-ToF MS** (matrix-assisted laser desorption/ionization time-of-flight mass spectrometry) measurements were performed on a Reflex III (Bruker) equipped with a N<sub>2</sub> laser ( $\lambda$  = 337 nm). An acceleration voltage of 20 kV was used in linear mode and the samples were prepared according to the dried droplet method. Therefore, matrix (trans-2-[3-(4-tert-butylphenyl)-2-methyl-2-propenylidene]malononitrile (DCTB), 10 g L<sup>-1</sup> in THF), analyte (10 g L<sup>-1</sup> in THF) and salt (silver trifluoroacetate, 10 g L<sup>-1</sup>) were dissolved and mixed in the ratio of 20 : 5 : 1 and 0.5 µL of the mixture was placed and dried on the target plate.

**<sup>1</sup>H-NMR** spectra were acquired with a Bruker Ultrashield 300 spectrometer using CDCl<sub>3</sub> as solvent.

For **cryo transmission electron microscopy** studies, a sample droplet of 2 µL was put on a lacey carbon filmed copper grid (Science Services, Munich, Germany). Subsequently, most of the liquid was removed with blotting paper leaving a thin film stretched over the lace holes. The specimens were instantly shock frozen by rapid immersion into liquid nitrogen cooled to approximately 90 K in a temperature-controlled freezing unit (Zeiss Cryobox, Carl Zeiss Microscopy GmbH, Jena, Germany). The temperature was monitored and kept constant in the chamber during all the sample preparation steps. The specimen was inserted into a cryotransfer holder (CT3500, Gatan, Munich, Germany) and transferred to a Zeiss / LEO EM922 Omega EFTEM (Zeiss Microscopy GmbH, Jena, Germany). Examinations were carried out at temperatures around 90 K. The TEM was operated at an acceleration voltage of 200 kV. Zero-loss filtered images (DE = 0 eV) were taken under reduced dose conditions (100 – 1000 e/nm<sup>2</sup>). All images were registered digitally by a bottom mounted CCD camera system (Ultrascan 1000, Gatan, Munich, Germany) combined and processed with a digital imaging processing system (Digital Micrograph GMS 1.9, Gatan, Munich, Germany).

The **differential scanning calorimetry** (DSC) measurements were performed on a Phoenix 204 F1 (Netzsch) under nitrogen atmosphere, using aluminum crucibles (temperature range: 20 – 200 °C, scanning rates: 10, 20 and 30 K min<sup>-1</sup>).

**Scanning electron microscopy** (SEM) micrographs were taken on a Zeiss LEO 1530 GEMINI. The acceleration voltage was set to 3 kV and the sample was sputter-coated with a 1.3 nm platinum layer. Scanning electron microscopy – energy dispersive X-Ray spectroscopy (SEM-EDX) were performed on the same device with an acceleration voltage of 15 kV.

### 7.7.3. Synthesis Procedures

#### Synthesis of the BCP S<sub>85</sub>V<sub>15</sub><sup>154</sup>

The PS-*b*-P4VP diblock copolymer (S<sub>85</sub>V<sub>15</sub><sup>154</sup>, ratio PS/P4VP = 85/15 (w/w),  $M_n = 154\,000\text{ g mol}^{-1}$ ,  $\bar{D} = 1.02$  (DMF-GPC)) was synthesized by sequential living anionic polymerization in THF using a laboratory autoclave (1 L, Büchi AG). Styrene was polymerized first for 30 min using *sec*-BuLi as initiator at -80 °C. After complete conversion of styrene a sample was taken for GPC and MALDI-ToF analyses. Subsequently, 1,1-diphenylethylene was added to the living polystyryllithium (equimolar amount to initiator), followed by the addition of 4-vinylpyridine (4VP). After 4 h the polymerization was terminated with degassed methanol followed by precipitation in deionized water to isolate the diblock copolymer. The molecular weight of the PS-*b*-P4VP diblock copolymer was determined from <sup>1</sup>H-NMR (CDCl<sub>3</sub>, Figure S10), employing the absolute molecular weight of the PS precursor obtained by MALDI-ToF MS ( $M_n$  (PS) = 131 000 g mol<sup>-1</sup>) for signal calibration.

#### Synthesis of the SCO CP-BCP composite

50 mg S<sub>85</sub>V<sub>15</sub><sup>154</sup> and 6.7 mg (15 μmol) [FeL(MeOH)<sub>2</sub>] were dissolved in 20 mL THF in a 50 mL Schlenk flask. The solution was refluxed for 2 h. After cooling, 5.9 mg (37.5 μmol, 2.5 eq) 4,4'-bipyridine was added and the solution refluxed again for 1 h. After a short cool down to RT, 6.7 mg (15 μmol) [FeL(MeOH)<sub>2</sub>] and 5.9 mg (37.5 μmol, 2.5 eq) 4,4'-bipyridine were added simultaneously and the solution was refluxed again for 1 h. The simultaneous addition of the reactants and the subsequent reflux of the solution were repeated three more times. In total, 33.5 mg [FeL(MeOH)<sub>2</sub>] and 29.5 mg 4,4'-bipyridine were added to the 50 mg polymer. Consecutively, the solvent was removed by cold distillation and the resulting dark brown polymeric solid was dried in vacuo. Elemental anal. (%) found: C 67.06, H 6.59, N 5.85.

#### Electrospinning

For the preparation of PS/SCO CP composite fibers the SCO CP-BCP particles were dispersed in degassed THF (2.5 g L<sup>-1</sup>), followed by the addition of PS (19 wt%). The fibers were spun on a

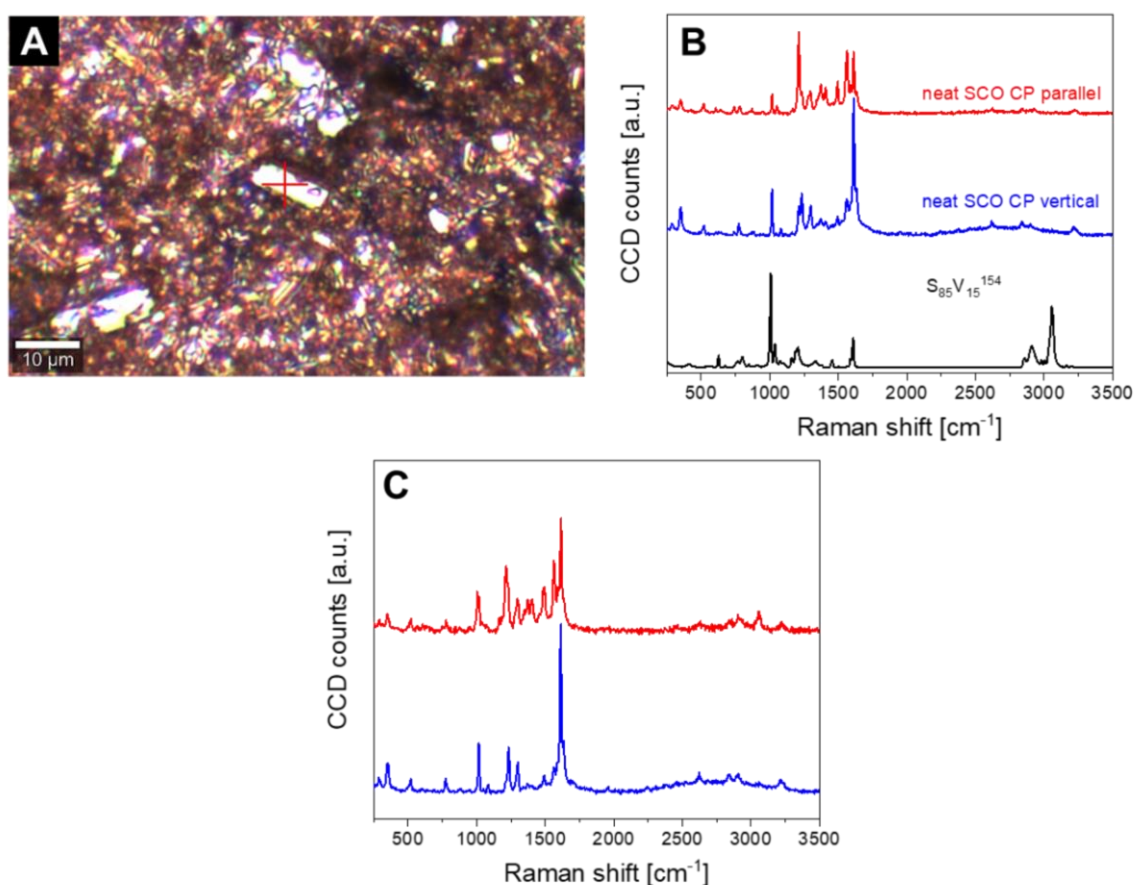
---

rotating disk collector ( $D = 13$  cm, 60 rpm) placed at a distance of 11 cm from the stainless-steel needle ( $d = 0.90$  mm) at a temperature of  $21.7^\circ\text{C}$  and a relative humidity of ca. 30%. For electrospinning, a high voltage of 10.5 kV at the needle and -1.0 kV at the collector were applied. The feed rate of the solution was  $1.2\text{ mL h}^{-1}$ .

#### 7.7.4. Characterization

##### Raman

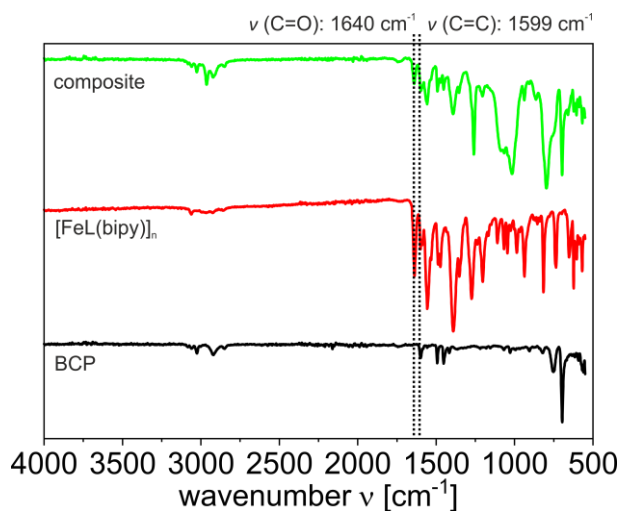
**Figure S1:** A) Digital photograph of neat SCO CP crystals, the position for Raman measurements is indicated by a red cross. B) Raman spectra of the neat  $\text{S}_{85}\text{V}_{15}^{154}$  diblock copolymer and the neat SCO CP with polarization of the excitation laser parallel (red) and vertical (blue) to the long axis of the SCO CP crystal shown in A). C) Raman spectra of SCO CP-BCP particles taken at different positions, showing identical Raman spectra with respect to that observed for the neat SCO CP crystals. The spectra in B) and C) were shifted vertically for a better comparison. The neat SCO CP crystals are strong Raman scatterers, which allows measurements at very low laser intensities of 0.1 mW. Under these conditions the neat  $\text{S}_{85}\text{V}_{15}^{154}$  diblock copolymer gives almost no Raman signals. Thus, for the SCO CP-BCP particles only Raman bands attributable to the SCO CP are visible.





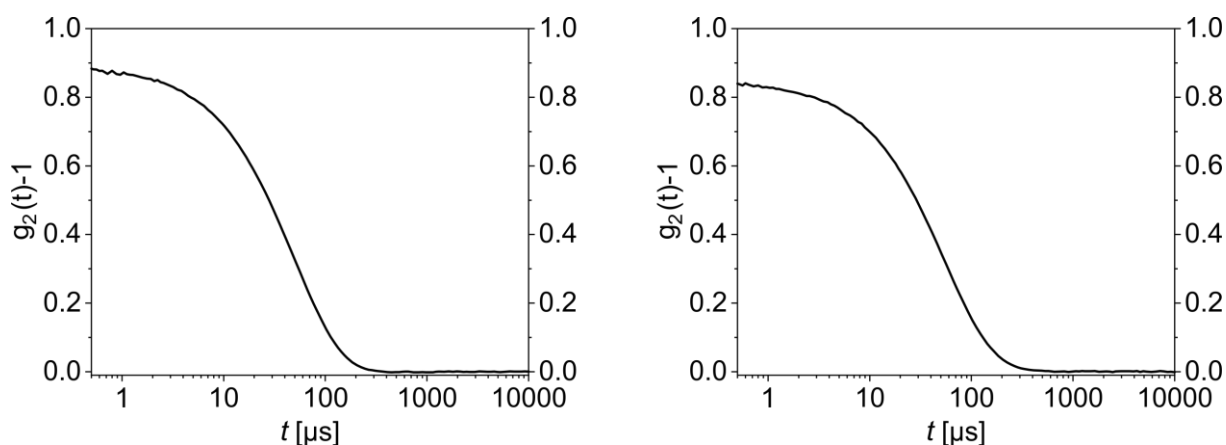
## IR

**Figure S2:** IR spectrum of the SCO CP-BCP composite (green), the bulk  $[\text{FeL}(\text{bipy})]_n$  (red) and the  $\text{S}_{85}\text{V}_{15}^{154}$  diblock copolymer (BCP, black).



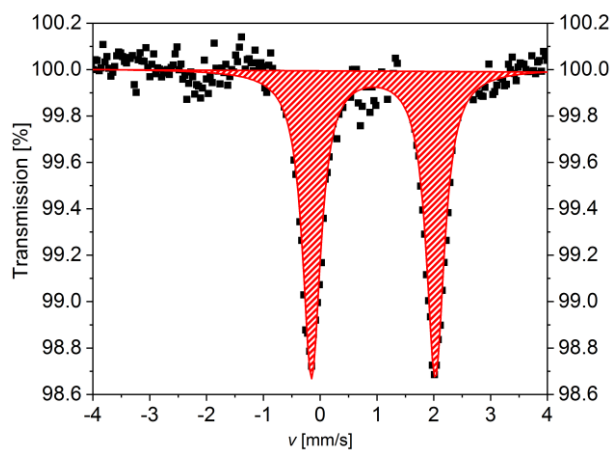
### DLS autocorrelation functions of the empty BCP micelles and the SCO CP-BCP composite particles

**Figure S3:** Autocorrelation function  $g_2(t)-1$  of the empty BCP micelle (left) and the SCO CP-BCP particles (right) corresponding to the size distribution graphs of Figure 1B and 1E in the manuscript.



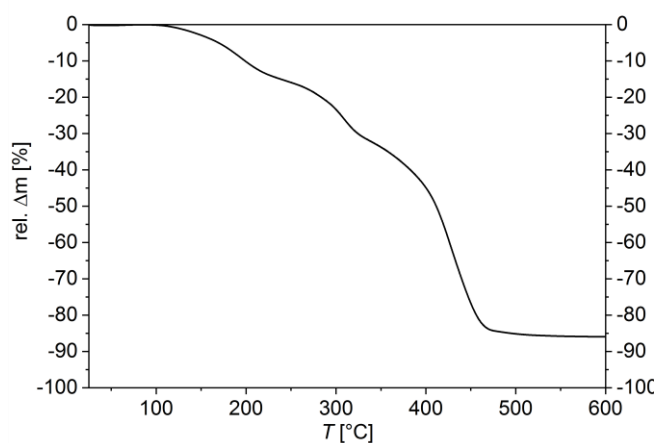
### Mössbauer spectroscopy of the SCO CP-BCP composite particles

**Figure S4:** Room temperature  $^{57}\text{Fe}$  Mössbauer spectrum of the SCO CP-BCP composite showing only one doublet for the CP. The spectrum is displayed in respect to  $\alpha\text{-Fe}$  as reference.



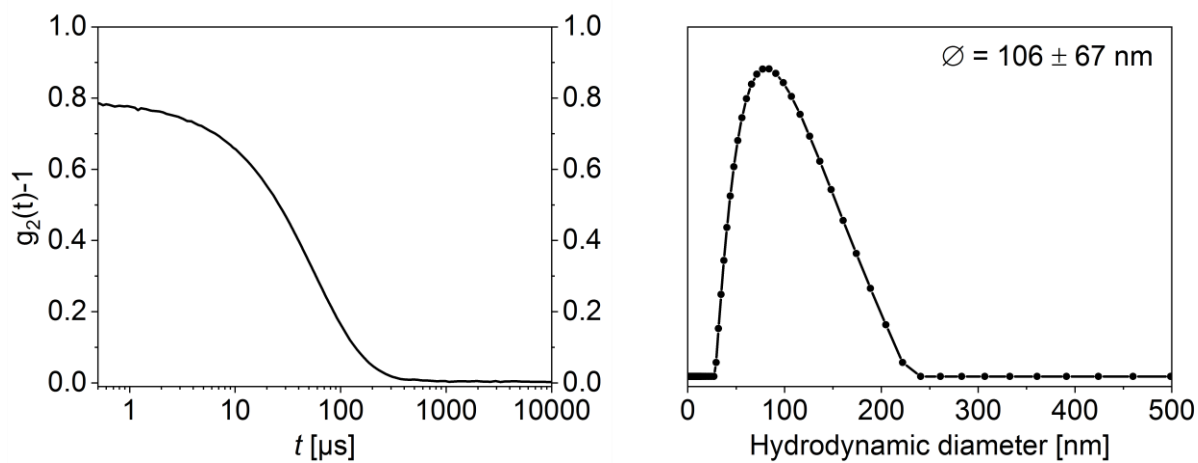
### TGA of the SCO CP-BCP composite particles

**Figure S5:** TGA measurement of the SCO CP-BCP showing no significant mass loss until 100 °C indicating that no residual solvent is present in the composite.



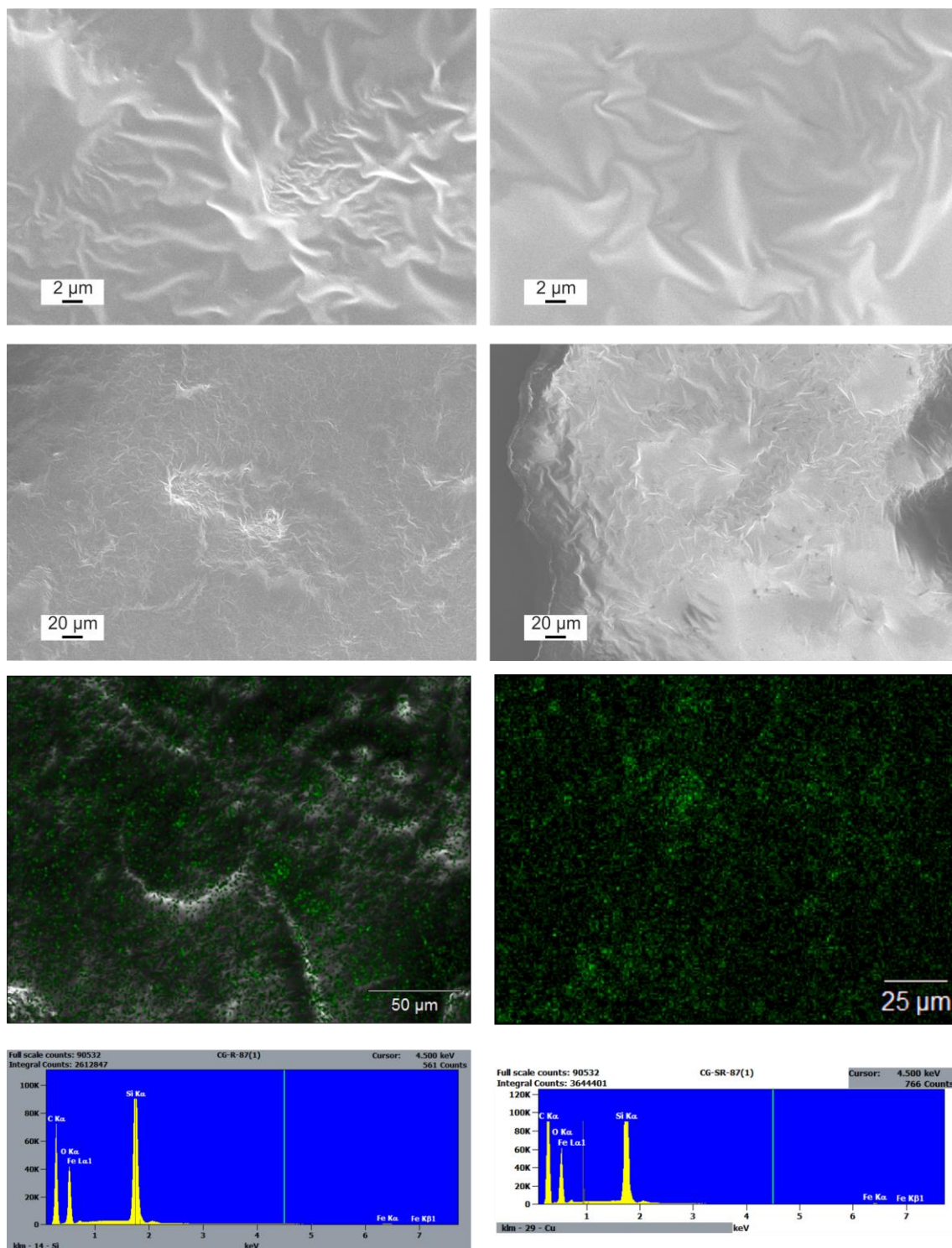
**DLS of the SCO CP-BCP composite particles after annealing**

**Figure S6:** Autocorrelation function  $g_2(t)-1$  vs.  $t$  (left) and the size distribution of the particles (right) of redissolved sample after the thermal annealing process.



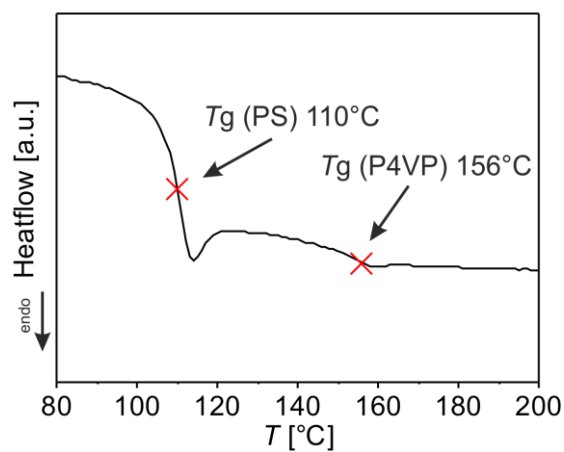
# SEM and SEM-EDX of the SCO CP-BCP composite particles before and after annealing

**Figure S7:** SEM images and SEM-EDX measurements of the sample before (left) and after thermal annealing (right). SEM-EDX measurements showing homogeneously distributed iron indicated by the green color. No indication for the formation of agglomerates or larger crystallites is observed.

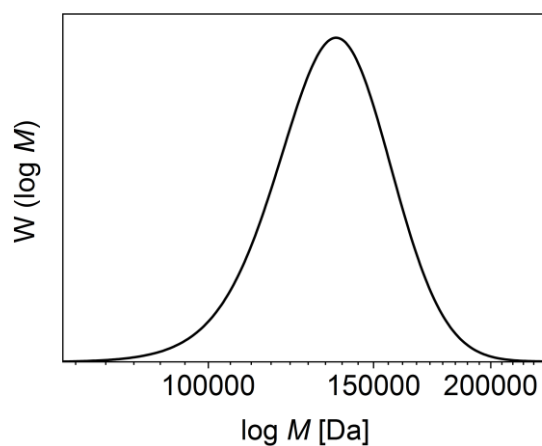


**DSC of the BCP**

**Figure S8:** DSC measurement of the pure PS-*b*-P4VP showing the glass transition temperature  $T_g$  for PS at 110 °C and P4VP at 156 °C.

**GPC of the BCP**

**Figure S9:** Size distribution of the pure  $S_{85}V_{15}^{154}$  measured by DMF-GPC.



## NMR of the BCP

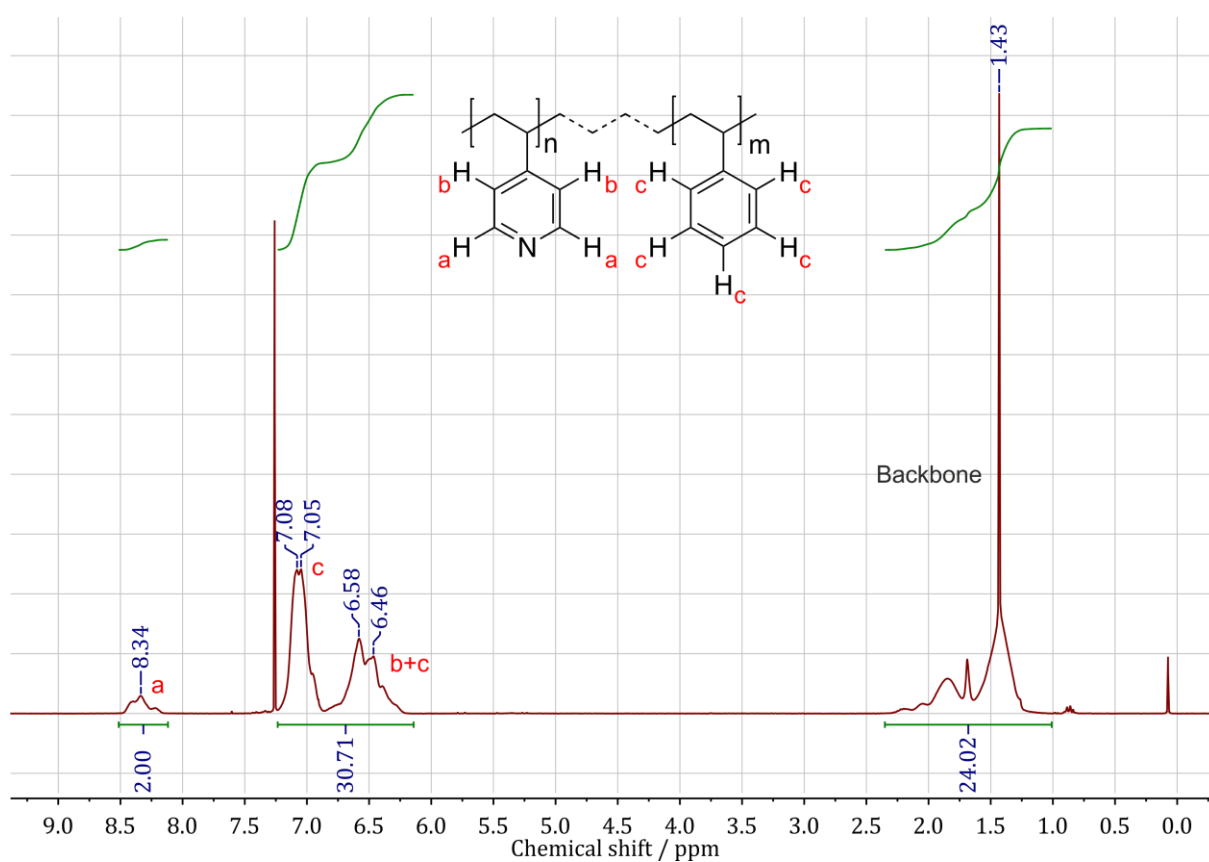
**Figure S10:**  $^1\text{H}$ -NMR spectrum of  $\text{S}_{85}\text{V}_{15}$ <sup>154</sup> diblock copolymer showing signals for the pyridine, styrene and aliphatic hydrogen atoms.

Signal a has been normalized to 2 protons from the 4-vinylpyridine. Signal c from the 5 styrene protons and signal b from 2 remaining 4-vinylpyridine overlap.

$$30.71 - 2 = 28.71 \text{ (styrene protons)}$$

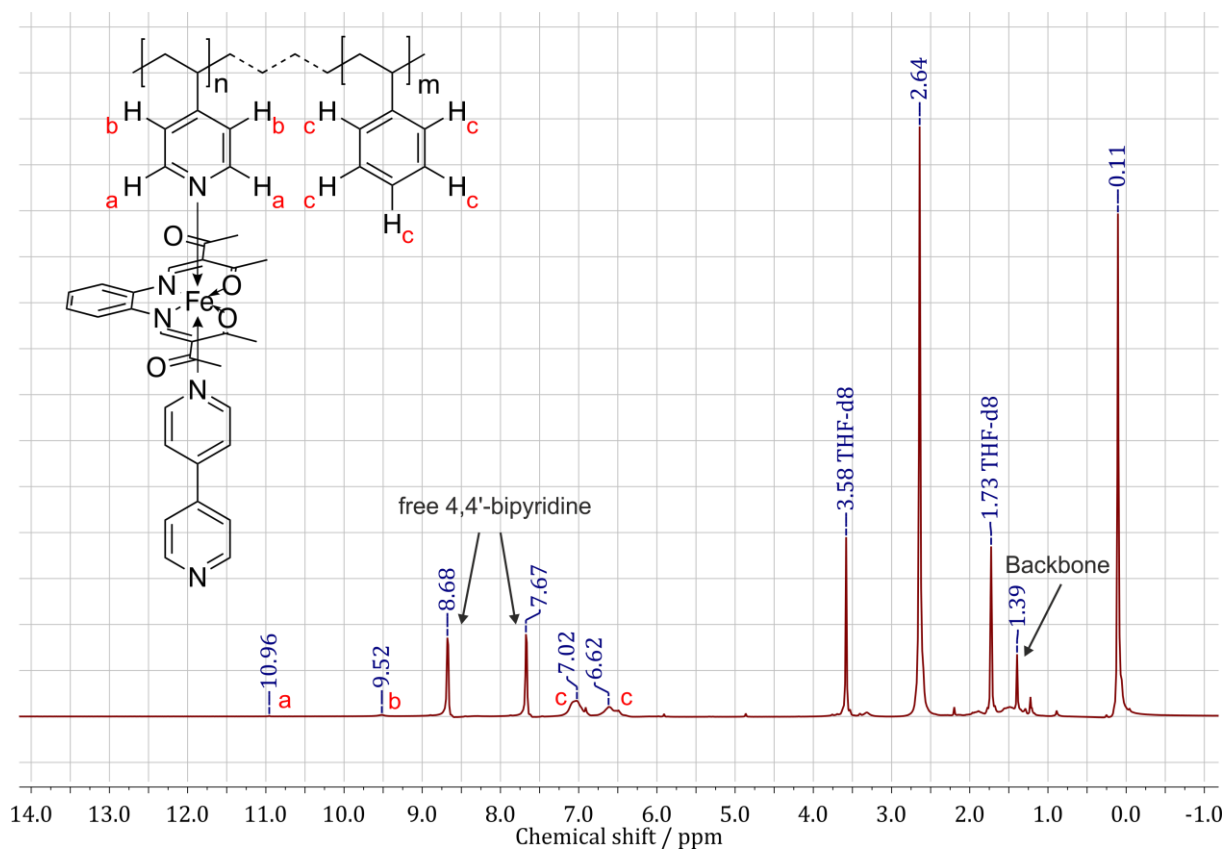
$$28.71 / 5 = 5.742$$

$$\rightarrow \text{P4VP} : \text{PS} = 1 : 5.742 \rightarrow \text{S85V15}$$



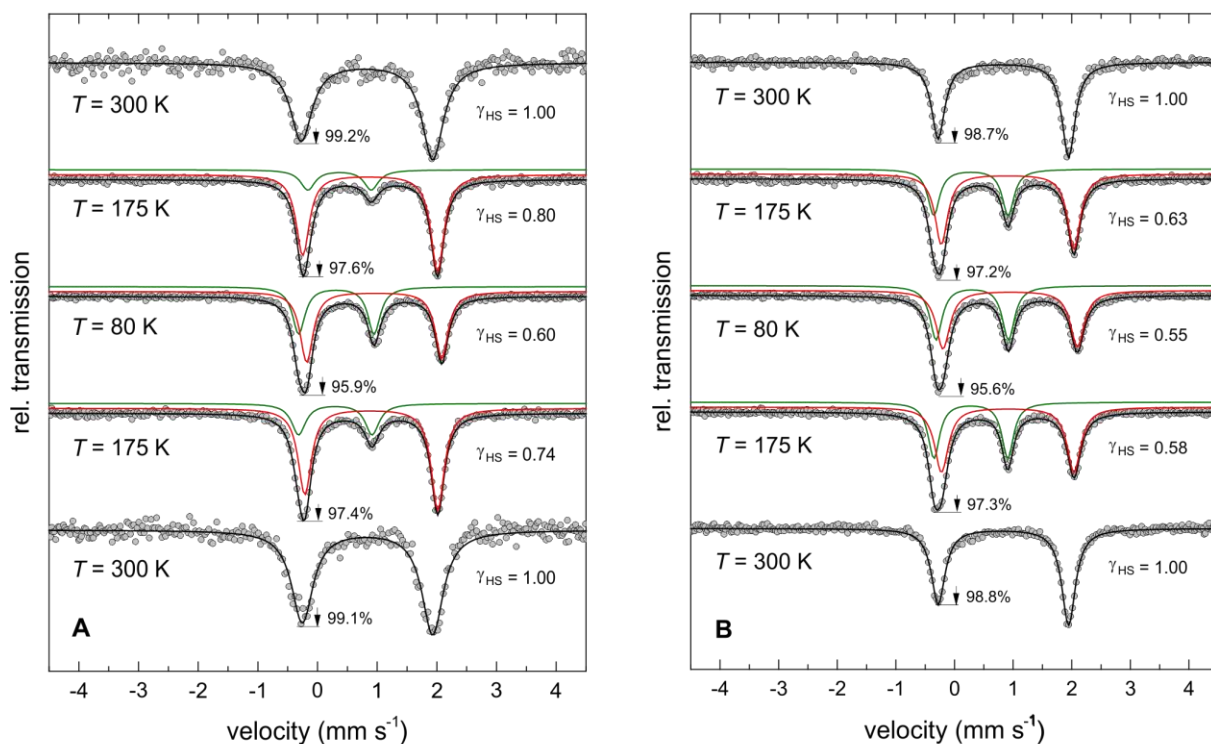
## NMR of the SCO CP-BCP

**Figure S11:**  $^1\text{H}$ -NMR spectrum of SCO CP-S<sub>85</sub>V<sub>15</sub><sup>154</sup> diblock copolymer showing signals for the pyridine, styrene and aliphatic hydrogen atoms. The signals of the pyridine protons a and b are shifted to 10.96 ppm and 9.52 ppm (compared to 8.34 ppm and 6.5 ppm for the pure polymer, see Figure S10) due to the coordination of the paramagnetic iron center while the signal of the styrene protons c do not change.



### Temperature-dependent Mössbauer spectra of the SCO CP-BCP composite particles

**Figure S12:** Zero-field  $^{57}\text{Fe}$  Mössbauer spectra of SCO CP-BCP recorded at temperatures between  $T = 300$  and  $80$  K before (A) and after (B) annealing at  $T = 393$  K for 1 h under nitrogen atmosphere. The measurements on both compounds were carried out starting at  $T = 300$  K and then at  $T = 175$ ,  $80$ ,  $175$  and  $300$  K. Symbols: Experimental data. Lines: Fit with one or two doublets of Lorentzian lines, respectively. The parameters of the fit are summarized in Table S1. The colored lines represent the corresponding sub-spectra of the fit, which are attributed to the Fe(II) low-spin (green) and Fe(II) high-spin sites (red), respectively.





## 7. Confined Crystallization of Spin-Crossover Nanoparticles in Block-Copolymer Micelles

**Table S1:** Summary of Mössbauer parameters determined for SCO CP-BCP before and after annealing at  $T = 393$  K for 1 h (under nitrogen atmosphere) by a fit with one or two doublets of Lorentzian lines, respectively, with isomer shift  $\delta$ , quadrupole splitting  $\Delta E_Q$  and Lorentzian line width  $\Gamma_{FWHM}$  (full width at half maximum).  $A_2/A_1$  describes the relative intensities of the two corresponding lines of a given doublet, while AREA quotes the relative (integral) intensities of the individual doublets, attributed to the molar fraction of the high-spin and low-spin Fe species in SCO CP-BCP, respectively. The measurements on both compounds were carried out starting at  $T = 300$  K and then at  $T = 175, 80, 175$  and 300 K.

Before annealing					
$T$ [K]	$\delta^{[a]}$ [mm s <sup>-1</sup> ]	$\Delta E_Q$ [mm s <sup>-1</sup> ]	$\Gamma_{FWHM}$ [mm s <sup>-1</sup> ]	$A_2/A_1^{[b]}$	AREA [%]
300	0.951(5)	2.200(9)	0.44(1)	1.23(4)	100
175	1.020(2)	2.224(5)	0.264(4)	1.20(2)	79.7
	0.412(7)	1.22(1)	0.28(2)	1*	20.3
80	1.071(1)	2.265(2)	0.262(4)	0.94(1)	60.1
	0.437(1)	1.263(3)	0.254(5)	1*	39.9
175	1.022(2)	2.230(3)	0.268(5)	1.17(3)	74.0
	0.420(6)	1.232(9)	0.28(1)	1*	26.0
300	0.959(4)	2.184(7)	0.44(1)	1.13(4)	100
After annealing					
$T$ [K]	$\delta^{[a]}$ [mm s <sup>-1</sup> ]	$\Delta E_Q$ [mm s <sup>-1</sup> ]	$\Gamma_{FWHM}$ [mm s <sup>-1</sup> ]	$A_2/A_1^{[b]}$	AREA [%]
300	0.9551(2)	2.225(4)	0.277(5)	1.24(2)	100
175	1.027(2)	2.263(3)	0.264(5)	1.07(2)	63.2
	0.402(3)	1.268(6)	0.242(8)	1*	36.8
80	1.071(1)	2.292(3)	0.287(4)	0.97(2)	54.7
	0.424(3)	1.236(3)	0.252(4)	1*	45.3
175	1.020(1)	2.260(3)	0.283(5)	1.00(2)	58.0
	0.400(2)	1.260(3)	0.239(5)	1*	42.0
300	0.955(2)	2.224(4)	0.285(7)	1.27(3)	100

Values marked with an asterisk (\*) were fixed in the fit. **[a]** The isomer shifts ( $\delta$ ) were specified relative to metallic iron at room temperature but were not corrected in terms of the second-order Doppler shift. **[b]** In case of a polycrystalline powder with random orientations of the crystallites, the expectation value of this parameter  $A_2/A_1 = 1$ .<sup>[4]</sup> Deviations from this value, which are clearly observed at  $T = 300$  K, are attributed to the presence of texture effects due to partial orientations of crystallites on compacting the powder in the sample containment.

#### 7.7.5. References

- [1] E.-G. Jäger, E. Häussler, M. Rudolph, M. Rost, *Z. Anorg. Allg. Chem.* **1985**, 525, 67-85.
- [2] K. Lagarec; D. G. Rancourt, *Recoil, Mössbauer spectral analysis software for windows 1.0*, Department of Physics, University of Ottawa, Canada, **1998**.
- [3] R. A. Brand, *WinNormos-for-Igor, Version 3.0*, May **2009**.
- [4] N. N. Greenwood and T. C. Gibb, *Mössbauer Spectroscopy*, Chapman and Hall Ltd., London **1971**.

#### 7.7.6. Author Contributions

C. Göbel synthesized the SCO CP BCP nanoparticles, did most of the formal analysis (SQUID, TEM, DLS, IR Mössbauer, elemental analysis, ...) and did write the original draft.

C. Hils synthesized and characterized the electrospun fibers of the composite nanoparticles in PS.

M. Drechsler did the cryo-TEM measurements and helped with the TEM measurements in general.

D. Baabe measured and interpreted the temperature-dependent Mössbauer spectra.

A. Greiner helped with the project administration and the funding acquisition.

H. Schmalz synthesized and characterized the BCP and supervised the electrospinning and the Raman measurements and was involved in the writing of the manuscript.

B. Weber was responsible for the funding acquisition and project administration and involved in the writing of the manuscript.

## 8. Synthesis of Zn-based 1D and 2D coordination polymer nanoparticles in block copolymers

Christoph Göbel,<sup>a</sup> Gerald Hörner,<sup>a</sup> Andreas Greiner,<sup>b</sup> Holger Schmalz<sup>\*b</sup> and Birgit Weber<sup>\*a</sup>

<sup>a</sup> Department of Chemistry, Inorganic Chemistry IV, Universität Bayreuth, Universitätsstr. 30, 95447 Bayreuth, Germany

<sup>b</sup> Department of Chemistry, Macromolecular Chemistry II and Keylab Synthesis and Molecular Characterization, Bavarian Polymer Institute, Universität Bayreuth, Universitätsstr. 30, 95440 Bayreuth, Germany

Published in *Nanoscale Adv.* **2020**, 2, 4557–4565 (doi: 10.1039/D0NA00334D) and reproduced under the terms of the CC-BY 3.0 license.

**Abstract:** Nanoparticles of the 1D and 2D coordination polymers  $[\text{Zn}(\text{OAc})_2(\text{bipy})]_n$  and  $[\text{Zn}(\text{TFA})_2(\text{bppa})_2]_n$  were prepared, employing polystyrene-*block*-poly(4-vinylpyridine) diblock copolymers with different weight fractions of the 4-vinylpyridine (4VP) block and comparable overall molecular weights of  $M_n \approx 155 \text{ kg mol}^{-1}$  as template (SV-15 and SV-42 with 15 and 42 wt% 4VP, respectively).  $[\text{Zn}(\text{OAc})_2(\text{bipy})]_n$  nanoparticles were successfully synthesised within the 4VP core of SV-42 micelles, showing a core size of  $D_{\text{core}} = 47 \pm 5 \text{ nm}$  and a hydrodynamic diameter of  $D_h = 157 \pm 46 \text{ nm}$ , determined by transmission electron microscopy (TEM) and dynamic light scattering (DLS). The crystallinity of the composite is quite low, showing only low intensity reflexes in the powder X-ray diffraction (PXRD) pattern with the highest particle load. No indications for larger microcrystals were detected by scanning electron microscopy (SEM), proving the successful integration of the coordination polymer nanoparticles within the micellar cores. Nanocomposites of the 2D coordination network  $[\text{Zn}(\text{TFA})_2(\text{bppa})_2]_n$  were synthesised using both diblock copolymers. The particle core sizes (from TEM) and hydrodynamic diameters (from DLS) correlate with the 4VP fraction of the micelles, resulting in  $D_{\text{core}} = 46 \pm 6 \text{ nm}$  for SV-42 and  $15 \pm 2 \text{ nm}$  for SV-15 and  $D_h = 340 \pm 153 \text{ nm}$  and  $177 \pm 57 \text{ nm}$ , respectively. The successful synthesis was proven by PXRD and SEM images, confirming the absence of larger crystallites. Hence, it is possible to synthesise nanocomposites of Zn-based 1D and 2D coordination polymers by a direct approach utilising diblock copolymer micelles as template.

### 8.1. Introduction

Devices built up from functional molecular materials are an interesting approach to realize new functionalities for new fields of applications. Examples for promising molecule-based systems are porous coordination networks (MOFs, metal organic frameworks), Prussian blue based materials, or molecular magnetic materials including spin crossover coordination polymers.<sup>[1-9]</sup> Nanoparticles and nanocomposites of such materials are often considered to play a key role in future device engineering.<sup>[10-15]</sup> However, the synthesis of well-defined, stable nanoparticles or nanocomposites of molecule-based materials is a highly demanding task, as a wide range of techniques successfully used for solid state materials (e.g. the reduction of metal salts<sup>16-20</sup> or the hydrothermal synthesis<sup>[21-23]</sup>) are inapplicable. For molecular materials, some synthetic procedures like the inverse micelle technique<sup>[24-28]</sup> or micro-fluidic approaches using fast precipitation<sup>[29-31]</sup> have already been established to achieve that task. However, each new material has its needs regarding the reaction conditions (e.g. reaction temperature, solvent, reactant solubility, air, or moisture sensitivity). Furthermore, some of the approaches have limitations regarding the size limits that can be reached. This makes a fine-tuning of the reaction conditions indispensable to not only achieve a successful synthesis of the nanomaterial of the desired size, but also to preserve the desired properties. Furthermore, some synthesis procedures have been proven more suitable for the formation of functional materials than others, because they allow for example the even distribution of the nanomaterial or nanocomposite on surfaces or prevent the aggregation of the formed nanoparticles.<sup>[32,33]</sup>

Nanoparticles of 2D<sup>[34-36]</sup> or 3D<sup>[24,37,38]</sup> coordination networks (CNs) have been prepared with a wide range of bridging ligands and metal ions. However, the formation of 2D and 3D CN nanoparticles directly in the core of block copolymer micelles is quite rare. To the best of our knowledge, only 6 examples of 2D or 3D CN nanoparticles formed in a polymer matrix can be found in the literature.<sup>[39-44]</sup> A more commonly used technique is the immobilization of pre-formed nanoparticles in block copolymer micelles or polymer matrices (bulk polymers, gels, etc.),<sup>[45-55]</sup> in some cases even size-selective employing polymer cages.<sup>[56]</sup>

We have previously shown that the use of polystyrene-block-poly(4-vinylpyridine) (PS b P4VP) diblock copolymers (BCPs) is ideal for the size-controlled synthesis of 1D Fe(II) spin crossover (SCO) coordination polymer (CP) nanoparticles with core sizes of  $16 \pm 2$  nm and  $48 \pm 4$  nm. It was possible to retain the SCO properties with hysteresis at both particle sizes. Thermal treatment of the 16 nm particles triggers a confined crystallization of the NPs leading to SCO properties comparable to those of the bulk material.<sup>[57,58]</sup> In other cases, the synthesis in confinement results in different morphologies for NPs and bulk material and therefore different SCO properties.<sup>[59]</sup>

---

Herein, we report the successful adaptation of our general synthetic concept to a completely new type of CPs and for the first time to a 2D CN to illustrate its general applicability. The double-stranded 1D CP  $[\text{Zn}(\text{OAc})_2(\text{bipy})]_n$ <sup>[60]</sup> (bipy = 4,4'-bipyridine) and the layer-like 2D CN  $[\text{Zn}(\text{TFA})_2(\text{bppa})_2]_n$ <sup>[61]</sup> (TFA = trifluoroacetic acid, bppa = 1,3-di(4-pyridyl)propane) were used for the formation of Zn-CP/CN-BCP nanocomposites. The nanocomposites were synthesised using two PS b P4VP diblock copolymers (SV-15 and SV-42) as templates, which have an almost identical molecular weight but differ in the weight fraction of the 4VP blocks (see Table 1).

**Table 1:** Overview of the used BCPs in this work.

BCP	$M_n$ [g mol <sup>-1</sup> ] <sup>a)</sup>	$\bar{D}$ <sup>b)</sup>	PS:P4VP [w/w] <sup>c)</sup>	$D_{\text{core}}$ [nm] <sup>d)</sup>	$D_h$ [nm] <sup>e)</sup>
SV-15	154 000	1.02	85:15	15 ± 2	75 ± 28
SV-42	157 000	1.09	58:42	45 ± 5	125 ± 34

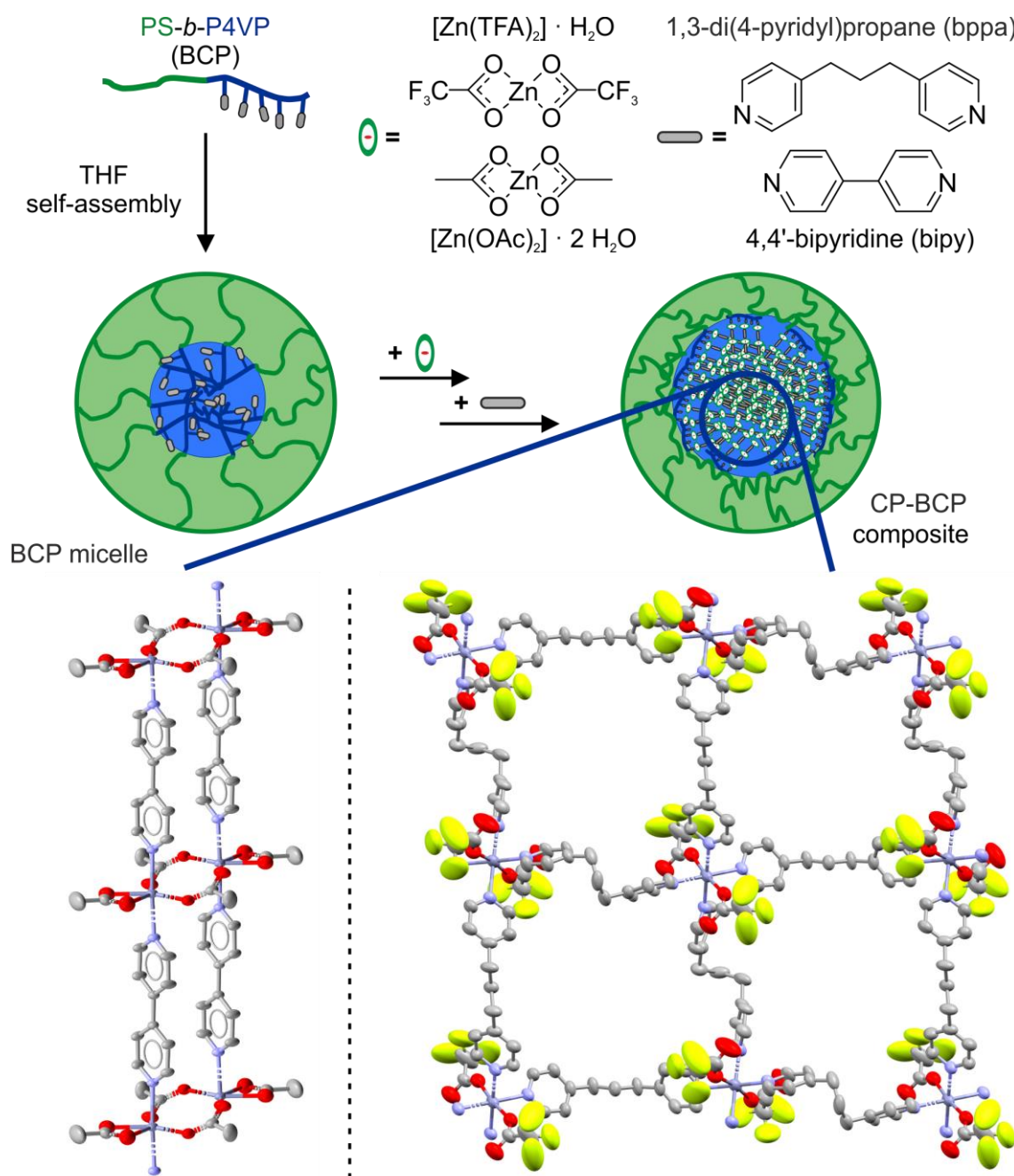
<sup>a)</sup> calculated from proton nuclear magnetic resonance (<sup>1</sup>H NMR) measurements, using the molecular weight of the PS precursor measured by matrix-assisted laser desorption-time of flight mass spectrometry (MALDI-ToF MS); <sup>b)</sup> from gel permeation chromatography (GPC) in N,N-dimethylformamide using narrowly distributed PS standards for calibration; <sup>c)</sup> calculated from <sup>1</sup>H NMR measurements; <sup>d)</sup> core diameters of empty BCP micelles, see Fig. S1 for TEM images and core size distributions; <sup>e)</sup> hydrodynamic diameters of the empty BCP micelles, see Fig. S2 for DLS measurements.

## 8.2. Results and Discussion

### 8.2.1. Synthetic procedures

The synthesis procedure was adapted from the literature and adjusted to the requirements of the Zn-based CPs (Scheme 1).<sup>[27]</sup> Dissolving the diblock copolymer in THF leads to the formation of BCP micelles due to the significantly lower solubility of the P4VP block compared to the PS block. Thus, the less-soluble P4VP core, where the synthesis of the NPs takes place, is surrounded by soluble PS corona chains. The nanocomposite samples containing the 1D CP  $[\text{Zn}(\text{OAc})_2(\text{bipy})]_n$  were synthesised employing SV-42 diblock copolymer micelles in THF (Table 2). The Zn(II) precursor  $[\text{Zn}(\text{OAc})_2] \cdot 2 \text{H}_2\text{O}$  was added and the solution was refluxed for 1h. Subsequently, the solution was cooled down, the bridging ligand bipy was added and the solution was refluxed again for 1h. At this point, the synthesis can be stopped by removal of the solvent via rotary evaporation (sample **1**; 1 cycle) or  $[\text{Zn}(\text{OAc})_2] \cdot 2 \text{H}_2\text{O}$  and bipy can be added simultaneously up to 4 more times (samples **2** to **4**; 3 – 5 cycles). The resulting light-yellow solids were dried in vacuo.

The BCPs SV-15 and SV-42 were used for the synthesis of nanocomposites containing the 2D CN  $[\text{Zn}(\text{TFA})_2(\text{bppa})_2]_n$  (Table 2). Here, the synthesis protocol had to be adapted due to the very low solubility of the desired 2D CN. The respective BCPs were dissolved under reflux in THF to trigger the self-assembly to micelles,  $[\text{Zn}(\text{TFA})_2] \cdot \text{H}_2\text{O}$  was added and the mixture was heated to reflux for 1h to initiate the coordination of the zinc(II) precursor at the pyridine units in the P4VP core of the micelle.



**Scheme 1:** Synthetic approach for the preparation of Zn-based CP-BCP nanocomposites. An excerpt of the crystal structures of both CP bulk materials is given below (left:  $[\text{Zn}(\text{OAc})_2(\text{bipy})]_n$ , right:  $[\text{Zn}(\text{TFA})_2(\text{bppa})_2]_n$ ).

To avoid a precipitation of the CN and to decelerate its formation, the bridging ligand bppa was dissolved in THF and added dropwise to the reaction solution over 15 min, followed by a 1h reflux. The solvent was removed by rotary evaporation and subsequent drying in vacuo to yield light-yellow samples **5** and **6** (1 cycle each). The reaction procedure can be repeated to yield samples **7** and **8** (2 cycles each) with a higher complex loading. The formation of nanocomposites with higher cycle counts (>2) was tested, but the formation of microcrystals was observed by SEM (see Fig. S3). Therefore, no further addition of reactants was conducted after the second addition of bppa (for experimental details see experimental section).

**Table 2:** Overview of the synthesised nanocomposites.

Sample	CP/CN	BCP	cycles	$D_{\text{core}}$ [nm] <sup>a)</sup>	$D_{\text{h}}$ [nm] <sup>b)</sup>
<b>1</b>	$[\text{Zn}(\text{OAc})_2(\text{bipy})]_{\text{n}}$	SV-42	1	$50 \pm 4$	$141 \pm 48$
<b>2</b>			3	$47 \pm 4$	$155 \pm 42$
<b>3</b>			4	$47 \pm 4$	$152 \pm 41$
<b>4</b>			5	$47 \pm 5$	$157 \pm 46$
<b>5</b>	$[\text{Zn}(\text{TFA})_2(\text{bppa})_2]_{\text{n}}$	SV-15	1	$13 \pm 1$	$139 \pm 39$
<b>6</b>		SV-42	1	$49 \pm 4$	$160 \pm 46$
<b>7</b>		SV-15	2	$15 \pm 2$	$177 \pm 57$
<b>8</b>		SV-42	2	$46 \pm 6$	$340 \pm 153$

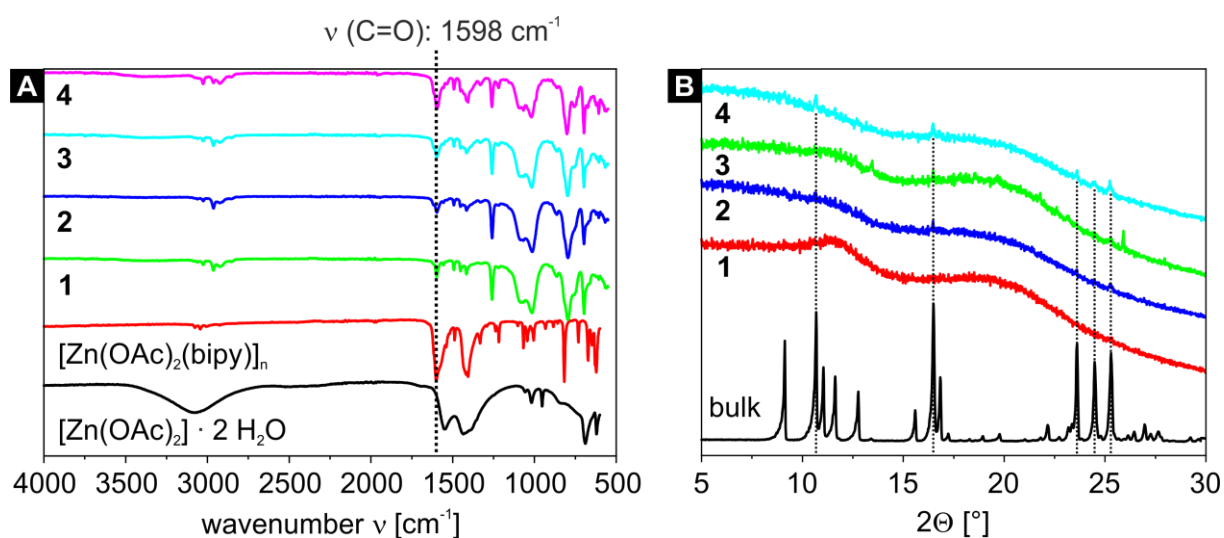
<sup>a)</sup> core diameters of the nanocomposite particles; <sup>b)</sup> hydrodynamic diameters of the nanocomposite particles.

### 8.2.2. Characterisation of nanocomposites

In total, eight different nanocomposites have been synthesised (Table 2), of which four contain the 1D CP  $[\text{Zn}(\text{OAc})_2(\text{bipy})]_{\text{n}}$  (samples **1** – **4**) and another four the 2D CN  $[\text{Zn}(\text{TFA})_2(\text{bppa})_2]_{\text{n}}$  (samples **5** – **8**). All nanocomposite materials were characterised by transmission electron microscopy (TEM) and dynamic light scattering (DLS) to evaluate the particle sizes in the dry state and in dispersion. Furthermore, the nanocomposites were analysed by elemental analysis (C, H, N), infrared spectroscopy (IR), powder X-ray diffraction (PXRD), and scanning electron microscopy (SEM). IR measurements were supported by computational calculations.

### 8.2.3. $[\text{Zn}(\text{OAc})_2(\text{bipy})]_n$ nanocomposites

IR measurements of the starting material  $[\text{Zn}(\text{OAc})_2] \cdot 2 \text{H}_2\text{O}$ , the bulk material  $[\text{Zn}(\text{OAc})_2(\text{bipy})]_n$  and the samples **1** – **4** are displayed in Fig. 1A. The nanocomposites show a characteristic band at  $1598 \text{ cm}^{-1}$ , which increases in intensity relative to other bands when higher cycle counts are reached. This is in excellent agreement with the spectrum of independently synthesised bulk  $[\text{Zn}(\text{OAc})_2(\text{bipy})]_n$ , which features a band at  $1600 \text{ cm}^{-1}$ . Thus, this band can be safely assigned to the C=O stretching mode of the neat CP. Peak assignment in the fingerprint area between  $1400 \text{ cm}^{-1}$  and  $1800 \text{ cm}^{-1}$  proved valuable to identify the nature and purity of the nanocomposites, which was further supported by numerical frequency calculations of optimized model structures. The CP was approximated as binuclear  $[\text{Zn}_2(\text{OAc})_4(\text{py})_4]$ , whereas the H-bond network of the precursor was taken into account in pentanuclear  $[\text{Zn}(\text{OAc})_2(\text{OH}_2)] \times 4 [\text{Zn}(\text{OAc})_2(\text{OH}_2)]$  (see Experimental Section for computational details, animations of diagnostic modes are given in the SI, anim\_1-6). In fact, the calculated C=O stretching mode in the CP model  $[\text{Zn}_2(\text{OAc})_2(\text{py})_2]_n$  is located at  $1601 \text{ cm}^{-1}$ , almost identical to samples **1** – **4** and the bulk material. This is a distinct difference to the C=O band of the precursor  $[\text{Zn}(\text{OAc})_2] \cdot 2 \text{H}_2\text{O}$ , which is experimentally found at  $1549 \text{ cm}^{-1}$  (computed value:  $1534 \text{ cm}^{-1}$ ). The formation of single-stranded  $[\text{Zn}(\text{OAc})_2(\text{bipy})]_n$  can be similarly ruled out, as C=O based stretching modes computed for the model  $[\text{Zn}(\text{OAc})_2(\text{py})_2]$  are predicted at  $1500 \text{ cm}^{-1}$ , proving the successful synthesis of the 1D CP in the P4VP core of the SV-42 micelles.

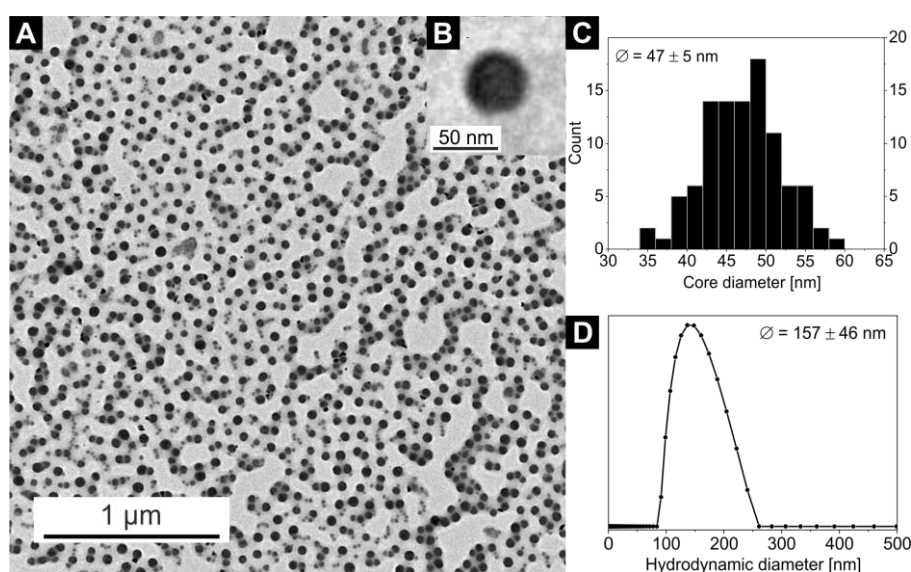


**Fig. 1:** IR spectra of the starting material  $[\text{Zn}(\text{OAc})_2] \cdot 2 \text{H}_2\text{O}$ , the CP  $[\text{Zn}(\text{OAc})_2(\text{bipy})]_n$  and the four  $[\text{Zn}(\text{OAc})_2(\text{bipy})]_n$  nanocomposite samples **1** – **4** (A) and a comparison of the PXRD patterns of the bulk material  $[\text{Zn}(\text{OAc})_2(\text{bipy})]_n$  and the  $[\text{Zn}(\text{OAc})_2(\text{bipy})]_n$  nanocomposite samples **1** – **4** (B). PXRD reflexes that correlate with the bulk material are marked with a dashed line.



Further proof is given by the PXRD patterns of the samples **1** – **4**. Samples **1** – **3** are highly amorphous as indicated by the powder diffraction patterns. Only sample **4** with five reaction cycles shows five reflexes that also correspond to the dominant reflexes of the bulk material (Fig. 1B) indicating a successful formation of the CP inside the micellar core.

Exemplary for all nanocomposites with the  $[\text{Zn}(\text{OAc})_2(\text{bipy})]_n$  CP, the TEM and DLS measurements of sample **4** are displayed in Fig. 2. The corresponding core diameter and hydrodynamic diameter of all samples are summarized in Table 2. The DLS measurement shows narrowly distributed nanocomposite particles with a hydrodynamic diameter of  $D_h = 157 \pm 46$  nm. As the electron-rich  $[\text{Zn}(\text{OAc})_2(\text{bipy})]_n$  CP is incorporated inside the micelle core of the BCP, only the core of nanocomposite particles is clearly visible in TEM, resulting in notably smaller diameters compared to DLS. The TEM image of sample **4** shows spherical particle cores with a core size of  $D_{\text{core}} = 47 \pm 5$  nm (Fig. 2). In line with the results for other coordination polymers reported so far,<sup>[57–59]</sup> particles core sizes and hydrodynamic diameters of samples **1** – **3** are nearly identical and slightly increased compared to the empty template. Respective data of all samples confirming these results can be found in Fig. S4 and Fig. S5 together with the autocorrelation function of sample **4** (Fig. S6).

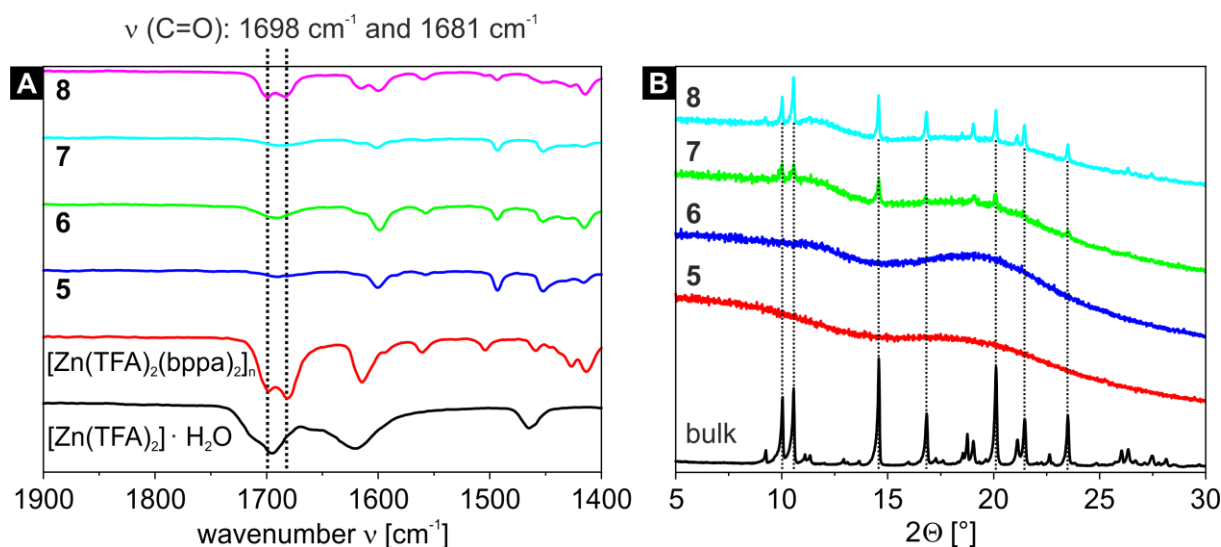


**Fig. 2:** (A) TEM image of sample **4**, the cores of the micelles with the embedded  $[\text{Zn}(\text{OAc})_2(\text{bipy})]_n$  CP nanoparticles appear black, (B) an inset with a zoom on a single nanoparticle, (C) core size distribution  $D_{\text{core}}$  (from TEM) and (D) hydrodynamic diameter distribution  $D_h$  (from DLS) of the nanocomposite sample **4** (for DLS autocorrelation function see Fig. S6).

The samples **1** – **4** were also characterised by SEM, revealing the absence of microcrystals on the sample surface (Fig. S7). Thus, the CP is regioselectively formed inside the cores of the BCP micelles.

### 8.2.4. $[\text{Zn}(\text{TFA})_2(\text{bppa})_2]_n$ nanocomposites

IR measurements were also performed for the four nanocomposites containing the  $[\text{Zn}(\text{TFA})_2(\text{bppa})_2]_n$  CN (samples **5** – **8**, Fig. 3A, S8) and were compared to the starting material  $[\text{Zn}(\text{TFA})_2] \cdot \text{H}_2\text{O}$  and the bulk material  $[\text{Zn}(\text{TFA})_2(\text{bppa})_2]_n$ . The starting material shows a C=O band at  $1695\text{ cm}^{-1}$  with a shoulder at  $1715\text{ cm}^{-1}$ , whereas the bulk CN shows two characteristic bands in the range of C=O vibrations at  $1698\text{ cm}^{-1}$  and  $1681\text{ cm}^{-1}$ . Computation of a truncated mononuclear model of the CN,  $[\text{Zn}(\text{TFA})_2(\text{py})_4]$ , similarly gives two bands at  $1668\text{ cm}^{-1}$  and  $1662\text{ cm}^{-1}$ . For samples **5** – **7** only one band was detected at  $1690\text{ cm}^{-1}$ , which is exactly between the two bands of the bulk CN. For sample **8** two bands for the CN were determined at  $1699\text{ cm}^{-1}$  and  $1684\text{ cm}^{-1}$ , being in good agreement with the bulk material. Again, a relative increase in intensity of the carbonyl band is detectable with higher cycles. Thus, it was possible to incorporate the 2D CN into the 4VP cores of both micellar templates (SV-15 and SV-42). In line with the PXRD results of the  $[\text{Zn}(\text{OAc})_2(\text{bipy})]_n$  CP nanocomposites, the samples **5** and **6** (one loading cycle) are completely amorphous as represented by the diffraction patterns. Nevertheless, samples **7** and **8** (two loading cycles) already show some reflexes at positions that match with the bulk material, indicating the successful formation of the desired CN inside the BCP micelles (Fig. 3B).

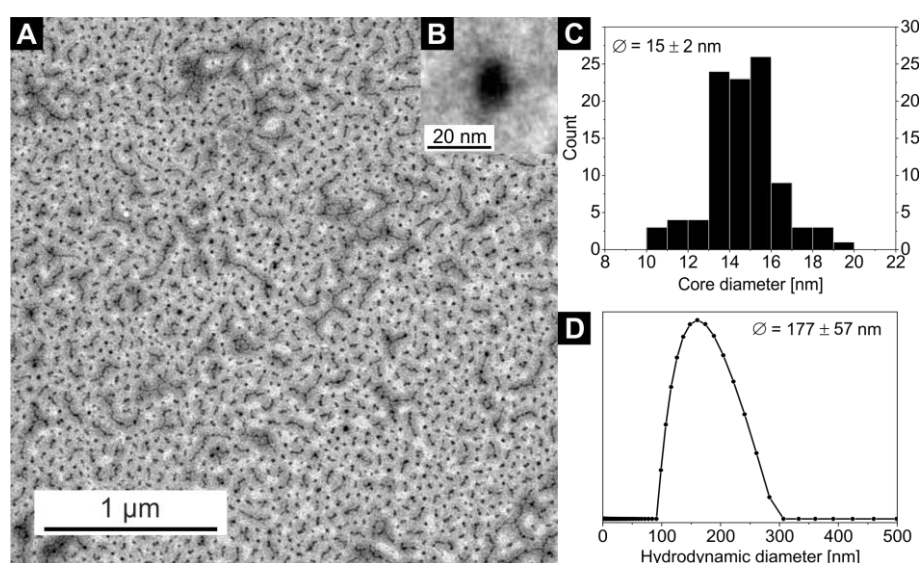


**Fig. 3:** Detailed view on the spectral range of 1900 cm<sup>-1</sup> to 1400 cm<sup>-1</sup> of the IR spectra of the starting material [Zn(TFA)<sub>2</sub>] · H<sub>2</sub>O, the CN [Zn(TFA)<sub>2</sub>(bppa)<sub>2</sub>]<sub>n</sub> and the four [Zn(TFA)<sub>2</sub>(bppa)<sub>2</sub>]<sub>n</sub> nanocomposite samples 5 – 8 (A). The complete spectra can be found in Fig. S8. Comparison of the PXRD patterns of the bulk material [Zn(TFA)<sub>2</sub>(bppa)<sub>2</sub>]<sub>n</sub> and the [Zn(OAc)<sub>2</sub>(bipy)]<sub>n</sub> nanocomposite samples 5 – 8 (B). Most intense PXRD reflexes that correlate with the bulk material are marked with a dashed line.

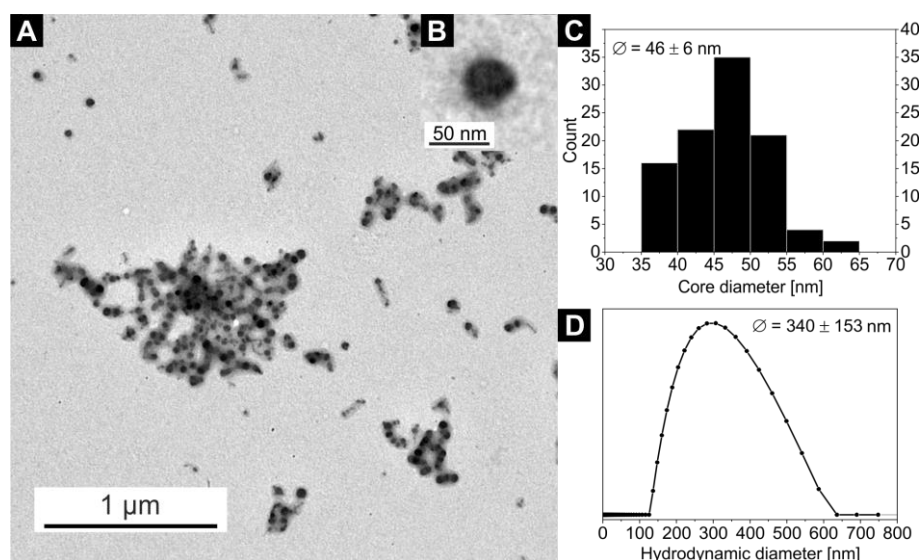
Particle sizes of the nanocomposites were also analysed by TEM and DLS (Fig. 4, 5; Fig. S9-S11). While sample 5 only shows spherical particles with core sizes of  $D_{\text{core}} = 13 \pm 1$  nm (Fig. S9), sample 7 shows spherical particles which, however, tend to form chain-like aggregates (Fig. 4). This behaviour was also observed in other samples of the same nanocomposite (Fig. S12). In fact, the formation of spherical particles rather than worm-like micelles in THF would be expected due to the low 4VP fraction of the utilised SV-15 diblock copolymer.<sup>[62,63]</sup> The presence of the anisotropic 2D CN together with the limited space available in the P4VP core of the highly asymmetric SV-15 BCP micelles ( $D_{\text{core}} = 15 \pm 2$  nm,  $D_h = 177 \pm 57$  nm for sample 7) could trigger the formation of chain-like structures, even at comparably low 4VP fractions. This may be an effect that occurs during drying of the sample on the TEM grid, since the hydrodynamic diameter distribution of sample 7 is rather narrow (Fig. 4C) and  $D_h$  is only slightly increased compared to that of sample 5 (Table 2).

The particle core sizes of samples 6 ( $D_{\text{core}} = 49 \pm 4$  nm, Fig. S9) and 8 ( $D_{\text{core}} = 46 \pm 6$  nm, Fig. 5) are in good agreement with the core sizes of samples 1 – 4 ( $D_{\text{core}} \approx 47 - 50$  nm, Fig. 2, S4), which were synthesised using the same BCP (SV-42, Table 2). This underlines the fact that the BCP determines the size of the nanocomposites. Again, the formed nanocomposite particles tend to form chain-like structures for sample 8 (2 loading cycles), as observed by TEM. Another interesting phenomenon arises upon comparing the DLS measurements of samples 6 and 8. While the

average hydrodynamic diameter of sample **6** was determined to  $D_h = 160 \pm 46$  nm (Fig. S10), which correlates well with the hydrodynamic diameters of the samples **1** – **4**, the average hydrodynamic diameter of sample **8** is more than twice as large ( $D_h = 340 \pm 153$  nm, Fig. 5) and the hydrodynamic diameter distribution is significantly broadened. This might point to the presence of chain-like (worm-like) structures already in solution. The shorter soluble PS blocks in the corona of SV-42 micelles might be less efficient in shielding the highly anisotropic CN in the micellar core and, thus, favouring the formation of chain-like structures. This assumption is supported by the fact that in Fig. 5A individual spherical CN nanoparticles can be recognized in the chain-like micellar structures.

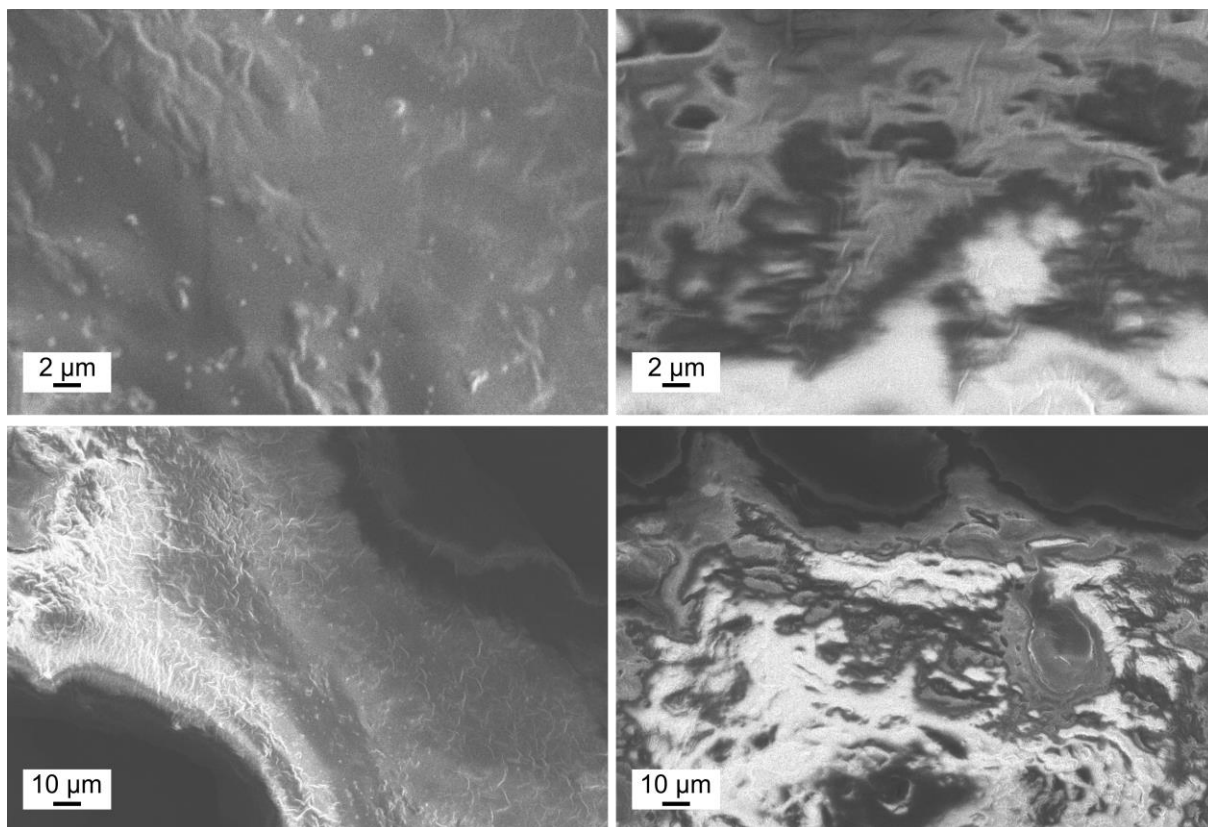


**Fig. 4:** (A) TEM image of sample **7**. (B) An inset with a zoom on a single nanoparticle. (C) Core size distribution  $D_{core}$  (from TEM) and (D) hydrodynamic diameter distribution  $D_h$  (from DLS) of nanocomposite sample **7** (for DLS autocorrelation function see Fig. S11).



**Fig. 5:** (A) TEM image of sample **8**. (B) An inset with a zoom on a single nanoparticle. (C) Core size distribution  $D_{\text{core}}$  (from TEM) and (D) hydrodynamic diameter distribution  $D_h$  (from DLS) of sample **8** (for DLS autocorrelation function see Fig. S11).

The SEM images for the samples **5** – **8** (Fig. 6, S13) show the absence of microcrystals on the surface of the nanocomposites, proving that the 2D CN is incorporated inside the P4VP cores of the micellar BCP. However, if samples with more than 2 reaction cycles were synthesised, the very low solubility of the 2D CN  $[\text{Zn}(\text{TFA})_2(\text{bppa})_2]_n$  led to a fast precipitation of the CN, thus, resulting in the formation of microcrystals on the polymer surface and in the reaction solution. Consequently, the formation of truncated cuboctahedron crystals on the nanocomposite surface was observed by SEM (Fig. S3).



**Fig. 6:** SEM images of sample **7** (left) and sample **8** (right) at two different magnifications. No microcrystals can be observed on the polymer surface for both samples.

### 8.3. Conclusions

The synthesis of well-defined 1D, 2D and 3D coordination polymer (CP) and network (CN) nanoparticles is highly challenging. Self-assembled polymeric micelles derived from block copolymers (BCPs) that offer coordination sites inside the micellar core may be an elegant and generally applicable concept for the direct synthesis of these CP and CN nanoparticles (NPs). We were able to show that our established synthetic approach can be adapted to other 1D CP like the double-stranded  $[\text{Zn}(\text{OAc})_2(\text{bipy})]_n$  and more importantly to the 2D CN  $[\text{Zn}(\text{TFA})_2(\text{bppa})_2]_n$ . Employing micelles of the BCP SV-42 as template, it was possible to achieve spherical NPs of the 1D CP  $[\text{Zn}(\text{OAc})_2(\text{bipy})]_n$  and the 2D CN  $[\text{Zn}(\text{TFA})_2(\text{bppa})_2]_n$  with nanocomposite core sizes of  $D_{\text{core}} = 47 \pm 5$  nm and  $D_{\text{core}} = 46 \pm 6$  nm, respectively. The average hydrodynamic diameter was determined to  $D_h = 157 \pm 46$  nm for the  $[\text{Zn}(\text{OAc})_2(\text{bipy})]_n$  and to  $D_h = 340 \pm 153$  nm for the  $[\text{Zn}(\text{TFA})_2(\text{bppa})_2]_n$  nanocomposites. Moreover, even smaller composite NPs of the 2D CN  $[\text{Zn}(\text{TFA})_2(\text{bppa})_2]_n$  were successfully prepared in SV-15 micelles, having a core size  $D_{\text{core}}$  as small as  $15 \pm 2$  nm and a hydrodynamic diameter of  $D_h = 139 \pm 39$  nm. No microcrystals were found on the nanocomposite surface as proven by SEM measurements. The crystallinity of the

nanocomposite samples increases with the loading cycles, showing characteristic reflexes in the PXRD at positions identical to the bulk materials. Since it was possible to synthesise NPs of the double-stranded 1D CP  $[\text{Zn}(\text{OAc})_2(\text{bipy})]_n$  and particularly the 2D CN  $[\text{Zn}(\text{TFA})_2(\text{bppa})_2]_n$ , we are convinced that our synthetic approach can be adapted to a wide range of other 1D, 2D, and even 3D CP and CN nanoparticles, which will be investigated in future work.

### 8.4. Experimental section

#### 8.4.1. Materials

4,4'-Bipyridine (bipy, 98 %), 1,3-di(4-pyridyl)propane (bppa, 98 %) and  $[\text{Zn}(\text{OAc})_2] \cdot 2 \text{H}_2\text{O}$  (97+ %) were obtained from Alfa Aesar and used as received. For the synthesis of  $[\text{Zn}(\text{TFA})_2] \cdot \text{H}_2\text{O}$ , zinc oxide (ZnO, 99.9%) from Sigma Aldrich, trifluoroacetic acid (TFA, 99%) from Alfa Aesar and ethanol (EtOH, p.a., Fisher Chemical) were used as received. Tetrahydrofuran (THF, p.a.) was obtained from Fisher Chemical and used as received in the synthesis of the coordination polymers and the nanocomposites.

The two polystyrene-*block*-poly(4-vinylpyridine) diblock copolymers (SV-15 and SV-42) were synthesised by sequential anionic polymerization of styrene and 4-vinylpyridine according to our previously published method.<sup>[57]</sup>

For **gel permeation chromatography** (GPC) in N,N-dimethylformamide (DMF) with lithium bromide ( $5 \text{ g L}^{-1}$ ), GRAM columns (300 x 8 mm, 10  $\mu\text{m}$  particle size, PSS Mainz) with 100 and 3000 Å pore sizes were used. The samples were measured on a SEC 1260 Infinity system (Agilent Technologies) at a flow rate of  $0.5 \text{ mL min}^{-1}$  at 23 °C, using a refractive index detector (Agilent Technologies). The calibration was done with narrowly distributed polystyrene standards (PSS calibration kit) and toluene (HPLC grade) was used as internal standard.

**MALDI-ToF MS** (matrix-assisted laser desorption/ionization time-of-flight mass spectrometry) measurements were performed on a Reflex III (Bruker) equipped with a  $\text{N}_2$  Laser ( $\lambda = 337 \text{ nm}$ ). An acceleration voltage of 20 kV was used in linear mode and the samples were prepared according to the dried droplet method. Matrix (trans-2-[3-(4-tert-butylphenyl)-2-methyl-2-propenylidene]malononitrile (DCTB,  $10 \text{ g L}^{-1}$  in THF), analyte ( $10 \text{ g L}^{-1}$  in THF) and salt (silver trifluoroacetate,  $10 \text{ g L}^{-1}$ ) were dissolved and mixed in the ratio of 20 : 5 : 1 and 0.5  $\mu\text{L}$  of the mixture was placed and dried on the target plate.

**$^1\text{H}$ -NMR** spectra were acquired with a Bruker Ultrashield 300 spectrometer using  $\text{CDCl}_3$  as solvent.

**Transmission electron microscopy** (TEM) was conducted on a Zeiss CEM902 electron microscope (Zeiss, Oberkochen, Germany). Samples were dispersed in THF at a concentration of 2 g L<sup>-1</sup>. The unfiltered solution was dropped on a carbon coated copper grid (mesh 200, Science Services, Munich). Electron acceleration voltage was set to 80 kV. Micrographs were taken with a MegaView III / iTEM image acquiring and processing system from Olympus Soft Imaging Systems (OSIS, Münster, Germany) and an Orius 830 SC200W / DigitalMicrograph system from Gatan (Munich, Germany). Particles size measurements were done with “ImageJ” image processing software developed by Wayne Rasband (National Institutes of Health, USA).

**Scanning electron microscopy** (SEM) micrographs were taken on a Zeiss LEO 1530 GEMINI. The acceleration voltage was set to 3 kV and the sample was sputter-coated with a 1.3 nm platinum layer.

**Dynamic light scattering** (DLS) measurements were done with an AntonPaar Litesizer 500 in quartz glass cuvettes from Helma at 25 °C in backscattering mode (175°). One measurement consists of six consecutive runs. Samples were dispersed in THF at a concentration of 2 g L<sup>-1</sup>. The unfiltered solution was used.

Room temperature **powder X-ray diffraction** (PXRD) data were collected with a STOE StadiP X-Ray diffractometer in transmission geometry between 5° and 30° 2θ for all samples, which were placed on flat surfaces. Cu-K<sub>α1</sub> radiation ( $\lambda = 1.541 \text{ \AA}$ ) was used for the measurements together with a Mythen 1K detector.

For **elemental analysis**, the carbon, nitrogen, and hydrogen contents were determined with a Vario EL III (Elementar Analysensysteme GmbH) with acetanilide as standard or at a Unicube (Elementar Analysensysteme GmbH) with sulfanilamide as standard. The samples were placed in tin boats and measured at least twice. The average of the measurements was used.

Transmission **infrared spectra** (IR) were collected on a Perkin Elmer Spectrum 100 FT-IR (ATR). The samples were measured directly as solids.

#### 8.4.2. Computation setting

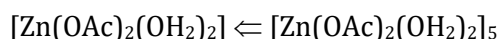
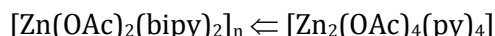
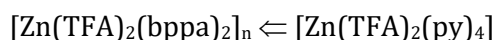
Theoretical structure calculations on the zinc(II) precursor complexes and coordination polymer/network models have been performed through density-functional theory (DFT) methods using the ORCA program package.<sup>[64]</sup> For all optimizations triple- $\xi$ -valence TZVP<sup>[65]</sup> basis sets were used with the generalized gradient approximated functional BP86.<sup>[66]</sup> Grimme’s third generation D3 correction of dispersion was used.<sup>[67,68]</sup> Medium effects were included in a dielectric continuum approach (COSMO), parameterized for acetonitrile;<sup>[69]</sup> the inclusion of a stationary dielectric background proved beneficial for the match between experimental and theoretically

---



observed structures. Optimized structures have been identified as stationary points through the absence of imaginary modes in harmonic frequency calculations; spurious low-frequency imaginary modes in some calculations due to -CH<sub>3</sub> rotations are typical artefacts of DFT-based numerical frequency scans. Coordinates of the computed structures are assembled in the SI, Tables S1 to S4. Graphical presentation of the vibrational modes are also available (anim\_1-6.gif).

**Phenomenological approach.** The input structure of [Zn(TFA)<sub>2</sub>(OH<sub>2</sub>)<sub>4</sub>] was extracted from the available XRD data.<sup>[70]</sup> In order to reduce computational cost, we have approximated the coordination polymers and the bulk [Zn(OAc)<sub>2</sub>] · 2 H<sub>2</sub>O precursor as truncated model complexes. Thereby we have put emphasis on the conservation of the first coordination sphere of the zinc centres. The bidentate bridging ligands were mimicked as monodentate pyridine ligands. In particular we employed the settings:



The highly H-bonded nature of the molecular modules in [Zn(OAc)<sub>2</sub>] · 2 H<sub>2</sub>O made it necessary to extract a pentanuclear motif from the crystal structure. Herein the central module possesses a conserved H-bond network (C=O and coordinated water) to serve as the theoretical probe; H-bond donor and acceptor sites of the terminal modules remained unsaturated. As a matter of fact, this model gives very satisfying agreement with the experimental IR spectrum. Graphical representations of the DFT optimized structure models are given in the SI, Figures S14 and S15.

### 8.4.3. Synthesis

**Synthesis of [Zn(TFA)<sub>2</sub>] · H<sub>2</sub>O.** [Zn(TFA)<sub>2</sub>] · H<sub>2</sub>O was synthesized by dissolving 1 g (12.3 mmol, 1 eq) ZnO in 10 mL EtOH and 1.9 mL (2.8 g, 24.6 mmol, 2 eq) TFA in an ice bath and stirred until complete dissolution. The solution was filtered and the solvent was evaporated on a heating plate at 120 °C for several days. The resulting white powder was transferred into a Schlenk flask, dried in vacuo, and stored under argon. Yield: 3.42 g (11.7 mmol, 90 %). Elemental anal. (%) calc: C 16.49, H 0.65, found: C 16.51, H 0.70.

**Synthesis of [Zn(OAc)<sub>2</sub>(bipy)]<sub>n</sub> nanocomposites (samples 1 – 4).** 50 mg of the diblock copolymer SV-42 were placed and dissolved in a 50 mL flask in 20 mL THF under reflux until complete dissolution. The polymer solution was cooled down to rt, 2.2 mg (10 μmol, 1 eq) [Zn(OAc)<sub>2</sub>] · 2 H<sub>2</sub>O were added and the solution was refluxed for 1h. Subsequently, the reaction mixture was cooled down to rt and 2.4 mg (15 μmol, 1.5 eq) 4,4'-bipyridine were added to the

solution which was refluxed again for 1h. At this point, the synthesis can be stopped by removal of the solvent by rotary evaporation to obtain sample **1** (1 cycle). Alternatively, 2.2 mg  $[\text{Zn}(\text{OAc})_2] \cdot 2 \text{H}_2\text{O}$  and 2.4 mg 4,4'-bipyridine can be added simultaneously up to 4 more times (samples **2** to **4**; 3 – 5 cycles). All resulting light-yellow solids were dried in vacuo.

Elemental anal. (%) found:

Sample **1**: C 68.85, H 7.96, N 4.17.

Sample **2**: C 65.98, H 7.06, N 4.50.

Sample **3**: C 68.61, H 6.92, N 5.38.

Sample **4**: C 71.02, H 6.67, N 5.68.

**Synthesis of  $[\text{Zn}(\text{TFA})_2(\text{bppa})_2]_n$  nanocomposites (samples **5** – **8**).** 50 mg of the diblock copolymer SV-15 were placed in a 50 mL flask fitted with a magnetic stir bar. 20 mL THF were added and the polymer was dissolved under reflux until complete dissolution. The polymer solution was cooled down to rt and 2.0 mg (6.5  $\mu\text{mol}$ , 1 eq)  $[\text{Zn}(\text{TFA})_2] \cdot \text{H}_2\text{O}$  were added and the solution was refluxed again for 1h. Subsequently, the reaction solution was cooled down to rt. 2.8 mg (14  $\mu\text{mol}$ , 2.2 eq) 1,3-di(4-pyridyl)propane (bppa) were dissolved in 10 mL THF and the solution was added dropwise over 15 min. After the addition of the ligand solution, the reaction mixture was refluxed again for 1h. The synthesis can be stopped by removal of the solvent by rotary evaporation to obtain sample **5** (1 cycle). Alternatively, the synthesis procedure can be repeated exactly as before to synthesise sample **7** (2 cycles). The resulting light-yellow solids were dried in vacuo.

Besides the adjustment of the reactants, the synthetic procedure for samples **6** and **8** using the diblock copolymer SV-42 is identical to sample **5** and **7**, respectively. 5.8 mg (19  $\mu\text{mol}$ , 1 eq)  $[\text{Zn}(\text{TFA})_2] \cdot \text{H}_2\text{O}$  and 8.3 mg (42  $\mu\text{mol}$ , 2.2 eq) 1,3-di(4-pyridyl)propane were used during the synthesis.

Elemental anal. (%) found:

Sample **5**: C 84.08, H 7.66, N 2.42.

Sample **6**: C 70.81, H 8.26, N 4.82.

Sample **7**: C 67.24, H 7.36, N 2.64.

Sample **8**: C 64.40, H 7.02, N 5.05.

### 8.5. Conflicts of interest

There are no conflicts to declare.

### 8.6. Acknowledgements

Financial support of the University of Bayreuth and the SFB 840 (TP A10 and A2) is gratefully acknowledged. Christoph Göbel was supported by the BayNAT program of the University of Bayreuth. We acknowledge the Keylab Electron and Optical Microscopy of the Bavarian Polymer Institute for providing access to the electron microscopy facilities (SEM and TEM). We thank Magdalena Weber, Thomas Bindig and Samanta Jänsch for their contribution to the synthesis of the composites and the bulk materials, as well as Florian Puchtler (Inorganic Chemistry I, University of Bayreuth) for PXRD measurements and Dr. Christine Denner (Inorganic Chemistry II, University of Bayreuth) for SEM measurements.

### 8.7. Notes and references

- [1] T. Kitao, Y. Zhang, S. Kitagawa, B. Wang and T. Uemura, Hybridization of MOFs and polymers, *Chem. Soc. Rev.* **2017**, *46*, 3108–3133.
- [2] E. Coronado, Molecular magnetism, *Nature Rev. Mater.* **2019**. Doi: 10.1038/s41578-019-0146-8.
- [3] K. Senthil Kumar, Y. Bayeh, T. Gebretsadik, F. Elemo, M. Gebrezgiabher, M. Thomas and M. Ruben, Spin-crossover in iron(II)-Schiff base complexes, *Dalton Trans.* **2019**, *48*, 15321–15337.
- [4] J. Calbo, M. J. Golomb and A. Walsh, Redox-active metal–organic frameworks for energy conversion and storage, *J. Mater. Chem. A* **2019**, *7*, 16571–16597.
- [5] T. Rodenas, I. Luz, G. Prieto, B. Seoane, H. Miro, A. Corma, F. Kapteijn, Llabrés i Xamena, Francesc X and J. Gascon, Metal-organic framework nanosheets in polymer composite materials for gas separation, *Nat. Mater.* **2015**, *14*, 48–55.
- [6] P. Horcajada, T. Chalati, C. Serre, B. Gillet, C. Sebrie, T. Baati, J. F. Eubank, D. Heurtaux, P. Clayette, C. Kreuz, J.-S. Chang, Y. K. Hwang, V. Marsaud, P.-N. Bories, L. Cynober, S. Gil, G. Férey, P. Couvreur and R. Gref, Porous metal-organic-framework nanoscale carriers as a potential platform for drug delivery and imaging, *Nat. Mater.* **2010**, *9*, 172–178.
- [7] X. Roy, J. K.-H. Hui, M. Rabnawaz, G. Liu and M. J. MacLachlan, Prussian blue nanocontainers, *J. Am. Chem. Soc.* **2011**, *133*, 8420–8423.

- [8] M. Ohba, K. Yoneda, G. Agustí, M. C. Muñoz, A. B. Gaspar, J. A. Real, M. Yamasaki, H. Ando, Y. Nakao, S. Sakaki and S. Kitagawa, Bidirectional chemo-switching of spin state in a microporous framework, *Angew. Chem. Int. Ed.* **2009**, *48*, 4767–4771.
  - [9] E. A. Flügel, A. Ranft, F. Haase and B. V. Lotsch, Synthetic routes toward MOF nanomorphologies, *J. Mater. Chem.* **2012**, *22*, 10119–10133.
  - [10] K. Hosokawa, K. Nogi, M. Naitō and T. Yokoyama, eds., *Nanoparticle technology handbook*, Elsevier, Amsterdam, Netherlands, **2018**.
  - [11] D. J. Harding, in *Novel Magnetic Nanostructures*, ed. E. Rentschler, N. Domracheva and M. Caporali, Elsevier, **2018**, pp. 401–426.
  - [12] L. Salmon and L. Catala, Spin-crossover nanoparticles and nanocomposite materials, *C. R. Chimie* **2018**, *21*, 1230–1269.
  - [13] S. Rat, M. Piedrahita-Bello, L. Salmon, G. Molnár, P. Demont and A. Bousseksou, Coupling Mechanical and Electrical Properties in Spin Crossover Polymer Composites, *Adv. Mater.* **2018**, *30*, 1705275.
  - [14] K. Otsubo, T. Haraguchi and H. Kitagawa, Nanoscale crystalline architectures of Hofmann-type metal–organic frameworks, *Coord. Chem. Rev.* **2017**, *346*, 123–138.
  - [15] K. Senthil Kumar and M. Ruben, Emerging trends in spin crossover (SCO) based functional materials and devices, *Coord. Chem. Rev.* **2017**, *346*, 176–205.
  - [16] Y. Sun and Y. Xia, Shape-controlled synthesis of gold and silver nanoparticles, *Science* **2002**, *298*, 2176–2179.
  - [17] A. Henglein, Colloidal Palladium Nanoparticles: Reduction of Pd(II) by H<sub>2</sub>; Pd Core Au Shell Ag Shell Particles, *J. Phys. Chem. B* **2000**, *104*, 6683–6685.
  - [18] H. Wang, X. Qiao, J. Chen and S. Ding, Preparation of silver nanoparticles by chemical reduction method, *Colloids Surf. A* **2005**, *256*, 111–115.
  - [19] I. G. Koo, M. S. Lee, J. H. Shim, J. H. Ahn and W. M. Lee, Platinum nanoparticles prepared by a plasma-chemical reduction method, *J. Mater. Chem.* **2005**, *15*, 4125.
  - [20] Z. Fan, X. Chen, M. Kohn Serrano, H. Schmalz, S. Rosenfeldt, S. Förster, S. Agarwal and A. Greiner, Polymer Cages as Universal Tools for the Precise Bottom-Up Synthesis of Metal Nanoparticles, *Angew. Chem. Int. Ed.* **2015**, *54*, 14539–14544.
-

- [21] X. He, H. Li, Y. Liu, H. Huang, Z. Kang and S.-T. Lee, Water soluble carbon nanoparticles: hydrothermal synthesis and excellent photoluminescence properties, *Colloids Surf. B* **2011**, *87*, 326–332.
  - [22] T. J. Daou, G. Pourroy, S. Bégin-Colin, J. M. Grenèche, C. Ulhaq-Bouillet, P. Legaré, P. Bernhardt, C. Leuvrey and G. Rogez, Hydrothermal Synthesis of Monodisperse Magnetite Nanoparticles, *Chem. Mater.* **2006**, *18*, 4399–4404.
  - [23] H.-C. Chiu and C.-S. Yeh, Hydrothermal Synthesis of SnO<sub>2</sub> Nanoparticles and Their Gas-Sensing of Alcohol, *J. Phys. Chem. C* **2007**, *111*, 7256–7259.
  - [24] Vaucher, S., M. Li and S. Mann, Synthesis of Prussian Blue Nanoparticles and Nanocrystal Superlattices in Reverse Microemulsions, *Angew. Chem. Int. Ed.* **2000**, *39*, 1793–1796.
  - [25] T. Forestier, A. Kaiba, S. Pechev, D. Denux, P. Guionneau, C. Etrillard, N. Daro, E. Freysz and J.-F. Létard, Nanoparticles of Fe(NH<sub>2</sub>-trz)<sub>3</sub>Br<sub>2</sub>·3H<sub>2</sub>O (NH<sub>2</sub>-trz=2-amino-1,2,4-triazole) prepared by the reverse micelle technique: influence of particle and coherent domain sizes on spin-crossover properties, *Chem. Eur. J.* **2009**, *15*, 6122–6130.
  - [26] L. Salmon, G. Molnár, D. Zitouni, C. Quintero, C. Bergaud, J.-C. Micheau and A. Bousseksou, A novel approach for fluorescent thermometry and thermal imaging purposes using spin crossover nanoparticles, *J. Mater. Chem.* **2010**, *20*, 5499.
  - [27] Z. Zhang, R. C. Patel, R. Kothari, C. P. Johnson, S. E. Friberg and P. A. Aikens, Stable Silver Clusters and Nanoparticles Prepared in Polyacrylate and Inverse Micellar Solutions, *J. Phys. Chem. B* **2000**, *104*, 1176–1182.
  - [28] X. M. Lin, C. M. Sorensen, K. J. Klabunde and G. C. Hadjipanayis, Temperature Dependence of Morphology and Magnetic Properties of Cobalt Nanoparticles Prepared by an Inverse Micelle Technique, *Langmuir* **1998**, *14*, 7140–7146.
  - [29] J. H. González-Estefan, M. Gonidec, N. Daro, M. Marchivie and G. Chastanet, Extreme downsizing in the surfactant-free synthesis of spin-crossover nanoparticles in a microfluidic flow-focusing junction, *Chem. Commun.* **2018**, *54*, 8040–8043.
  - [30] J. Puigmartí-Luis, Microfluidic platforms: a mainstream technology for the preparation of crystals, *Chem. Soc. Rev.* **2014**, *43*, 2253–2271.
  - [31] S. Marre and K. F. Jensen, Synthesis of micro and nanostructures in microfluidic systems, *Chem. Soc. Rev.* **2010**, *39*, 1183–1202.
  - [32] S. Förster and M. Antonietti, Amphiphilic Block Copolymers in Structure-Controlled Nanomaterial Hybrids, *Adv. Mater.* **1998**, *10*, 195–217.
-

- [33] B. Weber, Synthesis of Coordination Polymer Nanoparticles using Self-Assembled Block Copolymers as Template, *Chem. Eur. J.* **2017**, *23*, 18093–18100.
  - [34] D. Liu, R. C. Huxford and W. Lin, Phosphorescent nanoscale coordination polymers as contrast agents for optical imaging, *Angew. Chem. Int. Ed.* **2011**, *50*, 3696–3700.
  - [35] A. Pramanik and G. Das, Precursory Ag-bipyridine 2D coordination polymer: a new and efficient route for the synthesis of Agnanoparticles, *CrystEngComm* **2010**, *12*, 401–405.
  - [36] Z. R. Ranjbar and A. Morsali, Sonochemical synthesis of a novel nano-rod two-dimensional zinc(II) coordination polymer; preparation of zinc(II) oxide nanoparticles by direct thermolyses, *Ultrason. Sonochem.* **2011**, *18*, 644–651.
  - [37] J. Larionova, Y. Guari, C. Sangregorio and C. Guérin, Cyano-bridged coordination polymer nanoparticles, *New J. Chem.* **2009**, *33*, 1177.
  - [38] H. Cao, *Synthesis and Applications of Inorganic Nanostructures*, Wiley-VCH Verlag GmbH & Co. KGaA, Weinheim, Germany, **2017**.
  - [39] V. Martínez, I. Boldog, A. B. Gaspar, V. Ksenofontov, A. Bhattacharjee, P. Gülich and J. A. Real, Spin Crossover Phenomenon in Nanocrystals and Nanoparticles of  $[\text{Fe}(\text{3-Fpy})_2\text{M}(\text{CN})_4]$  ( $\text{M}(\text{II}) = \text{Ni}, \text{Pd}, \text{Pt}$ ) Two-Dimensional Coordination Polymers, *Chem. Mater.* **2010**, *22*, 4271–4281.
  - [40] J. Larionova, L. Salmon, Y. Guari, A. Tokarev, K. Molvinger, G. Molnár and A. Bousseksou, Towards the Ultimate Size Limit of the Memory Effect in Spin-Crossover Solids, *Angew. Chem. Int. Ed.* **2008**, *47*, 8236–8240.
  - [41] Y. Guari, J. Larionova, K. Molvinger, B. Folch and C. Guérin, Magnetic water-soluble cyano-bridged metal coordination nano-polymers, *Chem. Commun.* **2006**, 2613–2615.
  - [42] Y. Guari, J. Larionova, M. Corti, A. Lascialfari, M. Marinone, G. Poletti, K. Molvinger and C. Guérin, Cyano-bridged coordination polymer nanoparticles with high nuclear relaxivity: toward new contrast agents for MRI, *Dalton Trans.* **2008**, 3658–3660.
  - [43] L. Catala, C. Mathonière, A. Gloter, O. Stephan, T. Gacoin, J.-P. Boilot and T. Mallah, Photomagnetic nanorods of the  $\text{Mo}(\text{CN})_8\text{Cu}_2$  coordination network, *Chem. Commun.*, **2005**, 746–748.
  - [44] T. Uemura and S. Kitagawa, Prussian blue nanoparticles protected by poly(vinylpyrrolidone), *J. Am. Chem. Soc.* **2003**, *125*, 7814–7815.
-

- [45] Q. Song, S. K. Nataraj, M. V. Roussanova, J. C. Tan, D. J. Hughes, W. Li, P. Bourgoïn, M. A. Alam, A. K. Cheetham, S. A. Al-Muhtaseb and E. Sivaniah, Zeolitic imidazolate framework (ZIF-8) based polymer nanocomposite membranes for gas separation, *Energy Environ. Sci.* **2012**, *5*, 8359.
  - [46] R. Weeber, M. Hermes, A. M. Schmidt and C. Holm, Polymer architecture of magnetic gels: a review, *J. Physics: Condensed matter* **2018**, *30*, 63002.
  - [47] S. Reinicke, S. Döhler, S. Tea, M. Krekhova, R. Messing, A. M. Schmidt and H. Schmalz, Magneto-responsive hydrogels based on maghemite/triblock terpolymer hybrid micelles, *Soft Matter* **2010**, *6*, 2760.
  - [48] M. Krekhova, T. Lang, R. Richter and H. Schmalz, Thermoreversible hydroferrogels with tunable mechanical properties utilizing block copolymer mesophases as template, *Langmuir* **2010**, *26*, 19181–19190.
  - [49] O. Eksik, J. Gao, S. A. Shojaee, A. Thomas, P. Chow, S. F. Bartolucci, D. A. Lucca and N. Koratkar, Epoxy nanocomposites with two-dimensional transition metal dichalcogenide additives, *ACS nano* **2014**, *8*, 5282–5289.
  - [50] J. Gass, P. Poddar, J. Almand, S. Srinath and H. Srikanth, Superparamagnetic Polymer Nanocomposites with Uniform Fe<sub>3</sub>O<sub>4</sub> Nanoparticle Dispersions, *Adv. Funct. Mater.* **2006**, *16*, 71–75.
  - [51] J. L. Wilson, P. Poddar, N. A. Frey, H. Srikanth, K. Mohomed, J. P. Harmon, S. Kotha and J. Wachsmuth, Synthesis and magnetic properties of polymer nanocomposites with embedded iron nanoparticles, *J. Appl. Phys.* **2004**, *95*, 1439–1443.
  - [52] J. Li, S. I. Seok, B. Chu, F. Dogan, Q. Zhang and Q. Wang, Nanocomposites of Ferroelectric Polymers with TiO<sub>2</sub> Nanoparticles Exhibiting Significantly Enhanced Electrical Energy Density, *Adv. Mater.* **2009**, *21*, 217–221.
  - [53] J. Schöbel, C. Hils, A. Weckwerth, M. Schlenk, C. Bojer, M. C. A. Stuart, J. Breu, S. Förster, A. Greiner, M. Karg and H. Schmalz, Strategies for the selective loading of patchy worm-like micelles with functional nanoparticles, *Nanoscale* **2018**, *10*, 18257–18268.
  - [54] J. Schöbel, M. Burgard, C. Hils, R. Dersch, M. Dulle, K. Volk, M. Karg, A. Greiner and H. Schmalz, Bottom-Up Meets Top-Down: Patchy Hybrid Nonwovens as an Efficient Catalysis Platform, *Angew. Chem. Int. Ed.* **2017**, *56*, 405–408.
-

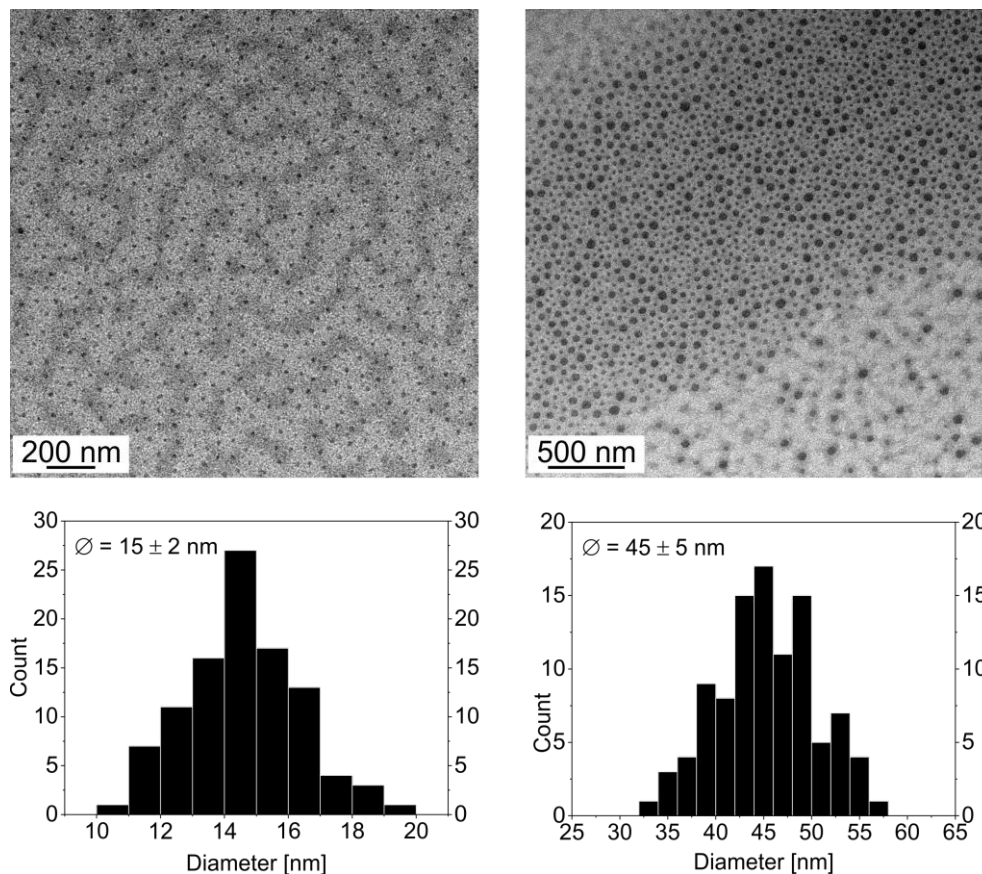
- [55] J. Schöbel, M. Karg, D. Rosenbach, G. Krauss, A. Greiner and H. Schmalz, Patchy Wormlike Micelles with Tailored Functionality by Crystallization-Driven Self-Assembly: A Versatile Platform for Mesostructured Hybrid Materials, *Macromolecules* **2016**, *49*, 2761–2771.
  - [56] Z. Fan, M. K. Serrano, A. Schaper, S. Agarwal and A. Greiner, Polymer/Nanoparticle Hybrid Materials of Precise Dimensions by Size-Exclusive Fishing of Metal Nanoparticles, *Adv. Mater.* **2015**, *27*, 3888–3893.
  - [57] C. Göbel, C. Hils, M. Drechsler, D. Baabe, A. Greiner, H. Schmalz and B. Weber, Confined Crystallization of Spin-Crossover Nanoparticles in Block-Copolymer Micelles, *Angew. Chem. Int. Ed.* **2020**, *59*, 5765–5770.
  - [58] O. Klimm, C. Göbel, S. Rosenfeldt, F. Puchtler, N. Miyajima, K. Marquardt, M. Drechsler, J. Breu, S. Förster and B. Weber, Synthesis of Fe(L)(bipy)<sub>n</sub> spin crossover nanoparticles using blockcopolymer micelles, *Nanoscale* **2016**, *8*, 19058–19065.
  - [59] C. Göbel, O. Klimm, F. Puchtler, S. Rosenfeldt, S. Förster and B. Weber, Synthesis of [Fe(L<sub>eq</sub>)(L<sub>ax</sub>)]<sub>n</sub> coordination polymer nanoparticles using blockcopolymer micelles, *Beilstein J. Nanotechnol.* **2017**, *8*, 1318–1327.
  - [60] B. Conerney, P. Jensen, P. E. Kruger, B. Moubaraki and K. S. Murray, Synthesis and structural characterisation of two coordination polymers (molecular ladders) incorporating [M(OAc)<sub>2</sub>]<sub>2</sub> secondary building units and 4,4'-bipyridine [M = Cu(II), Zn(II)], *CrystEngComm* **2003**, *5*, 454–458.
  - [61] Y. V. Kokunov, Y. E. Gorbunova, V. V. Kovalev and A. S. Kozyukhin, 2D-layered structure of coordination polymer, zinc trifluoroacetate-1,3-bis(4-pyridyl)propane, *Russ. J. Inorg. Chem.* **2014**, *59*, 187–191.
  - [62] N. Ali and S.-Y. Park, Micellar structures of poly(styrene-*b*-4-vinylpyridine)s in THF/toluene mixtures and their functionalization with gold, *Langmuir* **2008**, *24*, 9279–9285.
  - [63] D. J. Adams and P. D. Topham, in *Supramolecular Chemistry*, ed. P. A. Gale and J. W. Steed, John Wiley & Sons, Ltd, Chichester, UK, **2012**.
  - [64] F. Neese, The ORCA program system, *WIREs Comput. Mol. Sci.* **2012**, *2*, 73–78.
  - [65] A. Schäfer, H. Horn and R. Ahlrichs, Fully optimized contracted Gaussian basis sets for atoms Li to Kr, *J. Chem. Phys.* **1992**, *97*, 2571–2577.
  - [66] Becke, Density-functional exchange-energy approximation with correct asymptotic behavior, *Phys. Rev. A* **1988**, *38*, 3098–3100.
-



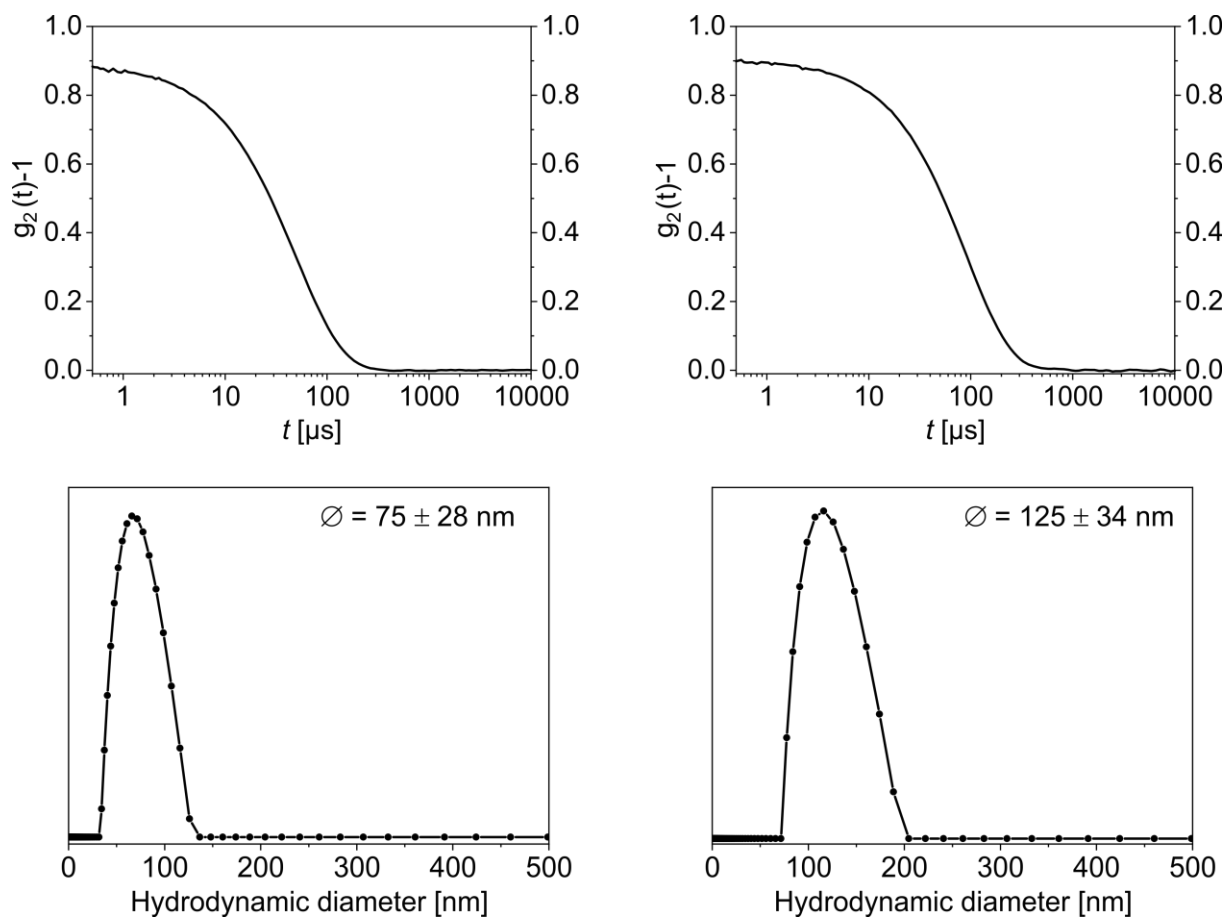
- [67] S. Grimme, S. Ehrlich and L. Goerigk, Effect of the damping function in dispersion corrected density functional theory, *J. Comput. Chem.* **2011**, *32*, 1456–1465.
- [68] S. Grimme, J. Antony, S. Ehrlich and H. Krieg, A consistent and accurate ab initio parametrization of density functional dispersion correction (DFT-D) for the 94 elements H-Pu, *J. Chem. Phys.* **2010**, *132*, 154104.
- [69] A. Klamt and G. Schüürmann, COSMO: a new approach to dielectric screening in solvents with explicit expressions for the screening energy and its gradient, *J. Chem. Soc., Perkin Trans. 2* **1993**, 799–805.
- [70] I. V. Morozov, E. V. Karpova, T. Y. Glazunova, A. I. Boltalin, M. A. Zakharov, D. S. Tereshchenko, A. A. Fedorova and S. I. Troyanov, Trifluoroacetate complexes of 3d elements: Specific features of syntheses and structures, *Russ. J. Coord. Chem.* **2016**, *42*, 647–661.

## 8.8. Supporting Information

### TEM of the empty micelles

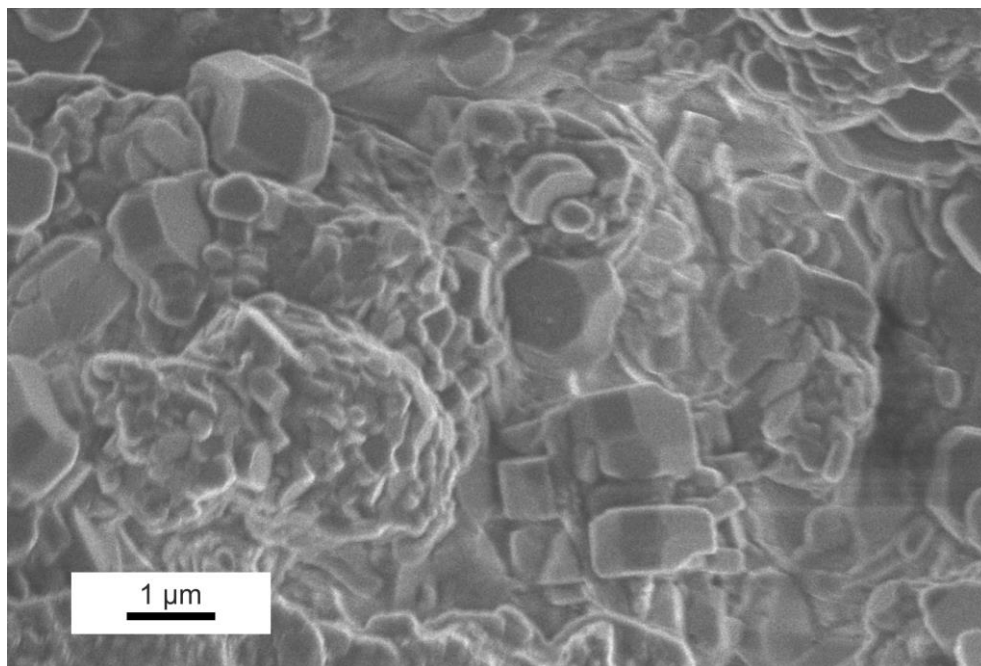


**Fig. S1:** TEM images of the empty SV-15 (top left) and SV-42 (top right) BCP micelles and the corresponding core size distributions (bottom row).

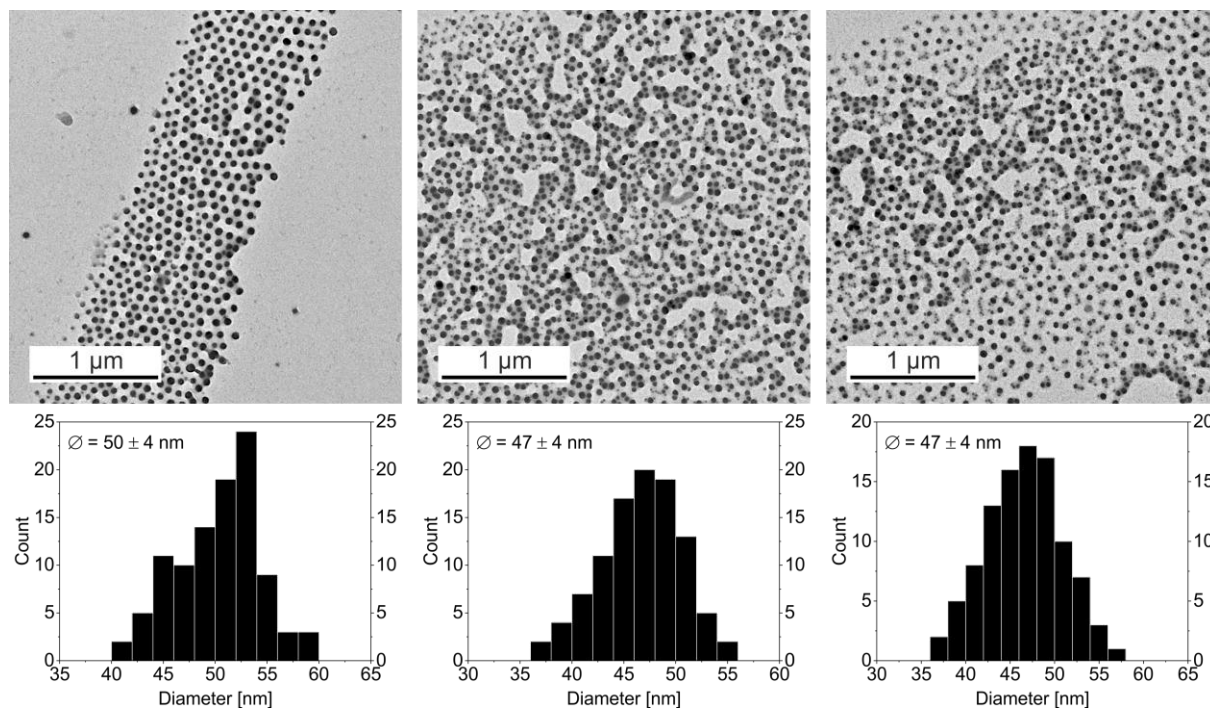
**DLS of empty BCP micelles**

**Fig. S2:** DLS measurements of the empty SV-15 (left) and SV-42 (right) BCP micelles. The autocorrelation functions  $g_2(t)-1$  vs.  $t$  are given in the top row and the hydrodynamic diameter distributions are given in the bottom row, respectively.

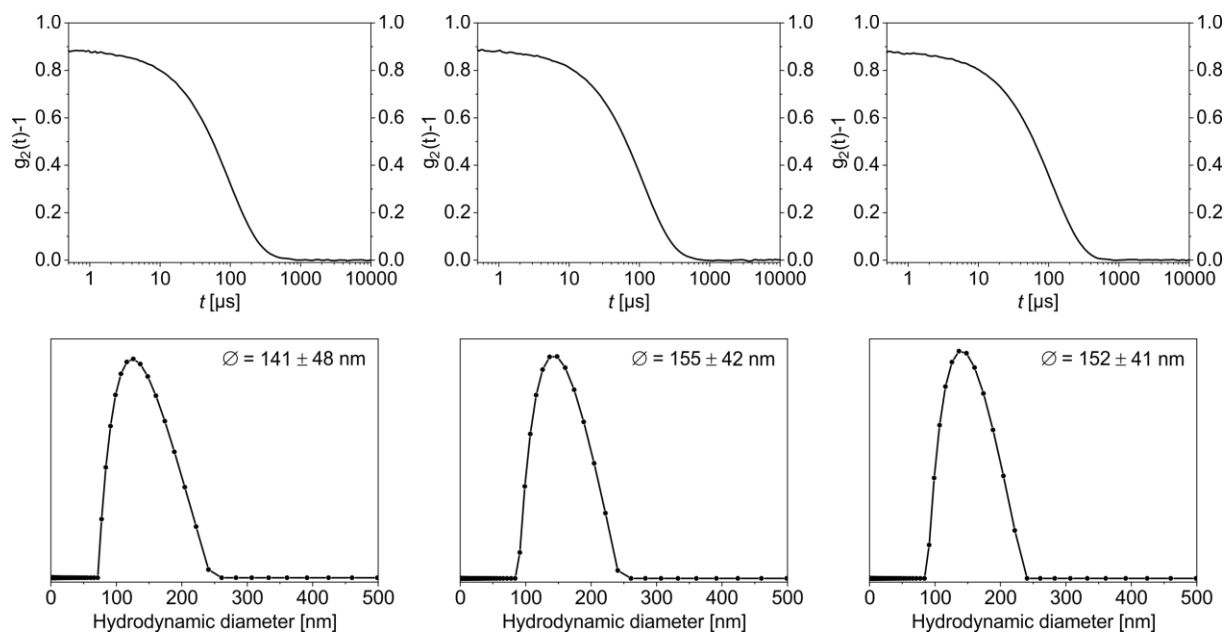
**SEM of a  $[\text{Zn}(\text{TFA})_2(\text{bppa})_2]_n$  composite with microcrystals**



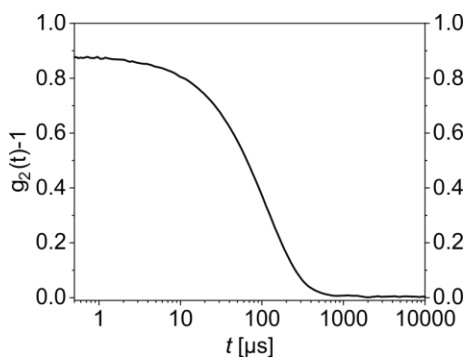
**Fig. S3:** SEM image of a  $[\text{Zn}(\text{TFA})_2(\text{bppa})_2]_n$  composite showing truncated cuboctahedron crystals of the CP on the sample surface.

**TEM of  $[\text{Zn}(\text{OAc})_2(\text{bipy})]_n$  nanocomposites (samples 1 – 3)**

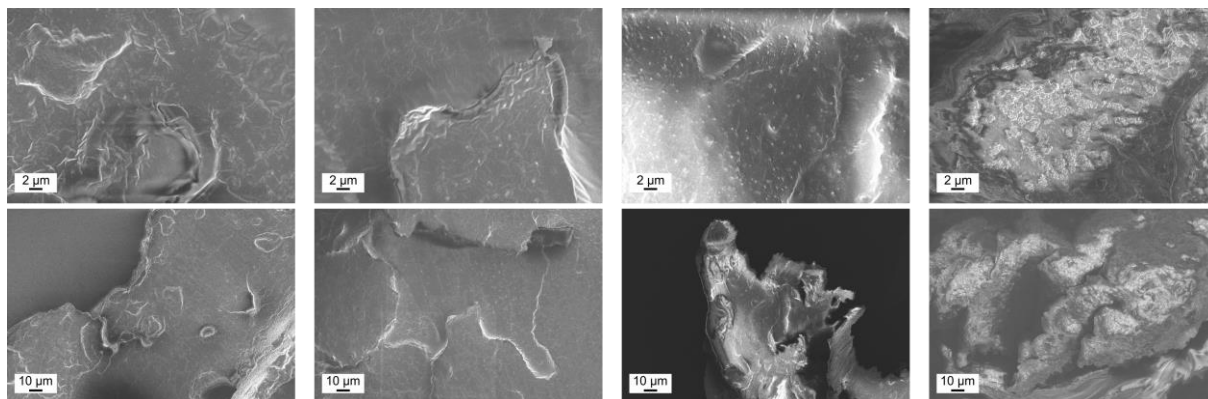
**Fig. S4:** TEM images (top row) of the  $[\text{Zn}(\text{OAc})_2(\text{bipy})]_n$  nanocomposite samples **1** (left), **2** (middle) and **3** (right) and the corresponding core size distributions (bottom row).

**DLS of  $[\text{Zn}(\text{OAc})_2(\text{bipy})]_n$  nanocomposites (samples 1 – 3)**

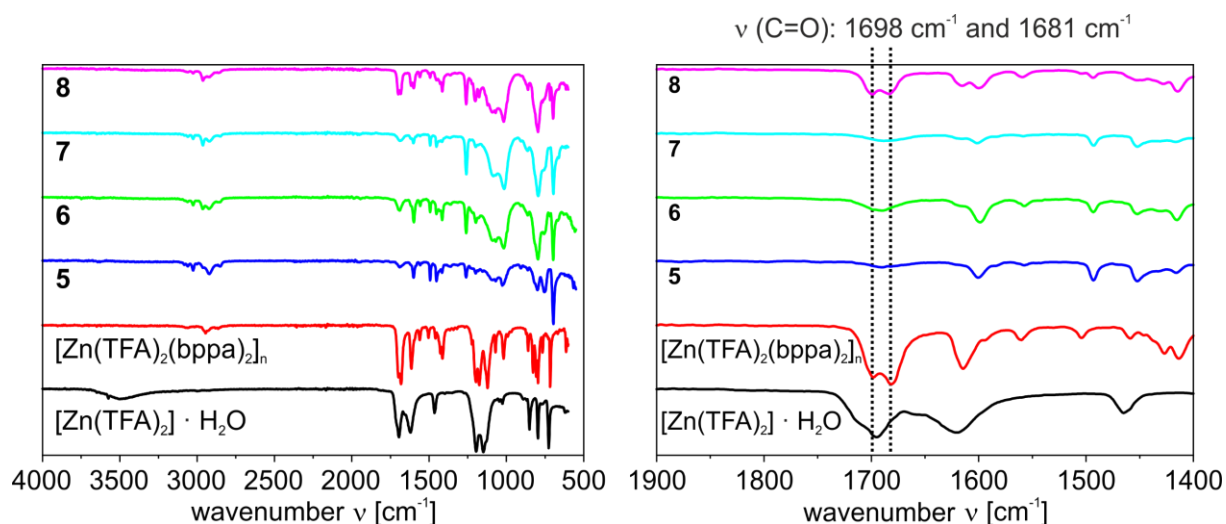
**Fig. S5:** DLS measurements of the  $[\text{Zn}(\text{OAc})_2(\text{bipy})]_n$  nanocomposite samples **1** (left), **2** (middle) and **3** (right). The autocorrelation functions  $g_2(t)-1$  vs.  $t$  are given in the top row and the hydrodynamic diameter distributions of the three samples are given in the bottom row, respectively.

**DLS of  $[\text{Zn}(\text{OAc})_2(\text{bipy})]_n$  nanocomposite sample 4**

**Fig. S6:** Autocorrelation function  $g_2(t)-1$  vs.  $t$  of  $[\text{Zn}(\text{OAc})_2(\text{bipy})]_n$  nanocomposite sample **4**.

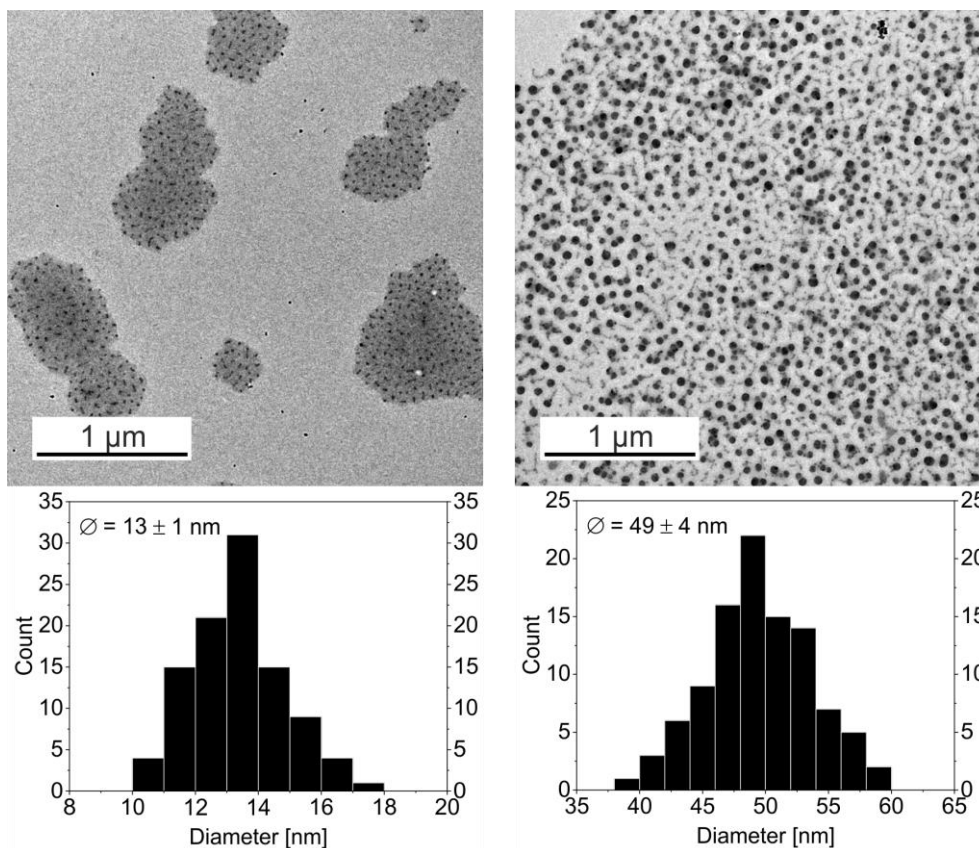
**SEM of  $[\text{Zn}(\text{OAc})_2(\text{bipy})]_n$  nanocomposites (samples 1 – 4)**

**Fig. S7:** SEM images of the  $[\text{Zn}(\text{OAc})_2(\text{bipy})]_n$  nanocomposite samples 1 – 4 (from left to right), showing the absence of microcrystals on the surface of the polymer.

**FT-IR of  $[\text{Zn}(\text{TFA})_2(\text{bppa})_2]_n$  nanocomposites (samples 5 – 8), starting material  $[\text{Zn}(\text{TFA})_2] \cdot \text{H}_2\text{O}$  and bulk material  $[\text{Zn}(\text{TFA})_2(\text{bppa})_2]_n$** 


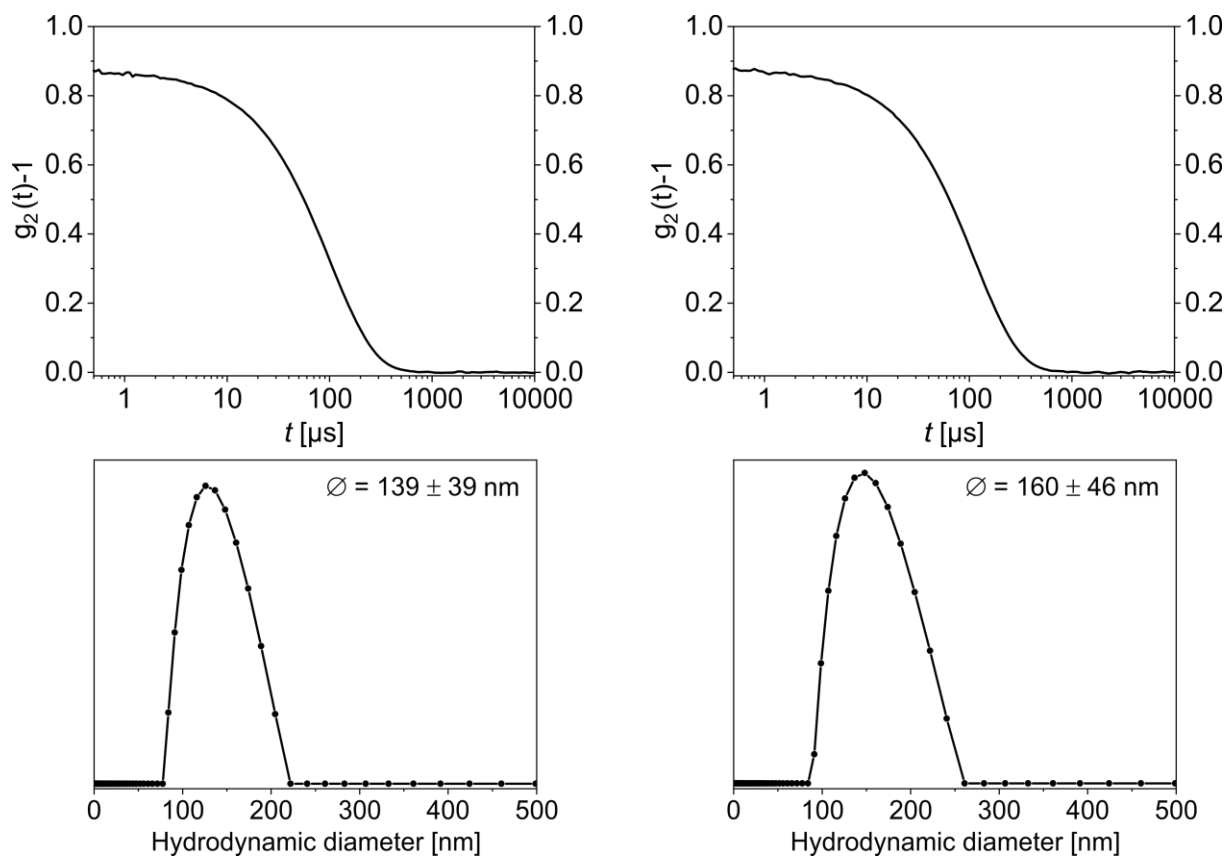
**Fig. S8:** IR spectra of the starting material  $[\text{Zn}(\text{TFA})_2] \cdot \text{H}_2\text{O}$ , the bulk material  $[\text{Zn}(\text{TFA})_2(\text{bppa})_2]_n$  and the  $[\text{Zn}(\text{TFA})_2(\text{bppa})_2]_n$  nanocomposite samples 5 – 8 in the spectral region of 4000  $\text{cm}^{-1}$  to 550  $\text{cm}^{-1}$  (left). Each material shows a C=O band at 1698  $\text{cm}^{-1}$ . This band is increasing in intensity compared to other bands in the samples 5 – 8 with higher cycle count. Additionally, the bulk material and sample 8 show a second C=O band at 1681  $\text{cm}^{-1}$ . A detailed view on the spectral region of 1900  $\text{cm}^{-1}$  to 1400  $\text{cm}^{-1}$  is also given (right).

TEM of  $[\text{Zn}(\text{TFA})_2(\text{bppa})_2]_n$  nanocomposites (samples 5 and 6)



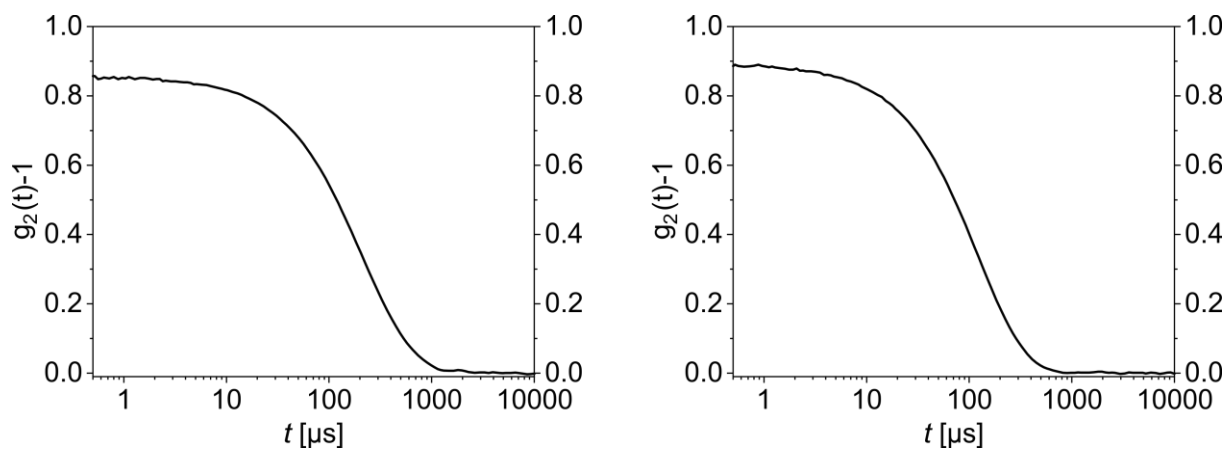
**Fig. S9:** TEM images (top row) of the  $[\text{Zn}(\text{TFA})_2(\text{bppa})_2]_n$  nanocomposite sample 5 (left) and sample 7 (right) with the corresponding core size distributions (bottom row).



**DLS of  $[\text{Zn}(\text{TFA})_2(\text{bppa})_2]_n$  nanocomposites (samples 5 and 6)**

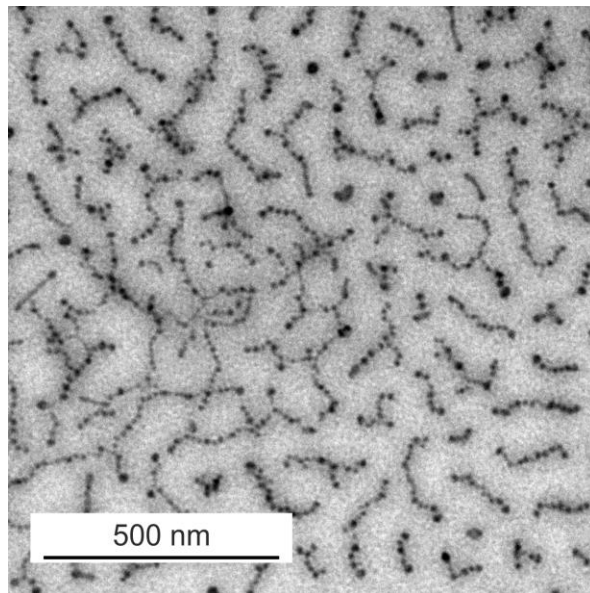
**Fig. S10:** DLS measurements of the  $[\text{Zn}(\text{TFA})_2(\text{bppa})_2]_n$  nanocomposite sample 5 (left) and sample 7 (right). The autocorrelation functions  $g_2(t)-1$  vs.  $t$  (top) are given together with the hydrodynamic diameter distributions (bottom), respectively.

### DLS of $[\text{Zn}(\text{TFA})_2(\text{bppa})_2]_n$ nanocomposites (samples 7 and 8)



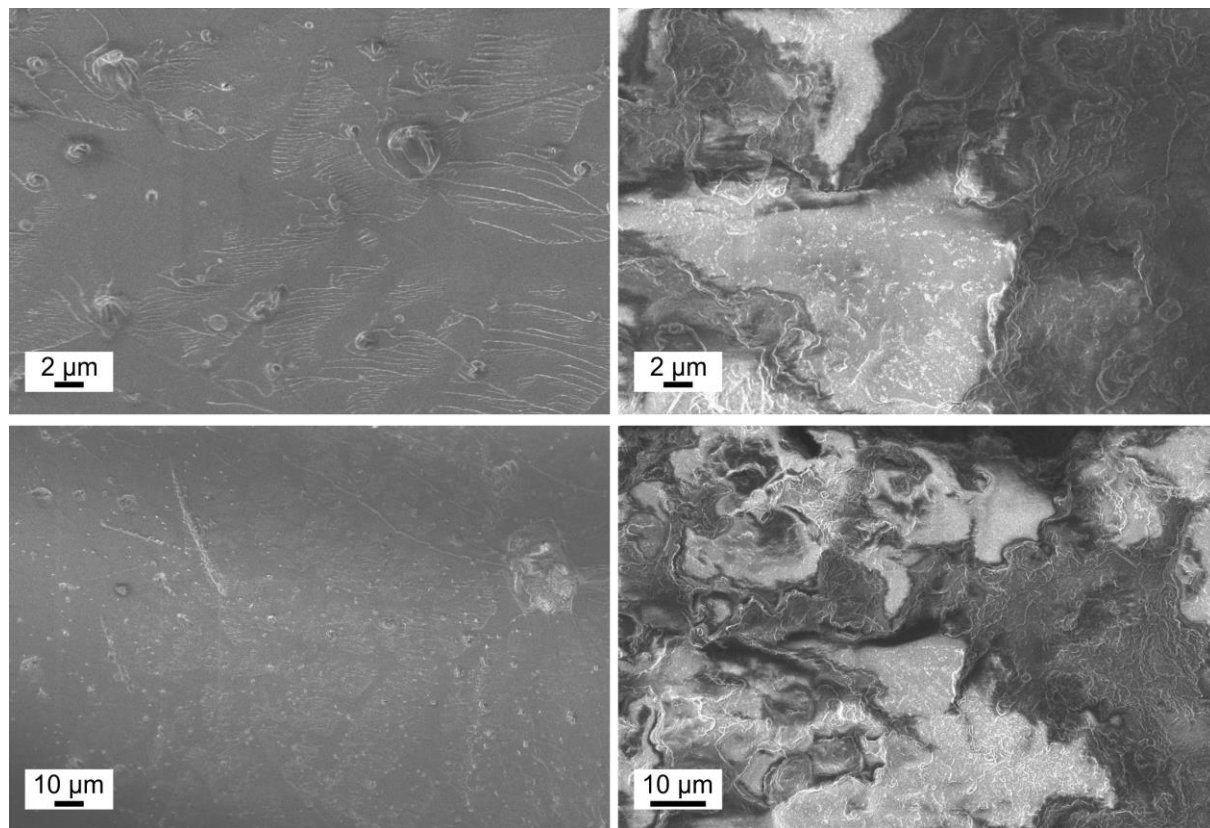
**Fig. S11:** DLS autocorrelation functions  $g_2(t)-1$  vs.  $t$  for the  $[\text{Zn}(\text{TFA})_2(\text{bppa})_2]_n$  nanocomposite sample 7 (left) and sample 8 (right).

### TEM image of $[\text{Zn}(\text{TFA})_2(\text{bppa})_2]_n$ nanocomposite particles showing a chain-like structure



**Fig. S12:** TEM image of a  $[\text{Zn}(\text{TFA})_2(\text{bppa})_2]_n$  nanocomposite showing spherical nanoparticles agglomerating into a chain-like structure.

**SEM of  $[\text{Zn}(\text{TFA})_2(\text{bppa})_2]_n$  nanocomposites (samples 5 and 6)**



**Fig. S13:** SEM images of the surfaces of the  $[\text{Zn}(\text{TFA})_2(\text{bppa})_2]_n$  nanocomposite sample 5 (left) and 6 (right), showing the absence of microcrystals.

**Table S1** Cartesian coordinates of optimized mononuclear [Zn(TFA)<sub>2</sub>(py)<sub>4</sub>].

<b>Zn</b>	-0.276558	2.13155	-0.688121	<b>C</b>	2.618426	2.648793	-1.569005
<b>C</b>	-2.558684	2.321083	1.34992	<b>C</b>	2.091016	3.981129	-3.909787
<b>C</b>	-3.634943	1.947722	2.152391	<b>C</b>	3.688449	3.11057	-2.3337
<b>H</b>	-4.126515	2.689182	2.782108	<b>C</b>	3.421095	3.78947	-3.525942
<b>C</b>	-4.06365	0.617259	2.126218	<b>H</b>	1.835119	4.502036	-4.832005
<b>C</b>	-3.396773	-0.289531	1.298695	<b>H</b>	4.710714	2.935822	-1.998467
<b>C</b>	-2.328578	0.162712	0.524653	<b>H</b>	4.236617	4.16198	-4.147007
<b>N</b>	-1.916161	1.446384	0.551077	<b>H</b>	-2.933268	-0.358319	-5.511315
<b>H</b>	-4.904818	0.293244	2.740859	<b>H</b>	-0.487621	-0.74814	-5.048261
<b>H</b>	-3.697914	-1.335982	1.247617	<b>C</b>	-2.4503	0.096526	-4.645458
<b>C</b>	-1.325065	5.107707	-1.324931	<b>C</b>	-1.093617	-0.122938	-4.392552
<b>C</b>	-2.680554	5.826038	-1.669412	<b>C</b>	-3.177244	0.911292	-3.772627
<b>O</b>	-1.504187	3.886117	-1.042195	<b>H</b>	-4.23595	1.112887	-3.935328
<b>O</b>	-0.290773	5.795446	-1.356083	<b>C</b>	-0.516221	0.475802	-3.27481
<b>F</b>	-3.514455	5.83803	-0.58362	<b>H</b>	0.538265	0.336595	-3.036538
<b>F</b>	-3.34782	5.189126	-2.677001	<b>C</b>	-2.522687	1.475067	-2.678918
<b>F</b>	-2.520068	7.119454	-2.05771	<b>N</b>	-1.21524	1.259285	-2.431962
<b>O</b>	0.948072	0.38585	-0.282998	<b>H</b>	-3.033678	2.132821	-1.975917
<b>C</b>	0.899188	-0.86024	-0.504605	<b>H</b>	0.889926	4.843032	0.20706
<b>F</b>	2.575286	-1.504364	1.128004	<b>N</b>	0.669849	2.971744	1.072421
<b>O</b>	-0.033477	-1.584279	-0.890865	<b>C</b>	1.080579	4.256022	1.109497
<b>C</b>	2.278471	-1.556079	-0.208062	<b>C</b>	0.865196	2.193684	2.155951
<b>F</b>	2.304245	-2.867454	-0.566749	<b>H</b>	0.52628	1.162019	2.06669
<b>F</b>	3.306825	-0.943911	-0.866857	<b>C</b>	1.69735	4.805904	2.233376
<b>H</b>	-2.193003	3.347177	1.321902	<b>H</b>	2.013104	5.848952	2.222128
<b>H</b>	-1.765515	-0.505185	-0.133403	<b>C</b>	1.474964	2.66792	3.315821
<b>N</b>	1.336027	2.837767	-1.937289	<b>C</b>	1.899086	3.999282	3.356466
<b>H</b>	0.02806	3.615491	-3.342848	<b>H</b>	1.614264	2.002657	4.16792
<b>C</b>	1.080161	3.491539	-3.086259	<b>H</b>	2.379917	4.400631	4.249703
<b>H</b>	2.767066	2.098145	-0.640641				

**Table S2** Cartesian coordinates of optimized mononuclear  $[\text{Zn}(\text{TFA})_2(\text{OH}_2)_4]$ .

<b>Zn</b>	-0.199982	2.219365	-0.819565	<b>F</b>	2.870924	-1.46113	-0.465698
<b>C</b>	-2.437158	3.974124	-1.711991	<b>O</b>	1.378556	2.990389	-2.088653
<b>C</b>	-3.118371	5.383708	-1.658205	<b>O</b>	-0.97931	1.354651	-2.574225
<b>O</b>	-1.363785	3.928002	-1.031129	<b>O</b>	0.76385	3.132065	0.856188
<b>O</b>	-2.9979	3.091999	-2.390561	<b>H</b>	1.148309	2.724078	-2.99955
<b>F</b>	-2.279444	6.345047	-2.139725	<b>H</b>	2.254866	2.593604	-1.927477
<b>F</b>	-3.433185	5.72459	-0.375359	<b>H</b>	-1.900113	1.738023	-2.607127
<b>F</b>	-4.259515	5.441048	-2.384408	<b>H</b>	-1.005062	0.386665	-2.336373
<b>O</b>	0.880295	0.501668	-0.317929	<b>H</b>	1.097118	4.03721	0.714768
<b>C</b>	0.610443	-0.659197	-0.763656	<b>H</b>	1.525826	2.619938	1.185344
<b>F</b>	1.448851	-1.848981	1.163788	<b>H</b>	-1.455476	0.838923	1.167272
<b>O</b>	-0.277888	-1.026652	-1.556466	<b>H</b>	-2.195995	2.184962	1.006609
<b>C</b>	1.569144	-1.758962	-0.192398	<b>O</b>	-1.773578	1.469986	0.495266
<b>F</b>	1.32034	-2.988172	-0.703597				

## 8. Synthesis of Zn-based 1D and 2D coordination polymer nanoparticles in block copolymers

**Table S3** Cartesian coordinates of optimized binuclear  $[\text{Zn}_2(\text{OAc})_4(\text{py})_4]$ .

<b>Zn</b>	-1.040115	2.513125	-0.382913	<b>H</b>	-5.696923	4.506213	2.811207
<b>C</b>	-2.96243	1.875928	1.916033	<b>H</b>	-5.792694	4.57468	0.295651
<b>C</b>	-4.134951	1.494851	2.567773	<b>C</b>	-4.851112	4.874377	2.229801
<b>H</b>	-4.152581	1.425702	3.655584	<b>C</b>	-4.906976	4.906796	0.835845
<b>C</b>	-5.269548	1.210607	1.804093	<b>C</b>	-3.693585	5.331081	2.866621
<b>C</b>	-5.191061	1.325613	0.413793	<b>H</b>	-3.610323	5.33908	3.953461
<b>C</b>	-3.983273	1.71735	-0.161824	<b>C</b>	-3.797708	5.369292	0.130142
<b>N</b>	-2.88689	1.986713	0.575294	<b>H</b>	-3.800846	5.417363	-0.956798
<b>H</b>	-6.201922	0.910837	2.284923	<b>C</b>	-2.630992	5.778233	2.086707
<b>H</b>	-6.053171	1.119917	-0.220738	<b>N</b>	-2.671043	5.78305	0.738308
<b>C</b>	-2.116779	4.472185	-2.532806	<b>H</b>	-1.710544	6.154208	2.531562
<b>C</b>	-2.773595	4.505906	-3.902184	<b>Zn</b>	-0.899269	6.353721	-0.347928
<b>O</b>	-2.219648	3.398193	-1.864961	<b>H</b>	0.104237	4.690391	3.906177
<b>O</b>	-1.539702	5.537509	-2.147051	<b>H</b>	-2.88528	10.440265	0.342268
<b>H</b>	-3.804072	4.877354	-3.787503	<b>O</b>	-1.827178	8.279209	-0.999132
<b>H</b>	-2.821974	3.500561	-4.336463	<b>O</b>	-0.433894	3.348217	1.407383
<b>H</b>	-2.241607	5.19167	-4.572485	<b>O</b>	0.28441	5.475333	1.137303
<b>O</b>	-0.118666	0.618096	0.222624	<b>C</b>	0.183202	4.390372	1.789039
<b>C</b>	-0.49666	-0.005734	-0.830268	<b>C</b>	-1.433592	8.879969	0.058689
<b>H</b>	-0.844955	-2.058756	-0.31609	<b>C</b>	0.835138	4.340433	3.160139
<b>O</b>	-1.160765	0.576392	-1.74323	<b>C</b>	-1.793617	10.344863	0.23991
<b>C</b>	-0.160394	-1.481965	-0.956534	<b>O</b>	-0.763442	8.27368	0.954519
<b>H</b>	-0.274406	-1.829548	-1.990281	<b>H</b>	1.119525	3.314394	3.421208
<b>H</b>	0.861934	-1.67791	-0.606167	<b>H</b>	-1.498757	10.917626	-0.651125
<b>H</b>	-2.047497	2.121448	2.455141	<b>H</b>	1.705015	5.006294	3.202147
<b>H</b>	-3.864027	1.843107	-1.237368	<b>H</b>	-1.311181	10.770675	1.127254
<b>N</b>	0.727106	3.092937	-1.480848	<b>H</b>	0.160066	6.631741	-3.209967
<b>H</b>	-0.233699	2.708939	-3.27163	<b>N</b>	0.952176	6.847868	-1.317088
<b>C</b>	0.694219	3.069126	-2.829138	<b>C</b>	1.060466	6.901399	-2.658548
<b>H</b>	1.85829	3.468648	0.212487	<b>C</b>	2.030619	7.151074	-0.565864
<b>C</b>	1.861236	3.490497	-0.875332	<b>H</b>	1.884325	7.073591	0.510861
<b>C</b>	1.773496	3.468255	-3.612598	<b>C</b>	2.247496	7.257683	-3.298217
<b>C</b>	2.986207	3.907784	-1.58462	<b>H</b>	2.290634	7.280232	-4.387279
<b>C</b>	2.93991	3.90701	-2.979376	<b>C</b>	3.251508	7.51875	-1.128899
<b>H</b>	1.695647	3.437278	-4.699437	<b>C</b>	3.36328	7.575124	-2.520706
<b>H</b>	3.876862	4.230122	-1.046522	<b>H</b>	4.098034	7.752546	-0.483299
<b>H</b>	3.798987	4.237735	-3.564046	<b>H</b>	4.306923	7.855114	-2.991314

**Table S4** Cartesian coordinates of optimized pentanuclear  $[\text{Zn}(\text{OAc})_2(\text{OH}_2)_2]_5$ .

<b>Zn</b>	5.726065	0.494003	8.327941	<b>O</b>	4.495698	0.328396	2.655941
<b>C</b>	7.576767	2.061351	7.338346	<b>H</b>	9.290131	-0.579866	-0.094676
<b>O</b>	7.329943	2.275238	8.561747	<b>H</b>	9.997967	-1.898719	0.903236
<b>O</b>	6.942583	1.102215	6.738581	<b>H</b>	8.679713	-2.237793	-0.251084
<b>C</b>	8.562674	2.904475	6.58257	<b>H</b>	4.605858	0.988915	1.947703
<b>O</b>	4.438492	-0.788251	7.453453	<b>H</b>	4.003741	0.779634	3.365792
<b>H</b>	8.804238	2.477104	5.603851	<b>Zn</b>	4.350915	-0.93309	12.711542
<b>H</b>	9.479234	3.012023	7.176843	<b>C</b>	2.777247	-1.352889	14.591116
<b>H</b>	8.145813	3.917608	6.447091	<b>O</b>	2.844574	-2.211846	13.649791
<b>H</b>	4.72249	-1.014434	6.500523	<b>O</b>	3.501032	-0.29099	14.537697
<b>H</b>	4.406257	-1.678066	7.923202	<b>C</b>	1.882804	-1.58569	15.782008
<b>C</b>	4.141839	2.400161	9.244153	<b>O</b>	5.438882	0.895884	12.434796
<b>O</b>	4.378142	2.48832	8.009765	<b>H</b>	1.491772	-0.636173	16.166626
<b>O</b>	4.590109	1.356521	9.887231	<b>H</b>	1.059888	-2.263437	15.527825
<b>C</b>	3.363211	3.446047	9.984888	<b>H</b>	2.480734	-2.051965	16.580676
<b>O</b>	6.893206	-0.741045	9.412241	<b>H</b>	5.233813	1.588927	13.087954
<b>H</b>	3.314978	3.234069	11.058328	<b>H</b>	5.208776	1.263051	11.539718
<b>H</b>	2.343323	3.483797	9.575683	<b>C</b>	6.3786	-2.445955	12.309049
<b>H</b>	3.812754	4.43848	9.821852	<b>O</b>	6.104527	-2.257003	13.521653
<b>H</b>	6.386333	-1.210457	10.153373	<b>O</b>	5.635395	-1.887297	11.39184
<b>H</b>	7.270564	-1.489555	8.848251	<b>C</b>	7.523575	-3.308126	11.853612
<b>Zn</b>	6.247793	-0.797615	3.210782	<b>O</b>	2.986926	-0.379035	11.191187
<b>C</b>	4.769857	-2.457133	4.43252	<b>H</b>	8.211867	-2.714045	11.234647
<b>O</b>	5.120717	-2.658191	3.231423	<b>H</b>	8.065827	-3.730242	12.70531
<b>O</b>	5.217017	-1.403892	5.041139	<b>H</b>	7.127656	-4.113954	11.218365
<b>C</b>	3.823919	-3.382797	5.142773	<b>H</b>	3.3805	0.319323	10.604158
<b>O</b>	7.173139	0.819177	4.143284	<b>H</b>	2.098017	-0.078456	11.450437
<b>H</b>	2.864806	-2.864106	5.289876	<b>Zn</b>	6.386117	-4.548498	8.085357
<b>H</b>	3.653864	-4.291828	4.557834	<b>C</b>	7.804019	-2.936456	6.766183
<b>H</b>	4.211275	-3.641221	6.135749	<b>O</b>	7.67498	-2.818637	8.049295
<b>H</b>	7.040393	0.926808	5.142661	<b>O</b>	7.260591	-3.931461	6.193439
<b>H</b>	6.989443	1.682529	3.733616	<b>C</b>	8.594842	-1.911402	6.01111
<b>C</b>	8.034098	-1.242865	1.52291	<b>O</b>	5.302876	-5.999501	6.982302
<b>O</b>	8.140504	-1.7695	2.680803	<b>H</b>	8.533403	-2.069319	4.930095
<b>O</b>	7.019975	-0.505152	1.245944	<b>H</b>	9.644913	-1.95798	6.336053
<b>C</b>	9.077077	-1.500526	0.463673	<b>H</b>	8.221455	-0.910359	6.264804

## 8. Synthesis of Zn-based 1D and 2D coordination polymer nanoparticles in block copolymers

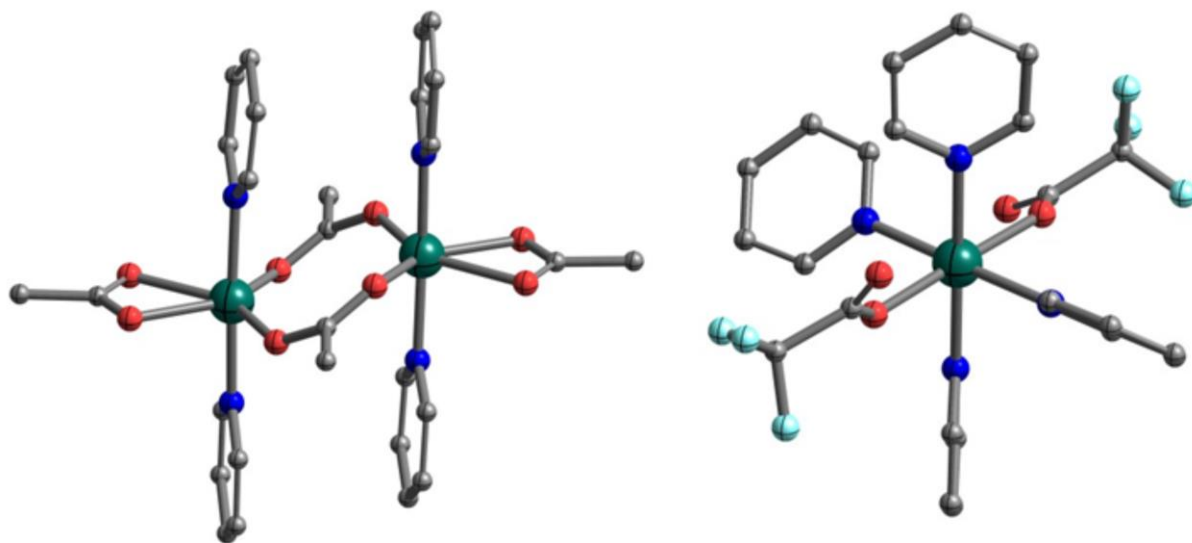
---

<b>H</b>	5.712069	-6.269124	6.140037
<b>H</b>	5.035959	-6.824538	7.427039
<b>C</b>	4.399596	-3.909588	9.511644
<b>O</b>	4.616195	-3.231135	8.443049
<b>O</b>	5.206657	-4.859403	9.805394
<b>C</b>	3.190224	-3.642464	10.356453
<b>O</b>	7.916924	-5.812738	8.801265
<b>H</b>	3.340347	-3.995439	11.381807
<b>H</b>	2.339579	-4.187481	9.918048
<b>H</b>	2.951738	-2.573056	10.362591
<b>H</b>	7.632825	-6.616835	9.273145
<b>H</b>	8.594608	-6.108401	8.165734
<b>Zn</b>	6.084227	6.088493	8.057789
<b>C</b>	8.248823	6.985807	7.092639
<b>O</b>	7.906957	7.50041	8.198146
<b>O</b>	7.499802	6.097775	6.524928
<b>C</b>	9.542791	7.3679	6.414416
<b>O</b>	4.839964	4.82196	6.923366
<b>H</b>	10.24172	6.519467	6.477942
<b>H</b>	9.997542	8.241923	6.892488
<b>H</b>	9.367612	7.568917	5.349024
<b>H</b>	5.188761	4.666444	6.028251
<b>H</b>	4.60035	3.92058	7.30779
<b>C</b>	4.202729	7.54232	8.895012
<b>O</b>	4.671409	7.822676	7.748668
<b>O</b>	4.705653	6.571988	9.58065
<b>C</b>	3.042024	8.31419	9.47475
<b>O</b>	7.022274	4.741686	9.365302
<b>H</b>	2.154206	7.663994	9.489471
<b>H</b>	2.821819	9.207264	8.880314
<b>H</b>	3.257687	8.597344	10.513423
<b>H</b>	6.644483	4.730826	10.261422
<b>H</b>	7.205003	3.78504	9.098501

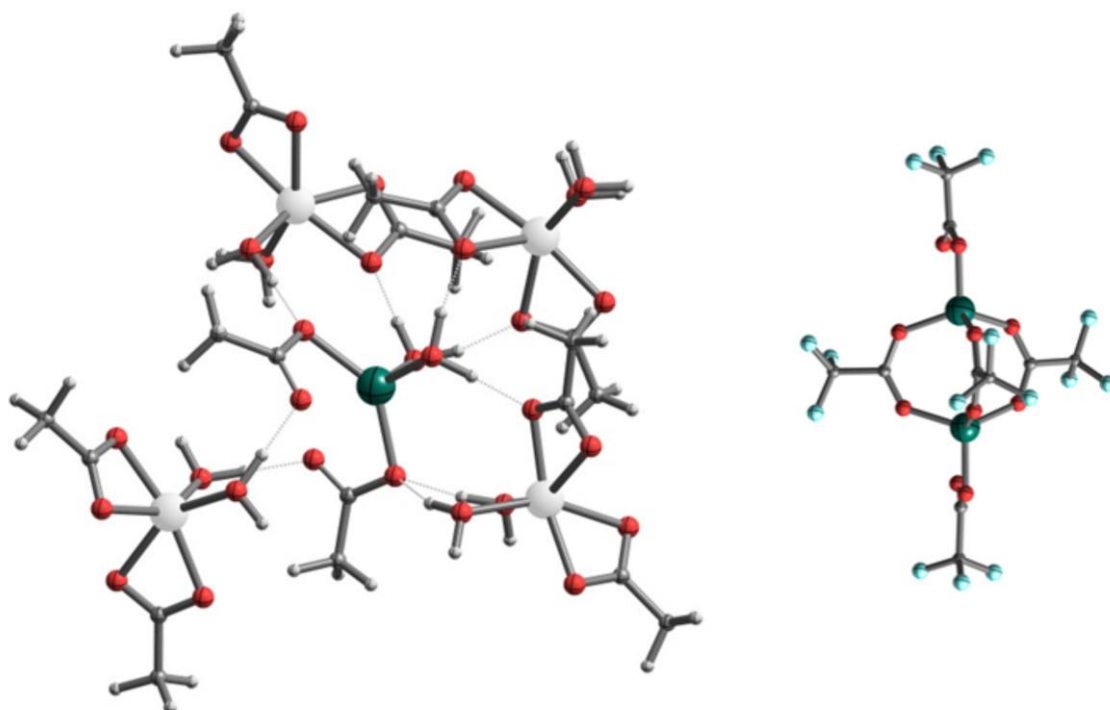
---



### Graphical representation of DFT optimized structures



**Fig. S14:** DFT-optimised structure of CP models; left:  $[\text{Zn}_2(\text{OAc})_4(\text{py})_4]$  as a model of 1D CP  $[\text{Zn}(\text{OAc})_2(\text{bipy})_2]_n$ ; right:  $[\text{Zn}(\text{TFA})_2(\text{py})_4]$  as a model of 2D CN  $[\text{Zn}(\text{TFA})_2(\text{bppa})_2]_n$ .



**Fig. S15:** DFT-optimised structure of precursor models; left:  $[\text{Zn}(\text{OAc})_2(\text{OH}_2)_2]_5$  as a model of bulk  $\text{Zn}(\text{OAc})_2 \times 2\text{H}_2\text{O}$  (terminal Zn centres given in white); right:  $[\text{Zn}_2(\text{TFA})_5]$  as a model of  $\text{Zn}(\text{TFA})_2$ .



## 9. Size and Shape Controlled Synthesis of Spin Crossover – Block Copolymer Nanocomposites

Christoph Göbel, Katharina Marquardt, Dirk Baabe, Markus Drechsler, Patrick Loch, Josef Breu, Holger Schmalz, Andreas Greiner\*, Birgit Weber\*

C. Göbel, Prof. B. Weber, Department of Chemistry, Inorganic Chemistry IV, Universität Bayreuth, Universitätsstr. 30, 95447 Bayreuth, Germany

Dr. K. Marquardt, Bayerisches Geoinstitut (BGI), Universität Bayreuth, Universitätsstr. 30, 95447 Bayreuth, Germany

Dr. Dirk Baabe, Institut für Anorganische und Analytische Chemie, Technische Universität Braunschweig, Hagenring 30, 38106 Braunschweig, Germany

Dr. M. Drechsler, Keylab Electron and Optical Microscopy, Bavarian Polymer Institute, Universität Bayreuth, Universitätsstr. 30, 95447 Bayreuth, Germany

Patrick Loch, Prof. J. Breu, Department of Chemistry, Inorganic Chemistry I, Universität Bayreuth, Universitätsstr. 30, 95447 Bayreuth, Germany

Prof. A. Greiner, Dr. H. Schmalz, Department of Chemistry, Macromolecular Chemistry II and Keylab Synthesis and Molecular Characterization, Bavarian Polymer Institute, Universität Bayreuth, Universitätsstr. 30, 95447 Bayreuth, Germany

**Abstract:** Five polystyrene-*block*-poly(4-vinylpyridine) (PS-*b*-P4VP) diblock copolymers have been used as template for the confined synthesis of the coordination polymer (CP) [FeL(bipy)]<sub>n</sub>. The size and shape of the block copolymers and the nanocomposites with [FeL(bipy)]<sub>n</sub> were investigated by transmission electron microscopy (TEM), cryo-TEM, and dynamic light scattering (DLS). Moreover, the magnetic properties of the nanocomposites were analyzed by susceptibility measurements in a SQUID magnetometer. The block copolymers differ in their weight fractions of PS and P4VP ranging from 85/15 to 39/61 (w/w, SV-15 to SV-61). All five neat block copolymers show spherical micelles in the TEM images with core sizes between 15 ± 2 nm and 73 ± 9 nm and in cryo-TEM images with sizes between 26 ± 2 nm and 71 ± 4 nm. The nanocomposites also show spherical particles until SV-42 with core sizes between 14 ± 2 nm and 58 ± 4 nm in TEM images and 30 ± 3 nm and 65 ± 5 nm in cryo-TEM images. The nanocomposites with SV-61 show worm-like structures in TEM and cryo-TEM measurements and the width was analyzed to 60 ± 8 nm and 84 ± 10 nm, respectively. The magnetic properties of the spin crossover material improve in the

larger particles and in the worm-like structures resulting in transition temperatures of  $T_{1/2\downarrow} = 211$  K and  $T_{1/2\uparrow} = 224$  K, a 13 K wide hysteresis and a residual high-spin fraction as low as  $\chi_{\text{HS}} = 14$  %. The worm-like structures were further analyzed by transmission electron microscopy – energy dispersive X-ray spectroscopy and the incorporation of the CP was proven by the presence of iron inside the polymeric structure.

### 9.1. Introduction

Spin crossover (SCO) compounds are a fascinating class of materials. They have been studied intensively over the last decades because of their unique switching properties by different external stimuli (e.g. temperature, pressure, light irradiation) between a high-spin (HS) and a low-spin (LS) state.<sup>[1]</sup> Switching between these two states changes physical properties like magnetism, structure, or color.<sup>[2]</sup> This offers interesting applications, e.g. as sensors<sup>[3]</sup>, display devices<sup>[4]</sup>, data storage<sup>[4]</sup>, or contrast agents<sup>[5]</sup>.

Another highly investigated field of research is the formation of nanoparticles of all kinds of compounds, because the properties of nanosized materials differ considerably compared to their bulk analogues (e.g. catalytic activity in noble metals<sup>[6]</sup> or photoluminescence in CdSe<sup>[7]</sup>), paving the way for new applications.<sup>[8]</sup> However, forming stable nanoparticles with defined properties (e.g. size, shape or magnetism)<sup>[9]</sup> is a key problem that needs to be addressed before application. Several methods like the inverse micelle technique, the reduction of metal salts, or a microfluidic approach have already been established for the synthesis of noble metal or metal oxide nanoparticles regarding the control of the particles size and shape.<sup>[10,11]</sup>

Syntheses of nanoparticles of SCO coordination polymers (CPs) and particularly networks have already been successfully performed. However, these syntheses are vastly depending on the reaction conditions and not all established methods are applicable. The key problem of predicting the size of the desired CP nanoparticles remains an unresolved issue. Since the properties of SCO nanoparticles are also dependent on their size, a size control is highly important. Typically, a higher residual HS fraction remains, the hysteresis is narrowed, and the transition temperature may be shifted in smaller particles.<sup>[12]</sup> Predictable and tunable properties become accessible by controlling the size of the resulting SCO nanoparticles. For applications as molecular actuators<sup>[13]</sup>, nanosized rod like structures are desirable to realize anisotropic volume expansion. Block copolymers (BCPs) are very promising for the formation of size- and shape-controlled SCO CP-BCP nanocomposites. BCPs can be used as micro- or nanoreactors because of their self-assembly properties into micelles with a defined size and shape in a suitable solvent.<sup>[14]</sup> Besides the formation of spherical particles, phase separation of BCPs also allows a defined structuring of the desired nanocomposite into rods, worm-like structures, gyroids, or lamellas or even the formation

of membranes.<sup>[15]</sup> Moreover, the formation of polymer-encapsulated composite materials may promise facile processing by established methods like electrospinning for the formation of fibers and fiber mats<sup>[16]</sup> or spin-coating or drop-casting for surface coating<sup>[17]</sup>.

Our recent works already had shown the potential of the BCP polystyrene-*block*-poly(4-vinylpyridine) (PS-*b*-P4VP) as a nanoreactor for the synthesis of different one dimensional spin crossover coordination polymers [FeL(bipy)]<sub>n</sub><sup>[18]</sup>, [FeL(bpea)]<sub>n</sub>, [FeL(bpee)]<sub>n</sub>, [FeL(bpey)]<sub>n</sub><sup>[19]</sup> and other coordination polymers<sup>[20]</sup>. Besides, the influence of the block copolymer shell on the crystallization and the SCO properties of the CP in the composite and the possibility of fiber formation by electrospinning was investigated.<sup>[21]</sup> We herein report the size and shape control of [FeL(bipy)]<sub>n</sub> SCO CP-BCP nanocomposites via confined crystallization and its influence on the magnetic properties. Five different BCPs were used for the syntheses of the SCO CP-BCP nanocomposites that vary in the weight fraction of the P4VP block. Spherical particles with  $D_{\text{core}} = 14$  nm to 58 nm can be synthesized in BCPs with 15 wt% to 42 wt% P4VP. A change in morphology from spheres to worm-like structures is observed for the nanocomposite samples employing a BCP with 61 wt% P4VP.

## 9.2. Results and Discussion

### 9.2.1. Characterization of PS-*b*-P4VP BCPs: size and shape

The influence of an increasing P4VP fraction on the particle size and particle morphology of a PS-*b*-P4VP block copolymer and the resulting polymeric micelles was investigated. The formation of rods and worm-like micelles of PS-*b*-P4VP BCPs was already reported for solvent annealed thin films.<sup>[22]</sup> Additionally, PS-*b*-P4VP BCPs showed morphological changes in solvent mixtures with THF or in solvents other than THF.<sup>[23]</sup> In some cases, the introduction of organic or inorganic material into the BCPs triggered the formation of rods.<sup>[24]</sup> In most cases the molecular weights used in the literature were only ranging from 20 000 g mol<sup>-1</sup> to 70 000 g mol<sup>-1</sup> with varying P4VP content, often accompanied by the presence of spheres.<sup>[23-25]</sup>

Phase separation of BCPs can also occur in solution depending on the affinity of the solvent to the different blocks. Therefore, spherical micelles can often be observed for BCPs but also the formation of rods, worm-like micelles, or vesicles is possible. In general, THF is a very good solvent for the PS block, while the solubility of P4VP is quite low.<sup>[26]</sup> With the P4VP fraction of the BCP being notably smaller than the PS fraction, P4VP will form the micelle core while the chains of the PS blocks will be elongated leading to spherical micelles.<sup>[22-25]</sup> Raising the fraction of the less soluble part of the block copolymer alters the packing parameter of the polymer chain which can lead to the before mentioned structures like rods, worms, or vesicles.<sup>[27]</sup>

---

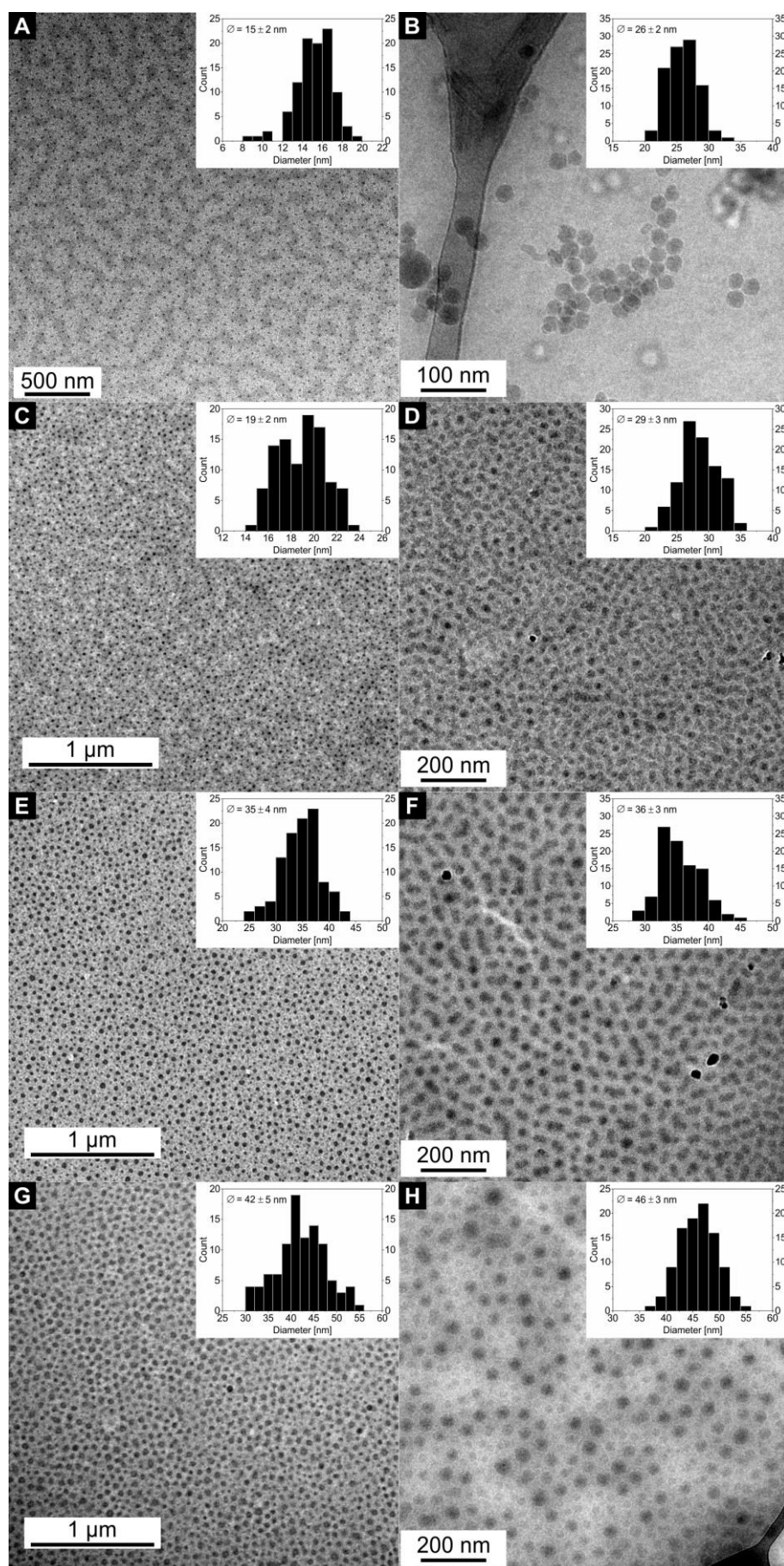
Five different BCPs with a target molecular weight between 120 000 g mol<sup>-1</sup> and 160 000 g mol<sup>-1</sup> with varying ratios of PS to P4VP have been synthesized. The composition, the used abbreviations, the molecular weight  $M_n$ , the dispersity  $\mathcal{D}$ , and the weight fractions of the two blocks can be found in **Table 1**. The general characterization of the BCPs by NMR, gel permeation chromatography (GPC), dynamic scanning calorimetry (DSC) and dynamic light scattering (DLS) can be found in **Figure S1** to **Figure S4**.

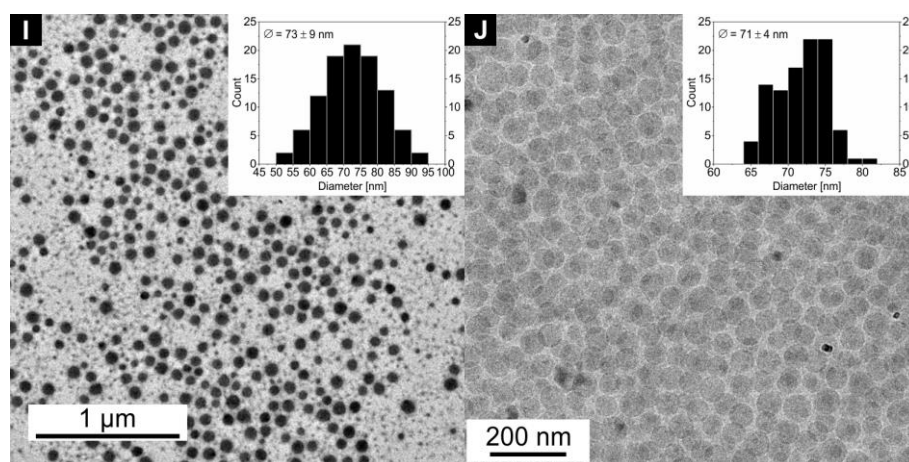
**Table 1:** Overview over the used block copolymers in this work.

BCP <sup>a)</sup>	Abbreviation	$M_n$ [g mol <sup>-1</sup> ] <sup>b)</sup>	$\mathcal{D}$ <sup>c)</sup>	Fraction PS [wt%] <sup>d)</sup>	Fraction P4VP [wt%] <sup>d)</sup>
S <sub>85</sub> V <sub>15</sub> <sup>154</sup>	SV-15	154 000	1.02	85	15
S <sub>79</sub> V <sub>21</sub> <sup>119</sup>	SV-21	119 000	1.05	79	21
S <sub>65</sub> V <sub>35</sub> <sup>131</sup>	SV-35	131 000	1.06	65	35
S <sub>58</sub> V <sub>42</sub> <sup>157</sup>	SV-42	157 000	1.09	58	42
S <sub>39</sub> V <sub>61</sub> <sup>162</sup>	SV-61	162 000	1.24	39	61

<sup>a)</sup> subscripts denote the content of the respective block in wt%, superscript gives the number average molecular weight in kg mol<sup>-1</sup>; <sup>b)</sup> calculated from NMR measurements employing the total molecular weight of the PS precursor derived from MALDI-ToF MS; <sup>c)</sup> from GPC (**Figure S2**); <sup>d)</sup> calculated from NMR (for an exemplary calculation see Figure S1).

All five BCPs were successfully synthesized with the target molecular weight and the P4VP fractions of the BCPs are ranging from 15 wt% (SV-15) to 61 wt% (SV-61). The particle size and the morphology of the five BCPs was characterized both in the dry state and in THF solution by TEM, DLS, and cryo-TEM. It is expected that they only show spherical micelles since the P4VP fraction is still too low to induce the formation of anisotropic structures like rods. In fact, only spherical particles were found by TEM measurements for all BCPs. However, the core diameter  $D_{\text{core}}$  of the particles increases continuously starting at  $15 \pm 2$  nm for SV-15 and reaching  $73 \pm 9$  nm for SV-61 (see **Table 2**). In addition, narrowly distributed particles were detected by DLS. At first, the measured hydrodynamic diameters  $D_h$  of the BCPs correlate with both the molecular weight and the P4VP fraction. The hydrodynamic diameters start at  $75 \pm 28$  nm for SV-15 and increase with the P4VP fraction up to SV-42 with  $125 \pm 34$  nm. Although having the highest molecular weight and P4VP content of all analyzed BCPs SV-61 does not show the largest hydrodynamic diameter. Instead, it is similar to SV-42 with  $119 \pm 29$  nm (**Figure S4**). The BCPs were also imaged by cryo-TEM to evaluate the particle size and shape in solution. Again, spherical particles were imaged for all five neat BCPs and diameters ranging from  $26 \pm 2$  nm for SV-15 to  $71 \pm 4$  nm for SV-61 were measured (Table 2).





**Figure 1:** TEM and cryo-TEM images of the BCPs SV-15 (A, B), SV-21 (C, D), SV-35 (E, F), SV-42 (G, H), and SV-61 (I, J). Only spherical nanoparticles are imaged for all neat BCPs. The size distributions are given in the insets.

**Table 2:** Hydrodynamic diameter  $D_h$  measured by DLS, core size  $D_{core}$  derived from TEM and core diameter/width evaluated from cryo-TEM measurements of the 5 different BCPs.

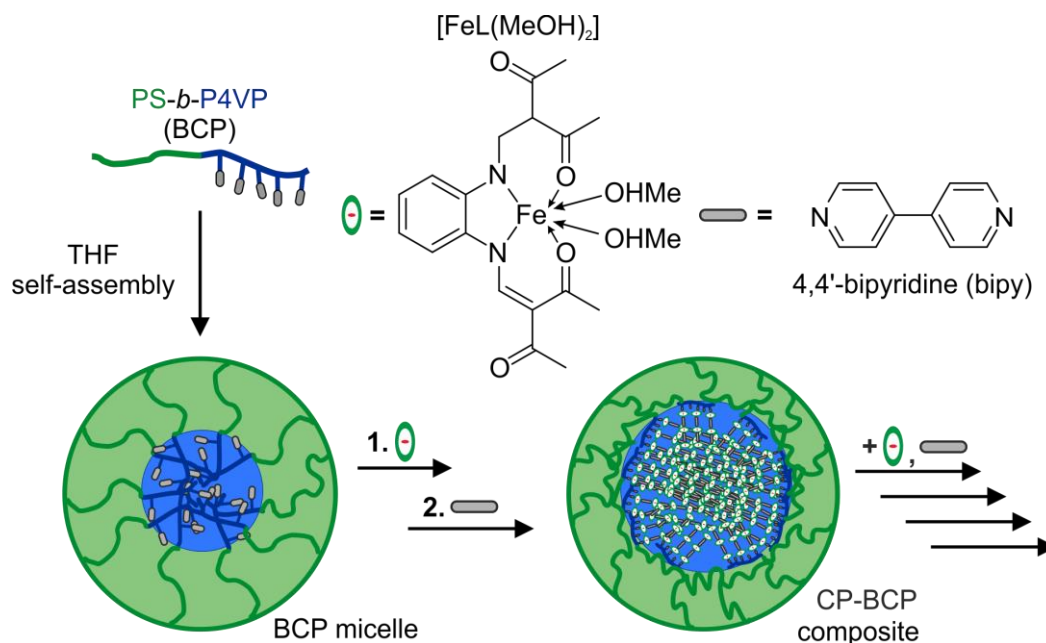
BCP	Hydrodynamic diameter $D_h$ [nm]	Core diameter TEM $D_{core}$ [nm]	Core diameter cryo-TEM $D_{cryo}$ [nm]
SV-15	$75 \pm 28$	$15 \pm 2$	$26 \pm 2$
SV-21	$90 \pm 28$	$19 \pm 2$	$29 \pm 3$
SV-35	$102 \pm 29$	$35 \pm 4$	$36 \pm 3$
SV-42	$125 \pm 34$	$42 \pm 5$	$46 \pm 3$
SV-61	$126 \pm 36$	$73 \pm 9$	$71 \pm 4$

### 9.2.2. Characterization of SCO CP-BCP nanocomposites: size, shape, and magnetism

25 different SCO CP-BCP nanocomposites have been prepared utilizing the five before mentioned BCPs through the incorporation of a SCO CP with different reaction cycles (5 samples each). A complete sample overview is given in **Table 3**. The reaction procedure is as follows: The block copolymer and the iron(II) complex  $[\text{FeL}(\text{MeOH})_2]$  are dissolved in THF under argon atmosphere and heated to reflux for 2 h. After cooling, the bridging ligand 4,4'-bipyridine (bipy) is added and the reaction mixture is refluxed for 1h. At this stage, the solvent can either be removed by cold distillation to yield a brown, polymeric solid (1 cycle, samples **#a**). Alternatively, up to four more reaction cycles can be executed by the simultaneous addition of the iron(II) complex and the bridging ligand and a subsequent heating to reflux for 1 h. After each reaction cycle the solvent can be removed to obtain the polymeric nanocomposites with 3 to 5 cycles (samples with two reaction cycles have not been prepared). The numbers 1 to 5 of the sample notation correspond



to the used BCP, while the cycle count (1, 3, 4, and 5) is denoted by the letters a to d. Additionally, samples with five cycles were prepared with a reduced excess of the bridging ligand bipy. These samples are labeled with the letter e. The reaction scheme is displayed in **Scheme 1**.



**Scheme 1:** Synthetic approach for the preparation of Fe-based CP-BCP nanocomposites.

On the one hand, the influence of the incorporation of the CP on the size and shape of the nanocomposites in comparison to the neat BCPs was investigated by TEM, DLS, and cryo-TEM. On the other hand, the influence of the different particle sizes and shapes on the magnetic properties was analyzed by magnetic susceptibility measurements and (temperature-dependent) Mössbauer spectroscopy. Further characterization was performed by (temperature-dependent) powder X-ray diffraction ((*T*-)PXRD), scanning electron microscopy (SEM), elemental analysis, and infrared measurements (IR). The detailed characterization of the sample **#e** is given in the following as typical representatives, while the characterization of the samples **1a-d**, **2a-d**, **3a-d**, **4a-d**, and **5a-d** is displayed in the SI, **Figure S5** to **Figure S40**.

**Table 3:** Complete overview of the as-prepared composite samples.

Sample <sup>a)</sup>	BCP	Number of cycles	Hydrodynamic diameter $D_h$ [nm]	Core diameter/width TEM $D_{core}$ [nm]	Core diameter/width cryo-TEM $D_{cryo}$ [nm]
<b>1a</b>	SV-15	1	$85 \pm 33$	$12 \pm 2$	-
<b>1b</b>	SV-15	3	$89 \pm 32$	$15 \pm 3$	-
<b>1c</b>	SV-15	4	$121 \pm 43$	$17 \pm 2$	-
<b>1d</b>	SV-15	5	$119 \pm 62$	$16 \pm 2$	-
<b>1e*</b>	SV-15	5	$113 \pm 67$	$14 \pm 2$	$30 \pm 3$
<b>2a</b>	SV-21	1	$99 \pm 33$	$23 \pm 2$	-
<b>2b</b>	SV-21	3	$113 \pm 34$	$26 \pm 3$	-
<b>2c</b>	SV-21	4	$116 \pm 36$	$26 \pm 3$	-
<b>2d</b>	SV-21	5	$125 \pm 38$	$26 \pm 3$	-
<b>2e*</b>	SV-21	5	$118 \pm 39$	$26 \pm 2$	$34 \pm 5$
<b>3a</b>	SV-35	1	$112 \pm 32$	$37 \pm 3$	-
<b>3b</b>	SV-35	3	$125 \pm 34$	$41 \pm 4$	-
<b>3c</b>	SV-35	4	$112 \pm 32$	$40 \pm 3$	-
<b>3d</b>	SV-35	5	$131 \pm 39$	$40 \pm 3$	-
<b>3e*</b>	SV-35	5	$139 \pm 38$	$48 \pm 4$	$49 \pm 6$
<b>4a</b>	SV-42	1	$131 \pm 34$	$53 \pm 5$	-
<b>4b</b>	SV-42	3	$146 \pm 46$	$52 \pm 5$	-
<b>4c</b>	SV-42	4	$168 \pm 57$	$53 \pm 4$	-
<b>4d</b>	SV-42	5	$153 \pm 46$	$53 \pm 4$	-
<b>4e*</b>	SV-42	5	$139 \pm 36$	$58 \pm 4$	$65 \pm 5$
<b>5a</b>	SV-61	1	$129 \pm 33$	$61 \pm 7$	-
<b>5b</b>	SV-61	3	$260 \pm 113$	$62 \pm 9$	-
<b>5c</b>	SV-61	4	$218 \pm 78$	$58 \pm 7$	-
<b>5d</b>	SV-61	5	-	$56 \pm 6$	-
<b>5e*</b>	SV-61	5	$214 \pm 75$	$60 \pm 8$	$84 \pm 10$

<sup>a)</sup> Samples marked with an asterisk (\*) were also characterized by TEM, DLS, and SEM after thermal annealing.

The core sizes  $D_{core}$  and the hydrodynamic diameter  $D_h$  were determined for all SCO CP-BCP nanocomposites by TEM, cryo-TEM, and DLS, respectively. The core sizes  $D_{cryo}$  in solution were analyzed by cryo-TEM for the samples **#e**. The 21 samples **1a** to **5a** all show spherical particles in TEM measurements, whereas rods and worm-like structures started to form with sample **5b** and following. The worm-like structures become predominant with sample **5c** and **5d** (**Figure S5** to **Figure S9**). The average core diameter  $D_{core}$  increases continuously with rising P4VP fraction from

14 ± 2 nm (**1e**) to 58 ± 4 nm (**4e**) (Table 3 and **Figure 2**). However,  $D_{\text{core}}$  (micelle width) of the worm-like structures remained nearly identical to the particle size of sample **4e** with 60 ± 8 nm (**5e**, **Figure 3**). The core diameter of the composite samples does not change significantly with an increased cycle count (Table 3).

Cryo-TEM measurements reflect the growth in the core sizes with increasing P4VP content. Spherical particles were observed for the SCO CP-BCP nanocomposite samples **1e**, **2e**, **3e**, and **4e** which were also slightly larger in diameter than the empty BCPs. Rods and worm-like structures were only observed in nanocomposites with SV-61, also marginally larger than the spherical particle cores observed for the neat BCP (71 ± 4 nm (SV-61) vs. 84 ± 10 nm (**5e**)).

The hydrodynamic diameter  $D_h$  of the composites was analyzed by DLS. It increased along the series from 113 ± 67 nm (**1e**) to 242 ± 147 nm (**5e**) (Table 3 and **Figure S10** to **Figure S14**). It is observed that the hydrodynamic diameter slightly increases with a higher cycle count which may be an effect of the crystallization of the CP inside the BCP's core. In addition, the hydrodynamic diameter of the SCO CP-BCP composite micelles is significantly larger than the empty BCP micelles due to an increase in the aggregation number of the polymer chains leading to an increased stretching of the polymer chains and, thus, a larger hydrodynamic diameter (see **Figure S4** and **Figure S10** to **Figure S14**). This effect diminishes in the composite particles when going from SV-15 to SV-42 because of the shorter PS chains. The formation of rods in sample **5e** is also indicated by the DLS measurement because of the larger size distribution.

The formation of rods or worm-like structures in sample **5e** in contrast to the formation of only spherical particles in the neat polymer SV-61 can be explained by considering the weight fractions of the soluble (PS) and the less soluble or insoluble parts (P4VP, CP) of the resulting nanocomposite. Due to the introduction of the CP into the P4VP core, the weight fraction of the latter parts increases.

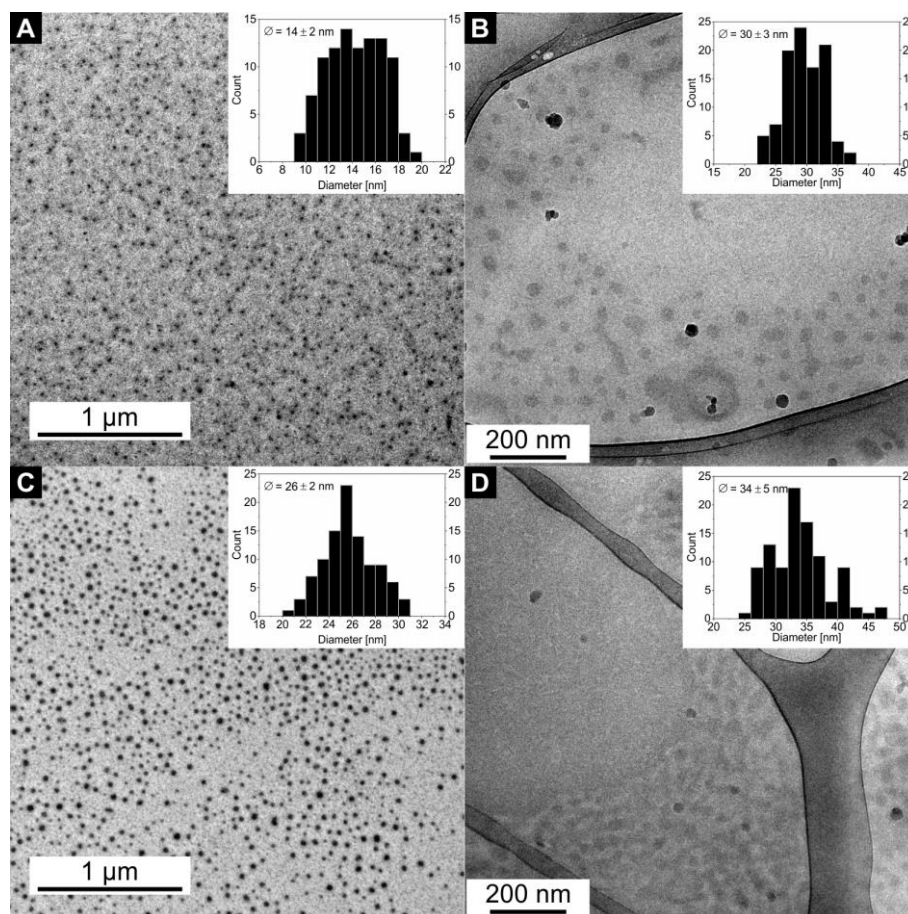
Exemplarily, a calculation of the weight fraction of these parts is given for sample **5e** by adding up the weight of the P4VP, the complex and one equivalent of the bridging ligand (the excess of 0.5 equivalents ligand are being considered soluble) and dividing it by the total weight of the sample. As a result, the total weight of the nanocomposite is 250.7 mg and the weight of insoluble part is 205.9 mg (82 %, **Table 4**). This indicates that the fraction of less soluble or insoluble parts needs to be about 80 % for the formation of rods or worm-like structures. This behavior has been observed in PS-*b*-P4VP micelles before.<sup>[25]</sup>

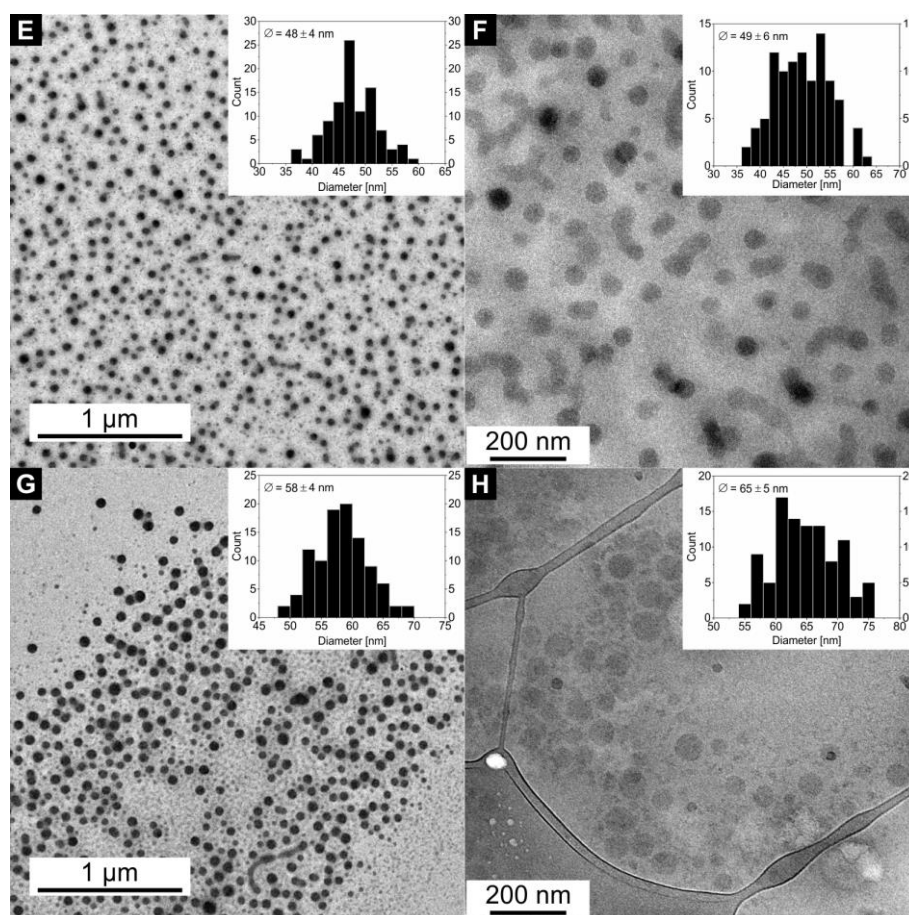
## 9. Size and Shape Controlled Synthesis of Spin Crossover – Block Copolymer Nanocomposites

**Table 4:** Model calculations on the fraction of the insoluble parts of the sample.

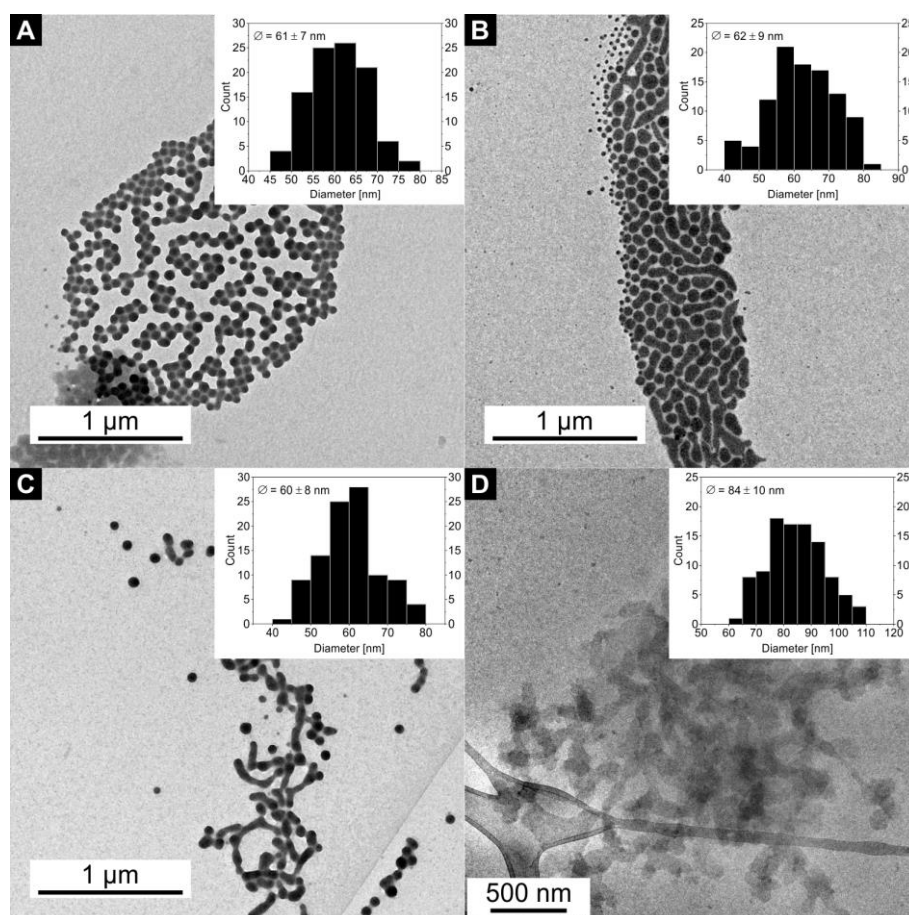
Insoluble parts			Whole sample		
Fraction	Calculation	Weight [mg]	Fraction	Calculation	Weight [mg]
P4VP	50 mg·0.61 wt%	30.5	BCP	50 mg·1	50
Complex [FeL] <sup>a)</sup>	0.86·5·29 mg	124.7	Complex [FeL] <sup>a)</sup>	0.86·5·29 mg	124.7
Ligand bipy <sup>b)</sup>	5·15.2 mg/1.5	50.7	Ligand bipy <sup>b)</sup>	5·15.2 mg	76
Total		205.9	Total		250.7

<sup>a)</sup> MeOH replaced by 4,4'-bipyridine during the synthesis and therefore considered as a solvent which is removed after the reaction; <sup>b)</sup> only 1 equivalent bipy is involved in the formation of the CP, the excess is regarded soluble.





**Figure 2:** TEM and cryo-TEM images of the SCO CP-BCP nanocomposite samples **1e** (A, B), **2e** (C, D), **3e** (E, F), and **4e** (G, H) that show spherical nanoparticles in both characterization methods. The size distributions are given in the insets.

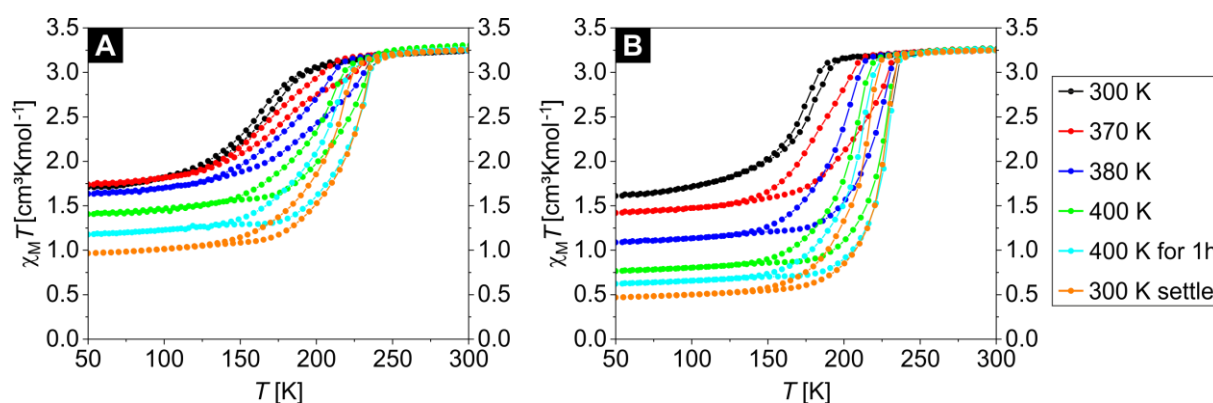


**Figure 3:** TEM images of SCO CP-BCP samples **5a** (A), **5b** (B), and **5c** (C) visualizing the transformation from spheres to worm-like micelles. Cryo-TEM confirms the presence of worm-like micelles in solution for sample **5e** (D). The corresponding size distributions are given in the insets.

The samples **1c-d**, **2c-d**, **3c-d**, **4c-d**, and **5c-d** were studied by room temperature Mössbauer spectroscopy. Samples **1e**, **2e**, **3e**, **4e**, and **5e** were additionally analyzed by temperature-dependent Mössbauer spectroscopy. Magnetic susceptibility measurements were performed on samples **1c-e**, **2c-e**, **3c-e**, **4c-e**, and **5c-e** with a SQUID magnetometer. (Temperature-dependent) Mössbauer spectroscopy gives an insight on the oxidation and spin states of the SCO CP-BCP composites. All Mössbauer spectra measured at rt only show one distinct doublet that corresponds to a Fe(II) HS species.<sup>[28]</sup> The spectra of all samples are presented in **Figure S17** to **Figure S21** along with the chemical shift  $\delta$ , the quadrupole splitting  $\Delta E_Q$  and the line width  $\Gamma$  (**Table S1**).

The magnetic properties are displayed as  $\chi_M T$  vs.  $T$  plots for the samples **1e** and **5e** in the temperature range from 50 K to 400 K in **Figure 4**. Samples **1c-e**, **2c-e**, **3c-e**, **4c-e**, and **5c-e** are displayed in the complete temperature range from 50 K to 400 K in **Figure S22** to **Figure S26**. Moreover, the residual HS fraction is calculated from the measurements by dividing the  $\chi_M T$  value

at 50 K by the starting value at 300 K. All samples were measured in six consecutive cooling and heating cycles (**Table 5** and **Table S2**). It was already shown that the SCO properties (hysteresis width, transition temperature, HS fraction) of the as-synthesized product can be altered by thermal annealing. This effect occurred due to the recrystallisation of the CP inside the polymeric micelles at annealing temperatures above the glass transition temperature  $T_g$  of PS proven by temperature-dependent powder X-ray diffraction ( $T$ -PXRD).<sup>[21]</sup> Here, we can also show that not only the enlargement of the particles and the morphological changes into rods or worm-like structures alters the SCO to be more complete from  $\gamma_{\text{HS}} = 30\%$  for sample **1e** to  $\gamma_{\text{HS}} = 14\%$  for sample **5e**. In addition, the optimization of the synthesis by reducing the amount of bridging ligand bipy improves the completeness of the SCO CP-BCP composite indicated by the residual HS fraction with  $\gamma_{\text{HS}} = 23\%$  vs.  $\gamma_{\text{HS}} = 14\%$  for samples **5d** and **5e**, respectively.  $T$ -PXRD pattern were measured for the samples **#e** and proved the recrystallisation of the CP. The relative intensity of the newly detected reflexes after thermal annealing increased continuously from sample **1e** to **5e** (**Figure S27**).



**Figure 4:** Comparison of the magnetic susceptibility measurements in the temperature range from 50 K to 300 K of the samples **1e** (A) and **5e** (B) in sweep mode (measurements 1 – 5) and settle mode (measurement 6) showing the lowering of the  $\chi_{\text{M}}T$  value and the increase in the abruptness of the spin transition in the larger particles. Detailed information about the cooling and heating cycles are noted in Table 5. The complete temperature range from 50 K to 400 K can be found in Figure S22 and Figure S26.

## 9. Size and Shape Controlled Synthesis of Spin Crossover – Block Copolymer Nanocomposites

**Table 5:** Summary of the cooling and heating cycles and the data derived from the magnetic measurements for the samples **1e**, **2e**, **3e**, **4e**, and **5e** showing the transition temperatures  $T_{1/2\downarrow}$  and  $T_{1/2\uparrow}$ , the hysteresis width, the  $\chi_M T$  value at 50 K, and the  $\gamma_{HS}$  value at 50 K.

Sample	Temperature range [K]	Mode	$T_{1/2\downarrow}$ [K]	$T_{1/2\uparrow}$ [K]	Hysteresis width [K]	$\chi_M T$ at 50 K [cm <sup>3</sup> Kmol <sup>-1</sup> ]	$\gamma_{HS}$ [%]
<b>1e</b>	300-50-370 <sup>a)</sup>	sweep	160	166	6	1.71	53
	370-50-380 <sup>b)</sup>		171	181	10	1.74	54
	380-50-400 <sup>c)</sup>		186	201	15	1.63	50
	400-50-400 <sup>d)</sup>		199	216	17	1.41	43
	400-50-300 <sup>e)</sup>		204	222	18	1.18	36
	300-50-300 <sup>f)</sup>	settle	208	221	13	0.97	30
<b>5e</b>	300-50-370 <sup>a)</sup>	sweep	169	174	5	1.61	50
	370-50-380 <sup>b)</sup>		183	210	27	1.42	44
	380-50-400 <sup>c)</sup>		195	218	23	1.09	34
	400-50-400 <sup>d)</sup>		203	223	20	0.77	24
	400-50-300 <sup>e)</sup>		207	226	19	0.62	19
	300-50-300 <sup>f)</sup>	settle	211	224	13	0.47	14

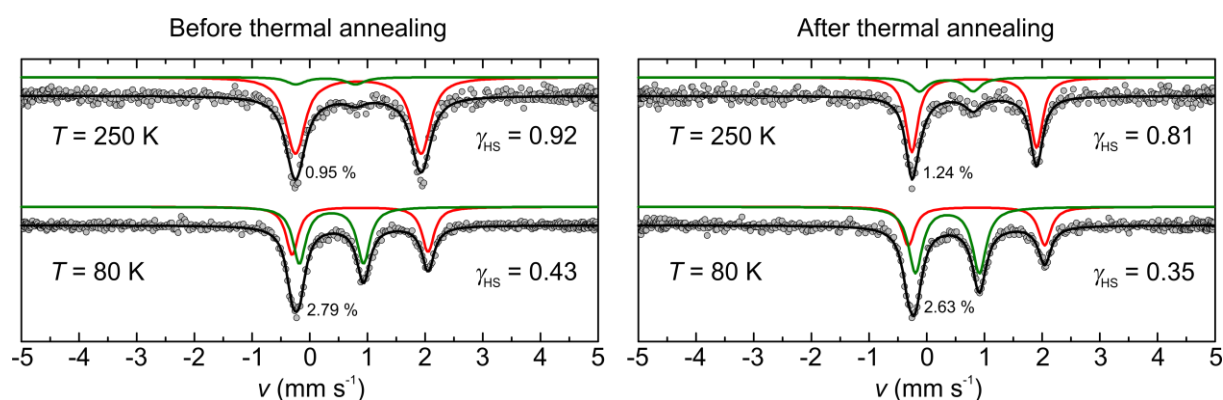
a) Figure 4, curve 1; b) Figure 4, curve 2; c) Figure 4, curve 3; d) Figure 4, curve 4; e) Figure 4, curve 5; f) Figure 4, curve 6.

Zero-field, temperature-dependent Mössbauer spectra were measured for the as-synthesized sample **5e** at 290 K, 250 K, 175 K, and 80 K and for the annealed ample **5e\*** at 250 K, 175 K, and 80 K. This allows a correlation between the magnetic and Mössbauer measurements by comparing the residual HS fractions.

As expected, the as-synthesized sample shows only one doublet at 290 K that represents an iron(II) HS species corresponding to the formed iron(II) CP [FeL(bipy)]<sub>n</sub> inside the BCP.<sup>[28]</sup> Upon cooling of the sample in the spectrometer, a second doublet corresponding to an iron(II) LS species arises. The residual HS fraction is lowered to 92% at 250 K and 69% at 175 K to reach its final value of 43 % at 80 K (see **Figure 5**, **Figure S28**, and **Table S4**), which is in good agreement with the residual HS fraction of the magnetic measurement of 51 % at 80 K. After thermal annealing, the measurement procedure was repeated (Figure 5 and Figure S28). As expected, it was found that upon cooling the HS fractions of the annealed sample are lower than the ones of the as-synthesized at the same temperatures. Additionally, the HS fraction of sample **5e\*** is decreased to 35% at 80 K. However, the  $\gamma_{HS}$  values of the annealed sample **5e\*** differ noticeably from the ones obtained from the magnetic measurements. The residual HS fraction is calculated to 81% from the Mössbauer spectrum while for the magnetic measurement the sample is almost



entirely in the HS state with a value of 99%. In contrary, at 80 K the  $\gamma_{\text{HS}}$  value is higher for the Mössbauer measurement with 35% than for the magnetic measurement with 15% (**Table S5**). The lower  $\gamma_{\text{HS}}$  value at 250 K for the Mössbauer measurement can be explained by matrix effect due to the mixing of the composite sample with Na<sub>2</sub>SO<sub>4</sub> for an even distribution of the sample. The higher  $\gamma_{\text{HS}}$  value can be explained by the different annealing environments for the two measurements. For the magnetic measurements, the neat sample was annealed over several measurement cycles inside the magnetometer under He/vacuum atmosphere until its final annealing temperature of 400 K, remaining inside the device for about 25 h. In contrast, the sample for the Mössbauer measurement was mixed with Na<sub>2</sub>SO<sub>4</sub> for a better distribution inside the sample holder. The annealing of the mixed Mössbauer sample was performed by heating the sample holder inside a Schlenk tube with nitrogen atmosphere in a drying oven at 393 K for 1 h. The measurements at the other temperatures can be found in Figure S28. The chemical shift  $\delta$ , the quadrupole splitting  $\Delta E_Q$ , the line width  $\Gamma$ , the asymmetry  $A_2/A_1$ , and the area of the doublets are given in Table S4.



**Figure 5:** Mössbauer spectra of sample **5e** at two different temperatures (250 K and 80 K) before thermal annealing (as-synthesized, left) and after thermal annealing (right).

SEM was additionally performed on the samples **#e** to analyze the surface of the nanocomposites. The surface was found to be crystal-free for the five nanocomposites before thermal annealing, indicating the successful incorporation of the CP into the polymeric micelles. (**Figure S30** to **Figure S34**).

The nanocomposites were again analyzed by TEM and DLS after annealing to exclude the formation of the CP outside the polymeric micelles. The samples were redispersed to prove that the particles are still narrowly dispersed after annealing and no formation of nano- or microcrystals can be observed. The average hydrodynamic diameters  $D_h$  after annealing range

from  $106 \pm 67$  nm (**1e\***) to  $246 \pm 149$  nm (**5e\***) (**Figure S35**). Particle core sizes and core widths of the annealed products  $D_{\text{core}}$  are  $14 \pm 2$  nm (**1e\***) to  $65 \pm 5$  nm (**5e\***) (**Table 6** and **Figure S36**). In Table 6 the comparison of the core size/core width and the hydrodynamic diameter of the as-synthesized and the annealed samples is given. The particles after annealing were found to be identical in size both in solution and in the dry state compared to the as-synthesized nanocomposites. Microcrystals were absent for both characterization methods. This indicates that the crystals found in the SEM measurements are not CP crystals but rather crystals of the excess of bipy which is rapidly dissolved upon the sample preparation process for TEM and DLS.

Magnetic measurements also point to the fact that no CP microcrystals are present in the sample. The change in the SCO properties is similar for sample **1e** and **5e**. In addition, a sample synthesized in toluene containing CP microcrystals in TEM measurements showed bulk-like behavior even without thermal annealing (**Figure S37**). Moreover, a toluene solution with microcrystals and a THF nanocomposite solution were kept until complete evaporation of the solvents. As expected, CP crystals precipitated from the toluene solution, while the THF nanocomposite solution resulted in the formation of a polymeric solid/film (**Figure S38**).

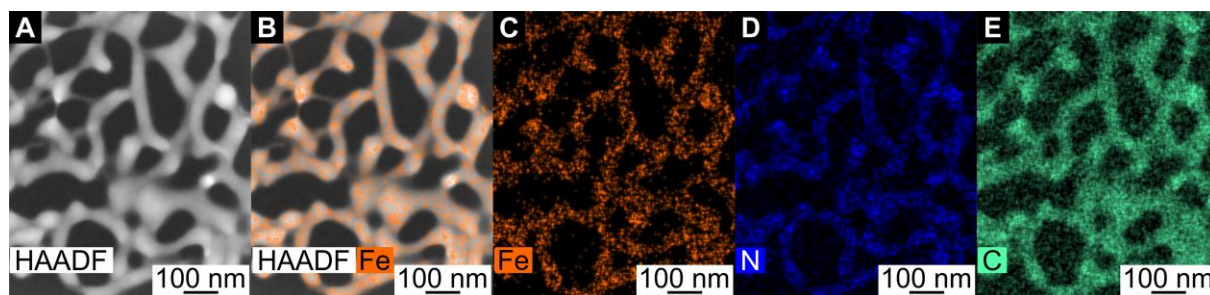
The five before mentioned samples were again characterized by SEM after thermal annealing (**Figure S29** to **Figure S33**). While the surface of the annealed samples **1e\*** and **2e\*** remained crystal-free, crystals were observed for the samples **3e\***, **4e\***, and **5e\***. Interestingly, the presence of crystals on the surface of sample **5e\*** is less prominent than for the other two samples, which may be an effect of an improved formation of the CP inside the elongated worm-like micelles.

Additionally, optical light microscopy was performed with two different dried up solutions from THF (BCP/bipy and SCO CP-BCP solutions), a powdered sample of the CP  $[\text{FeL}(\text{bipy})]_n$ , and a micrometer crystal of  $[\text{FeL}(\text{bipy})]_n$  obtained from a dried up SCO CP-BCP solution from toluene. The bipyridine crystallized in a starshaped structure, which was also detected for the dried up SCO CP-BCP solution from THF (see **Figure S39A, B**). Images of the powdered CP and the crystal obtained from a dried up SCO CP-BCP solution from toluene revealed unshaped structures (**Figure S39C**) and block shaped crystals (**Figure S39D**), respectively. Both latter CP samples were additionally much darker in color than the SCO CP-BCP sample from THF, supporting the assumption that the crystals observed by optical light microscopy and SEM are the crystallized excess of bipy used in the reactions.

**Table 6:** Comparison of the hydrodynamic diameter and the core diameter/width measured by DLS and TEM before annealing (as-synthesized samples; **1e**, **2e**, **3e**, **4e**, and **5e**) and after thermal annealing (**1e\***, **2e\***, **3e\***, **4e\***, and **5e\***).

Sample	Hydrodynamic diameter $D_h$ [nm]	Core diameter/width $D_{core}$ [nm]
<b>1e</b>	113 ± 67	14 ± 2
<b>1e*</b>	106 ± 67	14 ± 2
<b>2e</b>	118 ± 55	28 ± 3
<b>2e*</b>	109 ± 39	27 ± 3
<b>3e</b>	139 ± 38	48 ± 4
<b>3e*</b>	123 ± 34	48 ± 5
<b>4e</b>	139 ± 36	58 ± 4
<b>4e*</b>	140 ± 39	53 ± 4
<b>5e</b>	242 ± 147	60 ± 8
<b>5e*</b>	246 ± 149	65 ± 5

Transmission electron microscopy – energy dispersive X-ray (TEM-EDX) measurements were additionally performed on the sample **5d** to evaluate the spatial distribution of iron inside the SCO CP-BCP. It was expected that the iron can only be detected inside the polymeric structure. **Figure 6** shows the high-angle annular dark field (HAADF) image of sample **5d** (A) and the respective overlay of the HAADF image with the iron signal from EDX (B). The images of the distribution of only iron (C), nitrogen (D), and carbon (E) are presented as well. Iron was only detected inside the SCO CP-BCP composite and is homogenously distributed throughout the polymer structure. Image C shows that the iron signal is identical to the signals of nitrogen and carbon of the BCP. Two energy spectra were calculated by the integration of two different areas identical in size of the sample. One spectrum was taken on the area of the SCO CP-BCP composite and the other one outside of the SCO CP-BCP (**Figure S40**). The results confirm that iron was only found inside the SCO CP-BCP, indicating an incorporation of the SCO CP into the BCP.



**Figure 6:** HAADF image of sample **5d** showing the worm-like structures (A), an overlay of the iron signal received from TEM-EDX measurements and the HAADF image (B), and the individual images of the iron (C), nitrogen (D), and carbon (E) signals from TEM-EDX.

### 9.3. Conclusion

Five different BCPs with a varying P4VP content (SV-15 to SV-61) have been prepared. The TEM and cryo-TEM images of the neat BCPs showed spherical micelles with core sizes  $D_{\text{core}}$  of  $15 \pm 2$  nm (SV-15) to  $73 \pm 9$  nm (SV-61) and  $D_{\text{cryo}}$  of  $26 \pm 2$  nm (SV-15) to  $71 \pm 4$  nm (SV-61). These polymers were also utilized as nanoreactors in the synthesis of iron(II)-based CP NPs, well-defined in terms of size and shape. The nanocomposite particles with the BCPs SV-15 to SV-42 are also spherical and the size is similar to the neat BCP particles, underlining the templating effect of the BCPs. Interestingly, the morphology of the micelles changed to rods or worm-like micelles for the nanocomposites synthesized with SV-61 and the particle core widths were determined by TEM ( $D_{\text{core}} = 60 \pm 8$  nm) and cryo-TEM ( $D_{\text{cryo}} = 84 \pm 10$  nm), respectively. These results indicated that the introduction of the CP induced a morphological change by increasing the insoluble parts of the nanocomposite. Additionally, it was shown that the magnetic properties of the SCO CP-BCP nanocomposites can be altered by several factors to approximate a bulk-like behavior: (1) the reduction of the amount of the bridging ligand bipy from 2.5 eq to 1.5 eq. This resulted in a lower residual HS fraction  $\gamma_{\text{HS}}$  in all samples. (2) The enlargement of the spherical particle cores from 14 nm to 58 nm also resulted in a decrease of  $\gamma_{\text{HS}}$  from 30 % (**1e**) to 21 % (**4e**). (3) The thermal annealing of the SCO CP-BCP composites led to a shift in the transition temperature and, again, in a decrease of  $\gamma_{\text{HS}}$ . (4) The change of the morphology of the nanocomposite particles to rods or worm-like micelles allowed the CP to crystallize in longer strands. As a result, the  $\gamma_{\text{HS}}$  value ultimately reached 14 % (**5e**). In addition, TEM EDX of a nanocomposite containing worm-like structures (**5d**) proved that the iron containing SCO CP is only located inside the polymeric structure and no iron can be detected outside of the micelles.

#### 9.4. Acknowledgements

Financial support of the University of Bayreuth and the SFB 840 (TP A10 and A2) is gratefully acknowledged. Christoph Göbel was supported by the BayNAT program of the University of Bayreuth. We thank Dr. Jana Timm and Prof. Dr. Roland Marschall (Physical Chemistry III, Universität Bayreuth) for their contribution to the temperature-dependent PXRD measurements and Florian Puchtler (Inorganic Chemistry I, Universität Bayreuth) for room temperature PXRD. Dr. Christine Denner (Inorganic Chemistry II, Universität Bayreuth) for SEM measurements and Rika Schneider (Macromolecular Chemistry II, Universität Bayreuth) for DSC, GPC, and NMR measurements of the BCPs. The authors thank Prof. Dr. F. J. Litterst (Institut für Physik der Kondensierten Materie) at TU Braunschweig for providing access to the  $^{57}\text{Fe}$  Mössbauer spectrometer.

#### 9.5. References

- [1] M. A. Halcrow (Ed.) *Spin-Crossover Materials*, John Wiley & Sons Ltd, Chichester, **2013**.
- [2] P. Gülich, H.A. Goodwin (Eds.) *Topics in Current Chemistry*, 233–235, Springer, Berlin, Heidelberg, **2004**.
- [3] C. Bartual-Murgui, A. Akou, C. Thibault, G. Molnár, C. Vieu, L. Salmon, A. Bousseksou, *J. Mater. Chem. C* **2015**, 3, 1277–1285.
- [4] P. Gülich, H.A. Goodwin, *Spin Crossover in Transition Metal Compounds III*, Springer, Berlin, Heidelberg, **2004**.
- [5] a) R. N. Muller, L. Vander Elst, S. Laurent, *J. Am. Chem. Soc.* **2003**, 125, 8405–8407. b) I.-R. Jeon, J. G. Park, C. R. Haney, T. D. Harris, *Chem. Sci.* **2014**, 5, 2461–2465.
- [6] a) J. Oliver-Meseguer, M. Boronat, A. Vidal-Moya, P. Concepción, M. Á. Rivero-Crespo, A. Leyva-Pérez, A. Corma, *J. Am. Chem. Soc.* **2018**, 140, 3215–3218.; b) M. Ma, Y. Yang, W. Li, R. Feng, Z. Li, P. Lyu, Y. Ma, *J. Mater. Sci.* **2019**, 54, 323–334.; c) Y. Tong, G. Xue, H. Wang, M. Liu, J. Wang, C. Hao, X. Zhang, D. Wang, X. Shi, W. Liu, G. Li, Z. Tang, *Nanoscale* **2018**, 10, 16425–16430.
- [7] L. Qu, X. Peng, *J. Am. Chem. Soc.* **2002**, 124, 2049–2055.
- [8] a) S. Wang, C. Wang, Z. Peng, S. Chen, *Sci. Rep.* **2018**, 8, 9682; b) N. Ashouri, A. Mohammadi, R. Hajiaghvaei, M. Shekarchi, M. R. Khoshayand, *Desalin. Water Treat.* **2016**, 57, 14280–14289.; c) F. Sedighi, M. Esmaeili-Zare, A. Sobhani-Nasab, M. Behpour, *J. Mater. Sci.: Mater. Electron.* **2018**, 29, 13737–13745.

- 
- [9] a) C. Bartual-Murgui, E. Natividad, O. Roubeau, *J. Mater. Chem. C* **2015**, *3*, 7916–7924.; b) L. Moulet, N. Daro, C. Etrillard, J.-F. Létard, A. Grosjean, P. Guionneau, *Magnetochemistry* **2016**, *2*, 10.; c) A. D. Souza, P.D. Babu, S. Rayaprol, M.S. Murari, L. D. Mendonca, M. Daivajna, *J. Alloys Compd.* **2019**, *797*, 874–882.; d) A. G.Roca, L. Gutiérrez, H. Gavilán, M. E. F. Brollo, S. Veintemillas-Verdaguer, M. del Puerto Morales, *Adv. Drug Deliv. Rev.* **2019**, *138*, 68–104.;
- [10] a) H. Mistry, R. Reske, P. Strasser, B. R. Cuenya, *Catal. Today* **2017**, *288*, 30–36.; b) D. Decarolis, Y. Odarchenko, J. J. Herbert, C. Qiu, A. Longo, A. M. Beale, *Phys. Chem. Chem. Phys.* **2019**, DOI: 10.1039/c9cp03473k; c) M. Giménez-Marqués, M. L. García-Sanz de Larrea, E. Coronado, *J. Mater. Chem. C* **2015**, *3*, 7946–7953.; d) J. H. González-Estefan, M. Gonidec, N. Daro, M. Marchivie, G. Chastanet, *Chem. Commun.* **2018**, *54*, 8040–8043.; e) J. Wojnarowicz, T. Chudoba, I. Koltsov, S. Gierlotka, S. Dworakowska, W. Lojkowski, *Nanotechnology* **2018**, *29*, 065601.; f) Z. Fu, L. Li, M. Wang, X. Guo, *Colloid Polym. Sci.* **2018**, *296*, 935–940.; g) A. W. Jansons, J. E. Hutchison, *ACS Nano* **2016**, *10*, 6942–6951.
- [11] a) M. J. Ashley, M. R. Bourgeois, R. R. Murthy, C. R. Laramy, M. B. Ross, R. R. Naik, G. C. Schatz, C. A. Mirkin, *J. Phys. Chem. C* **2018**, *122*, 2307–2314.; b) I. Chakraborty, N. Feliu, S. Roy, K. Dawson, W. J. Parak, *Bioconjugate Chem.* **2018**, *29*, 1261–1265.; c) L. Huang, X. Zhang, Q. Wang, Y. Han, Y. Fang, S. Dong, *J. Am. Chem. Soc.* **2018**, *140*, 1142–1147.; d) Y. Dai, X. Zhang, *Macromol. Mater. Eng.* **2018**, *303*, 1800105.
- [12] a) H. Peng, S. Tricard, G. Flix, G. Molnár, W. Nicolazzi, L. Salmon, A. Bousseksou, *Angew. Chem. Int. Ed.* **2014**, *53*, 10894–10898.; b) A. Atitoaie, R. Tanasa, C. Enachescu, *J. Magn. Magn. Mater.* **2012**, *324*, 1596–1600. c) F. Volatron, L. Catala, E. Rivièrè, A. Gloter, O. Stéphan, T. Mallah, *Inorg. Chem.* **2008**, *47*, 6584–6586.; d) T. Forestier, S. Mornet, N. Daro, T. Nishihara, S. Mouri, K. Tanaka, O. Fouché, E. Freysz J.-F. Létard, *Chem. Commun.* **2008**, 4327–4329.
- [13] a) H. J. Shepherd, I. A. Gural'skiy, C. M. Quintero, S. Tricard, L. Salmon, G. Molnár, A. Bousseksou, *Nat. Commun.* **2013**, *4*, 2607.; b) M. D. Manrique-Juárez, F. Mathieu, V. Shalabaeva, J. Cacheux, S. Rat, L. Nicu, Thierry Leïchlé, L. Salmon, G. Molnár, A. Bousseksou, *Angew. Chem. Int. Ed.* **2017**, *56*, 8074–8078.; c) M. D. Manrique-Juárez, F. Mathieu, A. Laborde, S. Rat, V. Shalabaeva, P. Demont, O. Thomas, L. Salmon, T. Leichle, L. Nicu, G. Molnár, A. Bousseksou, *Adv. Funct. Mater.* **2018**, *28*, 1801970.
- [14] a) Y. Mai, A. Eisenberg, *Chem. Soc. Rev.* **2012**, *41*, 5969–5985.; b) D. J. Adams, P. D. Topham, *Supramolecular Chemistry: From Molecules to Nanomaterials*, John Wiley & Sons Ltd, Chichester, **2012**, doi: 10.1002/9780470661345.smc135.; c) F. H. Schacher, P. A. Rugar, I.
-

- Manners, *Angew. Chem. Int. Ed.* **2012**, *51*, 7898–7921.; d) M. Müllner, A. H. E. Müller, *Polymer* **2016**, *98*, 389–401.; e) Y. Lu, M. Ballauff, *Prog. Polym. Sci.* **2016**, *59*, 86–104.
- [15] a) K.-V. Peinemann, V. Abetz, P. F. W. Simon, *Nat. Mater.* **2007**, *6*, 992–996.; b) T. Hashimoto, K. Yamasaki, S. Koizumi, H. Hasegawa, *Macromolecules* **1993**, *26*, 2895–2904.; c) H.-A. Klok, S. Lecommandoux, *Adv. Mater.* **2001**, *13*, 1217–1229.; d) D. A. Hajduk, P. E. Harper, S. M. Gruner, C. C. Honeker, G. Kim, E. L. Thomas, L. J. Fetters, *Macromolecules* **1994**, *27*, 4063–4075.
- [16] a) D. Li, Y. Xia, *Nano Lett.* **2004**, *4*, 933–938.; b) C. Shao, H.-Y. Kim, J. Gong, B. Ding, D.-R. Lee, S.-J. Park, *Mater. Lett.* **2003**, *57*, 1579–1584.; c) X. Li, X. Yu, C. Cheng, L. Deng, M. Wang, X. Wang, *ACS Appl. Mater. Interfaces* **2015**, *7*, 21919–21930.
- [17] a) Y. Wang, J. He, H. Chen, J. Chen, R. Zhu, P. Ma, A. Towers, Y. Lin, A. J. Gesquiere, S.-T. Wu, Y. Dong, *Adv. Mater.* **2016**, *28*, 10710–10717.; b) H. Song, S. Lee, *Nanotechnology* **2007**, *18*, 055402.
- [18] O. Klimm, C. Göbel, S. Rosenfeldt, F. Puchtler, N. Miyajima, K. Marquardt, M. Drechsler, J. Breu, S. Förster, B. Weber, *Nanoscale* **2016**, *8*, 19058–19065.
- [19] C. Göbel, O. Klimm, F. Puchtler, S. Rosenfeldt, S. Förster, B. Weber, *Beilstein J. Nanotechnol.* **2017**, *8*, 1318–1327.
- [20] C. Göbel, G. Hörner, A. Greiner, H. Schmalz, B. Weber, Synthesis of Zn-based 1D and 2D coordination polymer nanoparticles in block copolymers, *Nanoscale Adv.* **2020**, *submitted*.
- [21] C. Göbel, C. Hils, M. Drechsler, D. Baabe, A. Greiner, H. Schmalz, B. Weber, *Angew. Chem. Int. Ed.* **2020**, *59*, 5765–5770.
- [22] T. H. Kim, J. Huh, J. Hwang, H.-C. Kim, S. H. Kim, B.-H. Sohn, C. Park, *Macromolecules* **2009**, *42*, 6688–6697.
- [23] a) N. Ali, S.-Y. Park, *Langmuir* **2008**, *24*, 9279–9285; b) H. Cho, H. Park, S. Park, H. Choi, H. Huang, T. Chang, *J. Colloid Interface Sci.* **2011**, *356*, 1–7; c) I. I. Perepichka, Q. Lu, A. Badia, C. G. Bazuin, *Langmuir* **2013**, *29*, 4502–4519.
- [24] a) L. Song, Y. M. Lam, C. Boothroyd, P. Wen Teo, *Nanotechnology* **2007**, *18*, 135605; b) S. Roland, D. Gaspard, R. E. Prud'homme, C. G. Bazuin, *Macromolecules* **2012**, *45*, 5463–5476.
- [25] S. Förster, M. Zisenis, E. Wenz, M. Antonietti, *J. Chem. Phys.* **1996**, *104*, 9956–9970.
- [26] S. O'Driscoll, G. Demirel, R. A. Farrell, T. G. Fitzgerald, C. O'Mahony, J. D. Holmes, M. A. Morris, *Polym. Adv. Technol.* **2011**, *22*, 915–923.
-

- [27] J. Israelachvili, *Intermolecular & Surface Forces*, Elsevier, Amsterdam, **1992**.
- [28] B. Weber, *Möss. Eff. Ref. Data J.* **2012**, 35, 238–254.



## 9.6. Supporting Information

### 9.6.1. General Procedures

**Materials:** All SCO CP-BCP syntheses were performed under inert conditions using argon 5.0 (purity  $\geq 99,999\%$ ) using Schlenk tube technique. The synthesis of the sample was repeated at least twice. Tetrahydrofuran (THF) p.a. for the SCO syntheses was obtained from Bernd Kraft and degassed with argon for at least 30 min.  $[\text{FeL}(\text{MeOH})_2]$  was synthesized as described before.<sup>[1]</sup> 4,4'-bipyridine was obtained from Alfa Aesar and used as received.

THF (Fischer Scientific,  $\geq 99.8\%$ ) for anionic polymerization was purified by successive distillation over calcium hydride ( $\text{CaH}_2$ , Merck) and potassium (K, Sigma-Aldrich) under  $\text{N}_2$  atmosphere. Styrene (S, Sigma-Aldrich,  $> 99\%$ ) was purified over dibutyl magnesium ( $\text{Bu}_2\text{Mg}$ , Sigma-Aldrich, 1M in heptane) and 4-vinylpyridine (4VP, Acros Organics, 95%) over triethyl aluminum ( $\text{Et}_3\text{Al}$ , Sigma-Aldrich, 1M in heptane), respectively, followed by condensing into storage ampoules. 1,1-Diphenylethylene (DPE, Acros Organics, 98%) was purified by addition of *sec*-butyllithium (*sec*-BuLi, Acros Organics, 1.3M in cyclohexane/hexane 92/8) and subsequent distillation.

For **gel permeation chromatography** (GPC) in *N,N*-dimethylformamide (DMF) with lithium bromide ( $5 \text{ g L}^{-1}$ ), GRAM columns (300 x 8 mm, 10  $\mu\text{m}$  particle size, PSS Mainz) with 100 and 3000 Å pore sizes were used. The sample was measured on a SEC 1260 Infinity system (Agilent Technologies) at a flow rate of  $0.5 \text{ mL min}^{-1}$  at 23 °C, using a refractive index detector (Agilent Technologies). The calibration was done with narrowly distributed polystyrene standards (PSS calibration kit) and toluene (HPLC grade) was used as internal standard.

**MALDI-ToF MS** (matrix-assisted laser desorption/ionization time-of-flight mass spectrometry) measurements were performed on a Reflex III (Bruker) equipped with a  $\text{N}_2$  Laser ( $\lambda = 337 \text{ nm}$ ). An acceleration voltage of 20 kV was used in linear mode and the samples were prepared according to the dried droplet method. Therefore, matrix (trans-2-[3-(4-*tert*-butylphenyl)-2-methyl-2-propenylidene]malononitrile (DCTB),  $10 \text{ g L}^{-1}$  in THF), analyte ( $10 \text{ g L}^{-1}$  in THF) and salt (silver trifluoroacetate,  $10 \text{ g L}^{-1}$ ) were dissolved and mixed in the ratio of 20 : 5 : 1 and 0.5  $\mu\text{L}$  of the mixture was placed and dried on the target plate.

**$^1\text{H}$ -NMR** spectra were acquired with a Bruker Ultrashield 300 spectrometer using  $\text{CDCl}_3$  as solvent.

The **differential scanning calorimetry** (DSC) measurements were performed on a Phoenix 204 F1 (Netzsch) under nitrogen atmosphere, using aluminum crucibles (temperature range: 20 – 200 °C, scanning rates: 10, 20 and 30  $\text{K}\cdot\text{min}^{-1}$ ).

Transmission **infrared (IR)** spectra were collected from a Perkin Elmer Spectrum 100 FT-IR (ATR). The samples were measured directly as solids.

For **elemental analysis**, the carbon, nitrogen, and hydrogen contents were determined with a Vario EL III (Elementar Analysensysteme GmbH) with acetanilide as standard or at an Unicube from Elementar Analysensysteme GmbH with sulfanilamide as standard. The samples were placed in tin boats and measured at least twice. The average of the measurements was used.

**Magnetic susceptibility** measurements were performed at a Quantum Design MPMS-XL-5 SQUID magnetometer. Field strength of 3 T was applied and a temperature range of 50 – 400 K was used to determine the temperature dependency of the magnetism and the spin crossover behavior. Sweep mode was used for the five cycles with a cooling and heating rate of 5 K min<sup>-1</sup>. The final measurement was performed in settle mode with a cooling and heating rate of 5 K min<sup>-1</sup> between 50 K and 300 K. The samples were prepared in gelatin capsules placed in a plastic straw. The measured values were corrected for the diamagnetism of the sample holder, the polymer matrix (measured values) and the ligand (tabulated Pascal constants).

The **room temperature <sup>57</sup>Fe Mössbauer** spectrum was recorded in transmission geometry with constant acceleration using a conventional Mössbauer spectrometer with a 50 mCi <sup>57</sup>Co(Rh) source. The samples were sealed in the sample holder in an argon atmosphere. The spectra were fitted using Recoil 1.05 Mössbauer Analysis Software.<sup>[2]</sup> The isomer shift values are given with respect to a  $\alpha$ -Fe reference at room temperature.

**Temperature-dependent zero-field <sup>57</sup>Fe Mössbauer** measurements on polycrystalline powder of SCO CP-BCP were conducted at variable temperatures between  $T = 80$  and 300 K. A conventional transmission spectrometer with sinusoidal velocity sweep. The temperature-dependent measurements between  $T = 80$  and 300 K were conducted on a CryoVac continuous-flow cryostat with He or N<sub>2</sub> contact gas. After positioning the sample container (made of Teflon or PEEK), the sample chamber was evacuated, flushed five times with He or N<sub>2</sub> gas, and kept at ca. 50 – 100 mbar during the measurement. The temperature was measured with a calibrated silicon diode located close to the sample container, providing a temperature stability of better than 0.1 K. The nominal activity of the <sup>57</sup>Fe Mössbauer source used was 50 mCi of <sup>57</sup>Co in a rhodium matrix, which was stored at ambient temperature during the measurement. Velocity calibration was done with an  $\alpha$ -iron foil at ambient temperature and the minimum experimental line width (FWHM) was < 0.24 mm s<sup>-1</sup>. Isomer shifts ( $\delta$ ) were specified relative to metallic iron at room temperature but were not corrected in terms of the second-order Doppler shift. The spectra were analysed by least-square fits using doublets of Lorentzian lines utilizing the software package NORMOS.<sup>[3]</sup>

**Scanning electron microscopy** (SEM) micrographs were taken on a Zeiss LEO 1530 GEMINI and a Zeiss Ultra plus. The acceleration voltage was set to 3 kV (with a Schottky-field-emission gun) using an in-lens secondary electron detector. The sample was sputter-coated with a 1.3 nm platinum layer.

Room temperature **powder X-ray diffraction** (PXRD) data were collected with a STOE StadiP X-Ray diffractometer in transmission geometry between 5° and 30° 2 $\theta$  for all samples, which were placed on flat surfaces. Cu-K $\alpha_1$  radiation ( $\lambda = 1.541 \text{ \AA}$ ) was used for the measurements together with a Mythen 1K detector.

**Temperature-dependent powder X-ray diffraction** (T-PXRD) pattern were recorded using a Bragg-Brentano type diffractometer (X'PERT-Pro, PANalytical with CuK $\alpha_1$ -radiation ( $\lambda = 1.541 \text{ \AA}$ ), equipped with a secondary monochromator to suppress fluorescence. The sample was placed on a flat surface in a flowing nitrogen atmosphere in an XRK chamber during the measurement.

**Transmission electron microscopy:** Transmission electron microscopy was taken at a Zeiss CEM902 electron microscope (Zeiss, Oberkochen, Germany) and a JEOL 2200FS electron microscope. Samples were dispersed in THF. The dispersion was dropped on a carbon coated copper grid (mesh 200, Science Services, Munich). Electron acceleration voltage was set to 80 kV (CEM902) and 200 kV (JEOL 2200FS). Micrographs were taken with a MegaView III / iTEM image acquiring and processing system from Olympus Soft Imaging Systems (OSIS, Münster, Germany) and an Orius 830 SC200W / DigitalMicrograph system from Gatan (Munich, Germany). Particles size measurements were done with “ImageJ” image processing software developed by Wayne Rasband (National Institutes of Health, USA).

For **cryo transmission electron microscopy** studies, a sample droplet of 2  $\mu\text{L}$  was put on a lacey carbon filmed copper grid (Science Services, Munich, Germany). Subsequently, most of the liquid was removed with blotting paper leaving a thin film stretched over the lace holes. The specimens were instantly shock frozen by rapid immersion into liquid nitrogen cooled to approximately 90 K in a temperature-controlled freezing unit (Zeiss Cryobox, Carl Zeiss Microscopy GmbH, Jena, Germany). The temperature was monitored and kept constant in the chamber during all the sample preparation steps. The specimen was inserted into a cryotransfer holder (CT3500, Gatan, Munich, Germany) and transferred to a Zeiss / LEO EM922 Omega EFTEM (Zeiss Microscopy GmbH, Jena, Germany). Examinations were carried out at temperatures around 90 K. The TEM was operated at an acceleration voltage of 200 kV. Zero-loss filtered images (DE = 0 eV) were taken under reduced dose conditions (100 – 1000 e/nm<sup>2</sup>). All images were registered digitally by a bottom mounted CCD camera system (Ultrascan 1000, Gatan, Munich, Germany) combined and processed with a digital imaging processing system (Digital Micrograph GMS 1.9, Gatan, Munich, Germany).

---

**Dynamic light scattering** (DLS) measurements were done at an AntonPaar Litesizer 500 in quartz glass cuvettes from Helma at 25 °C. One measurement consists of six consecutive runs.

**Optical light microscopy** was performed on a Keyence VHX-950F equipped with a VH-Z250F objective lens. Samples were prepared on a glass microscope slides from solution or directly as solids.

### 9.6.2. Synthesis Procedures

#### Synthesis of the PS-*b*-P4VP diblock copolymers

The PS-*b*-P4VP diblock copolymers were synthesized by sequential living anionic polymerization in THF using a laboratory autoclave (1 L, Büchi AG). Styrene was polymerized first for 30 min using *sec*-BuLi as initiator at -80 °C. After complete conversion of styrene, a sample was taken for GPC and MALDI-ToF analyses. Subsequently, 1,1-diphenylethylene was added to the living polystyryllithium (equimolar amount to initiator), followed by the addition of 4-vinylpyridine (4VP). After 4 h the polymerization was terminated with degassed methanol followed by precipitation in deionized water to isolate the diblock copolymer. The number average molecular weights of the PS-*b*-P4VP diblock copolymers were determined from <sup>1</sup>H-NMR (CDCl<sub>3</sub>), employing the absolute molecular weight of the PS precursor obtained by MALDI-ToF MS for signal calibration. As the solubility of the P4VP block in THF strongly decreases with its chain length<sup>[4]</sup>, micellization and, thus, a significant increase in solution viscosity occurred during the synthesis of the diblock copolymers with high P4VP fractions. Nevertheless, polymerization of 4VP proceeds within the core of the formed micelles to yield the desired diblock copolymers. However, this resulted in an increase in dispersity with increasing P4VP weight fraction (Table 1). The diblock copolymer S<sub>39</sub>V<sub>61</sub><sup>162</sup> was additionally purified by extraction with cyclohexane/THF (1/1 v/v) over night to remove a small fraction of PS homopolymer formed by termination upon addition of 4VP.

**Synthesis of the SCO CP-BCP nanocomposites in SV-15**

50 mg  $S_{85}V_{15}^{154}$  and 6.7 mg (15  $\mu\text{mol}$ )  $[\text{FeL}(\text{MeOH})_2]$  were dissolved in 20 mL THF in a 50 mL Schlenk flask. The solution was refluxed for 2 h. After cooling, 5.9 mg (37.5  $\mu\text{mol}$ , 2.5 eq) 4,4'-bipyridine was added and the solution was refluxed again for 1 h. After reaching RT, 6.7 mg (15  $\mu\text{mol}$ )  $[\text{FeL}(\text{MeOH})_2]$  and 5.9 mg (37.5  $\mu\text{mol}$ , 2.5 eq) 4,4'-bipyridine were added simultaneously and the solution was refluxed again for 1 h. The simultaneous addition of the reactants and the subsequent reflux of the solution were repeated up to three more times (samples **1a** to **1d**). Consecutively, the solvent was removed by cold distillation and the resulting dark brown polymeric solid was dried *in vacuo*. For sample **1e** the amount of 4,4'-bipyridine for each reaction cycle was reduced to 3.5 mg (22.5  $\mu\text{mol}$ , 1.5 eq).

**1a:** Elemental anal. (%) found: C 72.16, H 7.40, N 2.65.

**1b:** Elemental anal. (%) found: C 57.90, H 6.83, N 3.37.

**1c:** Elemental anal. (%) found: C 66.14, H 6.81, N 5.10.

**1d:** Elemental anal. (%) found: C 67.06, H 6.59, N 5.85.

**1e:** Elemental anal. (%) found: C 64.27, H 6.43, N 4.70.

**Synthesis of the SCO CP-BCP nanocomposites in SV-21**

50 mg  $S_{79}V_{21}^{119}$  and 9.4 mg (21  $\mu\text{mol}$ )  $[\text{FeL}(\text{MeOH})_2]$  were dissolved in 20 mL THF in a 50 mL Schlenk flask. The solution was refluxed for 2 h. After cooling, 8.2 mg (52.5  $\mu\text{mol}$ , 2.5 eq) 4,4'-bipyridine was added and the solution was refluxed again for 1 h. After reaching RT, 9.4 mg (21  $\mu\text{mol}$ )  $[\text{FeL}(\text{MeOH})_2]$  and 8.2 mg (52.5  $\mu\text{mol}$ , 2.5 eq) 4,4'-bipyridine were added simultaneously and the solution was refluxed again for 1 h. The simultaneous addition of the reactants and the subsequent reflux of the solution were repeated up to three more times (samples **2a** to **2d**). Consecutively, the solvent was removed by cold distillation and the resulting dark brown polymeric solid was dried *in vacuo*. For sample **2e** the amount of 4,4'-bipyridine for each reaction cycle was reduced to 4.9 mg (31.5  $\mu\text{mol}$ , 1.5 eq).

**2a:** Elemental anal. (%) found: C 71.85, H 6.33, N 4.11.

**2b:** Elemental anal. (%) found: C 68.00, H 6.80, N 6.20.

**2c:** Elemental anal. (%) found: C 66.92, H 6.64, N 6.61.

**2d:** Elemental anal. (%) found: C 68.88, H 5.77, N 7.52.

**2e:** Elemental anal. (%) found: C 62.13, H 6.21, N 5.77.

**Synthesis of the SCO CP-BCP nanocomposites in SV-35**

50 mg  $S_{65}V_{35}^{131}$  and 14.8 mg (33  $\mu\text{mol}$ )  $[\text{FeL}(\text{MeOH})_2]$  were dissolved in 20 mL THF in a 50 mL Schlenk flask. The solution was refluxed for 2 h. After cooling, 12.9 mg (82.5  $\mu\text{mol}$ , 2.5 eq) 4,4'-bipyridine was added and the solution was refluxed again for 1 h. After reaching RT, 14.8 mg (33  $\mu\text{mol}$ )  $[\text{FeL}(\text{MeOH})_2]$  and 12.9 mg (82.5  $\mu\text{mol}$ , 2.5 eq) 4,4'-bipyridine were added simultaneously and the solution was refluxed again for 1 h. The simultaneous addition of the reactants and the subsequent reflux of the solution were repeated up to three more times (samples **3a** to **3d**). Consecutively, the solvent was removed by cold distillation and the resulting dark brown polymeric solid was dried *in vacuo*. For sample **3e** the amount of 4,4'-bipyridine for each reaction cycle was reduced to 7.8 mg (50  $\mu\text{mol}$ , 1.5 eq).

**3a:** Elemental anal. (%) found: C 68.70, H 7.12, N 5.36.

**3b:** Elemental anal. (%) found: C 64.67, H 6.15, N 6.88.

**3c:** Elemental anal. (%) found: C 63.66, H 6.56, N 7.18.

**3d:** Elemental anal. (%) found: C 66.60, H 6.27, N 8.29.

**3e:** Elemental anal. (%) found: C 60.99, H 5.96, N 6.88.

**Synthesis of the SCO CP-BCP nanocomposites in SV-42**

50 mg  $S_{58}V_{42}^{157}$  and 17.9 mg (40  $\mu\text{mol}$ )  $[\text{FeL}(\text{MeOH})_2]$  were dissolved in 20 mL THF in a 50 mL Schlenk flask. The solution was refluxed for 2 h. After cooling, 15.6 mg (100  $\mu\text{mol}$ , 2.5 eq) 4,4'-bipyridine was added and the solution was refluxed again for 1 h. After reaching RT, 17.9 mg (40  $\mu\text{mol}$ )  $[\text{FeL}(\text{MeOH})_2]$  and 15.6 mg (100  $\mu\text{mol}$ , 2.5 eq) 4,4'-bipyridine were added simultaneously and the solution was refluxed again for 1 h. The simultaneous addition of the reactants and the subsequent reflux of the solution were repeated up to three more times (samples **4a** to **4d**). Consecutively, the solvent was removed by cold distillation and the resulting dark brown polymeric solid was dried *in vacuo*. For sample **4e** the amount of 4,4'-bipyridine for each reaction cycle was reduced to 9.4 mg (60  $\mu\text{mol}$ , 1.5 eq).

**4a:** Elemental anal. (%) found: C 66.51, H 6.63, N 5.63.

**4b:** Elemental anal. (%) found: C 69.14, H 5.74, N 8.67.

**4c:** Elemental anal. (%) found: C 64.83, H 6.35, N 8.22.

**4d:** Elemental anal. (%) found: C 66.19, H 6.20, N 9.04.

**4e:** Elemental anal. (%) found: C 61.64, H 5.85, N 7.63.

**Synthesis of the SCO CP-BCP nanocomposites in SV-61**

50 mg  $\text{S}_{39}\text{V}_{61}^{162}$  and 29 mg (65  $\mu\text{mol}$ )  $[\text{FeL}(\text{MeOH})_2]$  were dissolved in 20 mL THF in a 50 mL Schlenk flask. The solution was refluxed for 2 h. After cooling, 25.4 mg (162.5  $\mu\text{mol}$ , 2.5 eq) 4,4'-bipyridine was added and the solution was refluxed again for 1 h. After reaching RT, 29 mg (65  $\mu\text{mol}$ )  $[\text{FeL}(\text{MeOH})_2]$  and 25.4 mg (162.5  $\mu\text{mol}$ , 2.5 eq) 4,4'-bipyridine were added simultaneously and the solution was refluxed again for 1 h. The simultaneous addition of the reactants and the subsequent reflux of the solution were repeated up to three more times (samples **5a** to **5d**). Consecutively, the solvent was removed by cold distillation and the resulting dark brown polymeric solid was dried *in vacuo*. For sample **5e** the amount of 4,4'-bipyridine for each reaction cycle was reduced to 15.2 mg (97.5  $\mu\text{mol}$ , 1.5 eq).

**5a:** Elemental anal. (%) found: C 69.01, H 6.14, N 9.11.

**5b:** Elemental anal. (%) found: C 64.66, H 5.46, N 9.68.

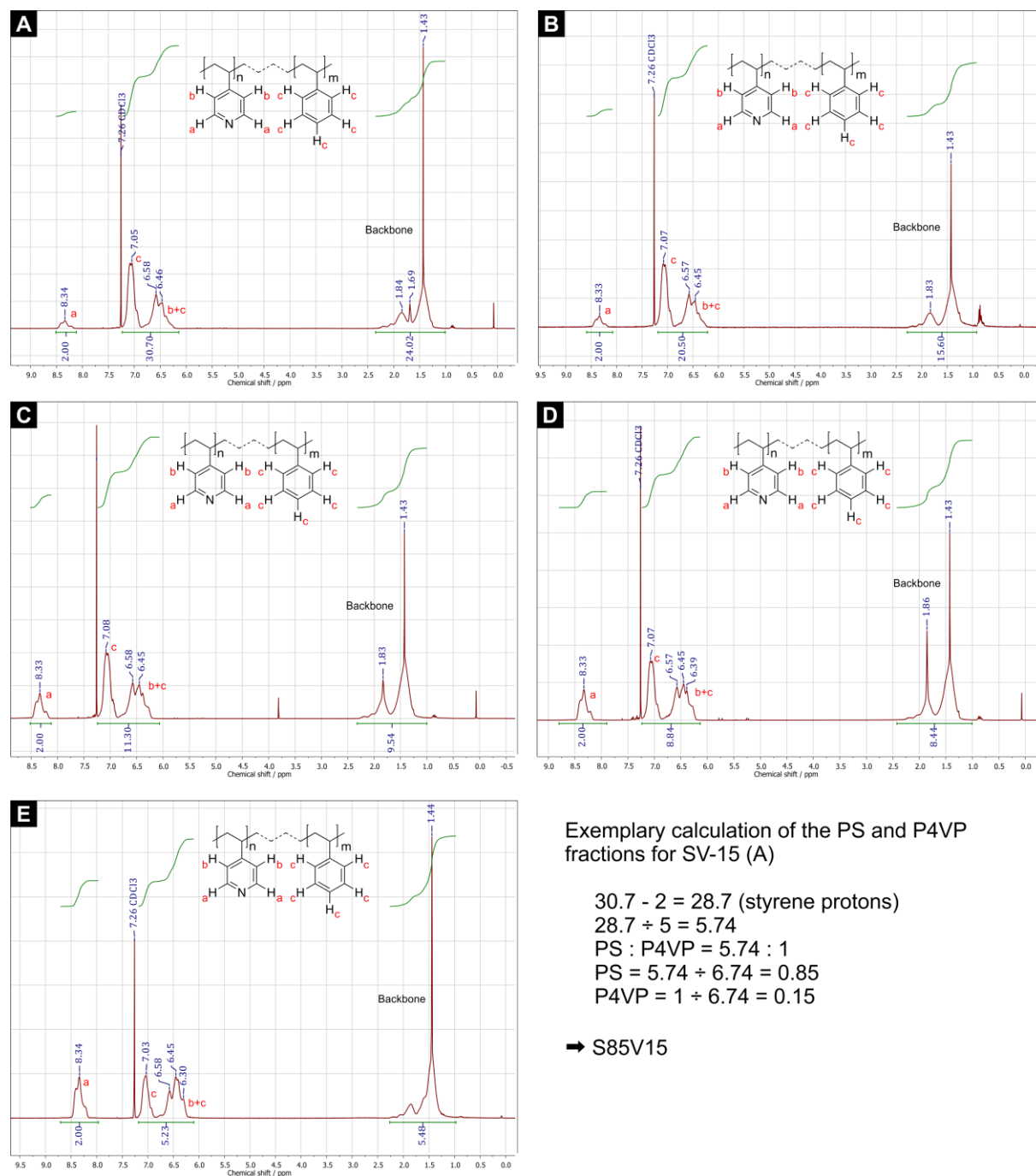
**5c:** Elemental anal. (%) found: C 65.97, H 5.50, N 10.49.

**5d:** Elemental anal. (%) found: C 66.22, H 5.70, N 10.64.

**5e:** Elemental anal. (%) found: C 62.60, H 5.62, N 8.93.

## 9.6.3. Characterization of the BCPs

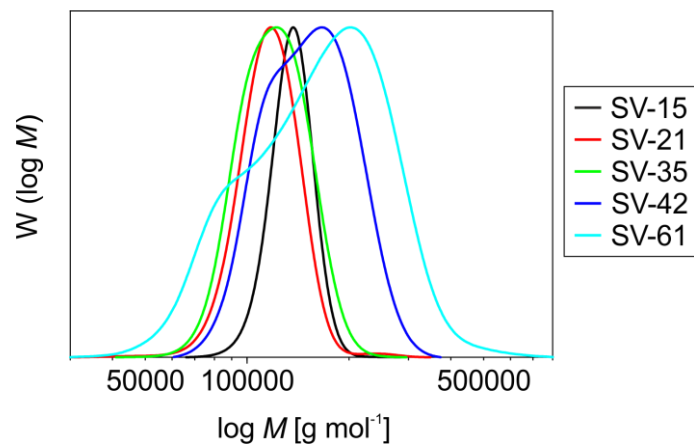
## NMR of the BCPs



**Figure S1:** NMR spectra of the five BCPs SV-15 (A), SV-21 (B), SV-35 (C), SV-42 (D), and SV-61 (E) and an exemplary calculation for the composition of the BCPs.

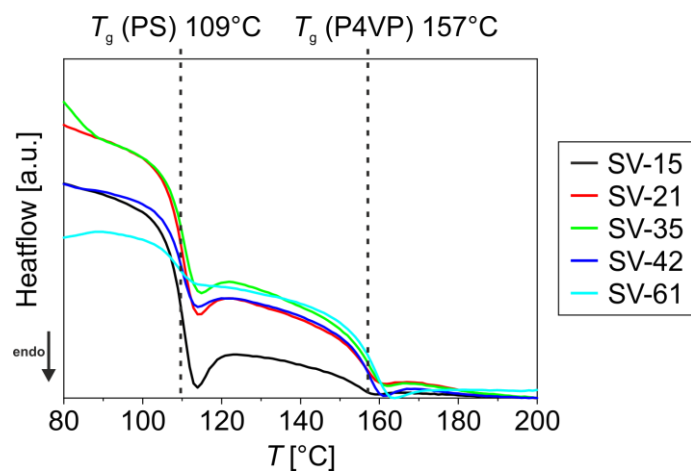


### GPC of the BCPs

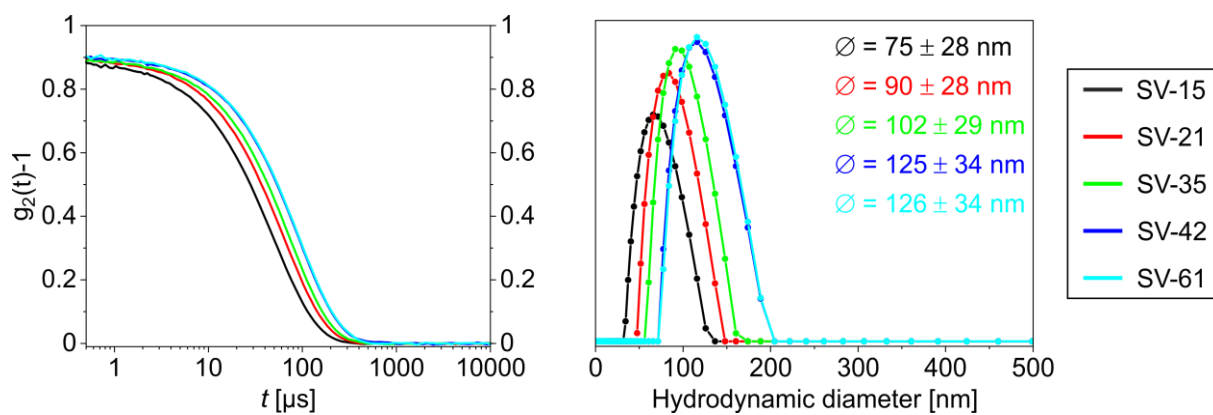


**Figure S2:** GPC data for the five BCPs SV-15 (black), SV-21 (red), SV-35 (green), SV-42 (blue), and SV-61 (light blue).

### DSC of the BCPs



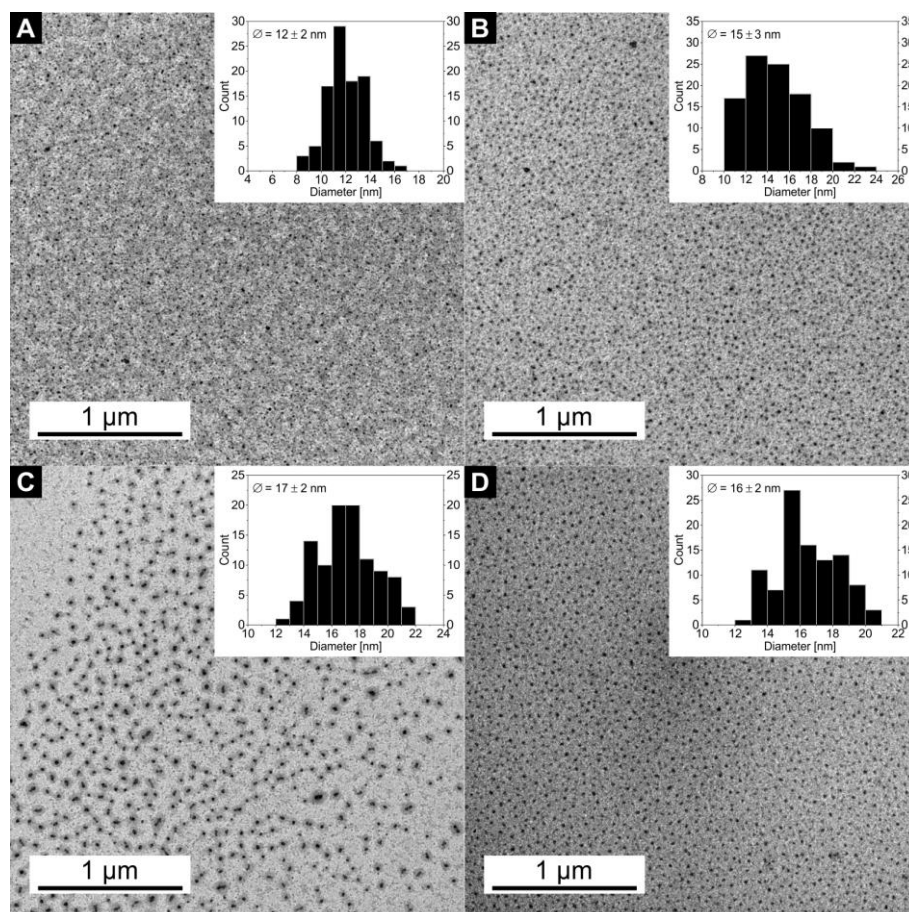
**Figure S3:** DSC measurements of the five BCPs SV-15 (black), SV-21 (red), SV-35 (green), SV-42 (blue), and SV-61 (light blue) showing the glass transition temperature  $T_g$  of PS and P4VP at 109 °C and 157 °C, respectively.

**DLS of the BCPs**

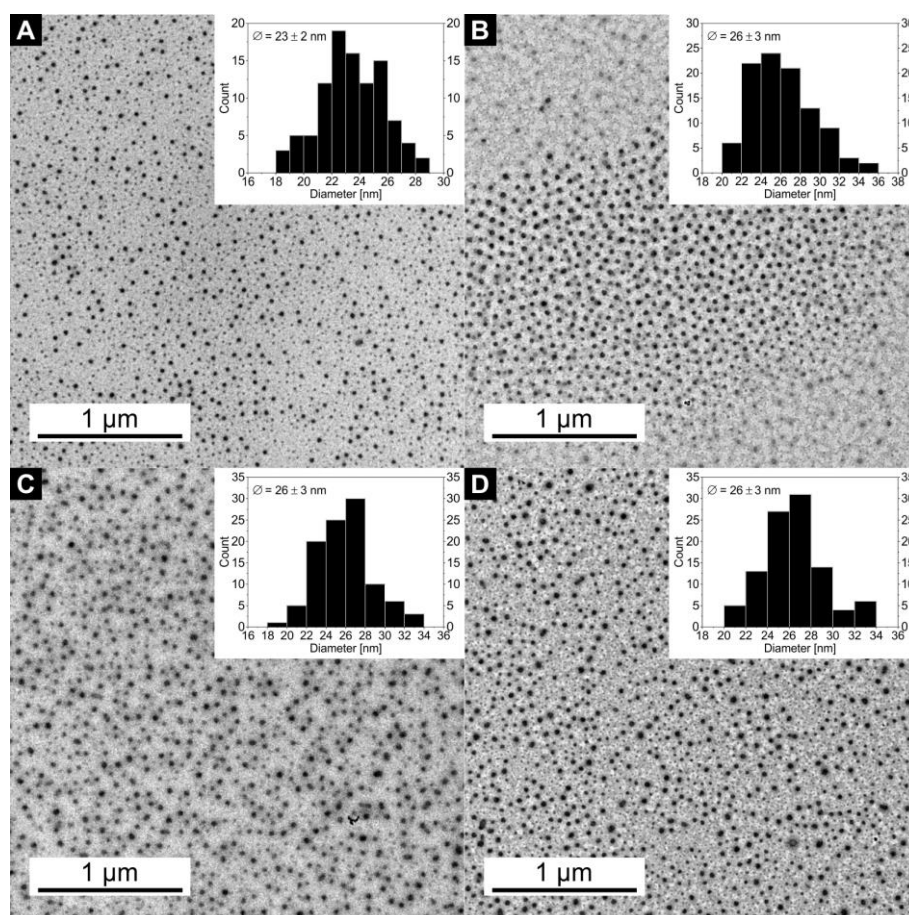
**Figure S4:** DLS autocorrelation functions and hydrodynamic diameters of the five BCPs SV-15 (black), SV-21 (red), SV-35 (green), SV-42 (blue), and SV-61 (light blue).

#### 9.6.4. Characterization of the SCO CP-BCP nanocomposites

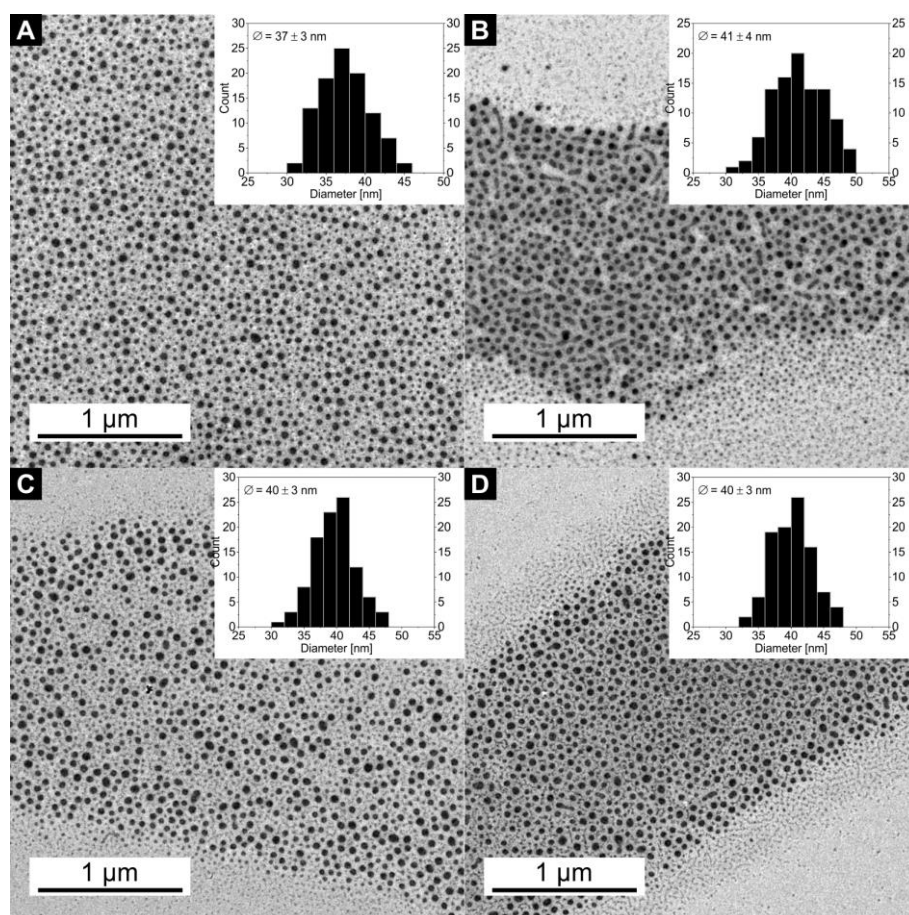
##### TEM



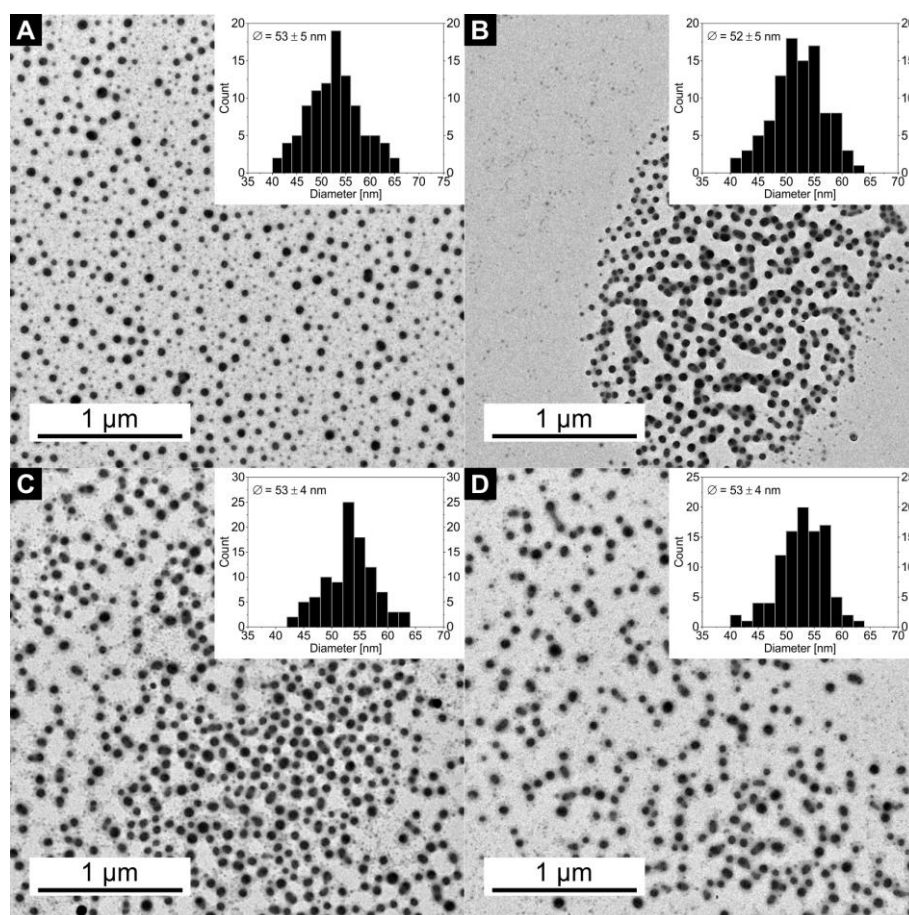
**Figure S5:** TEM images of the samples **1a** (A), **1b** (B), **1c** (C), and **1d** (D). The size distribution of each sample is given in the insets.



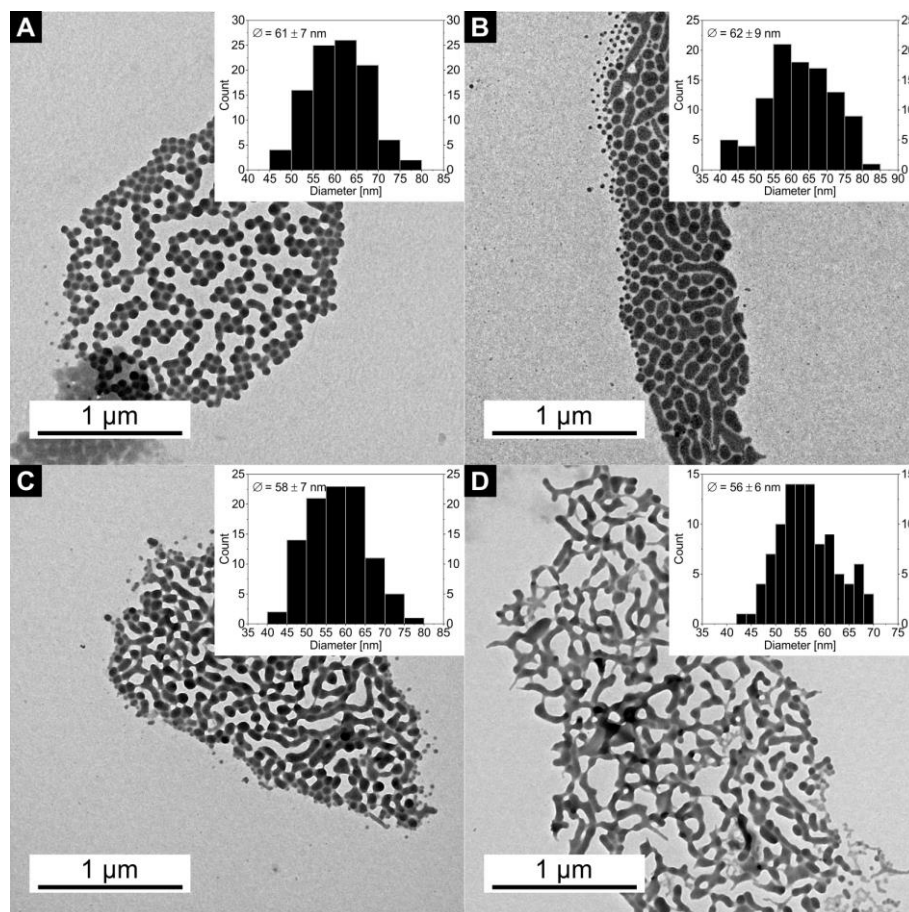
**Figure S6:** TEM images of the samples **2a** (A), **2b** (B), **2c** (C), and **2d** (D). The size distribution of each sample is given in the insets.



**Figure S7:** TEM images of the samples **3a** (A), **3b** (B), **3c** (C), and **3d** (D). The size distribution of each sample is given in the insets.

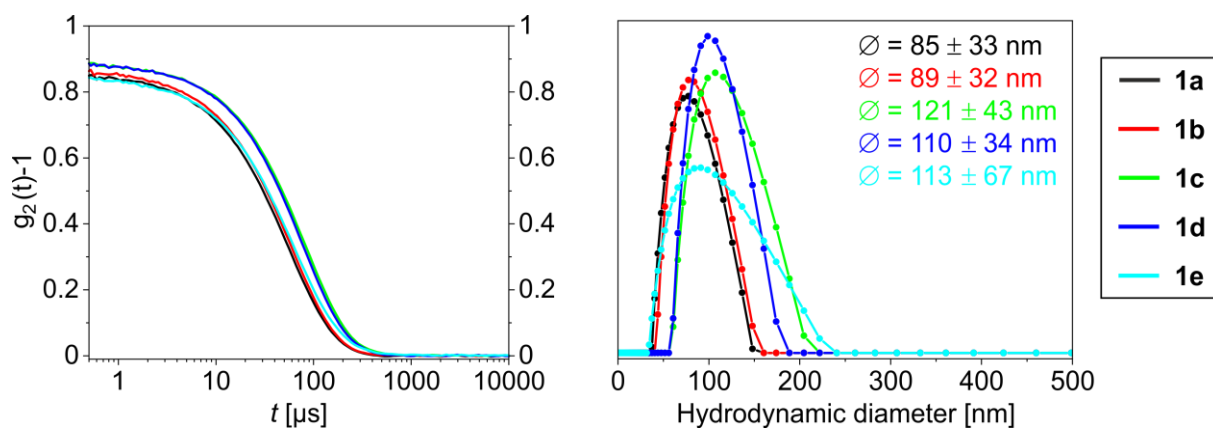


**Figure S8:** TEM images of the samples **4a** (A), **4b** (B), **4c** (C), and **4d** (D). The size distribution of each sample is given in the insets.



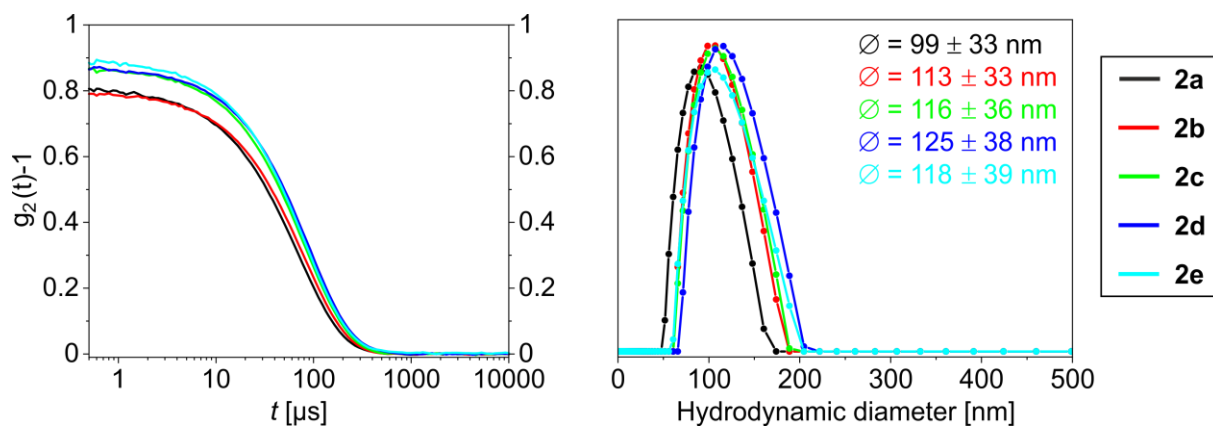
**Figure S9:** TEM images of the samples **5a** (A), **5b** (B), **5c** (C), and **5d** (D). The size distribution of each sample is given in the insets.

## DLS

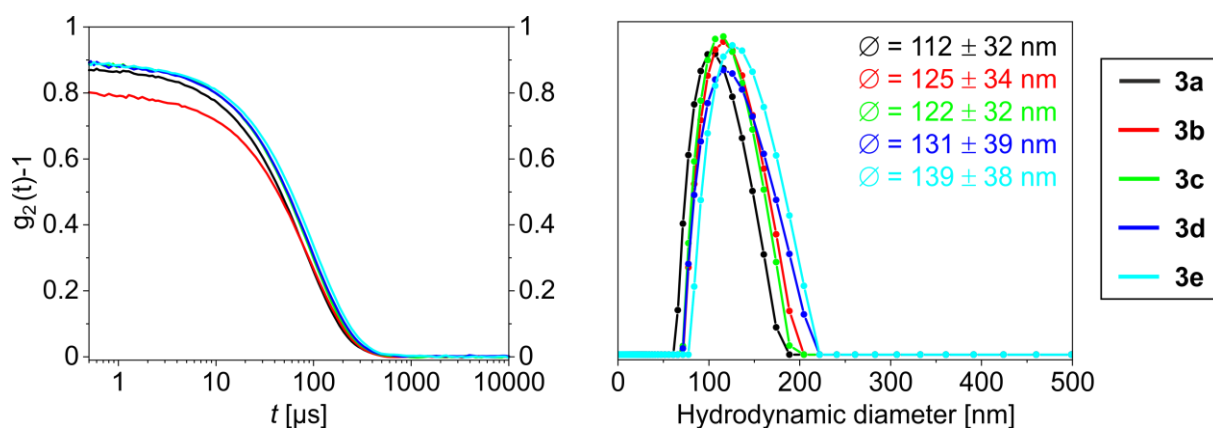


**Figure S10:** DLS autocorrelation functions (left) and the hydrodynamic diameter (right) of the nanocomposite samples **1a** (black), **1b** (red), **1c** (green), **1d** (blue), and **1e** (light blue).

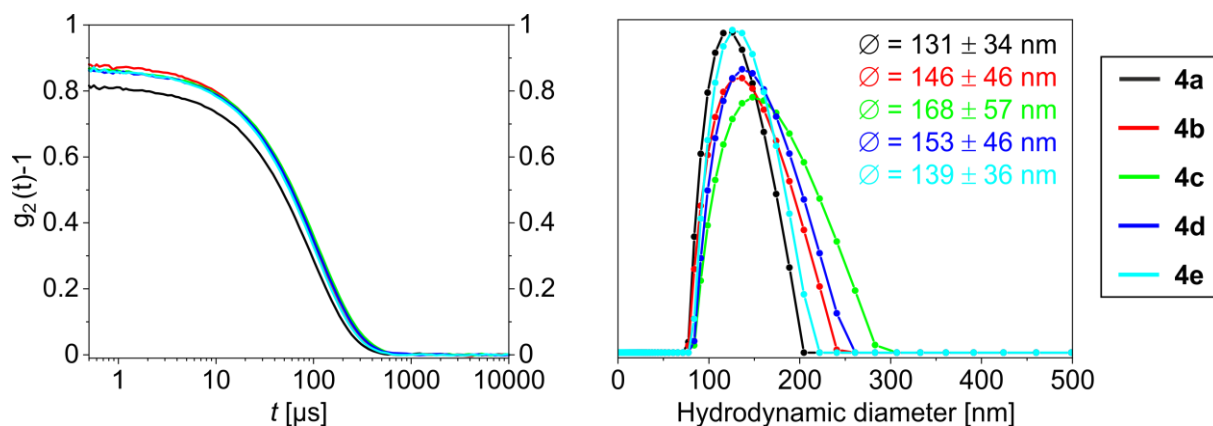




**Figure S11:** DLS autocorrelation functions (left) and the hydrodynamic diameter (right) of the nanocomposite samples **2a** (black), **2b** (red), **2c** (green), **2d** (blue), and **2e** (light blue).

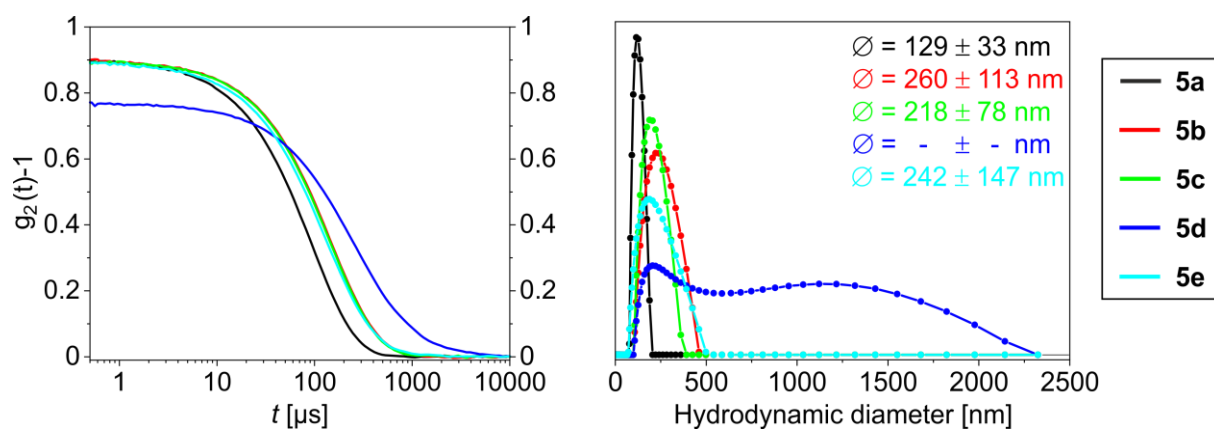


**Figure S12:** DLS autocorrelation functions (left) and the hydrodynamic diameter (right) of the nanocomposite samples **3a** (black), **3b** (red), **3c** (green), **3d** (blue), and **3e** (light blue).



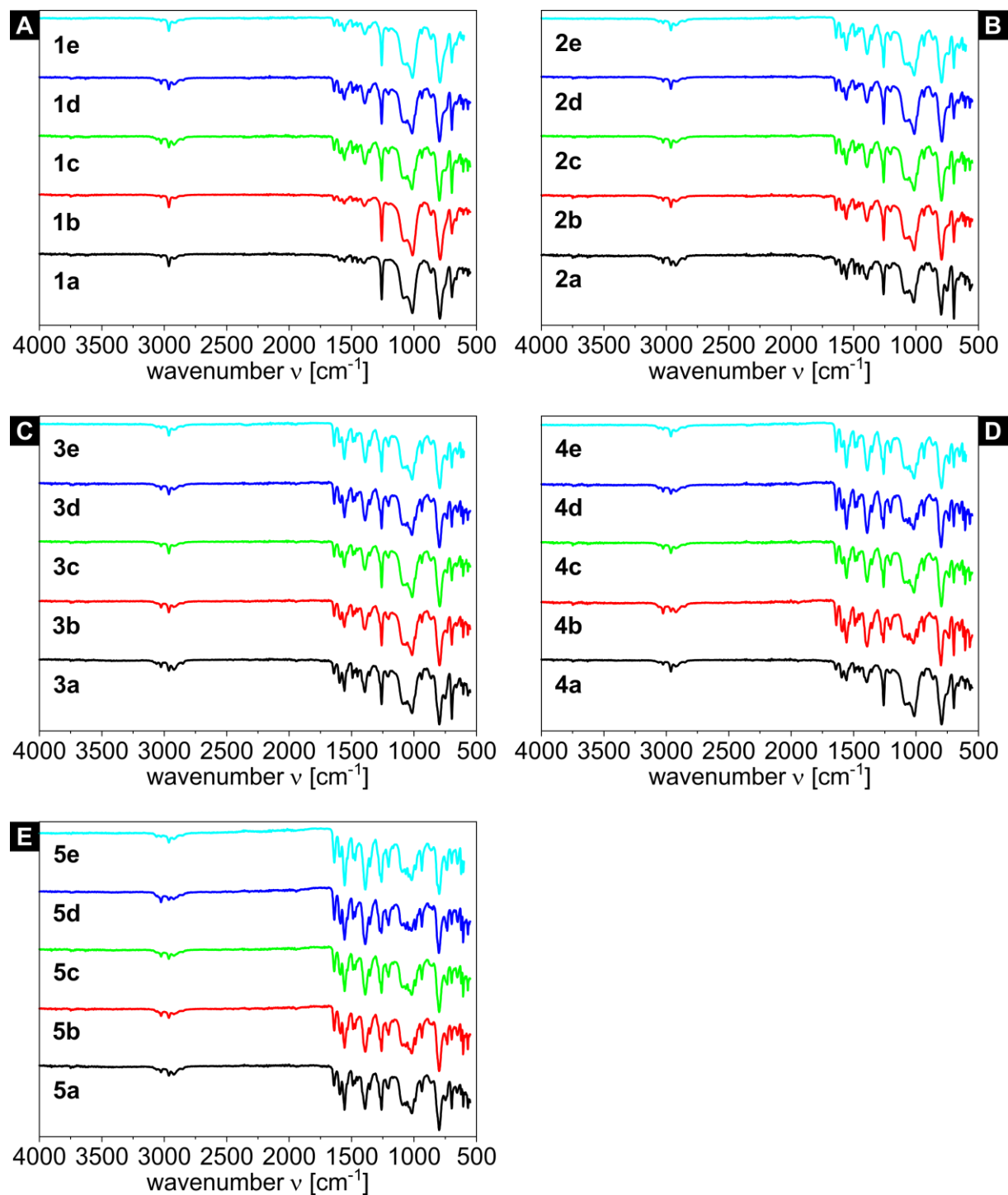
**Figure S13:** DLS autocorrelation functions (left) and the hydrodynamic diameter (right) of the nanocomposite samples **4a** (black), **4b** (red), **4c** (green), **4d** (blue), and **4e** (light blue).





**Figure S14:** DLS autocorrelation functions (left) and the hydrodynamic diameter (right) of the nanocomposite samples **5a** (black), **5b** (red), **5c** (green), **5d** (blue), and **5e** (light blue).

## IR



**Figure S15:** IR spectra of the samples 1a-1e (A), 2a-2e (B), 3a-3e (C), 4a-4e (D), and 5a-5e (E).

## PXRD

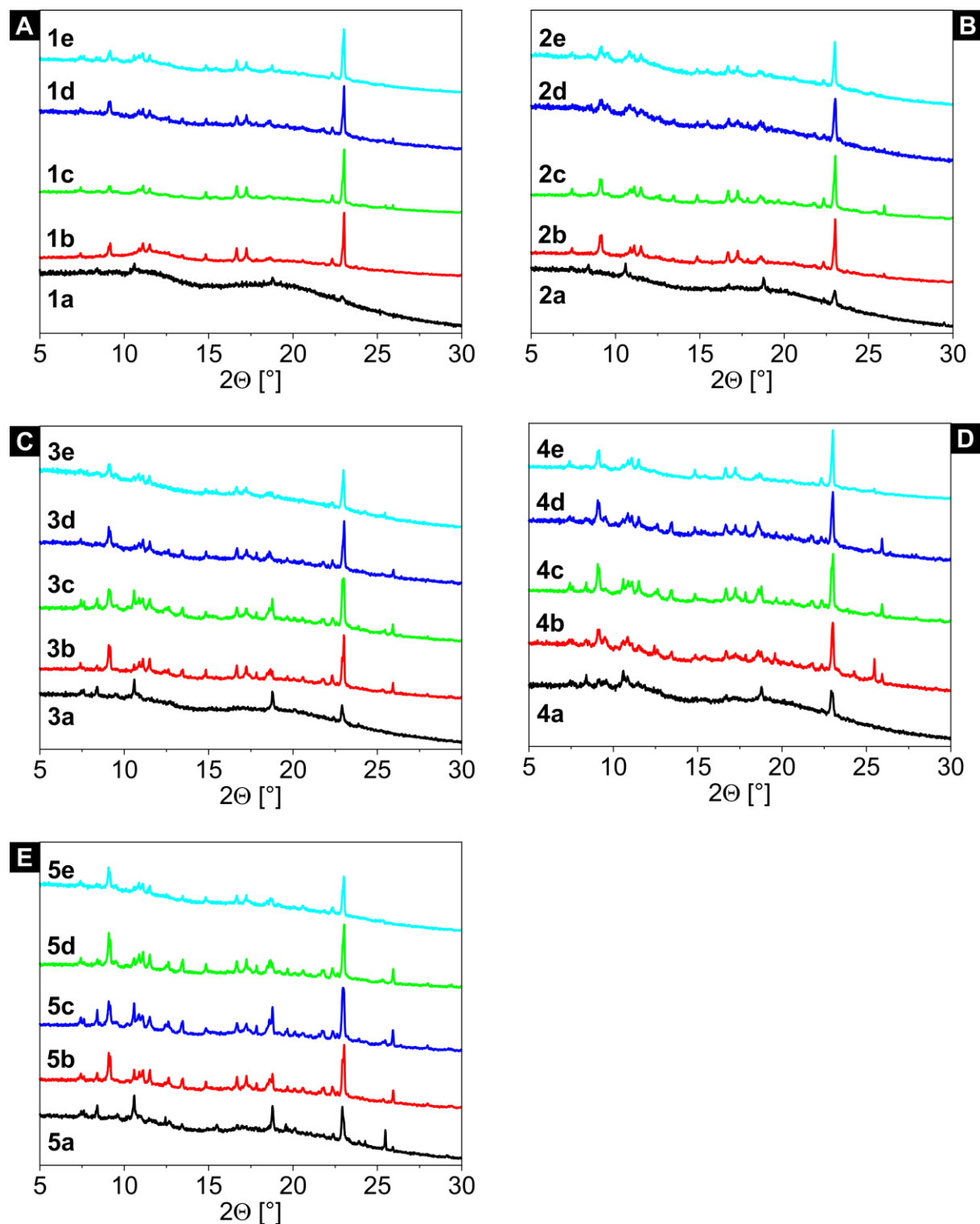
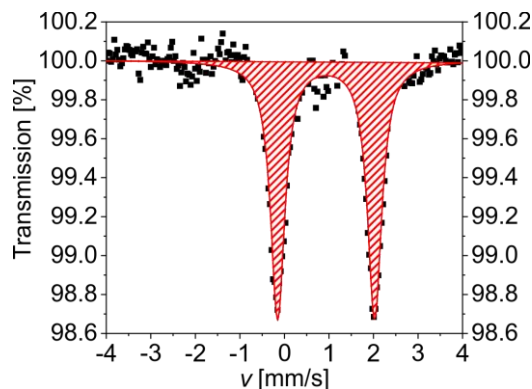
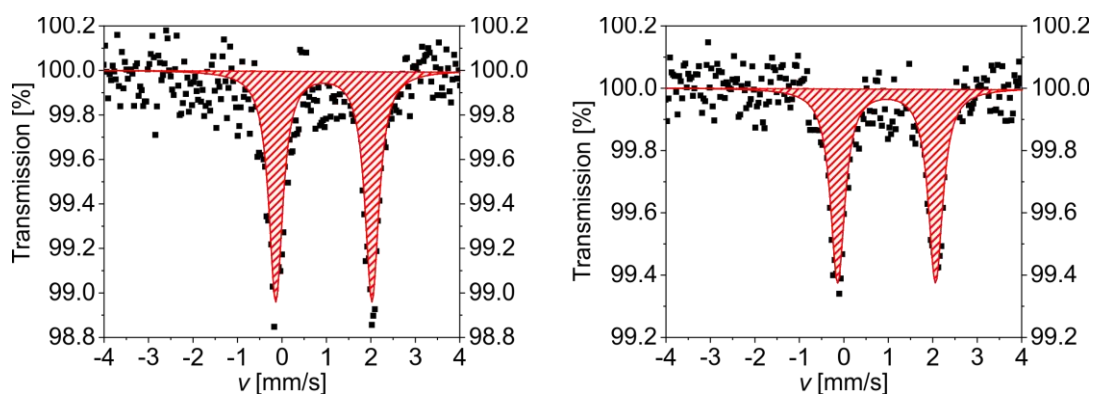


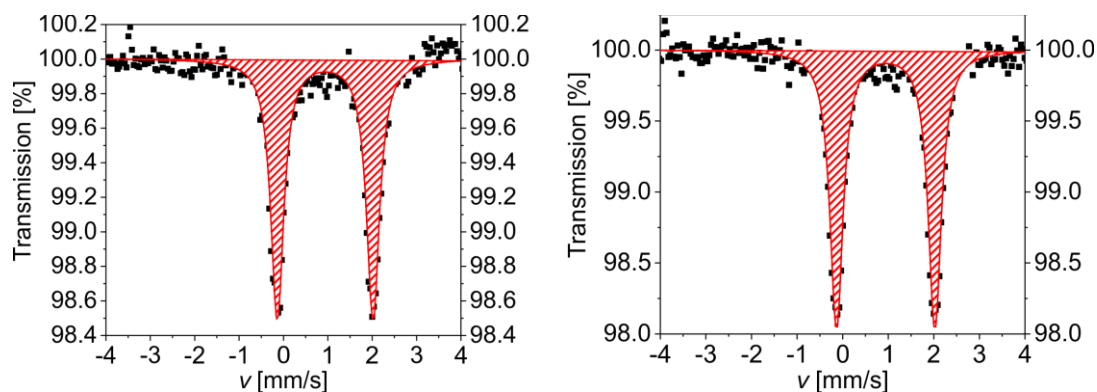
Figure S16: PXRD pattern of the samples 1a-1e (A), 2a-2e (B), 3a-3e (C), 4a-4e (D), and 5a-5e (E).

**Mössbauer spectroscopy**

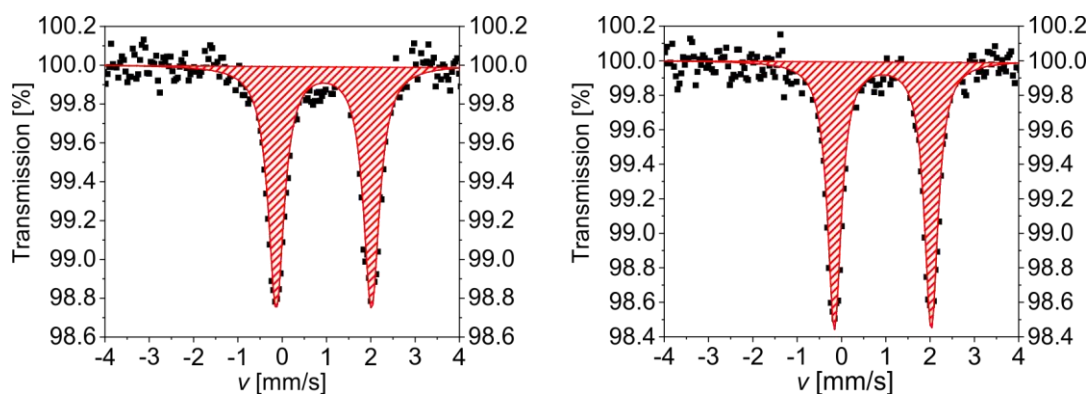
**Figure S17:** Room temperature  $^{57}\text{Fe}$  Mössbauer spectrum of the sample **1d** showing only one doublet characteristic for the CP. The spectrum is displayed in respect to  $\alpha\text{-Fe}$  as reference.



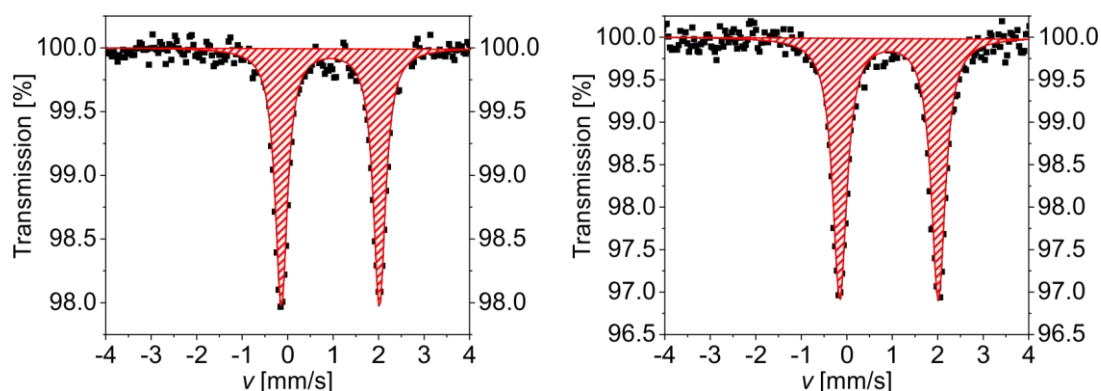
**Figure S18:** Room temperature  $^{57}\text{Fe}$  Mössbauer spectrum of the samples **2c** and **2d** showing only one doublet characteristic for the CP. The spectrum is displayed in respect to  $\alpha\text{-Fe}$  as reference.



**Figure S19:** Room temperature  $^{57}\text{Fe}$  Mössbauer spectrum of the samples **3c** and **3d** showing only one doublet characteristic for the CP. The spectrum is displayed in respect to  $\alpha\text{-Fe}$  as reference.



**Figure S20:** Room temperature  $^{57}\text{Fe}$  Mössbauer spectrum of the samples **4c** and **4d** showing only one doublet characteristic for the CP. The spectrum is displayed in respect to  $\alpha\text{-Fe}$  as reference.

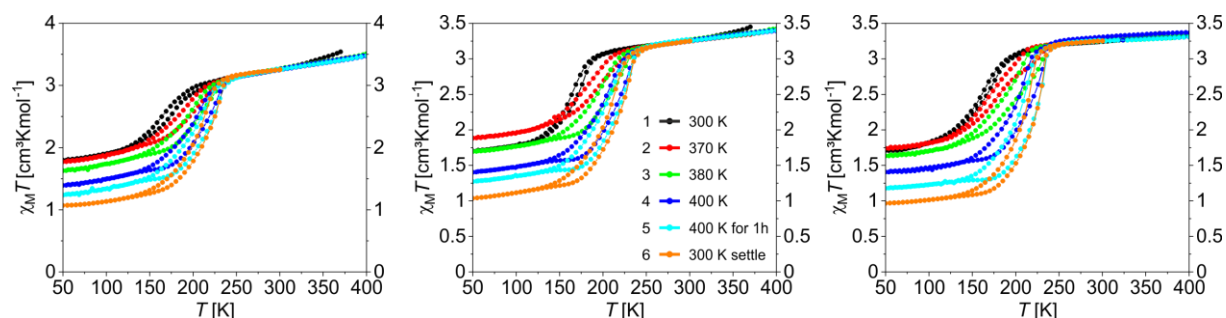


**Figure S21:** Room temperature  $^{57}\text{Fe}$  Mössbauer spectrum of the samples **5c** and **5d** showing only one doublet characteristic for the CP. The spectrum is displayed in respect to  $\alpha\text{-Fe}$  as reference.

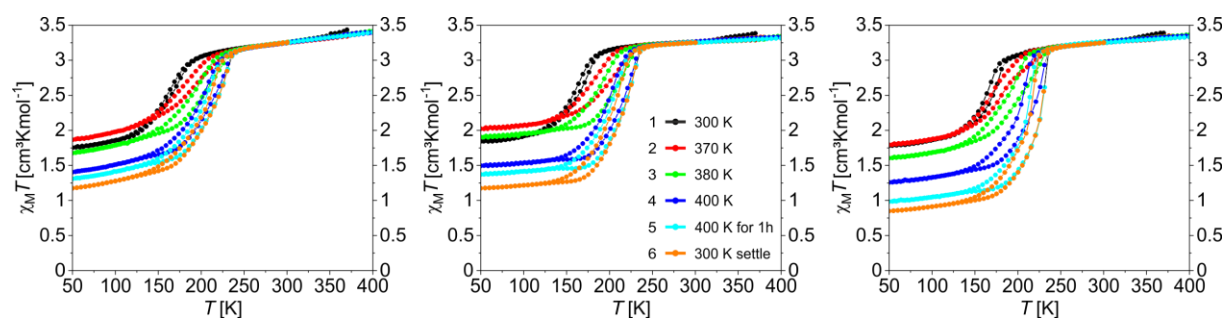
**Table S1:** Chemical shift  $\delta$ , quadrupole splitting  $\Delta E_Q$ , line width  $\Gamma$ , and the area of the iron(II) HS sites of the samples **1d**, **2c-d**, **3c-d**, **4c-d**, and **5c-d**.

Sample	$\delta$ [mm s <sup>-1</sup> ]	$\Delta E_Q$ [mm s <sup>-1</sup> ]	$\Gamma$ [mm s <sup>-1</sup> ]	Area [%]
<b>1d</b>	0.937(6)	2.177(13)	0.193(10)	100
<b>2c</b>	0.951(10)	2.16(2)	0.191(15)	100
<b>2d</b>	0.962(17)	2.20(3)	0.20(3)	100
<b>3c</b>	0.940(7)	2.158(13)	0.176(10)	100
<b>3d</b>	0.944(6)	2.157(11)	0.173(9)	100
<b>4c</b>	0.940(9)	2.151(18)	0.216(14)	100
<b>4d</b>	0.934(7)	2.186(15)	0.184(11)	100
<b>5c</b>	0.939(5)	2.16(10)	0.160(7)	100
<b>5d</b>	0.930(6)	2.166(12)	0.186(10)	100

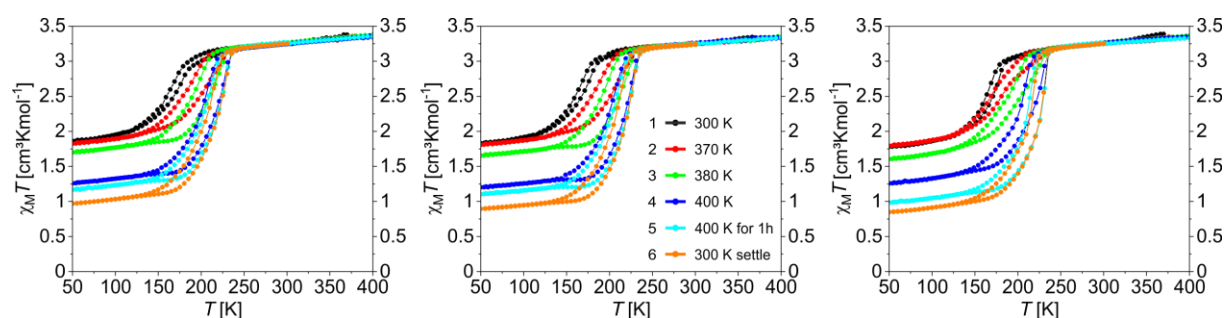
## Magnetic measurements



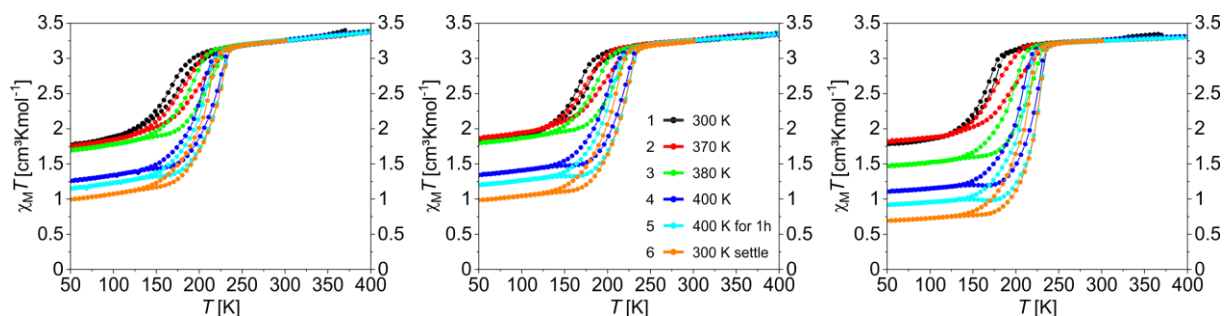
**Figure S22:** Magnetic susceptibility data for the samples **1c** (left), **1d** (middle), and **1e** (right) given as  $\chi_M T$  vs.  $T$  plot measured in sweep (measurement 1-5) and settle mode (measurement 6) in the whole measured temperature range from 50 K to 400 K.



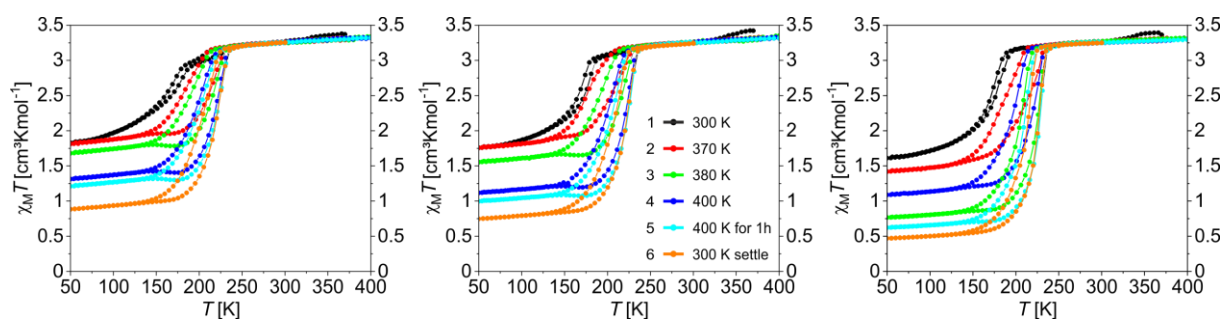
**Figure S23:** Magnetic susceptibility data for the samples **2c** (left), **2d** (middle), and **2e** (right) given as  $\chi_M T$  vs.  $T$  plot measured in sweep (measurement 1-5) and settle mode (measurement 6) in the whole measured temperature range from 50 K to 400 K.



**Figure S24:** Magnetic susceptibility data for the samples **3c** (left), **3d** (middle), and **3e** (right) given as  $\chi_M T$  vs.  $T$  plot measured in sweep (measurement 1-5) and settle mode (measurement 6) in the whole measured temperature range from 50 K to 400 K.



**Figure S25:** Magnetic susceptibility data for the samples **4c** (left), **4d** (middle), and **4e** (right) given as  $\chi_M T$  vs.  $T$  plot measured in sweep (measurement 1-5) and settle mode (measurement 6) in the whole measured temperature range from 50 K to 400 K.



**Figure S26:** Magnetic susceptibility data for the samples **5c** (left), **5d** (middle), and **5e** (right) given as  $\chi_M T$  vs.  $T$  plot measured in sweep (measurement 1-5) and settle mode (measurement 6) in the whole measured temperature range from 50 K to 400 K.

## 9. Size and Shape Controlled Synthesis of Spin Crossover – Block Copolymer Nanocomposites

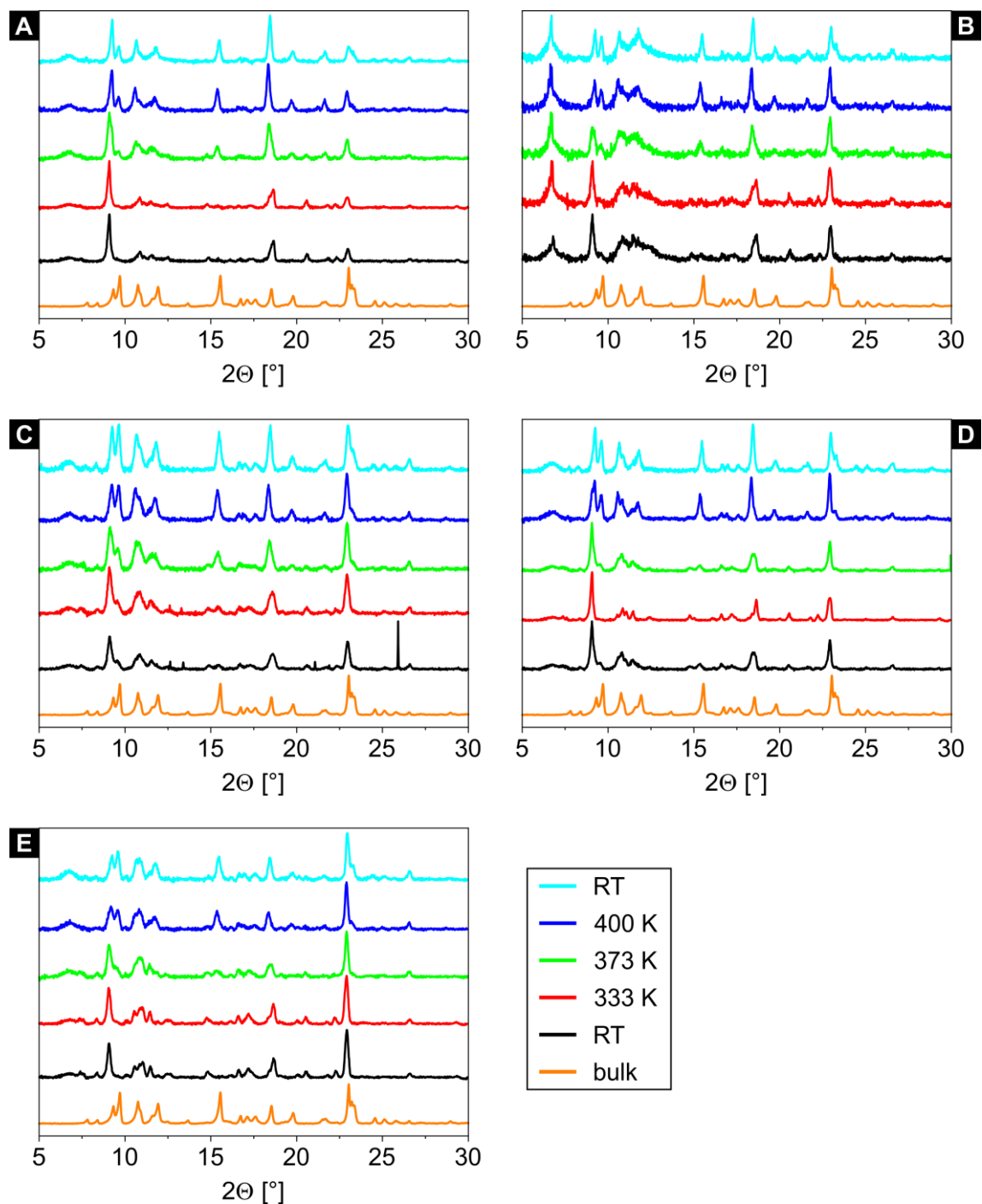
**Table S2:** Summary of the cooling and heating cycles and the data derived from the magnetic measurements for the samples **2e**, **3e**, and **4e**, showing the transition temperatures  $T_{1/2\downarrow}$  and  $T_{1/2\uparrow}$ , the hysteresis width, the  $\chi_M T$  value at 50 K, and the  $\gamma_{HS}$  value at 50 K.

Sample	Temperature range [K]	Mode	$T_{1/2\downarrow}$ [K]	$T_{1/2\uparrow}$ [K]	Hysteresis width [K]	$\chi_M T$ at 50 K [cm <sup>3</sup> Kmol <sup>-1</sup> ]	$\gamma_{HS}$ [%]
<b>2e</b>	300-50-370 <sup>a)</sup>	sweep	163	172	9	1.78	55
	370-50-380 <sup>b)</sup>		170	182	12	1.79	55
	380-50-400 <sup>c)</sup>		185	200	15	1.60	49
	400-50-400 <sup>d)</sup>		201	216	15	1.26	39
	400-50-300 <sup>e)</sup>		209	225	16	0.98	30
	300-50-300 <sup>f)</sup>	settle	212	223	11	0.85	26
<b>3e</b>	300-50-370 <sup>a)</sup>	sweep	162	167	5	1.76	54
	370-50-380 <sup>b)</sup>		172	186	14	1.81	56
	380-50-400 <sup>c)</sup>		189	205	16	1.57	48
	400-50-400 <sup>d)</sup>		200	216	16	1.26	39
	400-50-300 <sup>e)</sup>		205	222	17	1.05	32
	300-50-300 <sup>f)</sup>	settle	208	220	12	0.87	27
<b>4e</b>	300-50-370 <sup>a)</sup>	sweep	164	170	6	1.79	55
	370-50-380 <sup>b)</sup>		174	193	19	1.82	56
	380-50-400 <sup>c)</sup>		193	212	19	1.47	45
	400-50-400 <sup>d)</sup>		202	220	18	1.10	34
	400-50-300 <sup>e)</sup>		206	224	18	0.92	28
	300-50-300 <sup>f)</sup>	settle	209	222	13	0.69	21

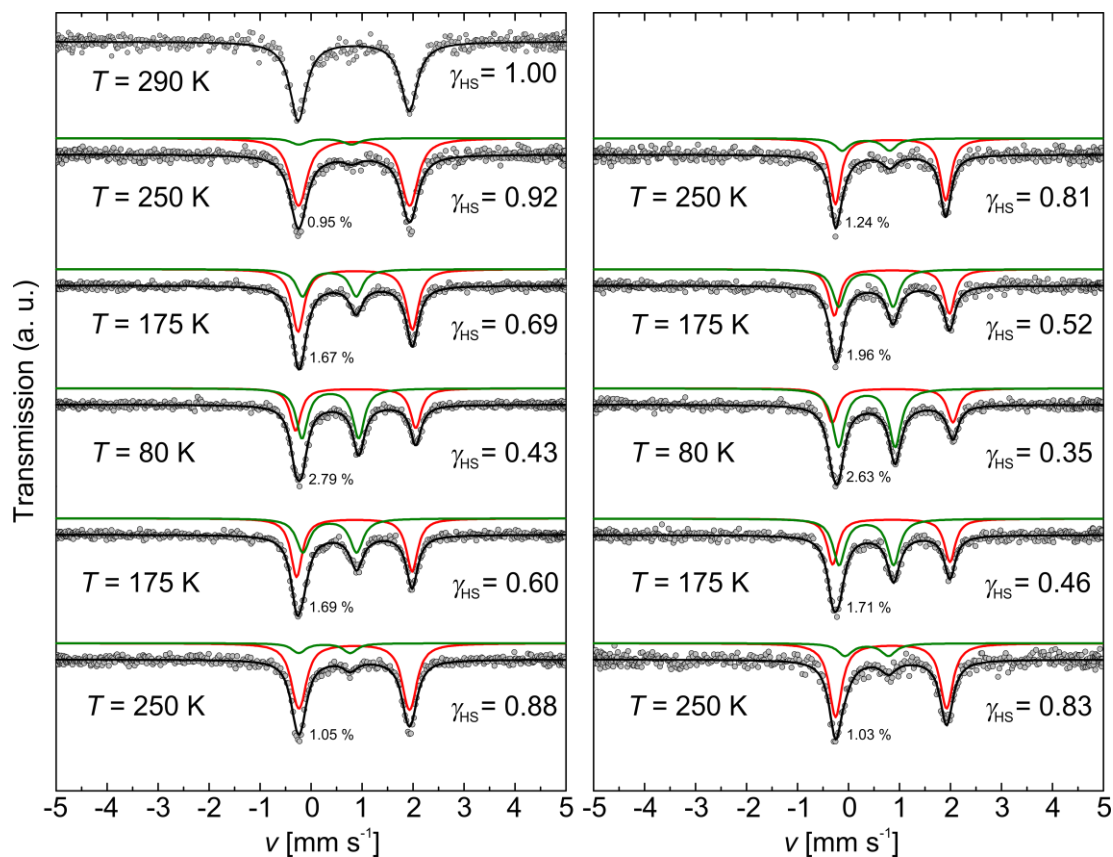
a) Figure 4, curve 1; b) Figure 4, curve 2; c) Figure 4, curve 3; d) Figure 4, curve 4; e) Figure 4, curve 5; f) Figure 4, curve 6.



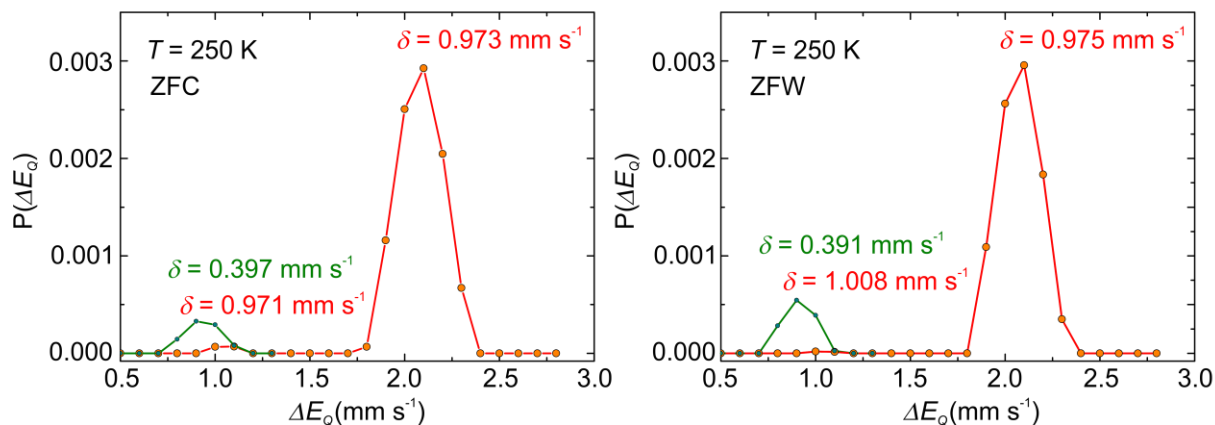
## Temperature-dependent PXRD of the samples #e



**Figure S27:** Temperature-dependent power X-ray diffraction pattern of the samples **1e** (A), **2e** (B), **3e** (C), **4e** (D), and **5e** (E) at five different temperatures and their comparison with the bulk material  $[\text{FeL}(\text{bipy})]_n$ .

**Temperature-dependent Mössbauer spectroscopy of the sample 5e and 5e\***

**Figure S28:** Zero-field  $^{57}\text{Fe}$  Mössbauer spectra of the as-synthesized sample **5e** (left) and the annealed sample **5e\*** (right) recorded at 290 K (sample **5e** only), 250 K, 175 K, and 80 K and back. The measurements were carried out upon zero-field cooling (ZFC) and zero-field warming (ZFW).  $\gamma_{\text{HS}}$  describes the determined molar fraction of Fe(II) HS molecules. Symbols: Experimental data. Lines: Fit with doublets of Lorentzian lines (expect for the measurements at 250 K where an alternative fit was used, cf. Figure S29 and Table S3). The colored lines illustrate the corresponding sub-spectra of the fit, which are attributed to the Fe(II) low-spin (green) and Fe(II) high-spin sites (red), respectively. The parameters of the fits are summarized in Table S3 and Table S4.



**Figure S29:** Distribution of quadrupole splitting values, determined by an alternative fit of the Mössbauer spectrum of sample **5e** at 250 K after ZFC (left) and ZFW (right).

**Table S3:** Chemical shift  $\delta$ , quadrupole splitting  $\Delta E_Q$ , line width  $\Gamma$ , the area of the different iron(II) sites, and the distribution width  $\sigma$  of the alternative fit of sample **5e** before annealing (as-synthesized) in ZFC and ZFW mode.

T [K]	Site	$\delta^a$ [mm s <sup>-1</sup> ]	$\Delta E_Q$ [mm s <sup>-1</sup> ]	$\Gamma$ [mm s <sup>-1</sup> ]	Area [%]	$\sigma$ [mm s <sup>-1</sup> ]
250 <sup>b)</sup>	Iron(II) HS	0.970(38)	2.168	0.35*	91.8	0.167
	Iron(II) LS	0.407(49)	1.037	0.35*	8.2	0.087
250 <sup>c)</sup>	Iron(II) HS	1.025(71)	2.171	0.3*	87.7	0.122
	Iron(II) LS	0.391(21)	1.013	0.3*	12.3	0.078

The fits were performed by assuming a distribution of quadrupole splitting values with distribution widths  $\sigma$  (cf. Figure S29). Values marked with an asterisk (\*) were fixed in the fit. <sup>a)</sup> Isomer shifts ( $\delta$ ) were specified relative to metallic iron at room temperature but were not corrected in terms of the second-order Doppler shift. <sup>b)</sup> ZFC. <sup>c)</sup> ZFW.

## 9. Size and Shape Controlled Synthesis of Spin Crossover – Block Copolymer Nanocomposites

**Table S4:** Chemical shift  $\delta$ , quadrupole splitting  $\Delta E_Q$ , line width  $\Gamma$ , and the area of the different iron(II) sites of the sample **5e** before annealing (as-synthesized) in ZFC and ZFW mode.

As-synthesized						
$T$ [K]	Site	$\delta^{aj}$ [mm s <sup>-1</sup> ]	$\Delta E_Q$ [mm s <sup>-1</sup> ]	$\Gamma$ [mm s <sup>-1</sup> ]	$A_2/A_1^{b)}$	Area [%]
290	Iron(II) HS	0.956(3)	2.177(8)	0.388(10)	0.87(4)	100
250 <sup>c)</sup>	Iron(II) HS	0.970(38)	2.168	0.35*	-	91.8
	Iron(II) LS	0.407(49)	1.037	0.35*	-	8.2
175	Iron(II) HS	0.987(2)	2.247(4)	0.286(7)	0.95(2)	69.0
	Iron(II) LS	0.490(5)	1.056(11)	0.297(14)	1*	31.0
80	Iron(II) HS	1.005(4)	2.362(6)	0.262(10)	0.93(3)	43.0
	Iron(II) LS	0.512(3)	1.118(6)	0.283(8)	1*	57.0
175	Iron(II) HS	0.998(3)	2.273(5)	0.279(6)	0.90(3)	59.8
	Iron(II) LS	0.497(5)	1.050(10)	0.305(13)	1*	40.2
250 <sup>c)</sup>	Iron(II) HS	1.025(71)	2.171	0.3*	-	87.7
	Iron(II) LS	0.391(21)	1.013	0.3*	-	12.3

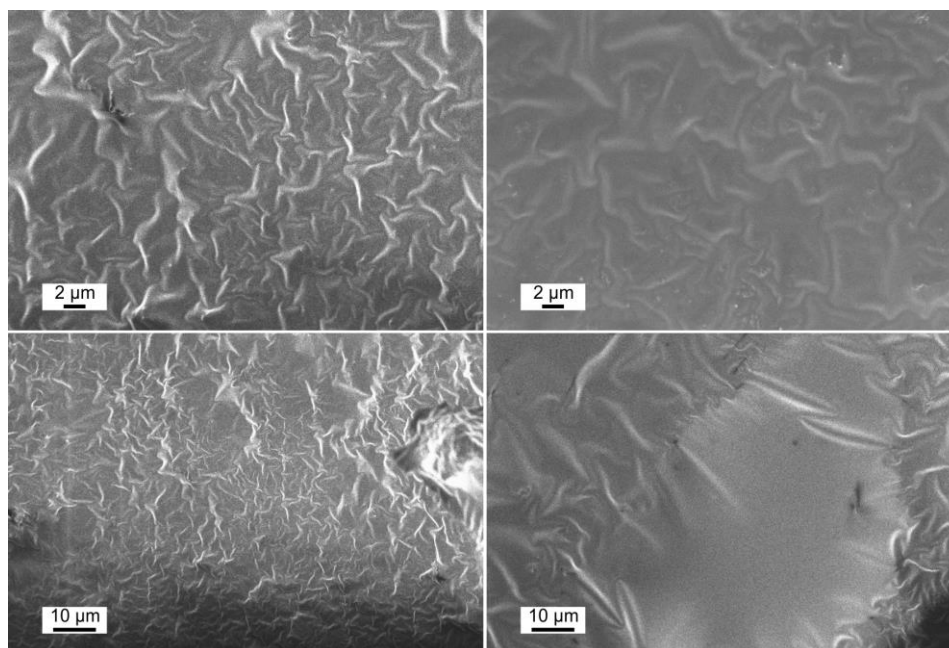
After annealing						
$T$ [K]	Site	$\delta^{aj}$ [mm s <sup>-1</sup> ]	$\Delta E_Q$ [mm s <sup>-1</sup> ]	$\Gamma$ [mm s <sup>-1</sup> ]	$A_2/A_1^{b)}$	Area [%]
290	Iron(II) HS	-	-	-	-	-
250 <sup>c)</sup>	Iron(II) HS	0.956(4)	2.167(7)	0.258(11)	0.94(5)	80.6
	Iron(II) LS	0.47(3)	0.94(5)	0.33(6)	1*	19.4
175	Iron(II) HS	0.981(4)	2.262(8)	0.258(11)	0.96(4)	52.1
	Iron(II) LS	0.470(5)	1.068(10)	0.289(15)	1*	47.9
80	Iron(II) HS	0.995(6)	2.368(13)	0.65(18)	0.99(4)	35.0
	Iron(II) LS	0.489(4)	1.110(7)	0.292(10)	1*	65.0
175	Iron(II) HS	0.969(3)	2.302(6)	0.259(13)	0.94(5)	46.3
	Iron(II) LS	0.479(6)	1.071(10)	0.291(15)	1*	53.7
250 <sup>c)</sup>	Iron(II) HS	0.965(4)	2.182(8)	0.301(12)	0.88(4)	82.8
	Iron(II) LS	0.49(3)	0.86(6)	0.35(7)	1*	17.2

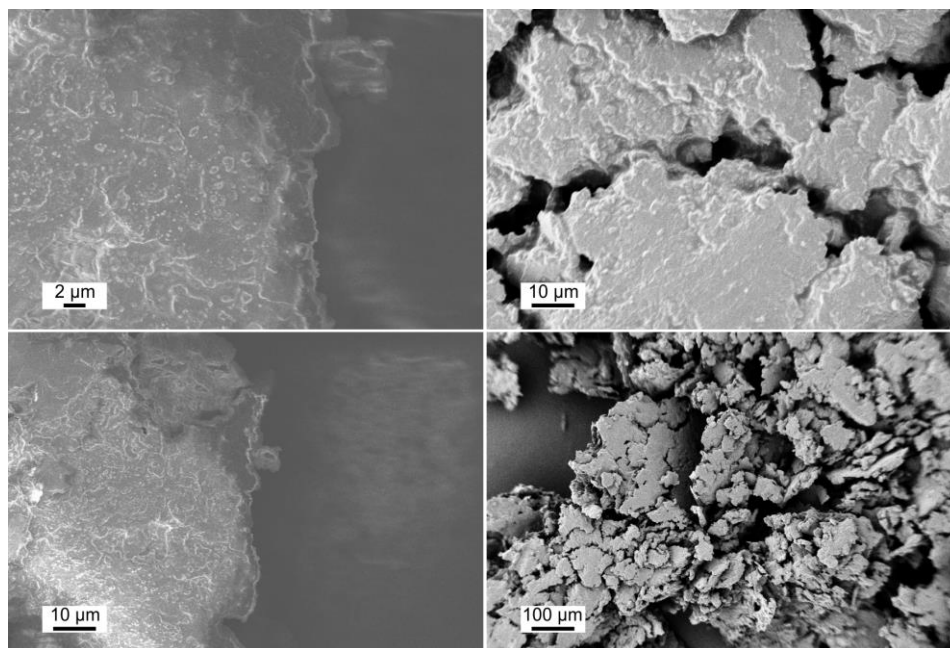
Values marked with an asterisk (\*) were fixed in the fit. <sup>a)</sup> Isomer shifts ( $\delta$ ) were specified relative to metallic iron at room temperature but were not corrected in terms of the second-order Doppler shift. <sup>b)</sup> In case of polycrystalline powders with random orientations of the crystallites, the expectation value of this parameter is  $A_2/A_1 = 1$ .<sup>[5]</sup> Deviations from this value, which are clearly observed e.g. at 290 K, are attributed to the presence of texture effects due to partial orientations of crystallites on compacting the powder in the sample containment. <sup>c)</sup> The fits were performed by assuming a distribution of quadrupole splitting values with distribution widths  $\sigma$  (cf. Figure S29 and Table S3).

**Table S5:** Comparison of the molar fraction of high-spin molecules  $\gamma_{\text{HS}}$  determined by Mössbauer spectroscopy and magnetic susceptibility measurements of the samples **5e** and **5e\***.

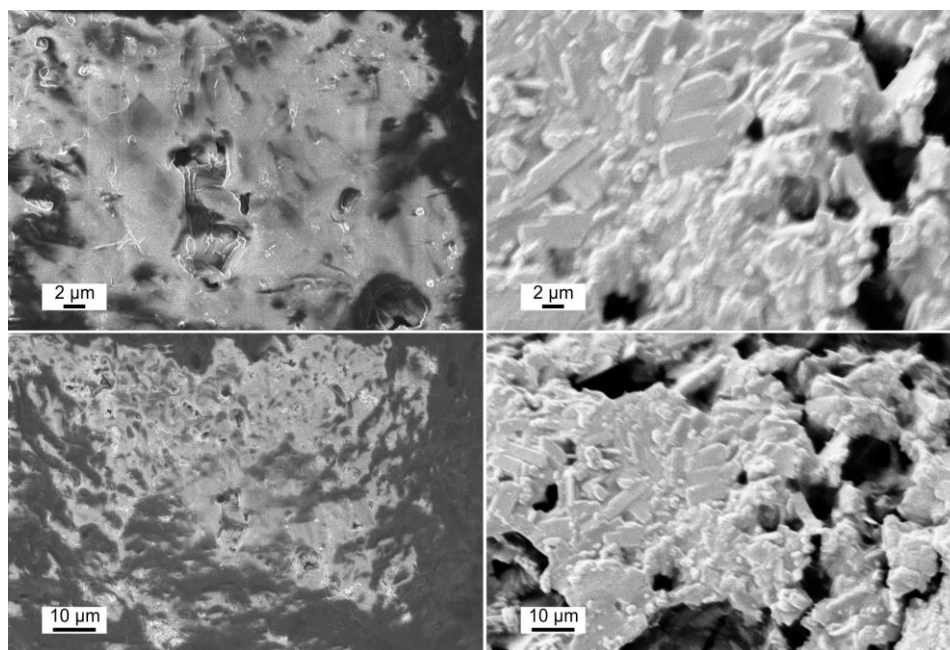
$T$ [K]	$\gamma_{\text{HS}}$ Mössbauer as-synthesised <sup>a)</sup>	$\gamma_{\text{HS}}$ Mössbauer annealed <sup>a)</sup>	$\gamma_{\text{HS}}$ SQUID as-synthesised <sup>b)</sup>	$\gamma_{\text{HS}}$ SQUID annealed <sup>b)</sup>
290	1.00	1.00	1.00	1.00
250	0.92	0.81	0.99	0.99
175	0.69	0.52	0.80	0.23
80	0.43	0.35	0.51	0.15
175	0.60	0.46	0.76	0.19
250	0.88	0.83	0.99	0.98
290	-	-	1.00	1.00

<sup>a)</sup> Values determined by Mössbauer spectroscopy upon zero-field cooling (290 K to 80 K) and zero-field warming (80 K to 250 K) (cf. Table S4). <sup>b)</sup> Values determined by magnetic susceptibility measurements upon field cooling (3 T, 300 K to 50 K) and field warming (3 T, 50 K to 300 K), assuming that the value of  $\chi_{\text{M}}T = 3.25 \text{ cm}^3 \text{ mol}^{-1} \text{ K}$  measured at  $T = 300 \text{ K}$  corresponds to  $\gamma_{\text{HS}} = 1.00$ .

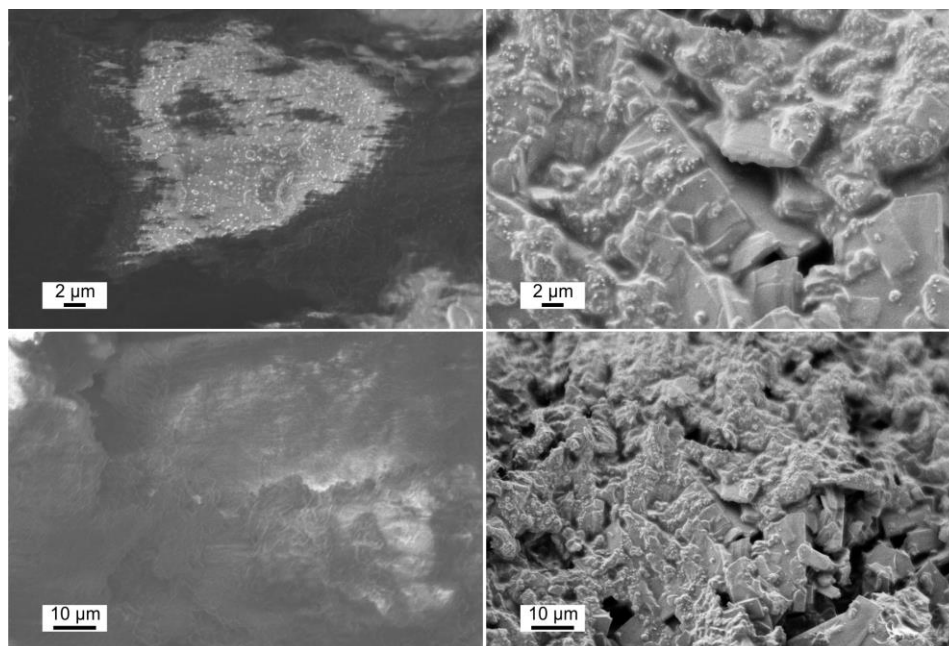
**SEM before and after thermal annealing of the samples #e****Figure S30:** SEM image of the samples **1e** before (left) and **1e\*** after thermal annealing (right) showing the absence of microcrystals on the polymer surface.



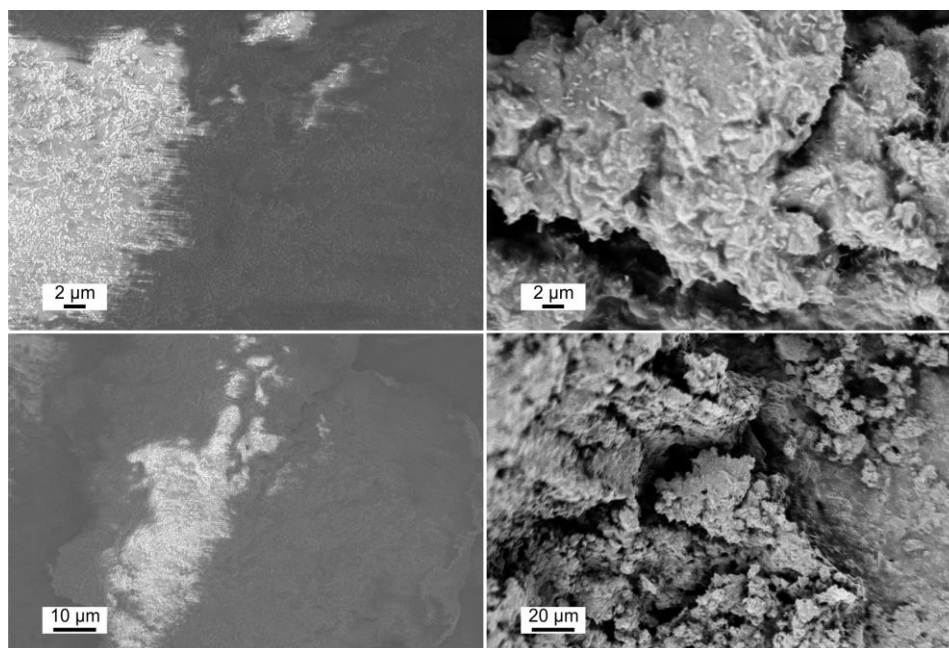
**Figure S31:** SEM image of the samples **2e** before (left) and **2e\*** after thermal annealing (right) showing the absence of microcrystals on the polymer surface.



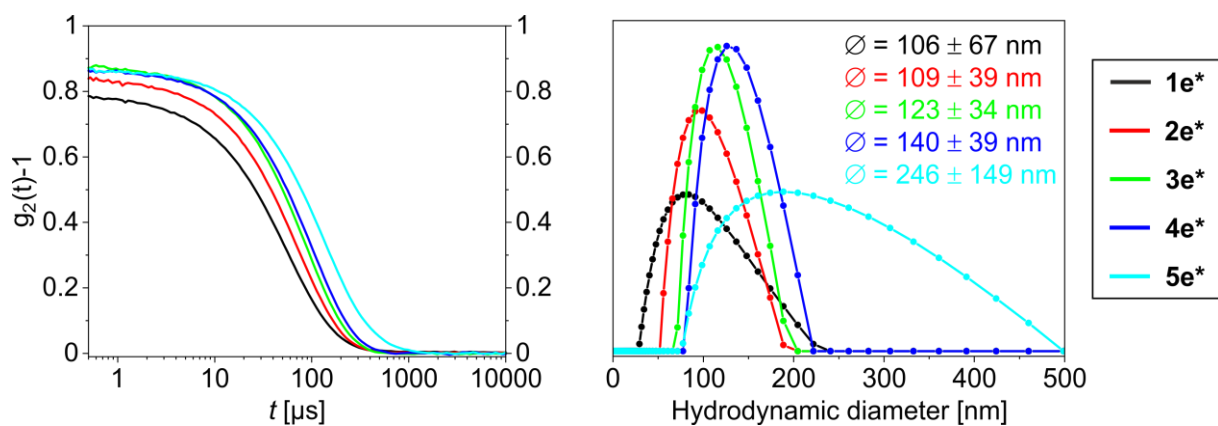
**Figure S32:** SEM image of the samples **3e** before (left) and **3e\*** after thermal annealing (right) showing the absence of microcrystals on the polymer surface.



**Figure S33:** SEM image of the samples **4e** before (left) and **4e\*** after thermal annealing (right) showing the absence of microcrystals on the polymer surface.



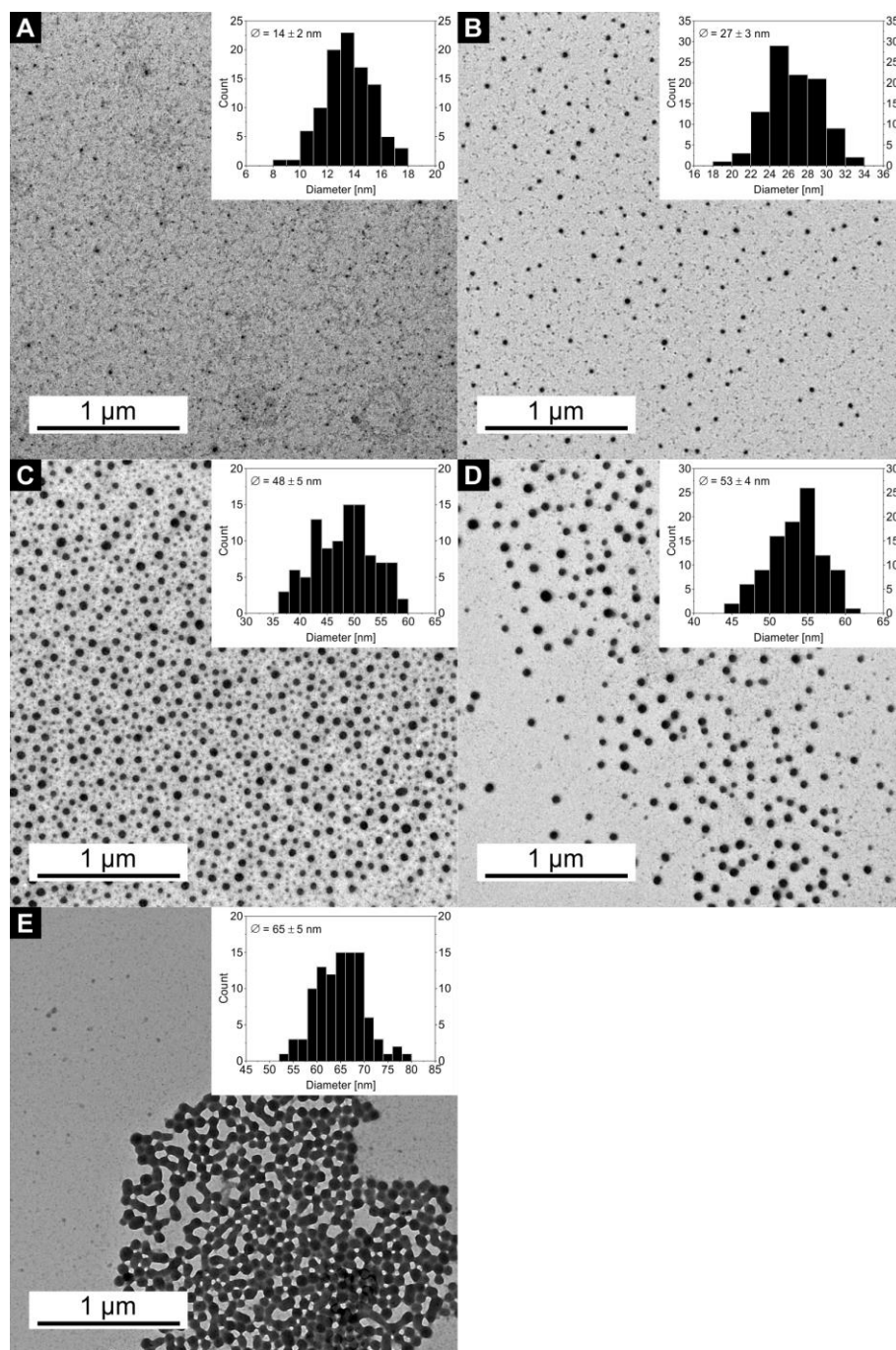
**Figure S34:** SEM image of the samples **5e** before (left) and **5e\*** after thermal annealing (right) showing the absence of microcrystals on the polymer surface.

**DLS after thermal annealing**

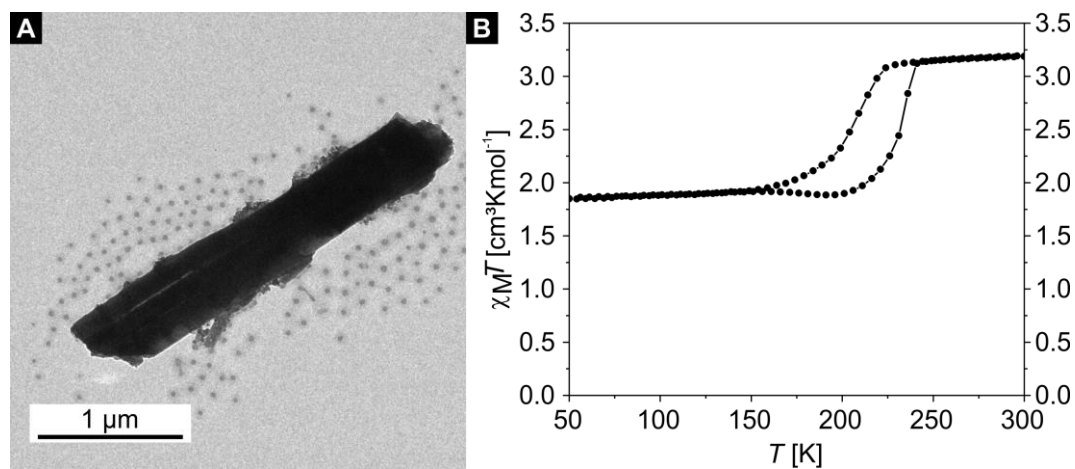
**Figure S35:** DLS autocorrelation functions (left) and the hydrodynamic diameter (right) of the nanocomposite samples **1e\*** (black), **2e\*** (red), **3e\*** (green), **4e\*** (blue), and **5e\*** (light blue) after thermal annealing.



TEM after thermal annealing



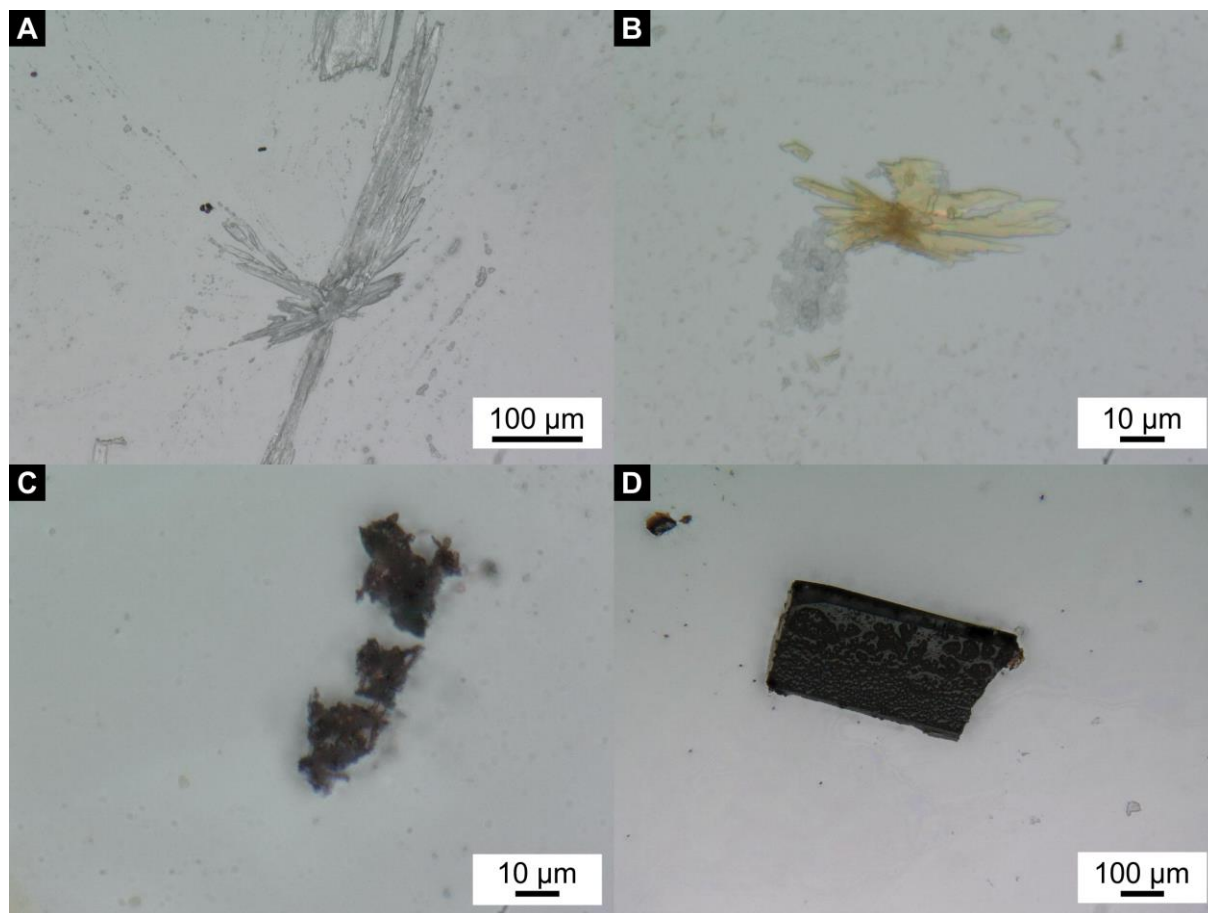
**Figure S36:** TEM images of the samples **1e\*** (A), **2e\*** (B), **3e\*** (C), **4e\*** (D), and **5e\*** (E) after thermal annealing. The size distribution of each sample is given in the insets.

**TEM and magnetic properties of a sample in toluene with microcrystals**

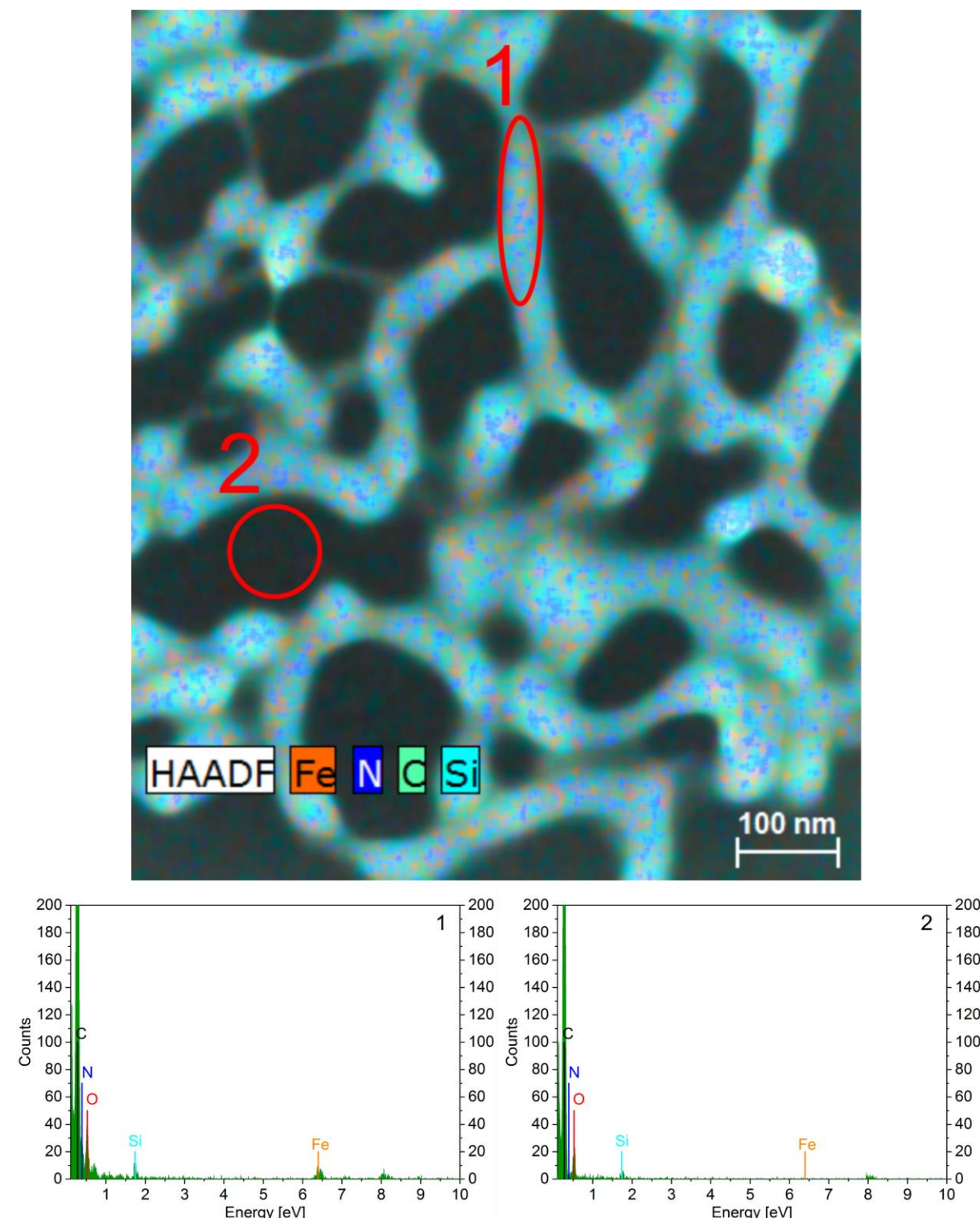
**Figure S37:** TEM image of an exemplary sample synthesized in toluene containing microcrystals of the SCO CP (A) and the corresponding magnetic measurement revealing bulk-like behaviour in the as-synthesized sample before thermal annealing (B).

**Comparison between dried up toluene and THF solutions**

**Figure S38:** Photographs of two different dried up solutions for TEM preparation. In the sample from toluene solution on the left, large microcrystals precipitated upon drying. In the nanocomposite sample from THF on the right, a polymeric solid/film remained.

**Optical light microscopy**

**Figure S39:** Images taken by optical light microscopy from dried up solutions of BCP/bipy showing the crystallization of bipy (A) and SCO CP-BCP nanocomposite from THF showing a similar crystallization behavior like pure bipy (B). Additionally, the powder sample of the CP [FeL(bipy)]<sub>n</sub> (C) and a crystal (D) obtained from a dried up toluene solution (cf. Figure S37, were imaged showing much darker colors, indicating that the crystals in image B are bipy crystals.

**TEM-EDX spectra**

**Figure S40:** TEM-EDX HAADF image of sample **5d** with the overlays of the iron, nitrogen, carbon, and silicon signals. The areas marked 1 (on the polymeric structure) and 2 (area without polymer) are equal in size and correspond to the respective spectra showing that iron is only found inside the polymeric structure.

#### 9.6.5. References

- [1] E.-G. Jäger, E. Häussler, M. Rudolph, M. Rost, *Z. Anorg. Allg.Chem.* **1985**, 525, 67–85.
- [2] K. Lagarec, D. G. Rancourt, *Recoil, Mössbauer spectral analysis software for windows 1.0*, Department of Physics, University of Ottawa, Canada, **1998**.
- [3] R. A. Brand, *WinNormos-for-Igor, Version 3.0*, May **2009**.
- [4] S. K. Varshney, X. F. Zhong, A. Eisenberg, *Macromolecules* **1993**, 26, 701–706.
- [5] N. N. Greenwood, T. C. Gibb, *Mössbauer Spectroscopy*, Chapman and Hall Ltd., London, **1971**.



---

**10. List of publications**

C. Göbel, T. Palamarciuc, C. Lochenie, B. Weber: "Synthesis of Microcrystals of the [Fe(L)(bipy)] Spin Crossover Coordination Polymer in a Poly-4-vinylpyridine Matrix", *Chem. Asian J.* **2014**, 9, 2232–2238.

O. Klimm, C. Göbel, S. Rosenfeldt, F. Puchtler, N. Miyajima, K. Marquardt, M. Drechsler, J. Breu, S. Förster, B. Weber: "Synthesis of [Fe(L)(bipy)]<sub>n</sub> spin crossover nanoparticles using blockcopolymer micelles", *Nanoscale* **2016**, 8, 19058–19065.

C. Göbel, O. Klimm, F. Puchtler, S. Rosenfeldt, S. Förster, B. Weber: "Synthesis of [Fe(L<sub>eq</sub>)(L<sub>ax</sub>)]<sub>n</sub> coordination polymer nanoparticles using blockcopolymer micelles", *Beilstein J. Nanotechnol.* **2017**, 8, 1318–1327.

J. Weßing, C. Göbel, B. Weber, C. Gemel, R. A. Fischer: "Diverse Reactivity of ECp\* (E = Al, Ga) toward Low-Coordinate Transition Metal Amides [TM(N(SiMe<sub>3</sub>)<sub>2</sub>)<sub>2</sub>] (TM = Fe, Co, Zn): Insertion, Cp\* Transfer, and Orthometalation", *Inorg. Chem.* **2017**, 6, 3517–3525.

U. Herber, J. Moegling, R. Siris, A. Hoffmann, P. Mayer, C. Göbel, C. Lochenie, B. Weber, S. Herres-Pawlis: "A Study on Fe(II), Zn(II) and Cu(II) Complexes with Novel Tridentate Bis(pyrazolyl)methane Ligands", *Z. Anorg. Allg. Chem.* **2018**, 644, 1576–1592.

J. Weihermüller, S. Schlamp, W. Milius, F. Puchtler, J. Breu, P. Ramming, S. Hüttner, S. Agarwal, C. Göbel, M. Hund, G. Papastavrou, B. Weber: "Amphiphilic Iron(II) Spin Crossover Coordination Polymers : Crystal Structures and Phase Transition Properties", *J. Mater. Chem. C* **2019**, 7, 1151–1163.

C. Göbel, C. Hils, M. Drechsler, D. Baabe, A. Greiner, H. Schmalz, B. Weber: "Confined crystallization of spin-crossover nanoparticles in block-copolymer micelles", *Angew. Chem. Int. Ed.* **2020**, 59, 5765–5770.

C. Göbel, G. Hörner, A. Greiner, H. Schmalz, B. Weber, *Nanoscale Adv.* **2020**, 2, 4557–4565.

K. Keisers, H. Hüppe, L. Iffland-Mühlhaus, A. Hoffmann, C. Göbel, U.-P. Apfel, B. Weber, S. Herres-Pawlis, *Inorg. Chem.* **2020**, 20, 15343–15354.





## 11. Contributions to national and international conferences

C. Göbel, S. Förster, H. Schmalz, B. Weber: **Poster presentation** and **flash presentation** “Size control of spin crossover nanoparticles using block copolymers”, 15<sup>th</sup> Bayreuth Polymer Symposium, BPS ‘17, Bayreuth, Germany, 17.10.2017 – 19.10.2017.

C. Göbel, S. Förster, H. Schmalz, A. Greiner, B. Weber: **Poster presentation** and **flash presentation** “Miniaturization of SCO coordination polymers using block copolymer micelles”, 3<sup>rd</sup> International Conference on Functional Molecular Materials, FUNMAT 2017, Kraków, Poland, 8.11.2017 – 10.11.2017.

C. Göbel, A. Greiner, H. Schmalz, B. Weber: **Poster presentation** “Transition temperature shift of spin crossover coordination polymers in block copolymer micelles by thermal annealing”, 15<sup>th</sup> Koordinationschemie-Treffen, KCT2019, Munich, Germany, 03.03.2019 – 05.03.2019.

C. Göbel, A. Greiner, H. Schmalz, B. Weber: **Oral presentation** “Confined crystallisation of spin crossover nanoparticles in block copolymer micelles”, 17<sup>th</sup> Mitteldeutsches Anorganiker Nachwuchssymposium, MANS-17, Bayreuth, Germany, 12.09.2019.

C. Göbel, A. Greiner, H. Schmalz, B. Weber: **Poster presentation** and **flash presentation** “Confined crystallisation of spin crossover nanoparticles in block copolymer micelles”, 16<sup>th</sup> Bayreuth Polymer Symposium, BPS ‘19, Bayreuth, Germany, 22.09.2019 – 24.09.2019.

C. Göbel, A. Greiner, H. Schmalz, B. Weber: **Oral presentation** “Confined crystallization of spin crossover nanoparticles in block copolymer micelles”, 16<sup>th</sup> Koordinationschemie-Treffen, KCT2020, Freiburg, Germany, 01.03.2020 – 03.03.2020.



**12. (Eidesstattliche) Versicherungen und Erklärungen**

(§ 9 Satz 2 Nr. 3 PromO BayNAT)

Hiermit versichere ich eidesstattlich, dass ich die Arbeit selbstständig verfasst und keine anderen als die von mir angegebenen Quellen und Hilfsmittel benutzt habe (vgl. Art. 64 Abs. 1 Satz 6 BayHSchG).

(§ 9 Satz 2 Nr. 3 PromO BayNAT)

Hiermit erkläre ich, dass ich die Dissertation nicht bereits zur Erlangung eines akademischen Grades eingereicht habe und dass ich nicht bereits diese oder eine gleichartige Doktorprüfung endgültig nicht bestanden habe.

(§ 9 Satz 2 Nr. 4 PromO BayNAT)

Hiermit erkläre ich, dass ich Hilfe von gewerblichen Promotionsberatern bzw. -vermittlern oder ähnlichen Dienstleistern weder bisher in Anspruch genommen habe noch künftig in Anspruch nehmen werde.

(§ 9 Satz 2 Nr. 7 PromO BayNAT)

Hiermit erkläre ich mein Einverständnis, dass die elektronische Fassung meiner Dissertation unter Wahrung meiner Urheberrechte und des Datenschutzes einer gesonderten Überprüfung unterzogen werden kann.

(§ 9 Satz 2 Nr. 8 PromO BayNAT)

Hiermit erkläre ich mein Einverständnis, dass bei Verdacht wissenschaftlichen Fehlverhaltens Ermittlungen durch universitätsinterne Organe der wissenschaftlichen Selbstkontrolle stattfinden können.

---

Ort, Datum

---

Unterschrift